



Patrícia Freitas Rodrigues

Mestre em Engenharia Metalúrgica

Structural Evolution of Ni-Ti Alloy Wires Produced by Hot and Cold Rotary Forging

Dissertação para obtenção do Grau de Doutor em
Ciência e Engenharia de Materiais

Orientador: Prof. Dr. Francisco Manuel Braz Fernandes,
Professor Associado com Agregação
Faculdade de Ciências e Tecnologia
Universidade Nova de Lisboa, Portugal

Co-orientador: Prof. Dr. Andersan dos Santos Paula,
Professora Associada
Instituto Militar de Engenharia (IME), Brasil

Júri:

Presidente	Prof. Doutor Paulo Manuel Assis Loureiro Limão Vieira
Arguentes	Prof. Doutora. Maria Teresa Freire Vieira Prof. Doutor Manuel Fernando Gonçalves Vieira
Vogais	Prof. Doutor Francisco Manuel Braz Fernandes Prof. Doutor Benoit Malard Prof. Doutor Rui Jorge Cordeiro Silva



FACULDADE DE
CIÊNCIAS E TECNOLOGIA
UNIVERSIDADE NOVA DE LISBOA

Outubro - 2018

Patrícia Freitas Rodrigues

Mestre em Engenharia Metalúrgica

**Structural Evolution of Ni-Ti Alloy Wires Produced by Hot
and Cold Rotary Forging**

Dissertação para obtenção do Grau de Doutor em

Ciência e Engenharia de Materiais

Orientador: Prof. Dr. Francisco Manuel Braz Fernandes,
Professor Associado com Agregação
Faculdade de Ciências e Tecnologia
Universidade Nova de Lisboa,

Co-orientador: Prof. Dr. Andersan dos Santos Paula,
Professora Associada
Instituto Militar de Engenharia (IME), Brazil

Júri:

Presidente	Prof. Doutor Paulo Manuel Assis Loureiro Limão Vieira
Arguentes	Prof. Doutora. Maria Teresa Freire Vieira Prof. Doutor Manuel Fernando Gonçalves Vieira
Vogais	Prof. Doutor Francisco Manuel Braz Fernandes Prof. Doutor Benoit Malard Prof. Doutor Rui Jorge Cordeiro Silva



Outubro - 2018

Structural Evolution of Ni-Ti Alloy Wires Produced by Hot and Cold Rotary Forging

Copyright © Patrícia Freitas Rodrigues, Faculdade de Ciências e Tecnologia, Universidade Nova de Lisboa.

A Faculdade de Ciências e Tecnologia e a Universidade Nova de Lisboa têm o direito, perpétuo e sem limites geográficos, de arquivar e publicar esta dissertação através de exemplares impressos reproduzidos em papel ou de forma digital, ou por qualquer outro meio conhecido ou que venha a ser inventado, e de a divulgar através de repositórios científicos e de admitir a sua cópia e distribuição com objectivos educacionais ou de investigação, não comerciais, desde que seja dado crédito ao autor e editor.

This thesis is dedicated

To my Parents, António and Selma

and my brother Charles

Dedico este trabalho

aos meus pais, António e Selma

e ao meu irmão Charles

Acknowledgements

To God, for the gift of life, for the opportunity to begin and conclude one more step in my life, for every moment of learning and overcoming.

To the New University of Lisbon, through the Department of Materials Sciences, Faculty of Science and Technology, for the opportunity to participate in the doctoral program in materials science and engineering.

To Coordenação de Aperfeiçoamento de Pessoal de Nível Superior (CAPES-Brazil) through the federal program " Ciências Sem Fronteiras", for the grant scholarship.

To CENIMAT and DCM, which through its employees and professors helped me many times.

To my Professor and Advisor Dr. Francisco Manuel Braz Fernandes for his attention, for his patience, for not letting me give up or discourage. For all the learning, exchange of knowledge, for countless discussions of the results. I thank you for all the academic opportunity that has provided me along these years. For helping me draw every step of this work, I am honored to have been your student.

To my Professor Dr. Andersan dos Santos Paula, for all dedication and friendship. For the unique opportunity to be completing this step with your collaboration. Throughout, conducting assays, conversations, discussions about results and content. I also thank you for all your personal and psychological support and for all the representativeness in my life.

To Professor Dr. Teresa Cidade coordinator of the doctoral program for all availability whenever I needed some guidance.

To the MIDAS project for the opportunity to break borders and be able to carry out a work with the various partnerships (Universidade Federal Fluminense, Instituto Militar de Engenharia, Universidade Politécnica de Timisoara, Universidade das Ilhas Baleares).

To all other professors of the group of structural materials for teaching and supporting in different assays.

To Professor Dr. Jorge Otubo and his team of the Aeronautical Technological Institute (ITA), Brazil for the material offered for studies.

To Rafaella Magalhães, by the partnership and discussion of results on orthodontics fields and the materials provided.

To the Morelli company for supplying the superelastic and thermo-activated orthodontic archwires.

To the GAC company for supplying the Bioforces orthodontic archwires used in this study.

To UNIDEMI in collaboration with Professor Dr. Telmo Santos and Parick Inacio to perform the localized heat treatment in the commercial superelastic orthodontic archwire Morelli.

To Dr. João Pedro Oliveira for all support, friendship and partnership. Thank you for each reading, results discussion and works conclusion.

To Professor Dr. Teresa Vieira, from the University of Coimbra, Portugal, I thank you for your suggestions as a member of the thesis Monitoring committee.

To Professor Dr. Rui Silva, from the New University of Lisbon, Portugal, I thank you for your support in measurements and providing materials and attention as a member of the thesis Monitoring committee.

To the laboratories of X-ray diffraction (synchrotron radiation): to Dr. Norbert Schell, Dr. Andreas Stark and Dr. Emad Maawad, for receiving us at the High Energy Materials Science Beamline P-07 from PETRA-III, Deutsches Electronen Synchrotron (DESY, Hamburg) and for their help during the experiments; and to the specialist Leonardo Wu for receiving us at the National Synchrotron Light Laboratory (LNLS, Campinas, SP, Brazil) and for his help during the experiments.

The team of beam time, Professor Francisco Manuel Braz Fernandes, João Pedro Oliveira, Professor Andersan dos Santos and Thiago Ferrão. Still to Edgar Camacho, for countless hours of rehearsal and then for support in developing scripts to facilitate our lives in representations and interpretations of results.

To Dr. Benoit Malard - CIRIMAT, ENSIACET, INP Toulouse, for providing the access to Electron Microprobe Analysis from UMS 3623 - Centre de MicroCaractérisation Raimond Castaing, Toulouse.

To Dr. Philippe De Parseval and Dr. Sophie Gouy from UMS 3623 - Centre de MicroCaractérisation Raimond Castaing for Electron Microprobe Analysis performed on some of the samples.

To Professor Dr Ritwik Basu from Indian Institute of Technology Bombay – India for EBSD tests performed in this work.

To the Military Institute of Engineering (IME Brazil) that through the team: Rodolfo, Saulo, Mônica, Andrey, Naiara, Thiago, conducted tests in the SEM and also exchange of knowledge and other activities developed.

To Dr. Shimeni Ribeiro for all these years of coexistence, works developed and EBSD tests performed in Universidade Federal Fluminense.

To the company Villares Metals, for conducting the chemical analysis of the starting materials of this work.

Last but not least, the people of my life...

To my parents Antônio Barizon, Selma Freitas, my brother Charles Barizon who during my life have always stood beside me to support me, not letting me give up and encouraging me to always dream, reaching out to me always. Our union makes a difference. My sister-in-law Andrea and our Princess Maria Antonia for every moment overcome, every smile and word that are fundamental to our happiness, together we are invincible.

To Miguel for being my base, for always being by my side, for smiling with me, for being happy in every victory, for wiping my tears, for sharing joys and frustrations, for encouraging me, for rooting for my success, for teaching me every day, for looking at me beyond of the eyes... for being simply you... You're my person!

To my relatives, uncles and cousins in which each, in his own way, contributed to that in this stage of my life.

To my friends and team "ME": Andreia, Edgar, Fernanda and Estefânia. Without you, I wouldn't have done half of what I accomplished. Your participation goes beyond a professional activity, you are part of my life. By our coexistence I'm sure no one does anything alone, together we are stronger.

To Andreia Lopes, in particular for being with me since the beginning. For sharing happy and less happy moments. For sharing with me words and thoughts, you have been very important in these years. I will take you to my life!

To the friends Portugal presented me: Alessandra and Manu for the coexistence and enormous help over these years.

To my friends of all time, present in several stages of my life, Ana Paula, Danusa, Júnior, Flávia, Gabriele, Itamara, Mariama, Millene, Nathália, Polliana, Eduardo, Lidiane, Victor, Carla, Tiago, Thaís. You are part of one more chapter of my life.

To the friends that visited me and shared a little more closely this moment: Ana Paula, Luís Fernando, Eduardo, Cristiane, Thaís, Nathália, Ricardo, Adriana, Vanessa, Leilson. Your presence was very important.

To Carol who has been a part of my life for many years, even far away, she has managed to be present at all times. My dear friend an ocean away is nothing. Thank you for always being my companion.

To Victor Lauriano for being important in my life, more than a friend from the beginning of this walk to life. Always supporting me at all professional and personal moments, smiling or crying... he's always been there for me.

To all who have in some way contributed to the realization of this work and who I have not mentioned here.

Thank you very much!

Agradecimentos

À Deus, pelo dom da vida, pela oportunidade de iniciar e concluir mais uma etapa em minha vida, por cada momento de aprendizagem e superação.

À Universidade Nova de Lisboa, por meio do Departamento de Ciências de Materiais da Faculdade de Ciências e Tecnologia, pela oportunidade de participação no Programa Doutoral em Ciências e Engenharia de Materiais.

Ao Coordenação de Aperfeiçoamento de Pessoal de Nível Superior (CAPES - Brasil) por meio do programa Federal “Ciências sem Fronteiras”, pela concessão da bolsa de estudos.

Ao CENIMAT, que através de seus funcionários e professores fizeram parte dessa caminhada com seus trabalhos desenvolvidos, ensinamentos e dedicação.

Ao meu professor orientador Doutor Francisco Manuel Braz Fernandes por sua atenção, por sua imensa paciência, por não me deixar desistir e desanimar. Por toda aprendizagem, troca de conhecimentos e por inúmeras discussões dos resultados. Agradeço ainda por toda oportunidade acadêmica que me proporcionou ao longo destes anos. Por me ajudar a desenhar cada passo deste trabalho, sinto-me honrada em ter sido seu orientada.

À minha professora orientadora Doutora Andersan dos Santos Paula, por todos esses anos de convivência dedicação e amizade. Pela oportunidade única de estar concluindo mais esta etapa com sua participação. Por todo ensinamento, realização de ensaios, conversas, debates sobre resultados e conteúdo. Agradeço ainda por todo apoio pessoal e psicológico e ainda por toda a representatividade em minha vida.

À Professora Doutora Teresa Cidade Coordenadora do Programa Doutoral por toda disponibilidade sempre que precisava de alguma orientação.

Ao Projeto MIDAS pela oportunidade de quebrar fronteiras e poder realizar um trabalho com as diversas parcerias (Universidade Federal Fluminense, Instituto Militar de Engenharia, Universidade Politécnica de Timisoara, Universidade das Ilhas Baleares).

Aos demais professores do grupo de materiais estruturais pelos ensinamentos e apoio em diversos ensaios.

Ao Doutor Jorge Otubo e sua equipe do Instituto Tecnológica da Aeronáutica (ITA), Brasil pelo material cedido para estudos.

À Rafaella Magalhães, pela parceria e imensas discussões de resultados sobre ortodontia e pelos materiais fornecidos.

À empresa Morelli pelo fornecimento dos fios superelásticos e termo-ativados.

À empresa GAC pelo fornecimento dos fios BioForces usados neste trabalho.

Ao UNIDEMI em colaboração com Professor Doutor Telmo Santos e ao Doutorando Parick Inacio realizaram o tratamento térmico localizado no fio superelástico comercial Morelli.

Ao colega Doutor João Pedro Oliveira por todo apoio, amizade e parceria. Obrigada por cada leitura, discussão de resultados e conclusões de trabalhos.

À Professora Doutora Teresa Vieira, da Universidade de Coimbra, Portugal, agradeço as suas sugestões enquanto membro da comissão de acompanhamento da tese.

Ao Professor Doutor Rui Silva, da Universidade Nova de Lisboa, Portugal, agradeço ao seu apoio em ensaios e disponibilização de materiais e atenção enquanto membro da comissão de acompanhamento da tese.

Aos laboratórios de difração de raios-X (radiação de sincrotrão): ao Dr. Norbert Schell, Dr. Andreas Stark e Dr. Emad Maawad, por nos receber no Deutsche Electron Synchrotron (DESY) e pela sua ajuda durante as experiências; e ao Especialista Leonardo Wu por nos receber no Laboratório Nacional de Luz de Sincrotrão (LNLS) e pela sua ajuda durante as experiências.

Os companheiros de tempo de feixe, Professor Doutor Francisco Manuel Braz Fernandes, ao Doutor João Pedro Oliveira, Doutora Andersan dos Santos e Mestre Thiago Ferrão. Ainda ao Mestre Edgar Camacho, pelas inúmeras horas de ensaio e depois pelo apoio ao desenvolver scripts para facilitar nossa vida em representações e interpretações dos resultados.

Ao Doutor Benoit Malard - CIRIMAT, ENSIACET, INP Toulouse, por viabilizar os ensaios de microsonda em UMS 3623 - Centre de MicroCaractérisation Raimond Castaing.

Ao Doutor Philippe De Parseval e a Doutora Sophie Gouy do UMS 3623 - Centre de MicroCaractérisation Raimond Castaing for Electron Microprobe Analysis pela realização das análises de microrsonda em algumas amostras do trabalho.

Indian Institute of Technology Bombay – India; em colaboração com o Professor Doutor Ritwik Basu pela realização das análises de EBSD.

Ao Instituto Militar de Engenharia (IME Brazil) que através da equipe: Rodolfo, Saulo, Mônica, Andrey, Naiara, Thiago, realizaram ensaios no MEV e ainda troca de conhecimentos e outras atividades desenvolvidas.

À Doutora Shimeni Ribeiro por todos esses anos de convivência, trabalhos desenvolvidos e análise de EBSD realizadas na Universidade Federal Fluminense.

À empresa Villares Metals, pela realização da análise química dos materiais de partida deste trabalho.

E por último, mas não menos importante, as pessoas de minha vida...

Aos meus pais Antônio Barizon, Selma Freitas, meu irmão Charles Barizon que no decorrer de minha vida sempre estiveram ao meu lado para me apoiar, não me deixar desistir e me estimulou a sonhar sempre me estendendo a mão em todos os momentos. A nossa união faz diferença. A minha cunhada Andrea e nossa princesa Maria Antonia porcada momento superado, cada sorriso e palavra que são fundamentais para nossa felicidade, juntos somos imbatíveis.

Ao Miguel por ser minha base, por estar ao meu lado sempre, por sorrir comigo, por ficar feliz em cada vitória, por enxugar minhas lágrimas, por dividir alegrias e frustrações , por me incentivar, por torcer pelo meu sucesso , por me ensinar todos os dias, por me olhar além dos olhos... por ser simplesmente você... Você é a minha pessoa!

Aos meus familiares, tios e primos em que cada um, à sua maneira, contribuiu para que nesta etapa de minha vida.

Aos meus amigos e equipe “ME”: Andreia, Edgar, Fernanda e Estefânia. Sem vocês não teria realizado metade do que realizei. A participação de vocês vai além de uma atividade profissional, vocês fazem parte de minha vida. Por nossa convivência eu tenho a certeza que ninguém faz nada sozinho, juntos somos mais fortes.

À Andreia Lopes, em especial, por estar comigo desde o início. Por dividir momentos felizes e menos felizes. Por dividir comigo palavras e pensamentos, você foi muito importante nestes anos. Vou te levar para vida!

Às minhas amigas que Portugal que presenteou: Alessandra e Manu pela convivência e pela enorme ajuda ao longo desses anos.

Aos meus amigos de sempre, presentes em diversas etapas de minha vida, Ana Paula, Danusa, Júnior, Flávia, Gabriele, Itamara, Mariama, Millene, Nathália, Polliana, Eduardo, Lidiane, Victor, Carla, Tiago, Thaís. Vocês fazem parte de mais um capítulo da minha vida.

Aos amigos que Deus proporcionou me visitar e dividir um pouco mais de perto este momento: Ana Paula, Cristiane, Luís Fernando, Eduardo, Thaís, Nathália, Ricardo, Adriana, Vanessa, Leilson. A presença de vocês foi muito importante.

À Carol que faz parte de minha vida a muitos anos, mesmo longe conseguiu ser presente em todos os momentos. Minha amiga querida um oceano de distância não é nada. Obrigada por ser sempre minha companheira.

Ao Victor Lauriano por ser importante na minha vida, mais que um amigo desde o início desta caminhada para vida. Sempre me apoiando em todos os momentos profissionais e pessoais, sorrindo ou chorando ... ele sempre esteve ao meu lado.

A todos que de alguma forma contribuíram para a realização deste trabalho e que aqui não tenha mencionado.

Muito Obrigada!

Abstract

Ni-Ti shape memory alloys (SMA), have interesting functional properties such as shape memory effect and superelasticity that enable their use in different segments. These functional characteristics are obtained through the thermomechanical processing (hot and cold). The hot deformation may promote the intended metallurgical transformations and the microstructural changes are improved by final cold deformation. These processes influence the final mechanical properties of the materials and, by consequence, their applications. This work focused on a Ni-rich Ni-Ti alloy, which may be used in the orthodontic archwires since the alloys used for this purpose need to show superelastic characteristics at room and oral temperature. It is sought by the mechanical and thermal treatments that the material displays an austenite finish temperature below room temperature.

In this work, the characteristics of the thermomechanical processing are studied using samples representative of the different processing steps. For each processing step, the effect of the process parameters on the phase transformation temperature, superelasticity and shape memory effects was assessed and correlated to its microstructure. The structural analysis of each sample was performed by different techniques, which allowed the identification of the thermomechanical processing evolution. It was noticed that the austenite finish temperature was close to room temperature for all the steps. For all the samples, an austenite matrix at room temperature was observed. Different heat treatments were applied to identify the most suitable changes to be proposed along the rotary forging steps. Thermomechanical treatments were performed to understand and verify the structural evolution (by X-ray diffraction, using synchrotron radiation) and the mechanical behavior during the hot and cold deformations. These treatments allowed us to observe and discuss restoration phenomena, such as dynamic recovery and recrystallization.

In addition, orthodontic archwires were studied in a reverse engineering approach to identify their structural characteristics and the corresponding functional behavior. The characterization of commercial functionally graded NiTi orthodontic archwire was performed and the introduction of graded functionality in conventional archwires was analyzed.

This study aimed to contribute to the development of processing strategies that will give rise to more consistently uniform characteristics of Ni-Ti shape memory alloys and a minimization of the failures occurring during processing.

Keywords: Shape Memory Alloys, Rotary Forging, Synchrotron Radiation, Dynamic Recrystallization, Orthodontic Archwires

Resumo

As ligas de Ni-Ti com memória de forma, possuem propriedades funcionais bem distintas, tais como memória de forma e superelasticidade, que viabilizam o seu uso em diversos segmentos. Essas características são obtidas a partir dos processamentos termomecânicos, a quente ou a frio, aplicados ao material. A deformação a quente promove as transformações metalúrgicas pretendidas e a microestrutura é modificada pelas deformações a frio subsequentes. Esses processamentos influenciam o comportamento mecânico e as propriedades finais e, por conseguinte, a sua aplicação final.

Este trabalho teve como foco o estudo de uma liga Ni-Ti rica em níquel, que pode ser usada para produção de fios ortodônticos e que apresente para tal comportamento superelástico próximo da temperatura ambiente e temperatura oral. Esse comportamento é obtido através de tratamentos mecânicos e térmicos aplicados.

Neste trabalho são estudadas as características do processamento termomecânico, através de cada uma das amostras representativas das diferentes etapas de processamento. Para as amostras das diferentes etapas de processamento, o efeito dos parâmetros de processo na temperatura da transformação de fase, os efeitos de memória de forma e superelasticidade foram avaliados e correlacionados com a sua microestrutura. A análise estrutural de cada amostra foi realizada por diferentes técnicas que permitiram a observação da evolução do processamento termomecânico. Obteve-se, para todos os passos de processamento estudados, uma temperatura de final de transformação em austenite próxima da temperatura ambiente. O material com uma matriz austenítica à temperatura ambiente foi observado para todas as amostras. Foram realizados tratamentos térmicos para identificar as alterações a propor nos tratamentos ao longo do forjagem rotativa. Foram realizados tratamentos termomecânicos para entender e verificar a evolução estrutural (por difração de raios-X usando radiação de sincrotrão) e o comportamento mecânico durante as deformações a quente e a frio. Estes tratamentos permitem observar e discutir fenômenos de recuperação e de recristalização dinâmicas.

Além disso, os arcos ortodônticos foram usados em uma abordagem de engenharia reversa para identificar a sua estrutura e as correspondentes características funcionais. Foi realizada a caracterização de arames ortodônticos comerciais e foi analisada a introdução de gradiente funcional em arcos convencionais.

Este estudo teve como objetivo contribuir para o desenvolvimento de estratégias de processamento que darão origem a características mais consistentemente uniformes das ligas com memória de forma e a uma minimização das falhas ocorridas durante o processamento.

Palavras-chave: Ligas com Memória de Forma, Forjagem Rotativa, Radiação de Sincrotrão, Recristalização Dinâmica, Arames Ortodônticos.

Contents

1.	INTRODUCTION	1
1.1.	Structure of the Study	2
2.	STATE OF THE ART	5
2.1.	Ni-Ti Shape Memory Alloys	5
2.1.1.	Phase Diagram and Crystal Structures	6
2.1.2.	Shape Memory Effect and Superelasticity	7
2.1.3.	Precipitation Phenomena	12
2.2.	Processing	16
2.2.1.	Casting Process	17
2.2.2.	Heat Solution Treatment Before Thermomechanical Process	18
2.2.3.	Thermomechanical Process	20
2.2.3.1.	Hot Working	20
2.2.3.2.	Cold Working	26
2.2.4.	Heat Treatments	26
2.2.5.	Functional Gradient	28
2.3.	Textural Evolution	31
2.4.	Orthodontic Archwires	34
3.	MATERIALS AND METHODS	39
3.1.	Ni-Ti Alloys	40
3.1.1.	As-cast and Remelted alloys	40
3.1.2.	Thermomechanical Process	41
3.1.3.	Heat Treatments	44
3.2.	Orthodontic Archwires	45
3.2.1.	Localized Heat Treatment Performed in Superelastic Orthodontic Archwire (Morelli SE)	45
3.3.	Characterization Techniques	46
3.3.1.	Scanning electronic microscopy (SEM)	46
3.3.2.	Electron Backscattered Diffraction (EBSD)	47

3.3.3.	Electron Microprobe Analysis (EMPA)	47
3.3.4.	Optical microscopy (OM).....	47
3.3.5.	X-Ray Diffraction Analysis (XRD).....	47
3.3.5.1.	Conventional X-Ray Source (XRD).....	48
3.3.5.2.	Synchrotron Radiation X-ray Diffraction (SR-XRD).....	49
3.3.5.3.	Petra III – P07/DESY	49
3.3.5.4.	LNLS - XRD 1 / CNPEM.....	53
3.3.6.	Differential Scanning Calorimetry (DSC).....	54
3.3.7.	Thermomechanical Analysis (TMA)	55
3.3.7.1.	Dilatometric Analysis	55
3.3.7.2.	Three-point Bending Tests	56
3.3.8.	Mechanical testing	56
3.3.8.1.	Three-point bending tests	56
4.	RESULTS AND DISCUSSION	59
4.1.	Starting Materials (as-cast and remelting condition).....	60
4.1.1.	Microstructural Characterizations of the alloys 1, 2 and 3 (first hot deformation and second cold deformation samples).....	64
4.1.2.	NiTi_1_Rem Alloy 1 As Remelted	66
4.1.3.	Starting Materials Summary.....	68
4.2.	Initial Thermomechanical Process (Rotary Forging Steps)	69
4.2.1.	Hot Rotary Forging Steps.....	69
4.2.1.1.	First Hot Rotary Forging Step.....	69
4.2.1.2.	Third Hot Rotary Forging Step	73
4.2.2.	Cold Rotary Forging Steps	76
4.2.2.1.	First Cold Rotary Forging Step	76
4.2.2.2.	Second Cold Rotary Forging Step.....	79
4.2.3.	Rotary Forging Process Evolution.....	81
4.2.3.1.	Microstructural and Compositional Evolution by Thermal and Chemical Analysis	82
4.2.3.2.	Microstructural Evolution by Optical Microscopy	85
4.2.3.3.	Microstructural Evolution by EBSD.....	87
4.2.3.4.	Microstructural Evolution by SEM	91
4.2.3.5.	Textural Evolution.....	93
4.2.4.	Rotary Forging Process Evolution Summary.....	95
4.3.	Heat Treatments	96
4.3.1.	Initial Solution Heat Treatment	97

4.3.2.	Solution Heat Treatment between deformations steps.....	98
4.3.2.1.	First Hot Forging Sample (NiTi_1_1F_1h)	98
4.3.2.2.	First Hot Forging Sample (NiTi_1_1F_1h) and First Hot Forging Sample (NiTi_1_1F_1h) heat treated at 800 °C during 10 minutes.	100
4.3.2.3.	Comparison of the First Hot Forging Sample heat treated at 800 °C during 10 minutes and First Hot Forging Sample heat treated at 800, 850, 900 and 950 °C during 120 minutes	101
4.3.3.	Intermediate Heat Treatment (850 °C during 15 minutes)	108
4.3.4.	Aging Treatment.....	110
4.3.5.	Thermomechanical Process Proposed (Rotary Forging Route)	113
4.4.	Thermomechanical Process Simulation	114
4.4.1.	Optimization of Hot and Cold Working Parameters Using Synchrotron Radiation	114
4.4.2.	Optimization of Hot Deformations with Different Strain Rate.....	124
4.4.3.	Aging Treatment Optimization	128
4.4.4.	Thermomechanical Process Simulation Summary	131
4.5.	Orthodontic Archwires.....	132
4.5.1.	Superelastic orthodontic archwire	133
4.5.2.	Thermo-active orthodontic archwire	135
4.5.3.	Ni-Ti orthodontic archwires with graded actuating forces	136
4.5.4.	Commercial Ni-Ti Orthodontic Archwires Summary	143
4.5.5.	Functionally Graded Orthodontic Archwires.....	143
5.	CONCLUSIONS AND FUTURE WORK.....	153
5.1.	As-cast and remelt	153
5.2.	Hot Forging Steps	153
5.3.	Cold Forging Steps.....	154
5.4.	Aging Heat Treatment	154
5.5.	Orthodontic Archwires Characteristics.....	154
5.6.	Future Work.....	155
6.	REFERENCES	157
7.	APPENDIX	167

List of Figures

Figure 2.1 - Phase diagram of Ti-Ni alloy with the phase equilibrium between the B2 and Ni_4Ti_3 phases added. (Otsuka, 2002) 6

Figure 2.2 - Scheme of transformation of (a) cubic (B2) austenite to (b) monoclinic (B19') phase. (Miyazaki, 2009) 7

Figure 2.3 - (a), (b) and (c) Schematic illustration of the mechanism of the shape-memory effect and superelasticity. (Otsuka, 2002) 8

Figure 2.4 - Typical superelastic behavior diagram of a shape memory alloy. (Chowdhury, 2017) 9

Figure 2.5 - Stress-temperature diagram for shape memory alloy. (Otsuka, 2005) 10

Figure 2.6 - Schematic drawing of stress-induced phase transformations as observed in a uniaxial tensile loading/unloading experiment with two-step transformations. Stress is plotted as a function of strain. (Olbricht, 2011) (b) stress x strain curves (compression and tension behavior). [adapted from (Sittner, 2005)] 12

Figure 2.7 - TTT diagram describing aging behavior for Ti-52 at%Ni. (Nishida, 1986) 13

Figure 2.8 - TTT (time-temperature-transformation) for the effect of shorter ageing temperature and time on the transformation temperature of Ti-50.8% Nitinol wire with a starting A_f temperature of 11 °C. (Pelton, 2000) 13

Figure 2.9 - A unified model for explaining the microstructure evolution at low Ni supersaturation (a and b) and high Ni supersaturation (c and d). It also explains both three-stage and two-stage transformation behavior of supersaturated Ti–Ni solid solution. (Fan, 2004) 15

Figure 2.10 - Dependence of M_s Temperature on Ni composition of Ni-Ti alloys, left Tang et al. (Tang, 1997), right Frenzel et al. (Frenzel, 2010) 16

Figure 2.11 - Schematic view of NiTi manufacturing process. [adapted from (Nakahata, 2011)] 17

Figure 2.12 - Metastable phase diagram of the Ti–Ni system with the Ni content rang studied. [adapted from (Povoden-Karadeniz, 2013)] 19

Figure 2.13 – Ni-Ti SMA true stress-true strain curves at different temperatures and strain rate $0.001 s^{-1}$. (Morakabati, 2011) 23

Figure 2.14 - Optical microstructures of Ni-Ti samples at 800 °C – (a) $0.001 s^{-1}$; (b) $0.01 s^{-1}$; (c) $0.1 s^{-1}$ and (d) $1 s^{-1}$. [adapted from (Jiang, 2013a)] 23

Figure 2.15 - Microstructural evolution of Ni-Ti alloy with increasing strain, deformed in compression at temperature of 1050 °C and a strain rate of $0.1 s^{-1}$. (Khamei, 2010) 24

Figure 2.16 - Work hardening rate analyses. It should be noted that third order polynomials were fitted to the ϑ – σ curves (until the peak point corresponding to $\vartheta=0$) to get smoother $-d\vartheta/d\sigma$ – σ curves. (Mirzadeh, 2014) 25

Figure 2.17 - DSC charts of the samples after solution treatment at 800 °C/15 min and aged at 400, 450, and 500 °C for 30 and 60 minutes. (Lekston, 2016) 27

Figure 2.18 - Designs of microstructural or compositional functionally graded (FG) Ni-Ti. (a) and (b) show examples of functionally graded in series and parallel configuration (d). (e) and (f) show examples of the series configuration mechanical behavior and parallel configuration mechanical behavior. [adapted from (Shariat, 2017)].....	29
Figure 2.19 - Tensile deformation behavior of Ti-50.8 at.%Ni wires after local over-aging by electrical resistance heating. (higher plateau – no heat-treated section and lower plateau – treated section). (adapted from (Shariat, 2017)).....	30
Figure 2.20 - The $\phi 2$ sections of the complete orientation distribution function (ODF) of (a) starting material and (b) 60 %, (c) 80% and (d) 90% deformed Ni-Ti. (Suresh, 2012)	32
Figure 2.21 - Observed reflection on wire axis and diffraction pattern of the B2 phase. (Willemse, 1991)	33
Figure 2.22 - Pole Figures $(110)_{B2}$ obtained from as-received, heat treated at 500 °C and deformed. (Paula., 2007)	33
Figure 2.23 - Sequence of the orthodontic treatment. (Files provided by Dr. Raffaella Magalhães with patient authorization).....	34
Figure 2.24 - Load-deflection curves of the wires with graded actuating forces at different temperature and the superelastic actuation is identified.....	35
Figure 3.1 – Vacuum Arc Remelting (VAR) a) During remelting process; b) After remelting process; and c) three processed ingots.....	41
Figure 3.2 – Scheme of the initial thermomechanical processing applied to the ingots, with forging stages, temperature and time of the intercalated heat treatments and sample diameters.....	42
Figure 3.3 - Equipment: a) 4 hammers and b) 2 hammers, used to rotary forging steps.....	42
Figure 3.4 - Scheme for the samples identification.....	44
Figure 3.5 - Schematic view of the electrical local heating system of Ni-Ti wire and temperature profile. (Unpublished data from Inácio and Santos)	46
Figure 3.6 - Schematic representation of the Bragg's law.....	48
Figure 3.7 - Examples of XRD results (1F1q sample), at high/low temperature: during heating and cooling, between –120 and 120 °C (a); Pole Figures (b) (Rodrigues, 2017a).....	49
Figure 3.8 - Scheme of the SR-XRD measurement at room temperature along the sample diameter.	50
Figure 3.9 - Schematic representation of the SR-XRD measurement at room temperature along gauge length (32 mm), total length of the localized heat treatment. Phi 0 and phi 90 to the normal direction. (more details in the text)	51
Figure 3.10 - Scheme of the direction of the beam, part of the interior of the equipment and the position of the detector in relation to the sample.....	52
Figure 3.11 - Scheme of the thermomechanical process with in-situ deformation experiments (thermomechanical cycles performed in DESY)	53
Figure 3.12 - Thermo-mechanical simulator, the Gleeble® Synchrotron system and scheme of the measurement.	53

Figure 3.13 - Scheme of the thermomechanical process applied with strain rate of 10^{-3} s^{-1} (hot deformations performed in LNLS).....	54
Figure 3.14 - Differential scanning calorimetry schemes.	55
Figure 3.15 - Displacements (0.5, 0.75 and 1.0 mm) analyzed in deflection curve (slope of the deactivation curve - superelastic behavior).....	57
Figure 4.1 - (a) DSC curves NiTi_1_as-cast and remelted samples (b) SR - XRD - NiTi_1_as-cast and remelted samples	60
Figure 4.2 - (a) DSC curves NiTi_2_as-cast and remelted samples (b) SR - XRD - NiTi_2_as-cast and remelted samples	61
Figure 4.3 - (a) DSC curves NiTi_3_as-cast and remelted samples (b) SR - XRD - NiTi_3_as-cast and remelted samples	62
Figure 4.4 – DSC results: (a) heating up to 500 °C, (b) A_f temperature (remelted condition, after solution heat treatment at 950 °C during 2 h and after heating up to 500 °C.	63
Figure 4.5 - (a) DSC curves (b) SR-XRD diffractograms of the 1, 2 and 3 alloys at first hot deformation step (1F_1h) and at first cold deformation step (6F_4h2c).	65
Figure 4.6 - SEM images of NiTi_1_rem: (a) Secondary electron image, (b) Backscattered image.....	67
Figure 4.7 – (a) EDS results of the NiTi_1_Rem sample, (b) Micrograph of the NiTi_1_rem. (c and b) EBSD map of NiTi_1_rem sample at room temperature.	68
Figure 4.8 – (a) DSC curves NiTi_1_1F_1h sample (b) SR - XRD of NiTi_1_1F_1h sample.	70
Figure 4.9 - XRD results at high/low temperature: (a)during heating and cooling, between -120 and 120 °C (b) separate diffractograms for three different temperatures (-120, 25 and 120 °C).....	71
Figure 4.10 – (a) Heat release by continuous heating of the NiTi alloy to different maximum temperatures. (b) DSC curves: NiTi_1_1F1h (N-HTT = NiTi_1_1F1h without heat treatment) and NiTi_1_1F_1h heat treated from 250 to 450 °C.	72
Figure 4.11 – Recovery recrystallization results: (a) DSC curves heat treated to 500 °C; (b) XRD at high temperature and (c) FWHM and d-spacing observed.	73
Figure 4.12 - (a) DSC curves NiTi_1_3F_3h sample (b) SR - XRD of NiTi_1_3F_3h sample.	74
Figure 4.13 - NiTi_1_3F_3h XRD results at high/low temperature: (a) during heating and cooling, between -120 and 120 °C (b) separate diffractograms for three different temperatures (-120, 25 and 120 °C).....	75
Figure 4.14 – NiTi_1_3F_3h - Recovery recrystallization results: (a) DSC curves heat treated to 500 °C; (b) XRD at high temperature and (c) FWHM and d-spacing observed.....	76
Figure 4.15 – (a) DSC curves NiTi_1_5F_4h1c sample (b) SR - XRD of NiTi_1_5F_4h1c sample.	77
Figure 4.16 – NiTi_1_5F_4h1c XRD results at high/low temperature: (a)during heating and cooling, between -120 and 120 °C (b) separate diffractograms for three different temperatures (-120, 25 and 120 °C).....	77

Figure 4.17 – NiTi_1_5F_4h1c - Recovery recrystallization results: (a) DSC curves heat treated to 500 °C; (b) DSC thermal characterization from -150 to 150 °C before and after heat treatment to 500 °C compared (1- before heat treatment -dash line and 2- after heat treatment – solid line).....	78
Figure 4.18 – (a) DSC curves NiTi_1_6F_4h2c sample (b) SR - XRD of NiTi_1_6F_4h2c sample.....	79
Figure 4.19 – NiTi_1_6F_4h2c XRD results at high/low temperature: (a)during heating and cooling, between -120 and 120 °C (b) separate diffractograms for three different temperatures (-120, 25 and 120 °C).....	80
Figure 4.20 – NiTi_1_6F_4h2c - Recovery recrystallization results: (a) DSC curves heat treated to 500 °C; (b) DSC thermal characterization from -150 to 150 °C before and after heat treatment to 500 °C compared (1- before heat treatment -dash line and 2- after heat treatment – blue line).	81
Figure 4.21 – DSC curves of the Rem., 1F1h,3F3h, 5F_4h1c and 6F_4h2c steps, cooling curves and heating curves.	82
Figure 4.22 – Chemical analysis (EMPA) results (a) elements at.%; (b) Comparison between at.%Ni x A _f ; (c) elements at.% global composition values, in addition Ni effective after Ti ₂ Ni ₄ O and TiC observation..	84
Figure 4.23 – Micrographs of the NiTi_1 alloy hot and cold deformations steps.	86
Figure 4.24 - Enlarged image quality maps of the NiTi_1 alloy hot and cold deformations steps.	88
Figure 4.25 - Enlarged image quality maps of NiTi_1_1F_1h sample	90
Figure 4.26 - Enlarged image quality maps of NiTi_1_3F_3h sample	90
Figure 4.27 - SEM images of the NiTi_1 alloy hot and cold deformations steps (backscatter mode).	92
Figure 4.28 - Variation of the 2θ peak position and intensity of the (110) _{B2} (200) _{B2} (211) _{B2} peaks along the azimuthal angle (transmission mode) and Pole Figure (110) _{B2} (reflection mode) of the NiTi_1 alloy hot and cold deformations steps.	94
Figure 4.29 - a) comparison between DSC curves (a) and superposition of the SR-XRD patterns (b) of NiTi_1_Rem sample and NiTi_1_Rem heat-treated at 800 °C during 30 minutes and 950 °C during 120 minutes.....	97
Figure 4.30 – Scheme of locations of the SR-XRD measurements on the samples and First structural characterization: A) Outer Spot - Debye–Scherrer rings, B) Inner Spot - Debye–Scherrer rings of first hot forging step (NiTi_1_1F_1h).	99
Figure 4.31 – DSC curves of the First Hot Forging Sample (NiTi_1_1F_1h)– Spot A (outer) and Spot B (inner)	100
Figure 4.32 – a) comparison between SR-XRD pattern of First Hot Forging Sample (NiTi_1_1F_1h) and First Hot Forging Sample (NiTi_1_1F_1h) heat-treated at 800 °C during 10 minutes c) DSC curves.	101
Figure 4.33 – a) DSC curves on cooling from the B2 regime and DSC curves on heating from the B19'. The five DSC curves show the influence of solution heat treatment. b) Peak temperatures - Mp cooling and Ap heating.	103
Figure 4.34 - Debye–Scherrer diffraction rings at the outer (A) and inner (B) of the mapped area presented in Figure 3 for each sample (800 °C/10 min, 800 °C/120 min, 850 °C/120 min, 900 °C/120 min and 950 °C/120 min.	103

Figure 4.35 – a) outer (A) b) (B) inner – Sequence of XRD line diagrams at different solution heat treatment obtained by the integration of the diffraction patterns recorded at room temperature.	105
Figure 4.36 – Cartesian and 3d plots transform of Debye–Scherrer diffraction rings (azimuthal angles) vs. 2θ for A and B spots for each heat-treated sample.....	106
Figure 4.37 - Microstructure of the specimens submitted to solution heat treatment.	107
Figure 4.38 - Partial phase diagram of Ti-Ni system. (adapted from (Somsen, 1999))	109
Figure 4.39 - DSC Curves of aging temperatures at 30 minutes soaking time: 350 °C, 400 °C and 450 °C.	112
Figure 4.40 – Rotary forging route proposed with forging stages, temperature and time of the intercalated heat treatments and sample diameters.....	113
Figure 4.41 - Thermomechanical treatment simulation scheme applied with highlighted of the heating, deformations and aging treatment steps.....	115
Figure 4.42 - SR - XRD patterns obtained during heating up to 850 °C and d-spacing evolution.....	116
Figure 4.43 – Hot (1, 2, 3 and 4) and cold (5 and 6) true stress-true strain curves and work hardening rate analysis (2^{nd} , 3^{rd} and 4^{th} deformations).	116
Figure 4.44 - FWHM, d-spacing and SR-XRD patterns of the hot and cold deformations during thermomechanical measurement with a strain rate of $10^{-3} s^{-1}$	118
Figure 4.45 - 3D plots transform of Debye–Scherrer diffraction rings (azimuthal angles) vs. 2θ – before, peak and after each deformation (hot and cold).	120
Figure 4.46 - Hot and cold deformations behavior and crystallographic orientation.....	121
Figure 4.47 - SR-XRD patterns after hot deformations (b) and after cold deformations (c).	121
Figure 4.48 – Superposition of SR-XRD patterns of each minute during aging treatment at 500 °C during 30 minutes.	123
Figure 4.49 - DSC curves of the initial (NiTi_1_rem. Heat treated at 950 °C/120 min.) and final (after thermomechanical simulation) samples.....	124
Figure 4.50 – Superposition of the SR-XRD patterns obtained during cooling after aging treatment at 500 °C during 30 min.....	124
Figure 4.51 – NiTi_1_Rem. true stress-true strain curves of the hot deformations (at 850 °C) evolutions with strain rate of $10^{-1} s^{-1}$ and comparison between the FWHM and 2θ evolution.	126
Figure 4.52 - DSC curves of the NiTi_1_Rem heat treated at 950 °C during 120 min and after hot deformations with strain rate of $10^{-1} s^{-1}$	127
Figure 4.53 – Superposition of the SR-XRD patterns (0, 10, 20 and 30 minutes) during stress-assisted aging treatment at 500 °C during 30 min under 70 MPa.	129
Figure 4.54 - Superposition diffractograms of the stress-free and stress-assisted aging treatment at 500 °C during 30 minutes.	130
Figure 4.55 – DSC curves of the NiTi_1_Rem sample after stress-free and stress-assisted aging.....	131
Figure 4.56 -DSC curves of the superelastic orthodontic archwire	134
Figure 4.57 - SR-XRD pattern at room temperature of the superelastic archwire.....	134

Figure 4.58 - DSC curves, dilatometry measurement curve and SR-XRD patterns at room temperature of the thermo - active archwire.	136
Figure 4.59 - Scheme of the sections S01, S02, S03 of the studied orthodontic archwire. Dimensions in mm.....	137
Figure 4.60 - DSC curves of three sections (S01, S02 and S03) of the Ni-Ti orthodontic archwires with graded actuating forces.	138
Figure 4.61 - DSC and three-point bending (TMA) results for the three sections of the Ni-Ti orthodontic archwires with graded actuating forces.	139
Figure 4.62 - SR-XRD patterns at room temperature for the three sections along the Ni-Ti orthodontic archwires with graded actuating forces length. a) superimposition of the XRD patterns of all scans along the wire to observe the graded functionally wire. b) diffraction patterns for the three sections to compare the phases present at room temperature.	139
Figure 4.63 - Plot of representative load-deflection data for the three sections of the Ni-Ti orthodontic archwires with graded actuating forces testing at room temperature.	140
Figure 4.64 - Force x Stroke curves for the three sections of the Ni-Ti orthodontic archwires with graded actuating forces (a) S01, (b) S02, (c) S03 at four temperatures (5, 20, 25 and 37 °C). (d) Slope 37 °C, (e) slope 25 °C and (f) slope 20 °C.	142
Figure 4.65 - DSC curves of the three zones of the Ni-Ti orthodontic archwire heat treated (300 °C during 10 minutes).....	144
Figure 4.66 - SR-XRD partners along the Ni-Ti orthodontic archwire heat treated (300 °C during 10 minutes) length.....	145
Figure 4.67 - Pole Figures of superelastic archwire.	146
Figure 4.68 – SR-XRD diffractograms - intensity versus 2θ of the $\phi 0$ and $\phi 90$ of the Ni-Ti orthodontic archwire heat treated (300 °C during 10 minutes) between 16 and 32 mm of length.	147
Figure 4.69 - In situ SXRd analysis during tensile test (a - $\phi 0$ and b - $\phi 90$) of the Ni-Ti orthodontic archwire heat treated (300 °C during 10 minutes).....	151
Figure 4.70 - Single diffractogram of each zone (zone 1 – treated zone, zone 2 – intermediate zone and zone 3 – no treated zone) during the tensile test - $\phi 0$ and $\phi 90$	152
Figure 4.71 – Comparison between: (a) maximum of the $(110)_{B2}$ intensity and (b) 2θ along the deformation of each zone - $\phi 0$ and $\phi 90$	152

List of Tables

<i>Table 3.1 – Alloys: 1, 2 and 3 Ni and Ti contents (%at).....</i>	<i>40</i>
<i>Table 3.2 – Ni-Ti orthodontic archwires: Commercial name, Manufacturer, type, dimension (mm) and LOT (product batch).....</i>	<i>45</i>
<i>Table 4.1 - Transformation Temperatures in degree Celsius of as-cast and remelting 1, 2 and 3 samples.</i>	<i>62</i>
<i>Table 4.2 - Remelted Samples Ni and Ti contents (%at) (WDS - analysis)</i>	<i>66</i>
<i>Table 4.3 - Phase transformation temperatures in degree Celsius for NiTi_1 samples.</i>	<i>82</i>
<i>Table 4.4 – Average of the Grain Size of the heat solution treated samples. (ASTM E-112-96, 2000).....</i>	<i>107</i>
<i>Table 4.5 - Phase transformation temperatures in degree Celsius for 1F_1h, 3F_3h and 5F_4h1c samples, before and after heat treatment (800 °C during 10 minutes and 850 °C during 15 minutes)</i>	<i>109</i>
<i>Table 4.6 – Values of austenitic transformation final temperature for the NiTi_6F_4h2c and NiTi_1_6F_4h2c aging treated samples, in Celsius degrees.</i>	<i>112</i>
<i>Table 4.7 – Phase transformation temperatures of the S01, S02 and S03 of the Ni-Ti orthodontic archwires with graded actuating forces, in Celsius degrees.....</i>	<i>138</i>
<i>Table 4.8 - Transformation temperature of the three zones of the Ni-Ti orthodontic archwire heat treated (300 °C during 10 minutes), in Celsius degree.</i>	<i>144</i>

List of Symbols and Abbreviations

SMA	Shape Memory Alloy
SME	Shape Memory Effect
SE	Superelasticity
B2	Austenite
R	R-phase
B19'	Martensite
SR-XRD	Synchrotron radiation X-ray diffraction
HEXRD	High energy x-ray diffraction
HZG	Helmholtz-Zentrum Geesthacht
HEMS	High-Energy Materials Science
DESY	Deutsche Electron Synchrotron
NOL	Naval Ordnance Laboratory
A	Austenite
A _s	Austenite start temperature
A _p	Austenite peak temperature
A _f	Austenite finish temperature
R _s	R-phase start temperature
R _p	R-phase peak temperature
R _f	R-phase finish temperature
M	Martensite
M _s	Martensite start temperature
M _p	Martensite peak temperature
M _f	Martensite finish temperature
%	Percentage
Md	Highest temperature to strain-induced martensite
TTT	Time-Temperature-Transformation
at.%	Atomic Percentage
°C	Temperature – Celsius degrees
DSC	Differential Scanning Calorimetry
VIM	Vacuum Induction Melting
VAR	Vacuum Arc Remelting
VAM	Vacuum Arc Melting
EBM	Electron Beam Melting
PVA	Particle Void Assemblies
DC	Direct Current
mm	Millimeters
DRV	Dynamic Recovery
DRX	Dynamic Recrystallization
s ⁻¹	Strain rate is in units of inverse time
wt%	Weight Percentage
XRD	X-ray diffraction
min.	Minutes
bcc	Body Centred Cubic Structure
ODF	ODF
φ	Diameter reduction
φ	Azimuthal Angle
°	Degrees
SS	Stainless steel
N	Newton
Pa	Pascal

MPa	Mega Pascal
WDS	Wavelength dispersion spectroscopy
EMPA	Electron Microprobe analysis
OM	Optical Microscopy
SEM	Scanning electron microscopy
EDS	Energy Dispersive X-ray Spectroscopy
EBSD	Electron Backscattered Diffraction
DT	Dilatometry
TMA	Thermal Analysis
ITA	Technological Institute of Aeronautics (Instituto Tecnológico de Aeronáutica)
g	Gram
Å	Angstrom
mbar	Atmospheric pressure
INT	National Institute of Technology (Instituto Nacional de Tecnologia – Brazil)
θ	Bragg angle
WD	Working distance
FEG	Tungsten field emission gun
kV	kilovolts
x	Amplitude
IME	Military Institute of Engineer (Instituto Militar de Engenharia – Brazil)
TSL	Tex-SEM Laboratories
d	Diameter
OIMTM	Orientation Imaging Microscopy
vol%	Percentage by volume
λ	Wavelength of x-rays
<i>d</i>	Interplanar distance
ICDD	International Centre for Diffraction Data
CuK α	Copper radiation
GeV	giga-electron volt, 10^9 eV
LNLS	Laboratório Nacional de Luz Síncrotron
keV	kilo-electron volt, 10^3
A	Ampere
2D	Two-dimensional
m	Meter
kN	Kilo-Newton
CNPEM	Centro Nacional de Pesquisa em Energia e Materiais
XTMS	Thermo-Mechanical simulation
LD	Loading Direction
min.	Time – minutes
mg	Milligram
FWHM	Full Width at Half Maximum
SIM	Stress-induced martensite

1

Introduction

The first chapter of this work presents a brief introduction to the subject, the aims, scope of the study and some general information about the investigation. The partners are highlighted in accordance to their contribution to this investigation. The sequence of the chapters is shown and explained to clarify the structure of the study.

Shape memory alloys (SMA) belong to the class of advanced materials which display two functional properties with great interest: their superelasticity and shape memory effect.

These alloys present the capability to return to an original shape or dimension when subjected to an adequate thermomechanical treatment. (Otsuka, 2005).

Usually, these materials can be deformed at relatively low temperature (martensitic field). After the increase of the temperature (austenitic field), they return to the shape they had before the deformation (Shape Memory Effect - SME).

On the other hand, when deformed in the austenitic field, they are susceptible to a reversible phase transformation of the martensitic type. This can be reversed by removing the applied load (Superelastic Effect - SE). (Otsuka, 2005) (Mohd, 2014) Ni-Ti alloys still display high resistance to fatigue and corrosion, great ductility and biocompatibility when compared to other shape memory alloys (e.g. Cu-base or Fe-base) (Saburi, 1998).

This work focused on a Ni-rich Ni-Ti alloy, which may be used in the orthodontic archwires, since the Ni-Ti alloys used for this purpose need to show superelastic characteristics at room and oral temperature. It is sought by the mechanical and thermal treatments that the material displays an austenite finish temperature below room temperature.

This processing usually involves thermomechanical treatments, which promote the improvement of the microstructure aiming the expected performance of the material. An in-depth understanding of production steps such as thermomechanical processes is required for the successful processing control.

Therefore, the present work aimed to study the functional behavior of Ni-rich Ni-Ti alloy, determining the mechanical properties that are associated with its microstructural characteristics. This study allows the association of processing variables (chemical composition, solidification and thermal and/or mechanical processing) to the in-service behavior of the wires. With this in mind, three main tasks were performed: (i) characterization of the thermomechanical processed samples, (ii) testing of the different processing alternatives, and (iii) evaluate the proposed processing through the thermomechanical analysis using synchrotron radiation-based X-ray diffraction (SR-XRD) technique. In situ deformation experiments were conducted with the high energy X-ray diffraction (HEXRD) setup of the HZG beamline HEMS (P07-EH3) at Petra III, DESY in Hamburg (Germany).

Bellow, the thesis chapters with a brief explanation are listed to clarify the structure of this document and make easier its reading.

1.1. Structure of the Study

The thesis is composed of five chapters, including the Introduction Chapter.

Chapter 2 - State of the Art - a critical analysis of existing knowledge;

This chapter presents a critical analysis of the existing knowledge. Firstly, it is presented an overview of the Ni-Ti alloys characteristics such as chemical composition, phases and precipitates that are present, phase transformations and corresponding relevant parameters. This part still describes how the SME and SE occur in shape memory alloys. A major focus is put on the relevant points related to the chemical composition of the Ni-Ti alloys, but with a greater attention to the Ni-rich alloys.

The second part presents some details of the Ni-Ti alloys processing. Thermal, mechanical and/or thermomechanical treatments modify the phase transformation temperatures and affect the SME and SE. Recovery and recrystallization are presented and also their influence in processing. The final part approaches the general

characteristics of the crystallographic texture and its evolution throughout the thermomechanical processing.

As the current study is focused on the thermomechanical processing of a material aiming its application to orthodontic archwires, finally in the third part, some characteristics of this type of wires are presented to identify the most important properties. Thus, a short evolution overview of the Ni-Ti orthodontic archwires is presented: from superelastic to functionally graded orthodontic archwires.

Chapter 3 - Methodology;

In this chapter the characteristics of the alloys studied (Ni-rich, equiatomic and Ti-rich in the as-cast and remelted conditions) are presented. Afterwards, their thermomechanical processing is presented, as well as the characterization techniques applied for each sample representative of the different processing steps. Some thermal treatments were carried out to simulate the conditions of the material before and after each stage of processing. In addition, alternative thermal and thermomechanical treatments are analyzed in order to assess the proposed changes of the processing route.

Chapter 4 – Results and Discussion;

The Results and Discussion sections is organized in subchapters focused on the characterization of the samples representative of the different thermomechanical steps, test of the processing parameters and simulation of the thermomechanical process.

Chapter 5 - Conclusions and Future Work

Conclusions and Future Work show the most important conclusions, as well as the potential future perspectives for this research.

2

State of the Art

This Chapter presents the literature review focused on the topics that are essential to the project understanding, as described in the results and discussion chapter. This presentation was divided into three main sections.

In the first section of this chapter, an overview of the Ni-Ti alloy system is given with relevance to the discussions on the composition control, and the phase transformations. The Shape Memory Effect (SME) and Superelasticity (SE) are also discussed.

The second section of this chapter is dedicated to the thermomechanical process in general. A short introduction about the mechanical, thermal and thermomechanical behavior is presented. The thermomechanical processes that are discussed in the current study concern only the hot and cold forging steps. Mechanisms of microstructural restoration such as recovery and recrystallization (static and dynamic), the precipitation phenomena, and the textural evolution involved in the process are also described.

Finally, as these processes aim the orthodontic archwires manufacturing, some aspects concerning the final characteristics of NiTi orthodontic wires are reviewed in the last section of this chapter. Thus, the relevant orthodontic archwires properties, as well as the innovative functionally graded archwire properties, currently used during the orthodontic treatment, are presented.

2.1. Ni-Ti Shape Memory Alloys

Shape memory alloys (SMA), are a group of metallic alloys that have attracted much interest for their great application as functional materials in many engineering fields, such as active, adaptive or intelligent structures, as well as certain biomedical applications. These alloys present two unique properties: shape memory effect and superelasticity. Among the SMA, the Ni-Ti alloys are the most important alloy group,

not only because of its functional properties but also because they present excellent mechanical properties, a very high resistance to corrosion and biocompatibility. (Otsuka, 2005) (Funakubo, 1987)

In the 60s, the Ni-Ti alloys, became very popular through the publicity of Naval Ordinance Laboratory (NOL). In that period, Buehler *et al.* (1961) observed the shape memory effect in this alloy. Thus, the NiTiNOL, referring to the near equiatomic composition (NiTi) was used as a tribute to this laboratory. (Buehler, 1961)

2.1.1. Phase Diagram and Crystal Structures

The phase diagram of Ni-Ti alloys system is fundamental to understand heat treatments of the alloys and improvement of the shape memory characteristics. The properties as SE and SME can occur in Ni-Ti alloys with nominal composition range from 48 to 52 at.% Ni. (Otsuka, 2002)

In the Ni-Ti binary phase diagram (Figure 2.1), it is possible to observe that the solubility changes significantly with increasing temperature on the Ni-rich side, while there is a steep boundary in the Ti-rich side. Moreover, a small variation of the ratio of Ni-Ti in the alloys can result in precipitation of second phases. (Otsuka, 2002)

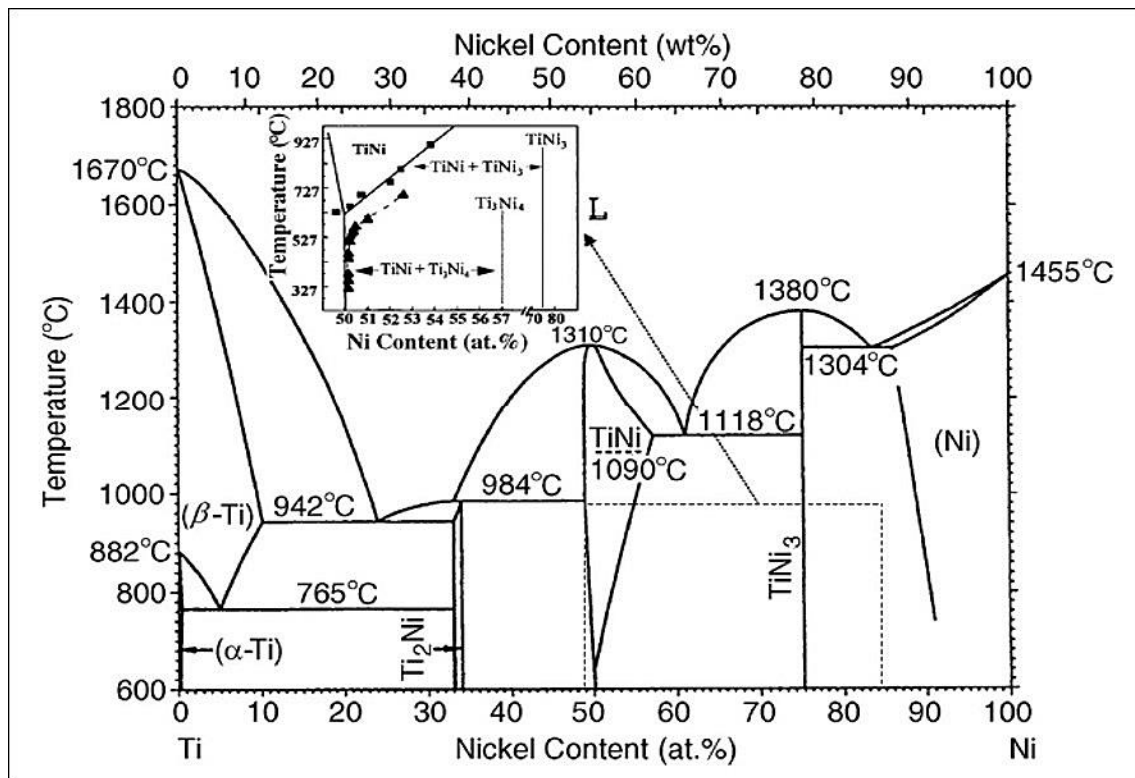


Figure 2.1 - Phase diagram of Ti-Ni alloy with the phase equilibrium between the B2 and Ni₄Ti₃ phases added. (Otsuka, 2002)

The functional properties displayed in these alloys are possible due to a reversible martensitic transformation. NiTi may present three distinct phases: martensite, R-phase and austenite. At high-temperature ranges, the stable phase is austenite (A) cubic symmetry B2 type (space group $Pm\bar{3}m$). At low-temperature the stable phase is martensite (M) monoclinic symmetry B19' type (space group $P2_1/m$). The transformation from B2 into B19' can occur directly or via R-phase (trigonal symmetry, space group $P\bar{3}$). It can be described by a stretch of the B2 - cubic crystal structure along the $\langle 111 \rangle$ direction. (Figure 2.2) The reversibility of the transformation of A to M and M to A is the condition for the unique behavior of this class of alloys. (Otsuka, 2005) (Miyazaki, 2009)

The intermediate transformation to R-phase before achieving the B19' phase can be observed if the alloy is subject to specific processing conditions as a variation of Ni content, thermal treatment or thermomechanical treatment. (Otsuka, 2005)

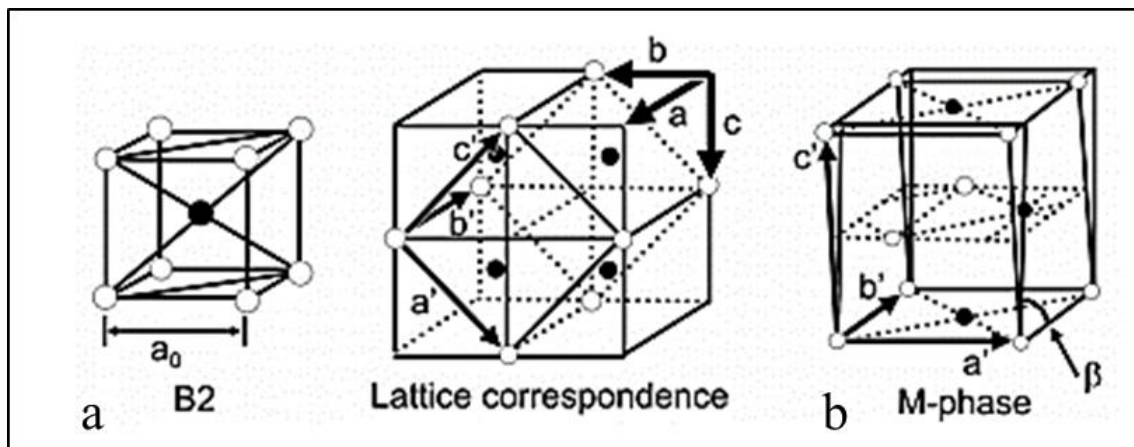


Figure 2.2 - Scheme of transformation of (a) cubic (B2) austenite to (b) monoclinic (B19') phase. (Miyazaki, 2009)

2.1.2. Shape Memory Effect and Superelasticity

When the material is cooled from austenite (A) domain, the martensite transformation starts at given temperature known as M_s temperature. The transformation from austenite to martensite is referred as direct transformation and finishes at martensite transformation finish temperature, known as M_f temperature. Thus, when the material at low-temperature phase (M) is heated up to a given temperature, the austenite phase transformation starts; this temperature is known as A_s temperature and the transformation finishes when the A_f temperature is reached. This transformation is

referred to as reverse transformation. A and M will be used in this text to indicate the phases, austenite and martensite, respectively. The subscripts “s” and “f” indicate the start and finish of the transformations. Thus, A_s , A_f , M_s and M_f are used to refer to the transformation temperatures of a given shape memory alloy.

In these alloys each martensitic crystal has a different orientation, called variant. Two distinct forms of martensite, twinned martensite or detwinned martensite may exist (Figure 2.3). The first one martensite is promoted by the combination of self-accommodated twins to keep the overall shape (thermally induced – Figure 2.3b) while in the other one is activated, typically as a result of external load applied (Figure 2.3c). (Otsuka, 2002).

Further, the martensitic transformation can be stress-induced, promoting the superelastic effect (Figure 2.3a). When a stress is applied to the material within a given range of temperature where austenite is thermally stable, the superelasticity occurs: the deformation during loading may be recovered after unloading, up to 10% strain. (Otsuka, 2005)(Dolce, 2001)

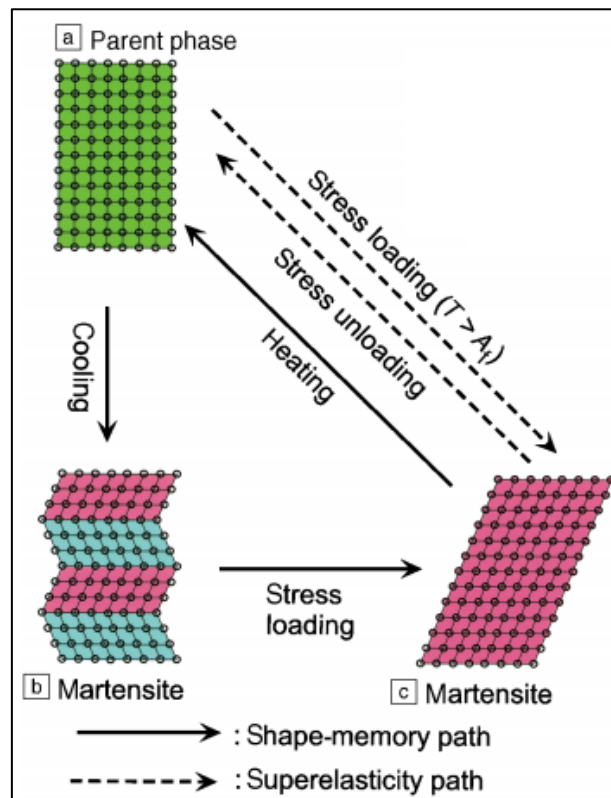


Figure 2.3 - (a), (b) and (c) Schematic illustration of the mechanism of the shape-memory effect and superelasticity. (Otsuka, 2002)

On the other hand, the shape memory effect occurs starting from the martensitic state. A shape memory alloy may be given a definite shape in the austenitic phase. So, when cooling this alloy up to the temperature range of martensite stability, the shape does not change significantly. When the material is deformed in the martensitic state up to a certain extent (in most cases up to 10%), this deformation can be retained by the material as long as the martensitic stability temperature range is maintained. However, the material starts recovering the original shape when it is heated above A_s temperature. When A_f is reached, the recovery by shape memory effect should have finished. Chowdhry *et al.*(2017) shows the schema of these phenomena in a stress-strain diagram, where the red loop describes the superelastic response of SMAs and the green + blue loops show the shape memory effect (Figure 2.4). (Chowdhury, 2017)

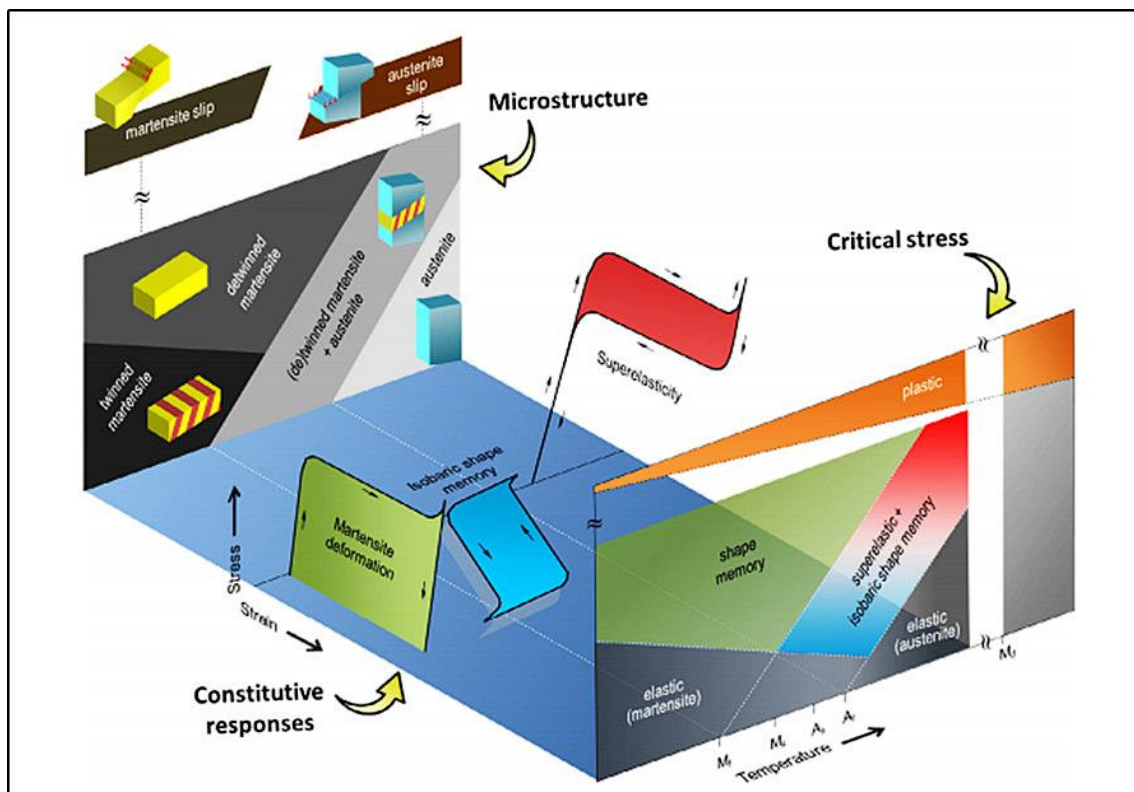


Figure 2.4 - Typical superelastic behavior diagram of a shape memory alloy. (Chowdhury, 2017)

The shape memory effect and superelasticity are closely related as shown through stress-temperature phase diagram (Figure 2.5). It is desired that the SMA show the shape memory and superelastic properties, but the temperature of the tests and the critical stress for dislocation slip, must be considered. The slope for the variation of the critical stress for the stress-induced martensitic transformation as a function of temperature is given by the Clausius–Clapeyron equation (Eq. 2.1). (Liu, 2008)

$$\frac{d\sigma}{dT} = -\frac{\Delta S}{\varepsilon} = -\frac{\Delta H^*}{\varepsilon T} \quad (\text{Eq. 2.1})$$

Where: σ is the applied stress, T is the temperature, ΔS is the change in entropy, ε is the applied strain, ΔH is the latent heats of transformation for the two transformations.

Increasing temperature requires a higher stress to promote the stress induced transformation. However, the critical stress to induce slip, promoting the plastic deformation, decreases with increasing temperature. Thus, the superelastic effect is inhibited above a given temperature, where the critical stress for dislocation slip occurs earlier than it. So, by the combined change of the transformation temperatures and the materials softening (Figure 2.5 - B) or hardening (Figure 2.5 – A), the “window” of superelasticity may be changed as a function of the relative positions of Clausius-Clapeyron and critical dislocation slip lines.

Thus, M_d is the temperature above which the stress-induced martensitic transformation is no longer favored. But, it is possible to control the critical stress for inducing dislocations slip at a given temperature: (i) by softening the material, the critical stress for slip decreases or (ii) hardening the material, the critical stress for slip increases. (Otsuka, 2005)

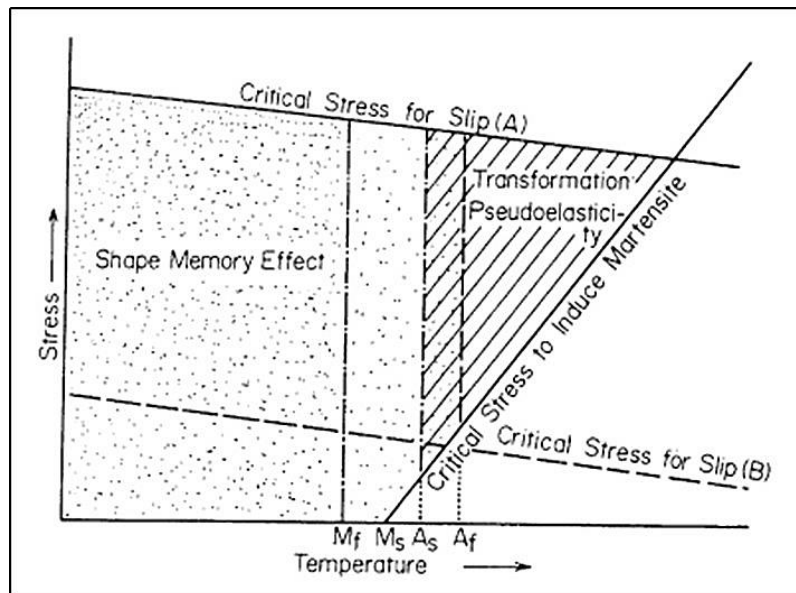


Figure 2.5 - Stress-temperature diagram for shape memory alloy. (Otsuka, 2005)

The intermediate R-phase can occur by deformation, below the critical stress for the formation of B19', which is associated with the stress-induced transformation B2 → R-phase.

The transformation strain associated with the A↔R transition is small (~1%); it displays attractive properties, such as fast response with respect to temperature change, high stability during mechanical or thermal cycling and narrow thermal hysteresis. Hence, the R-phase TiNi alloys have potential for commercial applications, especially in engineering and medical industries.

Olbricht *et al.* (2011), reported a model system for an uniaxial loading-unloading test at a temperature above A_f . In the curve (stress-strain), the first small loading plateau after the initial slope of the linear elastic behavior of B2 corresponds to the stress-induced R-phase formation (Figure 2.6a). The linear stress increase at the end of the plateau may be attributed to the elastic response of the R-phase; after this, the B19' starts to form. The B19' (stress-induced martensite - SIM) occurs along the upper plateau of the stress-strain curve. The increase of the stress following this second loading plateau represents the B19' elastic behavior. At a second critical stress σ_{M+} , B19' starts to form. The stress induced formation of B19' extends over a larger strain interval (~7%) than the stress-induced formation of R-phase (~1%). The increase of the stress after this second loading plateau represents the elastic behavior of B19'. They reported that the stress-induced formation of B19' finishes at the end of the upper loading plateau. The dashed horizontal line at σ_0 can be thought of as an equilibrium stress. The higher and lower loading and unloading plateaus, referred to as σ_{M+} and σ_{M-} , indicate the need for nucleation during the stress-induced formation of B19' (forward transformation) and R-phase (reverse transformation), respectively. This behavior is observed only if no plastic deformation occurs. (Olbricht, 2011) (Olbricht, 2013)

The tension and compression display similar behavior. However, the plateau stresses in tension and compression are different, while, in tension the initiation is followed by a drop-in stress and then a plateau, in compression the stress continues to increase, and the plateau is less distinct, as shown in Figure 2.6b. (Sittner, 2006)

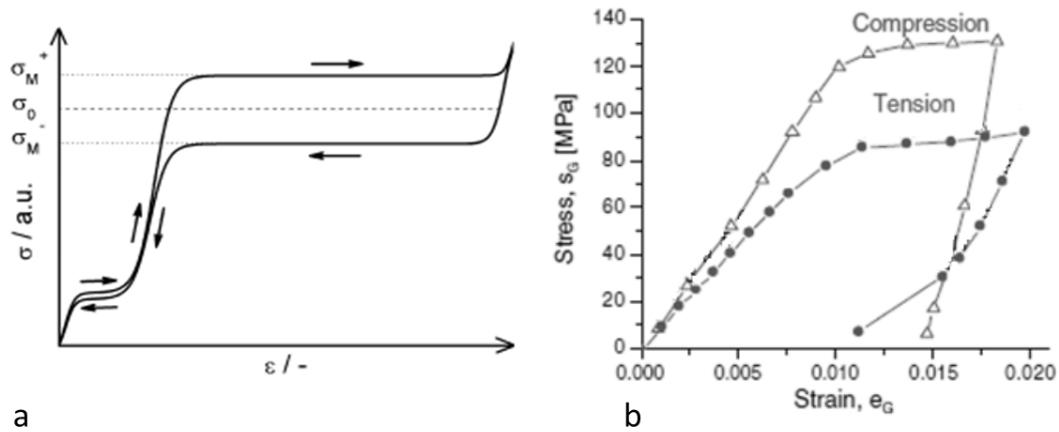


Figure 2.6 - Schematic drawing of stress-induced phase transformations as observed in a uniaxial tensile loading/unloading experiment with two-step transformations. Stress is plotted as a function of strain. (Olbricht, 2011) (b) stress x strain curves (compression and tension behavior). [adapted from (Sittner, 2005)]

Harrison reported about 20 physic characteristics that may be used to assess the changes associated with the functional characteristics of shape-memory alloys (transformation temperatures and strain recover). Harrison also highlights some technics such as hardness, resistivity measurement, differential scanning calorimetry (DSC) and thermomechanical tests, among techniques that are based on the SME itself. In the current study, in addition to functional properties, the structural differences were investigated, by some techniques as: DSC, dilatometry, three-points bending, optical microscopy, x-rays among other techniques. (Harrison, 1990)

2.1.3. Precipitation Phenomena

In Ni-rich Ni-Ti alloys, during aging or slow cooling from high temperatures, it is possible to observe the precipitation sequence: $B2 \rightarrow Ni_4Ti_3 \rightarrow Ni_3Ti_2 \rightarrow Ni_3Ti$ (Otsuka, 2002).

The precipitation processes in Ni-rich Ni-Ti alloys was studied by Nishida *et al.* (Nishida, 1986), who reported the TTT (time-temperature-transformation) diagram for Ti-52 at% Ni composition alloy, as shown in Figure 2.7. For shorter aging time and lower temperature, the Ni_4Ti_3 (metastable phase with a rhombohedral structure) are observed. The presence of this precipitate is important to improve the shape memory characteristics, since it is distributed on a very fine scale. For intermediate time and intermediate temperature, the Ni_3Ti_2 phase (metastable) appears. However, for longer aging time and higher aging temperature, the Ni_3Ti (stable) phase occurs. Ni_3Ti presents

tetragonal structure. The diffusional transformations in this system occurs in this order:
 $Ni_4Ti_3 \rightarrow Ni_3Ti_2 \rightarrow Ni_3Ti$.

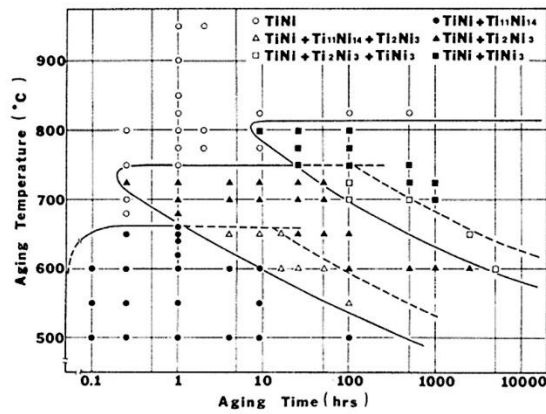


Figure 2.7 - TTT diagram describing aging behavior for Ti-52 at%Ni. (Nishida, 1986)

Pelton *et al.* (2000) reported a TTT diagram (Figure 2.8) considering shorter aging times for precipitation phenomena to occur, thus supporting the industrial application Ni-Ti alloy. This study showed that the heat treatments until 400 °C show an increase of the A_f , from 400 to 500 °C a decrease of transformation temperature was observed, and above 500 °C, the tendency of the evolution of the transformation temperature is inverted. The maximum in the precipitation reaction kinetics is observed at about 425 °C, the A_f increases considerably after this heat treatment temperature. (Pelton, 2000) It is known that these precipitates (Ni_4Ti_3 , Ni_3Ti_2 , Ni_3Ti) can be formed when the Ni-Ti alloy is slightly Ni-rich. But, for Ti-rich Ni-Ti alloys, only Ti_2Ni precipitates may exist. (Saburi, 1998)

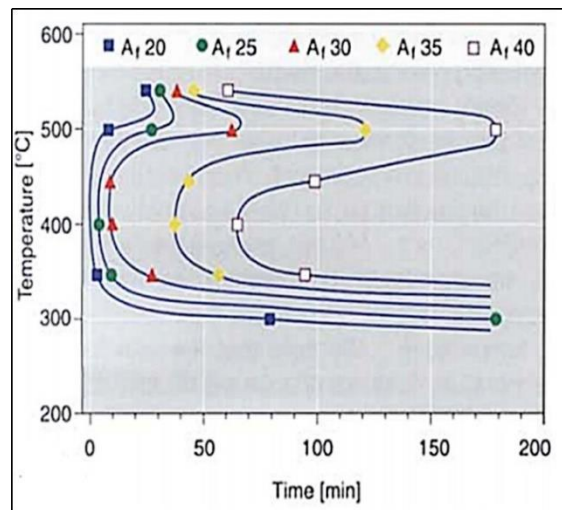


Figure 2.8 - TTT (time-temperature-transformation) for the effect of shorter ageing temperature and time on the transformation temperature of Ti-50.8% Nitinol wire with a starting A_f temperature of 11 °C. (Pelton, 2000)

Due to the presence of coherent Ni_4Ti_3 in the matrix, or to the presence of dislocation networks, the thermoelastic transformation occurs, either stress or thermally-induced (Otsuka, 2005).

Because of the precipitation phenomena (Ni_4Ti_3), the R-phase also can be observed during aging treatment. Due to association with a large lattice deformation, these precipitates promote a resistance to formation of B19'. However, R-phase transformation has a significant smaller lattice deformation and is much less affected by the presence of particles. These precipitates formed during aging favor the of R-phase formation previously to transforming to B19'. Thus, Ni-rich Ni-Ti alloys usually submit a two-stage transformation ($\text{B2} \leftrightarrow \text{R} \leftrightarrow \text{B19}'$). (Wang, 2014)

The Ni-rich Ni-Ti alloys after aging at intermediate temperatures (between 400 and 500 °C), also show an abnormal multiple-stage (3-stage) martensitic transformation.

Fan *et al.* (2004), reported a comparison between low and high Ni content alloys, and showed that the grain boundaries are a necessary ingredient for the formation of multiple-stage transformation, but not a sufficient condition. Ni content is an important factor in controlling the transformation behavior. The alloys which have low Ni content experimented the multi-stage transformation, while the alloys with high Ni content not.

The multi-stage transformation in alloys with low Ni content occurs due to the difference in the kinetics of Ni_4Ti_3 precipitation during aging treatment between the grain boundary and grain interior. This difference is result of a preferential precipitation around the grain boundary region and a practically grain interior precipitate-free. They suggested that the $\text{B2} \rightarrow \text{R} \rightarrow \text{B19}$ occurs in the grain boundary region, and $\text{B2} \rightarrow \text{B19}'$ occurs in the grain interior. The alloys with high Ni content show a small difference in the nucleation rate between grain boundary and grain interior due to large driving force for precipitation by the Ni supersaturation. This behavior occurs independent of the aging time. (Figure 2.9) (Fan, 2004)

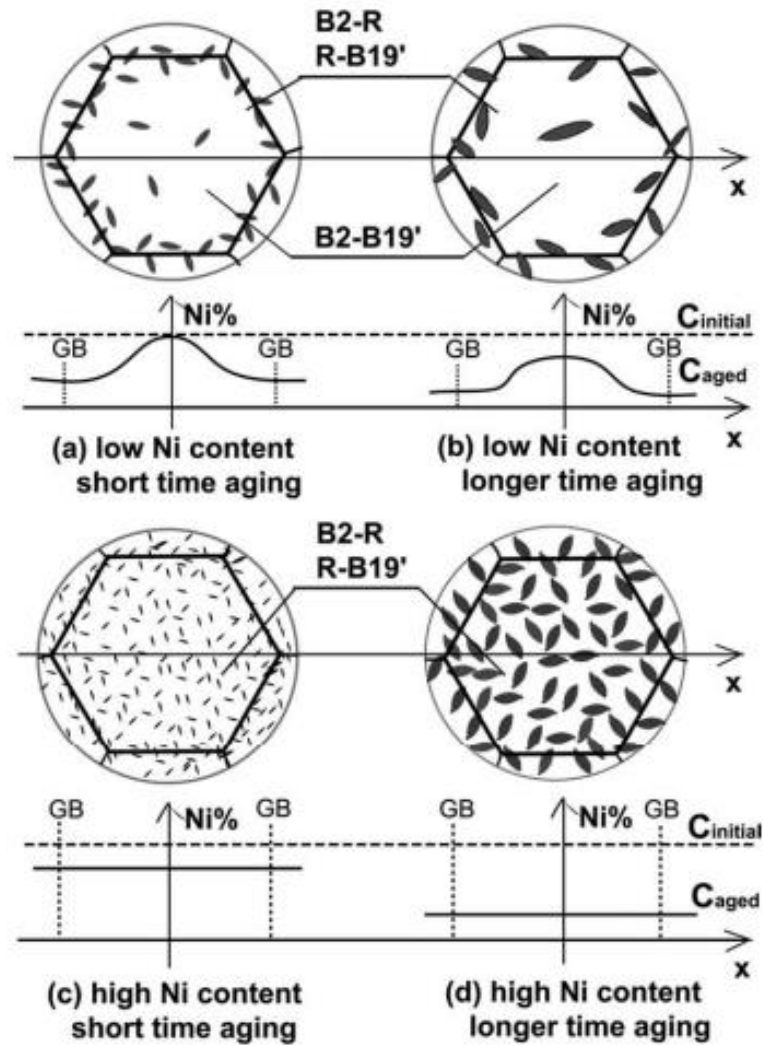


Figure 2.9 - A unified model for explaining the microstructure evolution at low Ni supersaturation (a and b) and high Ni supersaturation (c and d). It also explains both three-stage and two-stage transformation behavior of supersaturated Ti–Ni solid solution. (Fan, 2004)

The commercial Ni-rich Ni-Ti alloys, usually have a small volume fraction of precipitates, as Ni_4Ti_3 . These precipitates are distributed in the B2 matrix, affecting the transformation temperatures and mechanical characteristics of the alloy. A study by Tang *et al.* (Tang, 1997)(Tang, 1999), which was improved by Frenzel *et al.* (Frenzel, 2010) (Figure 2.10), analyzed the effect of the alloy composition on the M_s temperatures and reported that the change of 0.1 at.% Ni results in a change of about 10 °C of the transformation temperature (Elahinia, 2012). As this variation is much smaller than the normal composition tolerances for the engineering materials, the Ni-Ti manufacturing demand a lower tolerance, which results in higher costs.

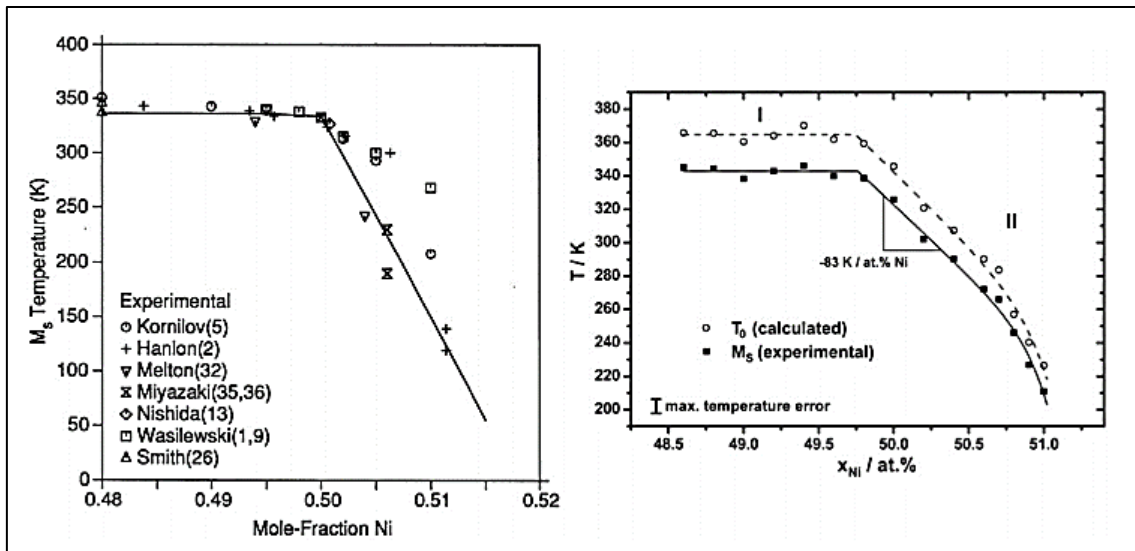


Figure 2.10 - Dependence of Ms Temperature on Ni composition of Ni-Ti alloys, left Tang *et al.* (Tang, 1997), right Frenzel *et al.* (Frenzel, 2010)

The current study focused on the thermomechanical process to produce in the future orthodontic archwires, and in this field, many customers request certification of the A_f temperature to ensure that the product is austenitic at human body temperature. Some customers specify that the measurements are obtained by differential scanning calorimetry (DSC).

2.2. Processing

Ni-Ti alloys exhibit good workability compared with other SMAs, but cold workability is poor when compared with other materials such as steel. As far as fabrication of Ni-Ti alloys is concerned, the casting methods followed by other mechanical and/or thermal processes such as hot or cold working and heat treatments (Figure 2.11), with the latter having an important role in the shape and application setting of the alloy (Nakahata, 2011). Moreover, the producing process of the Ni-Ti - SMA is critical and specifically affects ductility, machinability, composition homogeneity, elastic modulus, biocompatibility as well as transformation temperatures and microstructure. All these characteristics are fundamental for the applications of the material. As mentioned previously, this study is focused on the manufacturing requirements for wires and the following topics will detail the requirements.

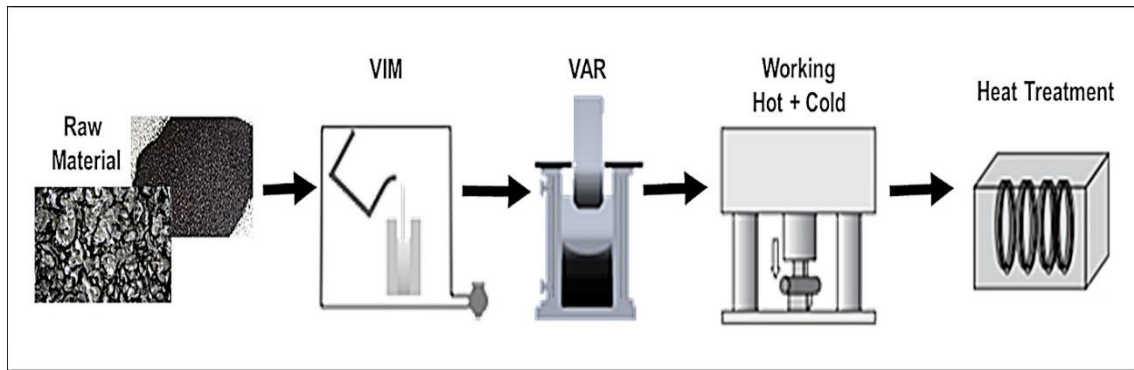


Figure 2.11 - Schematic view of NiTi manufacturing process. [adapted from (Nakahata, 2011)]

2.2.1. Casting Process

Ni-Ti alloys manufacturing starts at the melting step. Firstly, the raw materials must have as high purity as possible, since the existence of impurities, such as oxygen, nitrogen, and carbon can affect seriously the homogeneity of the alloy, thus creating uneven composition distribution and change of functional properties of the material.

Many techniques are used to accomplish the melting process, which includes Vacuum Induction Melting (VIM), Vacuum Arc Remelting (VAR) and Electron Beam Melting (EBM). However, in this study, only Vacuum Induction Melting and Vacuum Arc Remelting were used. These techniques are the main methods of melting commonly used for the Ni-Ti alloys manufacturing, providing a transformation temperature control of ± 5 °C. (Elahinia, 2012) (Reinholz, 2012) The cost of production by either method is similar and they both provide suitable material for current medical device requirements (ASTM E-112-96, 2000).

The VIM process is commercially exploited since the ingots from several grams to many kilograms may be processed. This process with graphite crucibles is attractive because it provides alloys with good chemical homogeneity, it is the cheapest method and can be easily handled. VIM process involves melting under vacuum or an inert gas atmosphere for the melting of all raw materials. However, it is known that melting SMA in graphite crucibles results in an increase of the impurities, such as carbon contents in the alloys. (Drennen, 1968) The Ni-Ti alloy melting dissolves carbon from the graphite crucibles and some TiC particles are formed during solidification, thus promoting an increases of the Ni-concentration and a decrease of the phase transformation temperature. (Frenzel, 2004a) The contamination by carbon can be minimized coating the graphite crucible with the Ti (bars or disk) to create a TiC diffusion barrier. (Zhang,

2005) (Saburi, 1998) (Suzuki, 1998) (Wu, 2002) (Frenzel, 2004b) Even with the inert or vacuum atmosphere to impede reactions with the atmospheric contaminants this method is incapable of completely stopping the peritectic reaction that forms $\text{Ni}_2\text{Ti}_4\text{O}$ and TiO_2 oxides. After casting, during the forming processes, these inclusions can form particle void assemblies (PVA) and thus promote crack propagation. The oxides are generally larger than carbides and fracture more readily to form the PVAs. (Frenzel, 2010) (Otubo, 2008) (Frenzel, 2007) (Panton, 2017) (Zhang, 2005) (Frenzel, 2004b) (Reinholz, 2012)

VAR process uses direct current (DC) to melt a compacted Ni-Ti into a water-cooled copper crucible that promotes less contamination. This process allows to give the ingot an adequate shape to begin the thermomechanical processing. (Coda, 2012) (Frenzel, 2004b)

At the beginning, Ni-Ti alloys have been produced satisfactorily by both vacuum induction and arc melting methods. But this process has a problem that is the necessity of multiple remelting to ensure chemical homogeneity. As-cast Ni-Ti samples have a lower ductility, limited functional properties and lower mechanical strength. (Mohd, 2014) (Frenzel, 2004a)

2.2.2. Heat Solution Treatment Before Thermomechanical Process

After melting the ingots, they are often solubilized to ensure homogeneity. Zhang *et al.* (2007), reported that the solution-treatment temperature is no much fundamental for the transformation temperature and shape memory properties of the Ti-Ni system, as long as the heat treatment is performed in the single-phase B2 regime and oxidation is avoided. (Zhang, 2007)

This study observed Ni-Ti alloys with a Ni range between 49.3 and 50.8% at. Figure 2.12 shows the partial phase diagram of the Ni %at. There it is highlighted the Ni range that was studied. According to the partial phase diagram represented by Povoden-Karadeniz *et al.* (2013), in the temperature range between 650 °C and 1310 °C a fully B2 matrix can be achieved. (Povoden-Karadeniz, 2013) Meanwhile, Zhang *et al.* (2007) also reported that the temperature over to 1090 °C can promote problems, such as oxidation and order-disorder transition in B2 portion of the Ti-Ni system. (Zhang, 2007)

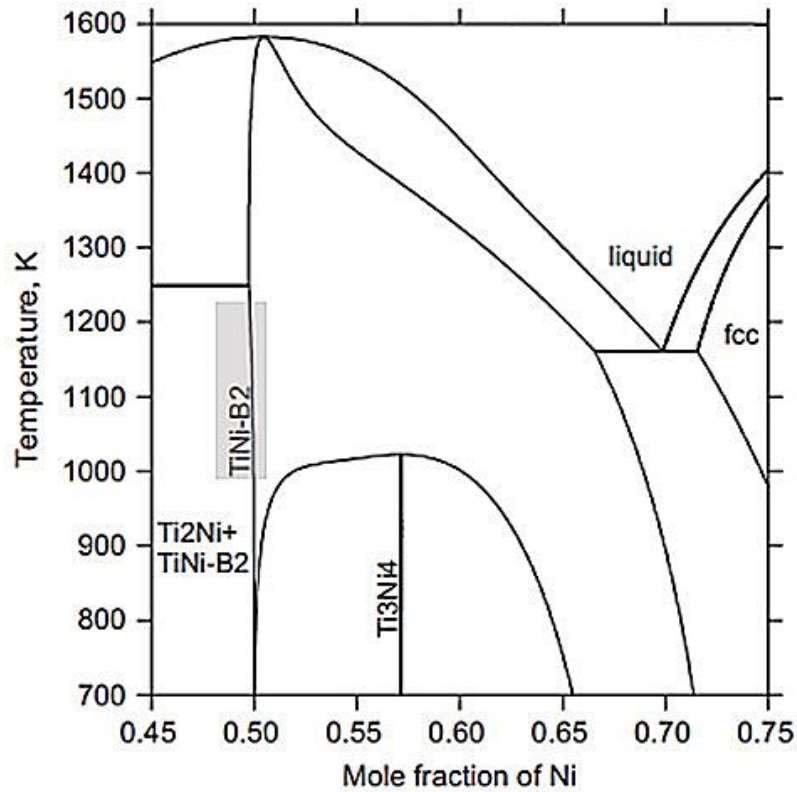


Figure 2.12 - Metastable phase diagram of the Ti–Ni system with the Ni content rang studied. [adapted from (Povoden-Karadeniz, 2013)]

However, few studies concerning the effect of the solution heat treatment on Ni-Ti alloys are reported in the literature.

Paryab *et al.* (2010), studied the effect of different heat treatment parameters on microstructure and hardness of Ni-Ti (58.5% wt. Ni) SMA. They observed that at high temperatures (800 °C) the matrix has a lower nickel content due to Ni₃Ti precipitation. This results in a higher Ms temperature, as compared to the matrix treated at 700 °C. (Paryab, 2010)

Simões *et al.* (2015), evaluated the influence of solubilization thermal treatments on a Ni-Ti SMA, produced by VIM process and reprocessed by plasma melting followed by injection molding, in order to compare the thermal properties regarding to the raw states. The thermal treatments were carried out at 850 °C with different times and they used the Differential Scanning Calorimetry (DSC) test to determine the phase transformation temperatures. (Simões, 2015)

As mentioned previously, to control the transformation temperature, it is necessary to control the Ni concentration with an accuracy of 0.1%. Since it is complex to control

Ni content around 50 at.% with accuracy, the manufacturers normally choose a physical control indicator instead of Ni concentration, e.g. through the transformation temperature.

2.2.3. Thermomechanical Process

The remelted Ni-Ti alloy has a microstructure that must be refined by additional deformation (hot and cold) processes to achieve the desirable properties.

Thermomechanical processing can be applied to promote the control of the alloys characteristics. From the engineering point of view, the control of thermomechanical treatment is fundamental in two aspects: (i) to promote the shape of semifinished products (metal sheets, tubes, bars) and (ii) to optimize the microstructure to obtain the most adequate properties. (Treppmann, 1997)

Among the final products, the wires are the most common. The knowledge about the Ni-Ti alloys properties and the effect of the processing variables are fundamental to adequate application of the alloy.

2.2.3.1. Hot Working

After production of the ingots, hot working steps are required: (i) to reduce the initial size of the ingot; (ii) to change the ingot structure and replace it with an improved one, with finer grain structure and higher chemical homogeneity; (iii) to define the texture adjustment; (iv) to incorporate the shape memory effect (SME). Hot working needs to be applied at a temperature above the recrystallization temperature. At this higher temperature, atomic mobility can repair the structural damage caused by the metal-working process.

Ni-Ti alloys present a good workability, especially at higher temperatures over 700 °C, where it becomes more stretchable due to its reduced strength. If the Ti content is locally higher, due to segregation, a liquid phase may appear at a temperature over 950 °C and cracks can form during processing. Thus, it is indicated to use a processing temperature between 800 to 900 °C. (Saburi, 1998)

Hot deformation temperatures at above 900 °C are not advised. Above this temperature, excessive surface oxidation appears. The oxide layer formed is adherent to the material and often leads to the risk of oxide inclusion. (Ramaiah, 2006)

The temperature of 800 °C provides good workability without massive oxide formation by higher temperatures range. The surface oxidation more difficult the thinner wires fabrication, which have relatively large surface areas. The most frequently used method to process rods with diameters greater than 4 mm, is hot working, such as hot forging. On the other hand, to produce thinner wires the cold working is indicated, to avoid surface oxidation. (Mirzadeh, 2014) Due to these oxidations, this process requires the removal of the superficial oxidation, following the solution heat treatment, so that the intermediate heat treatment steps can be done.

The properties of hot deformed materials are markedly influenced by the characteristics of the microstructure that is produced by the working process. The microstructure will be affected according to the composition of the material, temperature, rate and degree of deformation. The deformation alters the grains morphology and increases the dislocations density, and, as a consequence, the material's hardness is increased, and the deformation is more difficult to occur. However, as known, during the deformation at high temperatures some mechanisms of microstructural restoration, such as recovery and recrystallization may occur, and are called as dynamic recovery (DRV) and dynamic recrystallization (DRX). (Humphreys, 2004a)

Occurrence of DRV or DRX is inevitable during the hot deformation of Ni-Ti alloys. Understanding these mechanisms during the hot deformation establishes the bases for obtaining the suitable microstructure. Depending on the temperature and strain rate as well as the materials characteristics, one of them can be the controlling mechanism. There are many studies about the occurrence of these phenomena during hot deformation of Ni-Ti alloys. (Dehghani, 2010) (Morakabati, 2011) (Jiang, 2013a)

It was reported that dynamic recrystallization is the dominant phenomenon for Ni60wt%-Ti40wt% intermetallic alloy when deformed at 950 and 1150 °C (Dehghani, 2010).

Srinivasan *et al.* (1992), observed the hot deformation behaviors of the polycrystalline nickel in the temperature range between 750 and 1200 °C and strain range 0.003–100 s⁻¹ using processing maps developed based on dynamic material models. They reported a

comparison of the variations of grain size and efficiency at corresponding strain rates shows that the DRX temperature corresponding to a 50% change in the grain size is similarly to temperature for peak efficiency. However, the efficiency peak in the processing map represents the optimum temperature for dynamic recrystallization. (Srinivasan, 1992)

Morakabati *et al.* (2011), investigated the deformation behavior of a 49.8 Ni-50.2 Ti %at. alloy using the hot compression test in the temperature range of 700 °C - 1100 °C, and strain rate of 0.001 s⁻¹ to 1 s⁻¹. A processing map of the alloy was developed to evaluate the efficiency of hot deformation and to identify the instability regions of the flow. They reported the peak efficiency between the 24 - 28% at temperature range of 900 °C - 1000 °C, and strain rates higher than 0.01 s⁻¹ in the processing map. The hot ductility and the deformation efficiency of the alloy exhibit almost similar variation with temperature, showing maximum at temperature range of 900 and 1000 °C and minimum at 700 and 1100 °C. Besides, the minimum hot ductility lies in the instability regions of the processing map. The peak efficiency of 28% and microstructural analysis suggests that DRV can occur during hot working of the alloy. At strain rates higher than 0.1 s⁻¹, the peak efficiency domain shifts from the temperature range of 850 °C - 1000 °C to lower temperature range of 800 °C - 950 °C which is desirable for hot working of the Ni-Ti alloy. This study presents one type of stress-strain curves (Figure 2.13) is characterized by “nearly ascending curves”. The true stress increases slightly with increasing strain, this type of flow curves can be seen at temperatures lower than 900 °C. However an instability region has been found at 1000 °C and strain rates higher than 1 s⁻¹ and at 1100 °C and all range of strain rates. (Morakabati, 2011)

Jiang *et al.* (2013a) studied the mechanical behavior of Ni-Ti SMA under hot deformation with the strain rates of 0.001⁻¹ s⁻¹ and at the temperatures of 600 – 1000 °C. This study investigated the DRV and DRX by microstructural evolution. The influence of the strain rates, the deformation temperature and the deformation degree on the DRV and DRX of Ni-Ti SMA was obtained as well. The results show the combination of DRV and DRX at 600 °C and 700 °C, but the complete DRX occurs at higher temperatures (800 – 1000 °C). Thus, addition, the strain rates and the deformation temperatures have important effects on the size of the grains from DRX. They observed that decreasing the strain rate contributes to obtain the large equiaxed grains, as shown in Figure 2.14. (Jiang, 2013a)

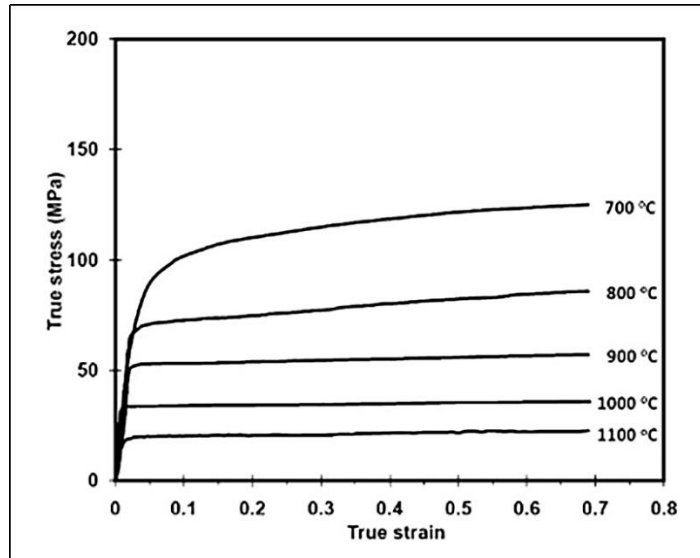


Figure 2.13 – Ni-Ti SMA true stress-true strain curves at different temperatures and strain rate 0.001 s^{-1} . (Morakabati, 2011)

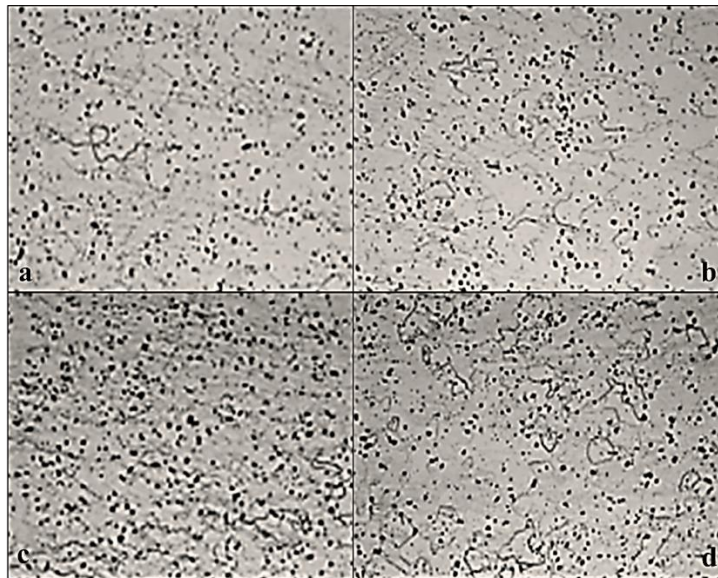


Figure 2.14 - Optical microstructures of Ni-Ti samples at 800 °C – (a) 0.001 s^{-1} ; (b) 0.01 s^{-1} ; (c) 0.1 s^{-1} and (d) 1 s^{-1} . [adapted from (Jiang, 2013a)]

Dehghani *et al.* (2010), studied the hot compression behavior of the Ti-60.0 wt.% Ni alloy, the test was carried out from 950 to 1050 °C and at a strain rate of 0.001 – 0.35 s^{-1} . They observed that the peak and steady-state stresses decrease with increasing deformation temperature and decreasing strain rate. These studies reported that this alloy experienced dynamic recrystallization. (Dehghani, 2010)

Khamei *et al.* (2010), studied the microstructural evolution during the hot deformation of the Ti-55Ni (at.%) and observed that the dominant softening mechanism, is dynamic recrystallization by a bulging and necklace mechanism. Usually the nucleation of DRX

grains in polycrystals proceeds from prior grain boundaries to non-recrystallized regions. The new grains are formed at the grain boundary serrations. After the repetition of this process, the necklace structure is formed. In addition, this study presents the influence of strain on the microstructure of specimen deformed at 1050 °C and at the strain rate of 0.1 s⁻¹ (Figure 2.15). The initial material has a homogenized microstructure with uniform grains. It is possible to observe that when the strain is increased to 0.2, the original grain boundaries become serrated, and a small number of dynamically recrystallized grains were observed on the boundaries. The strain increased from 0.4 to 0.7, the DRX grains are more evident. At a strain of 1.0 there is no significant sign of initial grains, the microstructure is completely recrystallized. Thus, the larger the deformation, more fraction of DRX grains are formed. (Khamei, 2010)

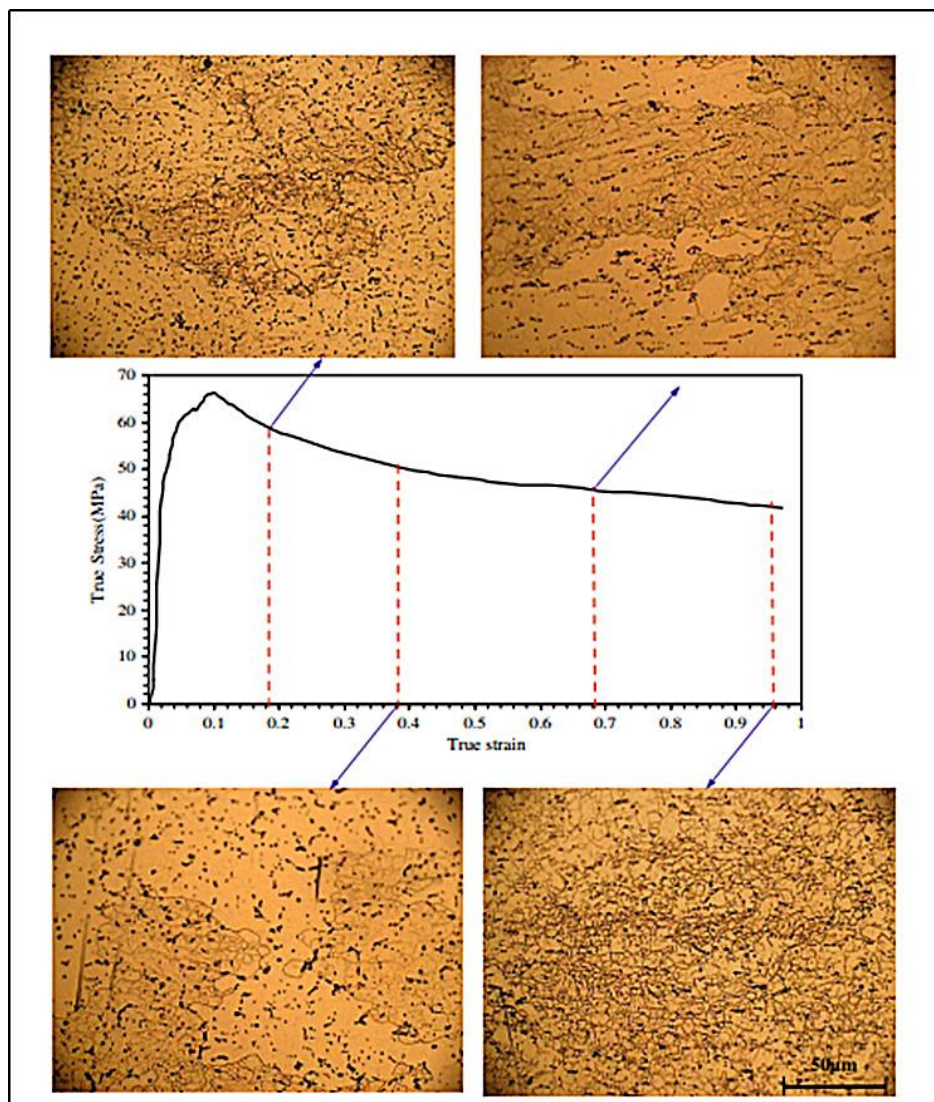


Figure 2.15 - Microstructural evolution of Ni-Ti alloy with increasing strain, deformed in compression at temperature of 1050 °C and a strain rate of 0.1 s⁻¹. (Khamei, 2010)

The onset of DRX can be detected from the inflections in plots of the work hardening rate (θ) versus σ (before the peak point of flow curves) as shown in Figure 2.16a. The $\theta - \sigma$ curves (Figure 2.16a) show inflection points, which is evident from the appearance of a global minimum in $-d\theta/d\sigma$ versus σ curves (Figure 2.16b). These observations are considered as signs for the occurrence of DRX. In each curve of Figure 2.16a, the work hardening rate (θ) linearly decreases with the flow stress. After that, the curves gradually change to another linear line and then drop toward $\theta = 0$ at peak stress. Afterwards, the work hardening rate becomes negative and then again tends to $\theta = 0$ at steady-state stress. This is better shown in Figure 2.16c and these results are consistent with the general DRX behavior (Mirzadeh, 2009) (Mirzadeh, 2010) (Mirzadeh, 2012). The characteristic points of flow curves were detected from $-d\theta/d\sigma$ versus σ (based on their minimums to find the critical stress for initiation of DRX, σ_C , as shown in Figure 2.16b), $\theta - \sigma$ (to find the peak stress, σ_P , and steady-state stress, σ_S , as shown in Figure 2.16c), $\theta - \varepsilon$ (to find the peak strain ε_P and steady-state strain ε_S , as shown in Figure 2.16d), and $\ln\theta - \varepsilon$ curves (based on their inflection points to find the critical strain for the onset of DRX, ε_C) (Mirzadeh, 2014).

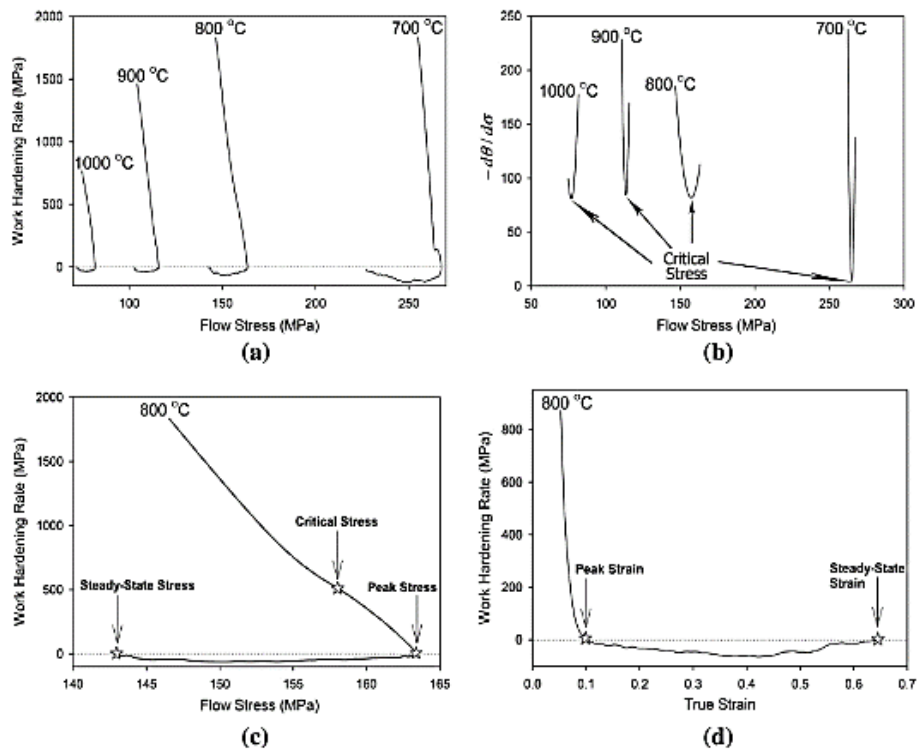


Figure 2.16 - Work hardening rate analyses. It should be noted that third order polynomials were fitted to the $\theta - \sigma$ curves (until the peak point corresponding to $\theta = 0$) to get smoother $-d\theta/d\sigma - \sigma$ curves. (Mirzadeh, 2014)

2.2.3.2. Cold Working

Cold deformation aims to acquire the final form and the required mechanical properties according to its final application. Comparing to the hot working, cold working is more difficult. The workability depends on the composition of the alloy. As mentioned previously, the hardness increases with increasing Ni content, especially if the alloy exceeds 51% at Ni.

Then, after hot deformation steps, the process is followed by a series of cold working processes, with intermediate annealing thermal treatments in a range of temperatures between 500 °C and 800 °C. This heat treatment promotes the rearrangement of the dislocations, imposed by deformation, thus increasing its ductility and restoring the structure. In this case, the recovery or recrystallization that occurs is called static; the annealing is usually carried out without stress or strain. These mechanisms occur when the material is annealed at high temperature (above recrystallization temperature) for a certain time. In addition, an oxide layer, formed by the heat treatment, on the wire surface improves the lubrication. (Suzuki, 1998)

Świec *et.al*, studied an alloy of nominal chemical composition of Ni_{50.4}Ti_{49.6} alloy after cold rolling in the martensitic state and further annealed. They reported that the cold deformation can affect the shape memory effect and transition temperatures. Due to reduction of the grain size, the hardness increases with increasing deformation degree. Transition temperatures decrease with the increase of deformation degree and the decrease of annealing temperature. (Świec, 2016)

2.2.4. Heat Treatments

Heat treatments on Ni-rich Ni-Ti alloys, aim to reduce and/or eliminate residual deformation introduced by deformation processes, as well as the solution and ageing treatment aim to control the presence, shape and distribution of the Ni-rich precipitate in the matrix. They are important to improve functional properties and the mechanical properties of Ni-Ti SMA.

To achieve optimized properties, before deformation by cold work, about 30-40%, a previous heat treatment must be applied. These materials are typically heat treated at about 500 °C.

After ageing treatment, the Ni-rich Ni-Ti alloy present the multi steps transformation. The literature presents factors to explain this, such as: heterogeneous distribution of stresses in the matrix of B2 around the precipitates of Ni_4Ti_3 , due to the degree of incoherence between the precipitates and the matrix of B2 and compositional heterogeneity in the matrix of B2 around the precipitates of Ni_4Ti_3 . (Khalil-Allafi, 2004) (Zhou, 2005)

Lekston. *et.al.*, showed the results of the research on Ni-Ti rods after hot rotary forging before the solution heat treatment at 800 °C/15 min, 750 °C/15 min and 700 °C/15 min followed by quenching into the mixture of water and ice. The samples quenched from 800 °C/15 min were aged at 300, 350, 400, 450, 500, 550 and 600 °C for 30 and 60 minutes. They reported that at room temperature the samples after solution treatment and aging present B2 and a small quantity of B19' phases. The DSC measurements showed one step reversible martensitic phase transitions $\text{B2} \leftrightarrow \text{B19}'$ for the alloy after solution treatments and the aged samples at 400 and 450 °C presented multi steps transitions (Figure 2.17). The sample after heat solution treatment at 800 °C showed the A_f near room temperature. (Lekston, 2016)

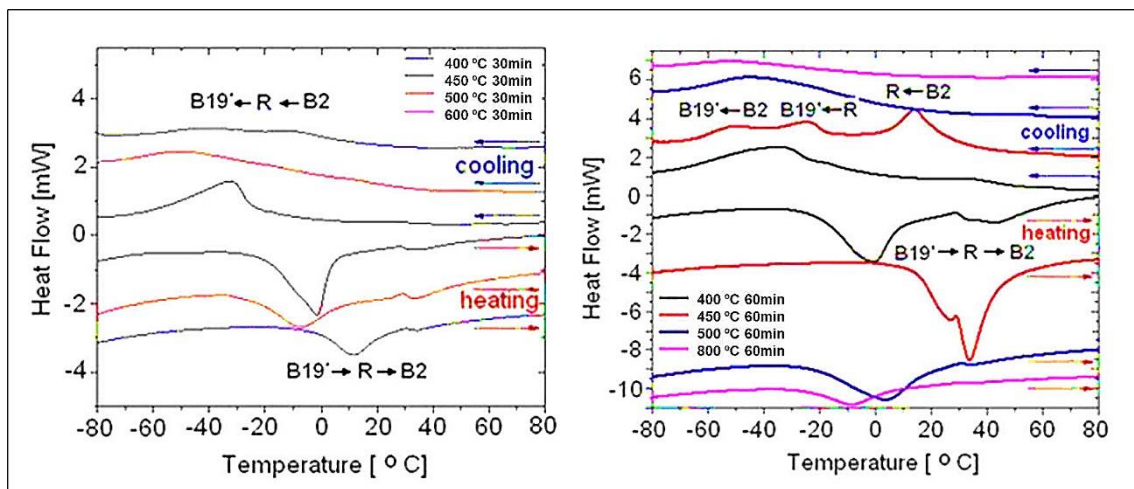


Figure 2.17 - DSC charts of the samples after solution treatment at 800 °C/15 min and aged at 400, 450, and 500 °C for 30 and 60 minutes. (Lekston, 2016)

Jiang *et.al.* (2013b), studied the influence on microstructural evolution and mechanical behavior of the Ni-Ti SMA with a nominal composition of $\text{Ni}_{50.9}\text{Ti}_{49}$ which was subjected to solution treatment at 850 °C during 2 hours and subsequent ageing for 2h at 300 °C, 450 °C and 600 °C. They reported that the solution treatment contributes to eliminate the Ti_2Ni phase in the as-received Ni-Ti sample. Solution treatment leads to ordered domain of atomic arrangement in Ni-Ti alloy. Moreover, solution treatment can

eliminate the dislocation defects in the as-received Ni-Ti sample. For the aged samples, all treatments showed a Ni_4Ti_3 precipitates, the R-phase and the B2 austenite coexist in the NiTi matrix at room temperature (Jiang, 2013b)

Yeung *et al.* (2004), explored the effects of heat treatment process in austenite phase transition temperature on a near-equiatomic Ni-Ti (Ti-55 wt.% Ni) and adjusted the transition temperature by heat treatment method. This study applied the solid solution treated at 800, 850 and 900 °C during 1 hour. They reported that the austenite transition can be manipulated by adjusting some heat treatment parameters such as: time and temperature. However, the temperature is the most critical factor to change the transition temperature. (Yeung, 2004)

2.2.5. Functional Gradient

Some applications of Ni-Ti SMAs, requiring a wider controllable range, a wider temperature/stress range than that associated to a specific composition/heat treatment may be required (Otsuka, 2005). In such a situation, the possible solution will be to use a functionally graded material (Shariat, 2017).

Functionally graded SMAs have the benefit of combining the functionalities of the SME and those of functionally graded structures. By suitable design, they may display a complex deformation behavior that is not observed in uniform shape memory alloys. Functional gradient may be introduced by: (i) a geometrical gradient (variable cross-section along a specific direction), (ii) a chemical composition gradient (either along the longitudinal direction, or along the thickness), (iii) a graded heat treatment, or (iv) may indirectly arise from a processing technique, such as welding. (Shariat, 2017)

Shariat *et al.* (2017) reported that depending on the direction of the property or geometry gradient relative to the direction of loading, the designs can be classified into two types of gradient configuration: series and parallel designs. They also present that the series design is in analogue to the Maxwell model in mechanics, in which the external load is applied in the direction of the gradient. The deformation (and transformation) occurs sequentially and extended from one end to the other (Figure 2.18)

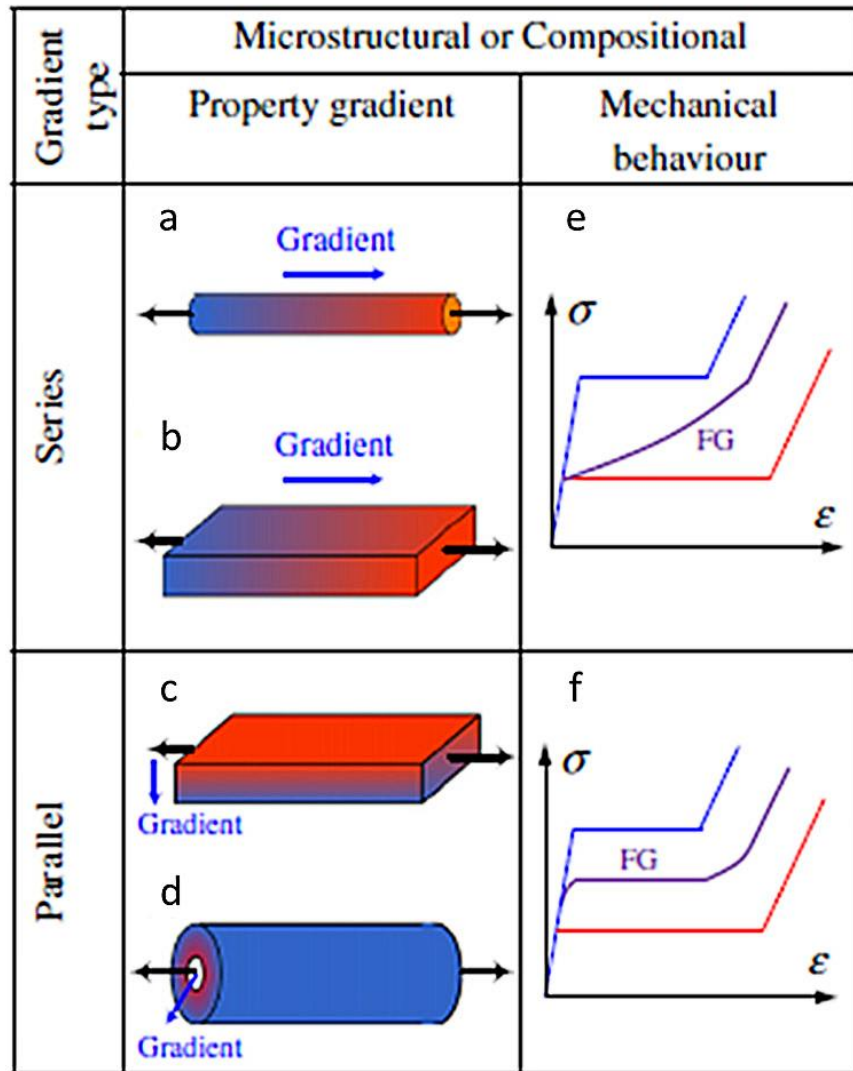


Figure 2.18 - Designs of microstructural or compositional functionally graded (FG) Ni-Ti. (a) and (b) show examples of functionally graded in series and parallel configuration (d). (e) and (f) show examples of the series configuration mechanical behavior and parallel configuration mechanical behavior. [adapted from (Shariat, 2017)]

In this current study was observed the characteristic of the microstructurally or compositionally graded Ni-Ti SMA performed by the series configuration.

The SMAs compositionally graded have variations in composition, such as Ni and Ti content, across the material. The heat treatment performed in a Ni-rich Ni-Ti alloy, after cold work below recrystallization temperature promotes a progressive increase of the M_s temperature with increasing the heat treatment temperature. Concurrently the critical stress for inducing the martensitic transformation at a specific temperature above the M_s temperature decreases. These treatments affect the mechanical properties and transformation, by the formation of the Ni-rich precipitates (coherent and incoherent). Thus, these heat treatments provide the formation of the microstructural gradient. The

alloy displays, variation in microstructural characteristics, across the material treatment direction, but the global composition is uniform. Stress, strain and transformation temperature are sensitive to heat treatment.

Shariat *et al.* (2017) and Meng *et al.* (2016) reported that a Ni-Ti wire with 50.8% at. Ni (as received sample) exhibits full pseudoelastic behavior during the deformation and after electrical heat treatment the sample exhibit two stress plateau over stress-induced transformation (Figure 2.19). The deformation of unheated section of the wire displays the stress plateau values close to as-received sample and display the pseudoelastic recovery upon unloading. The deformation of heated section of the wire displays lower stress plateau and shows no recovery upon unloading. They confirm that, this behavior is attributed to the over-aging of this section and transform the coherent precipitates (Ni_4Ti_3) into incoherent (Ti_2Ni_3 and TiNi_3) precipitates. The localized heat treatment promotes the formation of the Ni_4Ti_3 precipitates; the internal section, being the one that is heated to a higher temperature, will have a more intense precipitation which will give rise to Ti-richer matrix; this higher Ti content of the matrix brings as a consequence a higher transformation temperature and, ultimately, also a lower critical stress for the austenite – martensite stress-induced transformation. (Shariat, 2017) (Meng, 2016)

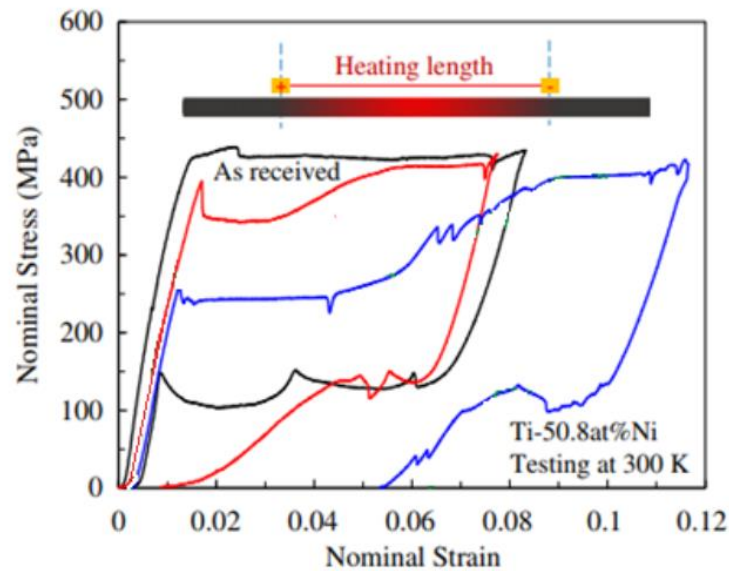


Figure 2.19 - Tensile deformation behavior of Ti-50.8 at.%Ni wires after local over-aging by electrical resistance heating. (higher plateau – no heat-treated section and lower plateau – treated section). (adapted from (Shariat, 2017))

2.3. Textural Evolution

As mentioned in earlier topics, the manufacturing of the Ni-Ti materials involves several processing procedures, such as rod drawing and heat treatment, aiming the modification of microstructure, the transformation temperatures and the mechanical properties. These procedures can also lead to texturing (crystallographic alignment) of the material. The texture has an influence on its mechanical properties.

Normally, in a polycrystalline material the grains have a crystallographic orientation different from the one presented by its neighboring grains. When the material with a deformation texture is recrystallized, the new structure of the grain can present a different texture from the deformation texture: the recrystallization texture. Ni-Ti alloys usually show the typical α <110> fiber texture for the bcc structure. (Miyazaki, 1989) (Laplanche, 2017)

Suresh *et al.* (2012), studied the evolution of grain boundary microstructure and crystallographic texture during hot rolling of a 50.6 % at.Ni Ni-Ti alloy. The alloy was produced by the vacuum arc melting technique. The starting material was heat treated at 1000 °C, followed by water quenching. The treated samples were hot rolled at 700 °C to total reductions of 60 %, 80 % and 90 %, with a 10 % reduction per pass and intermediate annealing at 700 °C during 3 min. The crystallographic texture of the deformed sample consists mainly of <111> fiber texture. The texture components on the fiber exhibit some correlation with the type of coincidence site lattice boundary. They reported the complete orientation distribution function (ODF) for starting material and the rolled samples, calculated from the X-ray diffraction pole figures. Figure 2.20 shows the ODFs for the starting materials and deformed materials, where 60 % rolled sample displays a very weak texture and the texture is strongly defined after 80 % rolling, but decreased again for the 90% rolling reduction.(Suresh., 2012)

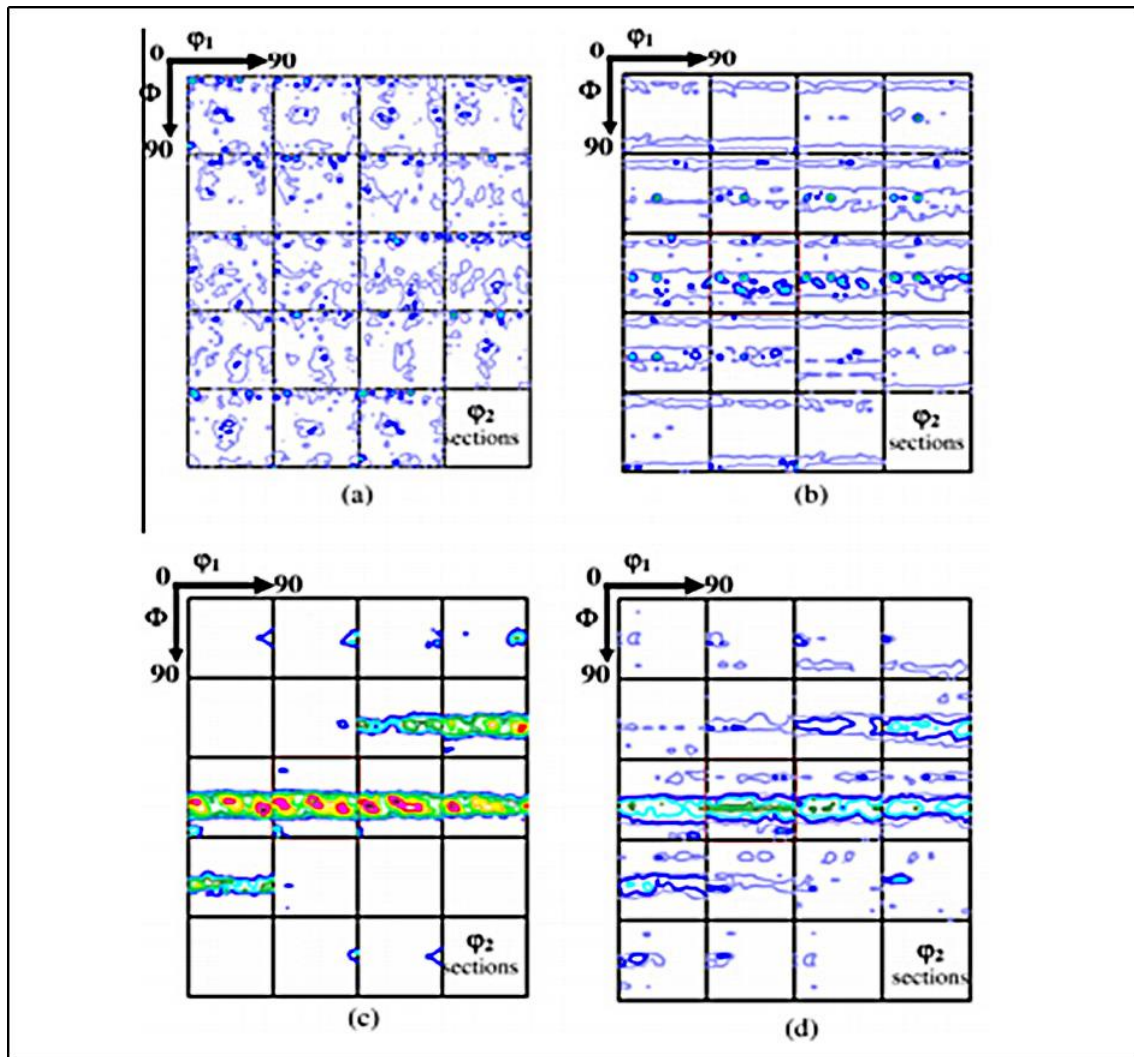


Figure 2.20 - The ϕ_2 sections of the complete orientation distribution function (ODF) of (a) starting material and (b) 60 %, (c) 80% and (d) 90% deformed Ni-Ti. (Suresh, 2012)

In the past, Willemse *et.al* (1991), investigated the texture of Ti-44Ni-5Cu (at %) shape memory alloy wire after cold drawing and annealing at 550 °C during 3 minutes under tensile stress. The textures were observed by x-ray diffraction patterns, using the transmission mode. The texture of the austenite (B2 structure) and martensite (B19' monoclinic) phases was determined as a function of the percent of cold deformation during the drawing process and the number of cycles on thermomechanical cycling. Figure 2.21 shows the example of the observation of the texture by x-ray diffraction patterns, where the [110], [1-10] [101] and [-101] directions are parallel to the wire axis. The preference for the [-101] component was reported. However, after heating the wire above A_f temperature and cooling at room temperature, this preference disappears. The preference develops again after thermomechanical cycling. (Willemse, 1991)

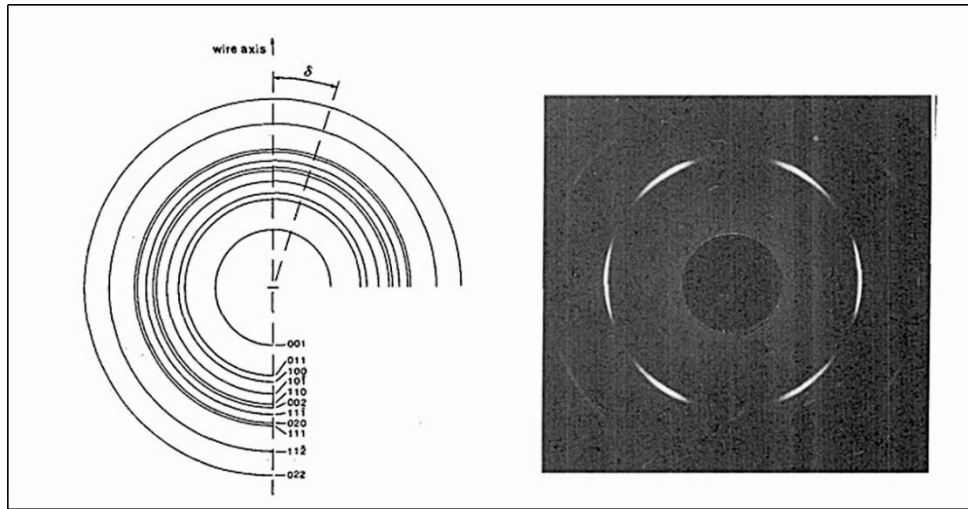


Figure 2.21 - Observed reflection on wire axis and diffraction pattern of the B2 phase. (Willemse, 1991)

Paula *et.al.* (2007), studied the evolution of texture in a plate of Ni-Rich Ni-Ti alloy (50.8at%Ni-Ti) SMA. (Figure 2.22 (a) as-received sample, (b) heat treated sample and (c) heat treated + cold rolled + heat treated sample). The texture analysis at room temperature was performed with the rolling direction aligned with $\varphi = 0^\circ$ and the transversal direction with $\varphi = 90^\circ$. Due to the thermal/mechanical alloy history (annealed, as-received condition, and subsequent thermal treatment at 500 °C during 30 minutes) different phase transformation temperatures are observed. They reported that the heat treatment at 500 °C promoted recrystallization and Ni_4Ti_3 precipitation was observed. This contributes to stress relief inside the austenite grains, the texture components observed close to $\chi = 18^\circ$ associated with texture components $\{210\}\langle 110\rangle_{\text{B2}}$ and other components close to $\chi = 30^\circ$ associated with texture components $\{211\}\langle 110\rangle_{\text{B2}}$, with RD in $\langle 110\rangle$, as shown in Figure 2.22. (Paula, 2007) (Ribeiro, 2011)

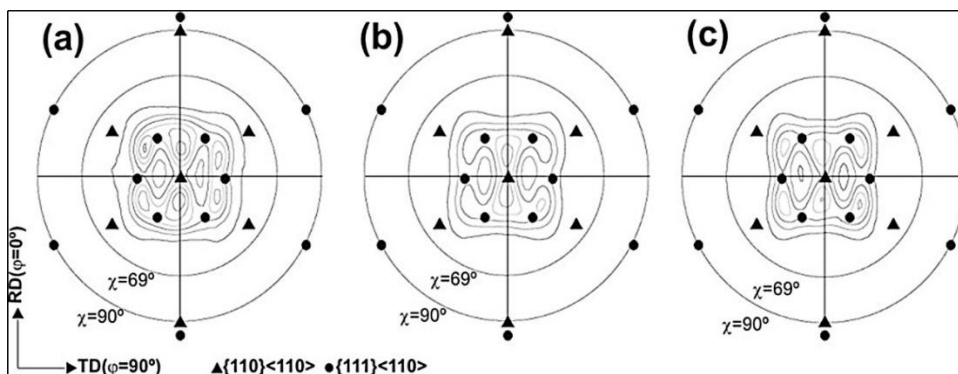


Figure 2.22 - Pole Figures $(110)_{\text{B2}}$ obtained from as-received, heat treated at 500 °C and deformed. (Paula., 2007)

Laplanche *et.al.*, studied the evolution of microstructure during processing of 51% at Ni-Ti alloys hot rolled. The process results in a heterogeneous microstructure which reflects a temperature gradient in the sheet. Near the surface, equiaxed and randomly oriented grains are observed, while the interior grains present a strong texture containing two main texture components $\{111\}\langle 110\rangle$ and $\{110\}\langle 110\rangle$; these interior grains are elongated along the rolling direction. On the other hand the cold rolling with a recrystallization heat treatment produces homogeneous microstructure, promoting, as a consequence, a random grain orientation along the rolling and transverse directions, while the normal direction shows a strong γ -fiber $\{111\}\langle uvw\rangle$ texture. (Laplanche, 2015)

2.4. Orthodontic Archwires

As this study focused on an alloy that is intended to be used in the orthodontic segment, with superelastic characteristics at room and oral temperature, it is fundamental to discuss some characteristics about this product. Through these characteristics it is possible to understand the properties that need to be achieved in order to obtain the most suitable functional properties for orthodontic segment.

The aim of orthodontic treatment is to move the teeth to the correct position through the application of forces (Figure 2.23).

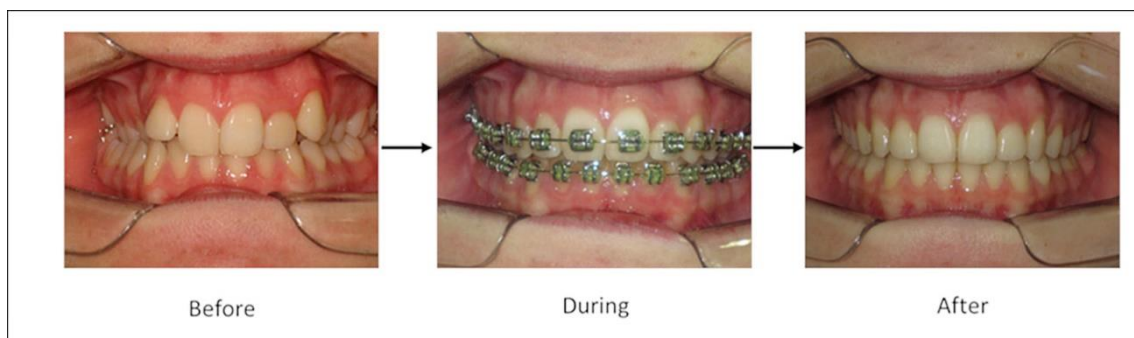


Figure 2.23 - Sequence of the orthodontic treatment.
(Files provided by Dr. Raffaella Magalhães with patient authorization)

The orthodontic mechanics principle is based on elastic energy storage and its conversion into mechanical work giving rise to tooth movement. (Cardoso, 2009)

However, the ideal situation is when this force produces tooth movement with light and continuous force, without damage to the teeth or periodontal tissues. When a force is applied, the orthodontic archwire needs to display an elastic behavior during a period of

weeks to months. For this reason, the superelasticity it is an important property, due to biological compatibility with the tooth movement, during a long period of deactivation.

The superelastic behavior can be analyzed by the shape of load-deflection tests (three-point bending test). The plateau during unloading (Figure 2.24 – yellow box) has been defined as the superelastic actuation region during the treatment (Nespoli, 2005). Figure 2.24 shows the load-deflection curves of the wires with graded actuating forces at different temperatures.

Moreover, different stages (initial, intermediate or final) of the orthodontic treatment require different orthodontic archwires. (Proffit, 2013) (Melsen, 2007)

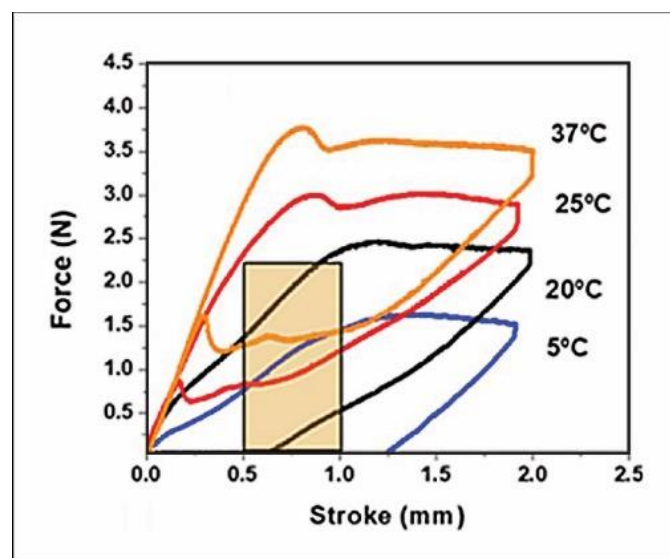


Figure 2.24 - Load-deflection curves of the wires with graded actuating forces at different temperature and the superelastic actuation is identified.

Since the beginning of the orthodontic history, the archwires have become more complex and convenient for different clinical cases. Due to the advancements in the technology over time, some improvements of the orthodontic archwires properties were performed.

Earlier, Edward Angle, who was an important professional at orthodontic field, has chosen the gold alloys as his favorite material for the orthodontic archwires. But the economic factors helped to determine the acceptance of stainless steel (SS) over gold. (Kusy, 2002) The SS alloys also show a good combination of mechanical properties and cost. (Muguruma, 2018) (Kusy, 2007) Afterwards, Elgin Watch Company developed a complex alloy: cobalt (40%), chromium (20%), iron (16%) and nickel (15%). This

cobalt – chromium alloy was marketed as Elgiu™ (Rocky Mountain Co). (Cardoso, 2009) These alloys show mechanical properties similar to stainless steel for the same dimensions of the wires producing force with the same magnitude. (Khamatkar, 2015)

In the 70s the Beta-titanium wires were introduced. They are also known as titanium-molybdenum alloy (TMA) (ORMCO, Orange, CA, USA) or Titanium- Niobium (ORMCO, Orange, CA, USA). Their first application on the orthodontic field occurred in the 1980s and a different titanium alloy was called as "high temperature". (Johnson, 2003) These alloys have: an excellent formability, lower forces, good resistance to corrosion and good biocompatibility but they are expensive. (Cash, 2004)

Just in the 80s was reported the use of a new superelastic Ni-Ti alloys. These alloys displayed elastic recovery and lower stiffness than other conventional Ni-Ti wires. However, in the 90s the thermoactivated Ni-Ti alloys were introduced. These alloys have a superelastic effect activated by oral temperature. (Gioka, 2002) Even in the 90s Ni-Ti with the addition of copper (CuNiTi) became available on the market. Still in 1990s occurred the emergence of gradually thermoactivated Ni-Ti wires. These wires show a range of different forces that can be generated by the same archwire in its different segments. (Kotha, 2014)

The archwires are chosen depending on their properties. For the initial stage of the treatment (leveling and alignment), the most commonly used archwires are Ni-Ti orthodontic archwires (SMA). As Ni-Ti archwires have the unique properties shape memory effect and superelasticity, they are useful for initial leveling and alignment of teeth. (Riley, 2009)

To support the discussion about Ni-Ti orthodontic archwires behavior in this study, two types of orthodontic archwires are presented: superelastic and thermally active archwires.

Ni-Ti superelastic orthodontic archwires usually are nearly equiatomic proportions or slightly Ni-rich, promoting the stability of the austenite phase at room temperature ($A_f \leq 25 \text{ }^\circ\text{C}$). However, the thermally active archwires are Ti-rich, and the A_f temperature is higher than for superelastic orthodontic archwires ($A_f > 25 \text{ }^\circ\text{C}$). Dependent on the composition, the A_f temperature for these archwires can be close to oral temperature ($\sim 34 \text{ }^\circ\text{C}$). The thermally active archwire has a fully B2 structure at oral temperature, whereas at room temperature is composed of martensite, austenite and

perhaps R-phase. Thus, these orthodontic archwires have the capability to be more easily applied to the malposed teeth. At lower temperatures (e.g. cold water 5 °C) the archwires can be deformed into the desired configuration and ligated in the teeth before heating above its transition temperature range, e.g. by human body temperature (~37 °C). At this temperature, the archwire attempts to return to its original form, displaying shape memory. (Hurst, 1990)

Many authors investigated the thermal and mechanical behavior of the Ni-Ti orthodontic archwires.

Iijima *et al.* (2002), studied three Ni-Ti SE archwires, in order to evaluate the effects of temperatures changes (from 37 to 60 °C) in the mechanical properties of the wires. This study concludes that the load delivered by the Ni-Ti wires increases on heating and decreases on cooling. (Iijima, 2002)

Through the heat treatment, as mentioned previously, the functional gradient can be introduced in the orthodontic archwire. This archwire shows light forces in the incisive segment, medium force in the premolar segment and a higher force in the molar region. The literature reported an actuating force of about 3 N in the molar region, 1.8 N in the premolar region and in the incisive region displayed a plateau force of 0.8 N (Malik, 2015). Currently, the archwires with graded actuating forces are commonly used during the orthodontic treatment. (Mullins, 1996)

As shown in section 2.1, the functional characteristics present in these alloys are a consequence of phase transformations that take place within well-defined temperature range or stress range, depending on being thermal or stress-induced. These temperature/stress ranges are a function of chemical composition and heat treatment of the material.

For applications, e.g. orthodontic treatments, requiring a wider controllable range, a wider temperature/stress range than that associated to a specific composition/heat treatment may be required. The use of functionally graded materials is a good solution. This type of materials can display the martensitic transformation at a different temperature or stress along their length. (Shariat, 2017)

Materials and Methods

In this section, the characteristics of each alloy studied, the thermal and thermomechanical treatment applied, and characterization techniques used in this investigation are reported.

The materials are described in three sections:

- Alloys in the as-cast and remelted conditions;
- Thermomechanical processing;
- Ni-Ti orthodontic archwire.

Three distinct Ni-Ti alloys in the as-cast and remelted condition were used for the thermomechanical processing (forging process). Three alloys with different Ni concentration from 49.3 to 50.8% at.Ni (global composition). The main alloy investigated in this study was 50.8% at.Ni alloy. Moreover, in parallel to this investigation, a study of the 49.3% at.Ni (slightly Ti-rich) and 49.9% at.Ni (very close to equiatomic composition) alloys was done, to understand the relationship between properties and structure.

The thermal and thermomechanical treatments were applied in order to understand the functional behavior, by controlling the thermophysical, structural/textural and mechanical characteristics. Thus, the forging process steps were analyzed to identify the main characteristics of the structural changes and their correlation with the processing parameters.

In addition, orthodontic archwires were used in a reverse engineering approach to identify the best process sequence that could be applied to achieve the most adequate characteristics of the product. Following this trend, the characterization of commercial

functionally graded Ni-Ti orthodontic archwire was performed and the introduction of graded functionality in conventional archwires was analyzed.

Different characterization techniques were used throughout the study: wavelength dispersion spectroscopy (WDS), Electronic Microprobe analysis (EMPA), optical microscopy (OM), scanning electron microscopic (SEM), energy dispersive X-ray spectroscopy (EDS), Electron Backscattered Diffraction (EBSD), X-ray diffraction using conventional lab sources (XRD), X-ray diffraction using synchrotron radiation (SR-XRD), differential scanning calorimetry (DSC), thermomechanical analysis (TMA - dilatometry (DT), mechanical tests (compression/tensile and three-point bending). The techniques are presented with their general characteristics.

3.1. Ni-Ti Alloys

The materials investigated in this study were three Ni-Ti alloys, which are Ni-rich “alloy 1” with 50.8% at. Ni, “alloy 2” with 49.9% at. Ni and “alloy 3” with 49.3% at. Ni (global composition), Table 3.1. These alloys were manufactured and supplied by Prof. Jorge Otubo of the Technological Institute of Aeronautics (ITA), Brazil.

Table 3.1 – Alloys: 1, 2 and 3 Ni and Ti contents (%at).

Alloy	Ni %at.	Ti %at
1	50.8	49.2
2	49.9	50.1
3	49.3	50.7

3.1.1. As-cast and Remelted alloys

Three ingots were produced by vacuum induction melting (VIM) under Argon atmosphere using a graphite crucible. After melting, the materials were cut into pieces with a mass of approximately 90g and remelted by Vacuum Arc Remelting (VAR), using a copper crucible to maintain low carbon levels (Figure 3.1a). The ingots remelted in the copper crucibles have an appropriate shape to start rotary forging, as shown in Figure 3.1b. For this study two ingots of each alloy were used (Figure 3.1c): one was used for rotary forging, another for complementary tests. The remelting parameters were: current 230A, direct polarity, constant current, vacuum at 10^{-2} mbar.

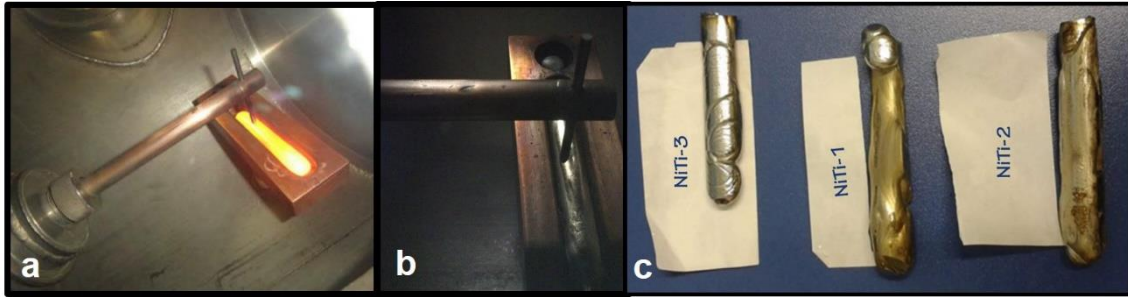


Figure 3.1 – Vacuum Arc Remelting (VAR) a) During remelting process; b) After remelting process; and c) three processed ingots.

The overall chemical composition of the materials was determined by wavelength dispersion spectroscopy (WDS – Oxford Instruments, controlled by INCA software, available at Instituto Nacional de Tecnologia (INT), Brazil). The WDS analysis was performed on an SEM FEG 450 with a tungsten filament. The WDS parameters were: 20 kV accelerating voltage, WD 12 mm and probe current of 13.3 nA for 5 spots in metal matrix of each sample were used. The magnification used was enough to choose the metallic matrix region inside the NiTi dendrites without influence of the interdendritic regions (TiC and/or oxides (TiO_2 and/or $\text{Ti}_4\text{Ni}_2\text{O}$)), using magnifications 10.000x and 20.000x.

Given that the aim of this study is to get a material that displays superelastic behavior at room temperature, the NiTi_1 alloy (Ni-rich alloy with 50.8% at.Ni, as shown before) was chosen as the main alloy for this study.

Moreover, the same rotary forging process was performed in all the three alloys. The alloys 2 and 3 (with different Ni contents, as mentioned previously) were analyzed to compare their results with alloy 1 results during discussion of the results.

3.1.2. Thermomechanical Process

This study was focused on the improvement of the manufacturing requirements for Ni-Ti wires. The following sections details the thermomechanical processing (rotary forging) steps which produced the main samples for this study.

The thermomechanical processing of the ingot started by heating at 800 °C during 30 minutes. After this heating, the ingots were shaped to the circular section wire by hot and cold forging steps until they reached a final diameter of around 3 mm.

In order to represent the processing applied and to facilitate its understanding, a schematic with the steps of rotary forging and intercalated heat treatments is shown in Figure 3.2.

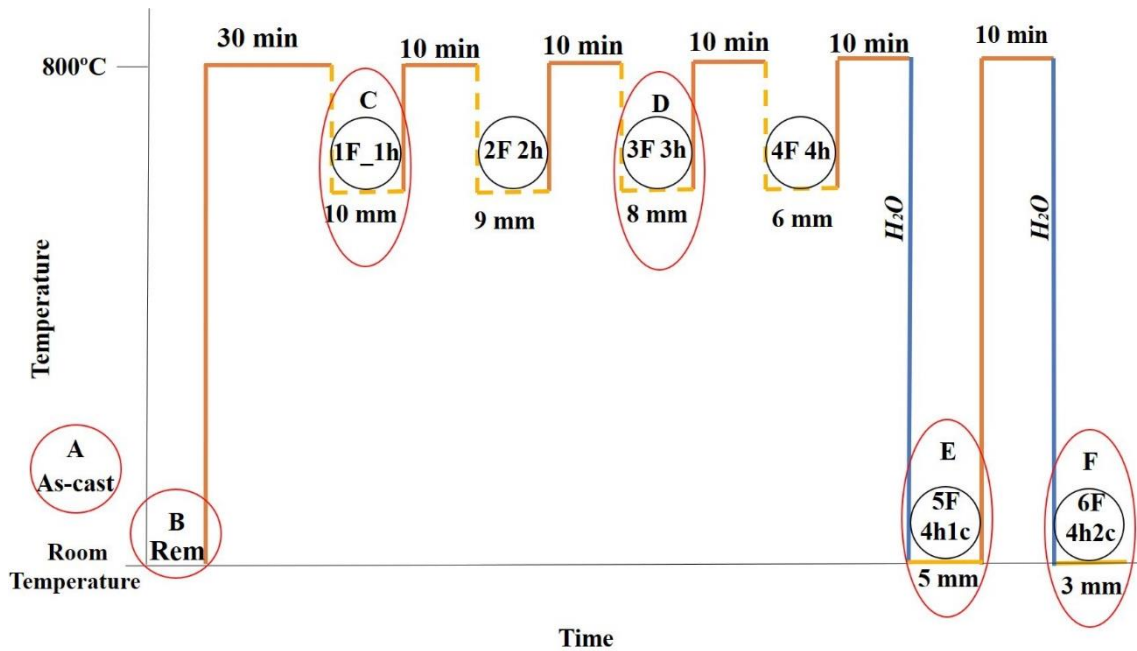


Figure 3.2 – Scheme of the initial thermomechanical processing applied to the ingots, with forging stages, temperature and time of the intercalated heat treatments and sample diameters.

For rotary forging process two forgers were used: four hammers (for the first two with bigger reductions – Figure 3.3a) and two hammers (for the four following reductions, two hot, and two cold deformations with smaller reductions – Figure 3.3b).

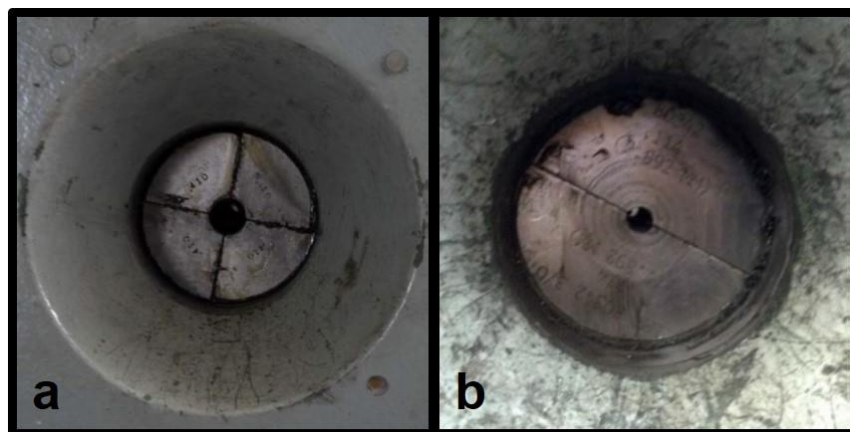


Figure 3.3 - Equipment: a) 4 hammers and b) 2 hammers, used to rotary forging steps

Before each forging step, the material was heated up to 800 °C during 10 minutes. After this heat treatment, the material was carried straight from the furnace to forgers. However, previously to fifth and sixth steps (cold rotary forging steps), the material was heated up to 800 °C during 10 minutes and quenched into water at room temperature.

As shown in Figure 3.2, the samples obtained for this study are: A, B, C, D, E and F; these samples represent the corresponding steps, with diameter reduction (Eq. 3.1) and are highlighted with a red circle in Figure 3.2. Where, φ is the diameter reduction; Δd is the change in the diameter and d_0 is the original diameter (in our case, $d_0 = 10 \text{ mm}$).

$$\varphi = \frac{\Delta d}{d_0} \quad 3.1$$

- Before the rotary forging process (Starting Material)

(A) as-cast (AC)

(B) remelted (Rem)

- Forging Steps

(C) 1st hot forging step (1F_1h), ($d_0 = 10 \text{ mm}$)

(D) 3rd hot forging step (3F_3h)

(E) 5th forging step – 1st. cold-forging step (5F_4h1c)

(F) 6th forging step – 2nd. cold-forging step (6F_4h2c)

At the 6th forging step a wire with about 3 mm in diameter was obtained.

Figure 3.4 shows a schematic of the designation of the samples referring to the applied rotary forging process.

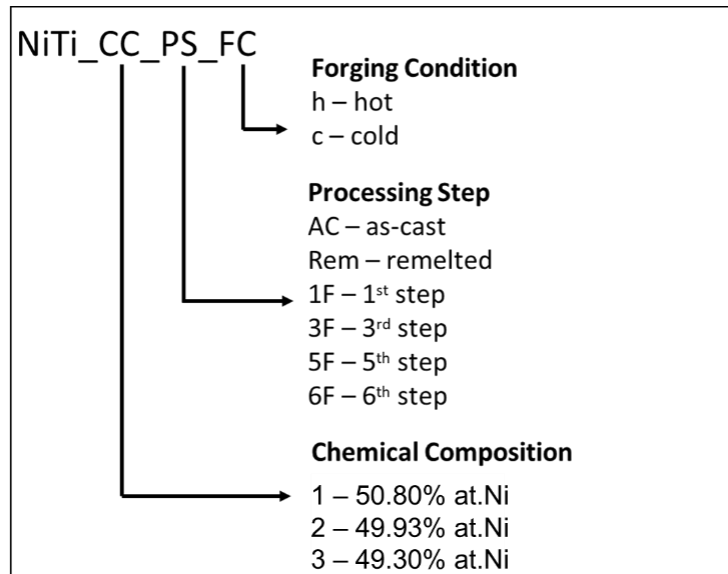


Figure 3.4 - Scheme for the samples identification.

3.1.3. Heat Treatments

The heat treatments were investigated by variation of temperature and holding time in different processing step samples.

From remelted condition, two different specimens were cut. To evaluate the effect of the conditions for the solubilization treatments, the samples were to a heat treatment condition: 30 minutes at 800 °C and 120 minutes at 950 °C.

From the first hot rotary forging step (1F_1h sample), five different specimens were cut along the longitudinal direction. These samples measure about 1 mm in height and 10 mm in diameter. To evaluate the effect of the conditions for the intermediate treatments, the samples were submitted to solution heat treatments conditions:

- 120 minutes at 800 °C, to be compared with the 800 °C during 10 minutes, used in the previous processing path;
- 120 minutes at 850 °C;
- 120 minutes at 900 °C;
- and 120 minutes at 950 °C.

After each condition, the samples were quenched into water. The heat treatment for all the Ni-Ti samples was carried out in a conventional furnace.

From the 1F_1h, 3F_3h, 5F_4h1c samples conditions, two different specimens were cut

to evaluate the effect of the intermediate treatments conditions. All these samples were subjected to two heat treatment conditions: 10 minutes at 800 °C and 15 minutes at 850 °C.

From 6F_4h2c sample condition, three different specimens were cut. To evaluate the effect of the conditions for the aging treatments, the samples were subjected to three heat treatment conditions: 30 minutes at 350 °C, 400 °C and 450 °C.

This set of tests aimed to verify the influence of the treatment conditions on the transformation characteristics of the samples of the different rotary forging steps.

3.2. Orthodontic Archwires

For this study were selected three different types of Ni-Ti orthodontic archwires: Superelastic supplied by Morelli – Brazil; Thermo Plus supplied by Morelli- Brazil and BioForce supplied by Dentsply GAC International – USA, Table 3.2.

Table 3.2 – Ni-Ti orthodontic archwires: Commercial name, Manufacturer, type, dimension (mm) and LOT (product batch).

Commercial Name	Manufacturer	Type	Dimension
Superelastic	Morelli	Superelastic	0.4 x 0.4
Thermo Plus	Morelli	Thermo-active	0.4 x 0.4
BioForce	GAC	Functionally Graded	0.4 x 0.4

3.2.1. Localized Heat Treatment Performed in Superelastic Orthodontic Archwire (Morelli SE)

The functional gradient was introduced in the Morelli SE orthodontic archwire. Sample has been cut with 55 mm length and a localized heat treatment at 300 °C for 10 minutes by Joule effect with 3.14 A, 1 V±0.5 has been carried on along a 32 mm long segment centered into the archwire. Inside this 32 mm long segment subjected to localized heat treatment, two segments of 8 mm length (hereafter referred to as external) have been separated from a central part 16 mm long (hereafter referred to as internal). A transition zone is indicated between internal and external zones. The three zones were investigated in order to relate the temperature profile and functional gradient introduced in the Morelli SE orthodontic archwire. The temperature measurement of the wire without disturbing the heat flow, was performed using an infrared camera Fluke Ti400 (Figure 3.5).

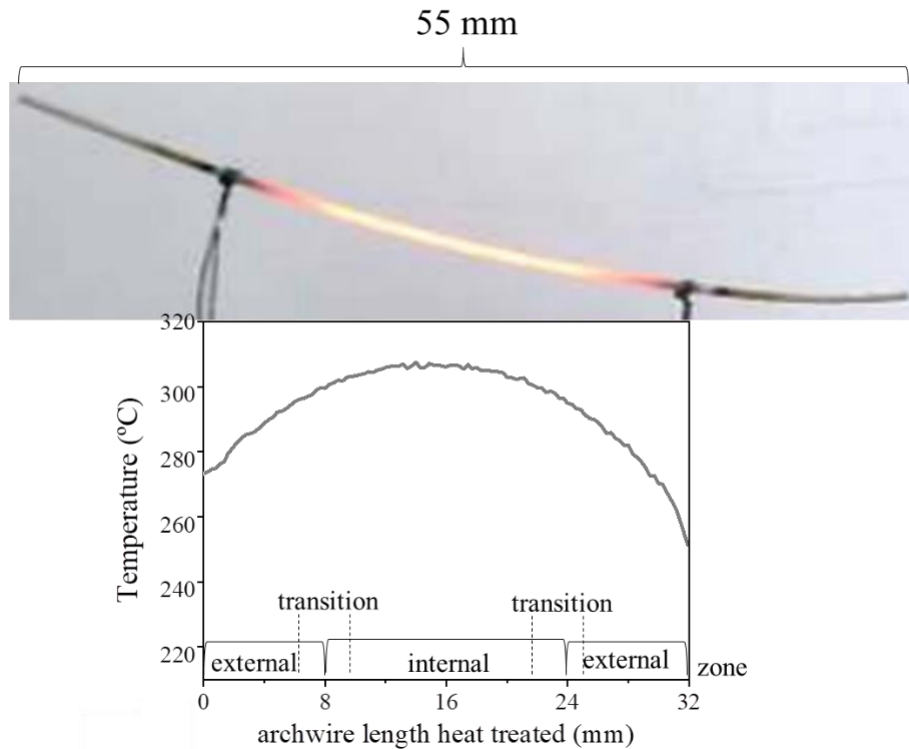


Figure 3.5 - Schematic view of the electrical local heating system of Ni-Ti wire and temperature profile. (Unpublished data from Inácio and Santos)

The details of the technique which was applied have been reported in previous study (Rodrigues, 2018); only some details about the sample are highlighted in this study for the convenience of the subsequent discussion about the influence of the heat treatment on the Ni-Ti orthodontic archwire.

3.3. Characterization Techniques

3.3.1. Scanning electronic microscopy (SEM)

The scanning electron microscopy was used to analyze the microstructure of each step of the rotary forging process. The samples were prepared by electrolytic polishing using 20 % H_2SO_4 and 80% Methanol solution, at room temperature, with 0.8A during 10 to 26 seconds. The scanning electron microscope used was a FEI Quanta 250 FEG (available at the Instituto Militar de Engenharia (IME) - Brazil) at an acceleration voltage of 20 kV. In addition, energy dispersive X-ray spectroscopy (EDS) was performed, to quantify the chemical composition of the matrix for the samples.

3.3.2. Electron Backscattered Diffraction (EBSD)

For electron backscattered diffraction (EBSD) analysis, measurements were performed in a FEI Quanta-3D field emission gun-scanning electron microscope (FEG-SEM) with Tex-SEM Laboratories (TSL)-Orientation Imaging Microscopy (OIMTM) EBSD system (available at the Indian Institute of Technology Bombay – India; in collaboration with Dr Ritwik Basu). The samples were subjected to electropolishing using a Struers Lectropol 5 system: 18 V DC, electrolyte of 80:20 (by volume) methanol: perchloric acid at 0 °C.

3.3.3. Electron Microprobe Analysis (EMPA)

The Electron microprobe analysis with field emission gun (FEG) performed using a CAMECA SX5FE to check the matrix composition for the rotary forging step samples. The experimental parameters employed were: accelerating voltage of 15 kV, beam current of 20 nA, counting time of 10s. The probe diameter varied during the investigation from 1 to 10 μm , the following standards were used:

- TiO_2 for Ti,
- pure Ni for Ni,
- Fe_2O_3 for O,
- SiC for C.

3.3.4. Optical microscopy (OM)

For microstructural observation, the specimens were mounted in epoxy resin and mechanically polished up to 4000 fine grit Silicon Carbide Paper. To reveal the microstructure of the samples, the following etching solution was used: 10 vol% HF + 45 vol% HNO_3 + 45 vol% H_2O . Optical microscopy was carried out using a Leica DMI5000M optical microscope.

3.3.5. X-Ray Diffraction Analysis (XRD)

XRD was applied to investigate the structural characteristics of the materials, such as the crystal structure, preferential orientation of the grains and the identification of the present phases.

The relationship between the wavelength of the incident x-rays, the angle of incidence and spacing between the crystal lattice planes of atoms is represented by the Bragg's law (Eq. 3.2 and Figure 3.6).

$$n\lambda = 2d\sin\theta \quad 3.2$$

Where: n is an integer number, λ is the wavelength of x-rays, d is the interplanar spacing of the crystal and θ is the angle of reflection. (Cullity, 1978)

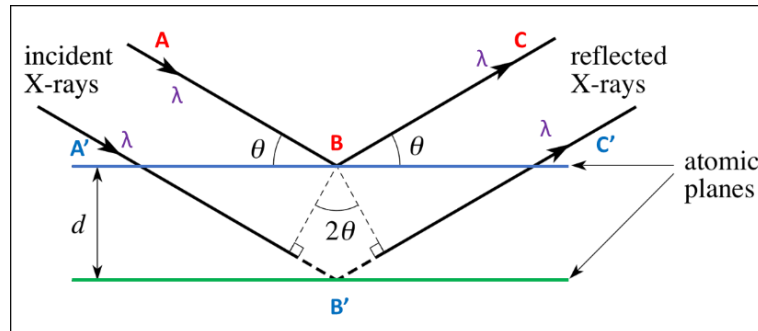


Figure 3.6 - Schematic representation of the Bragg's law.

For the SR-XRD measurement, the identification of the diffraction peaks was performed based on the ICDD database.

The XRD tests were run in 2 different systems (lab source and synchrotron radiation) that are described in the following sections.

3.3.5.1. Conventional X-Ray Source (XRD)

The conventional source was a rotating-anode based Bruker X-ray diffractometer, using $\text{CuK}\alpha$ radiation to perform non-ambient measurements and texture analysis (Figure 3.7). The non-ambient measurements were performed using a TTK-450 chamber (from Anton Paar), in the range -120 to $+120$ °C at intervals of 10 °C (Figure 3.7a), during heating and cooling. The 2θ scans covered the range from 36° to 50° ($\delta 2\theta = 0.04^\circ$; acquisition 1s per point), so that the $(110)_{\text{B}2}$ diffraction peak was observed, as well as other neighboring peaks (from $\text{B}19'$, R-phase and precipitates). This measurement also allows to determine the structural transformations sequences for the different thermomechanical steps. The texture measurements were performed with an Eulerian Cradle ($0 < \chi < 69$, $\delta\chi = 3^\circ$; $0 < \varphi < 360^\circ$, $\delta\varphi = 3^\circ$) for the $(110)_{\text{B}2}$, $(200)_{\text{B}2}$, and $(211)_{\text{B}2}$ diffraction peaks (Figure 3.7b).

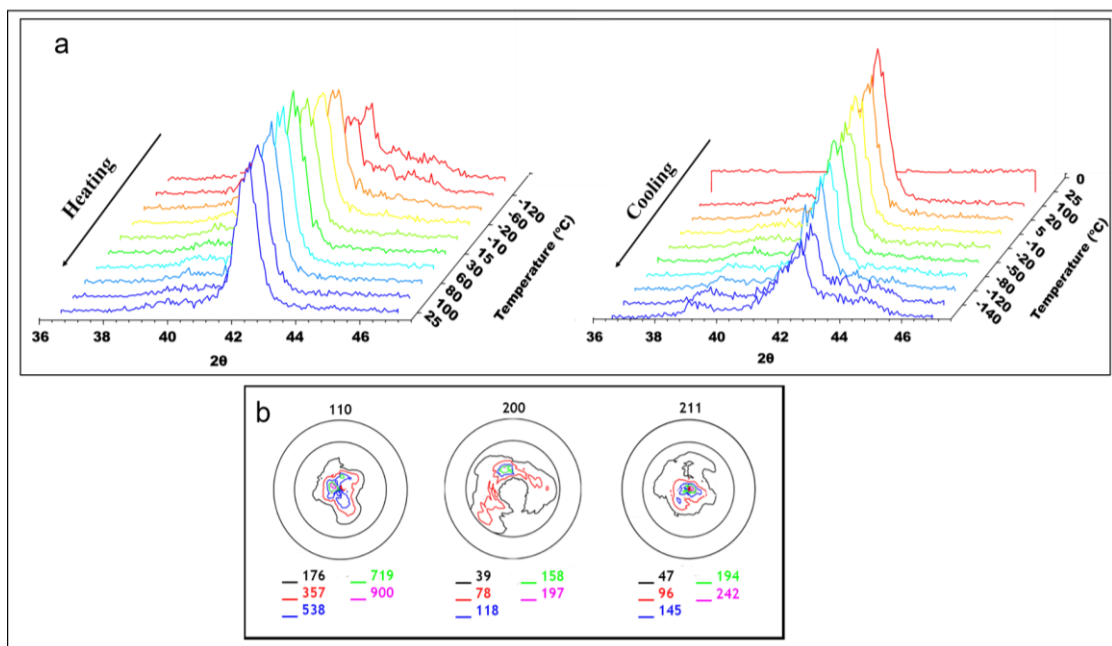


Figure 3.7 - Examples of XRD results (1F1q sample), at high/low temperature: during heating and cooling, between -120 and 120 °C (a); Pole Figures (b) (Rodrigues, 2017a)

3.3.5.2. Synchrotron Radiation X-ray Diffraction (SR-XRD)

This study was carried out in two different SR (Synchrotron Radiation) facilities:

PETRA III: an energy of 6 GeV, a current of 100 mA; and

LNLS: an energy of 1.37 GeV, a current of 250 mA

Each beamline was used with different experimental configurations. The LNLS (XRD1), promotes a beamline with low energy, which is primarily dedicated to θ - 2θ /GIXRD (Grazing Incidence X-ray Diffraction) material characterization, while PETRA III (P07) beamline is a high energy beamline, allowing x-ray diffraction in transmission mode.

3.3.5.3. Petra III – P07/DESY

Three different structural characterizations using synchrotron radiation, were performed, in beamline P07 High-Energy Materials Science (HEMS) of Petra III/DESY (Deutsches Elektronen-Synchrotron), located at Hamburg - Germany.

The first measurements used a wavelength of 0.143 Å (87 keV); a beam spot 200×200 μm^2 was used to scan the samples, at room temperature, along its diameter (as shown in Figure 3.8) and a two-dimensional (2D) detector PERKIN ELMER XRD

1621 was placed at 1.35 m from the sample. The raw 2D images were treated using Fit2D program (Hammersley, 1996) in order to calculate the individual XRD patterns by integration from 0° to 360° (azimuthal angles).

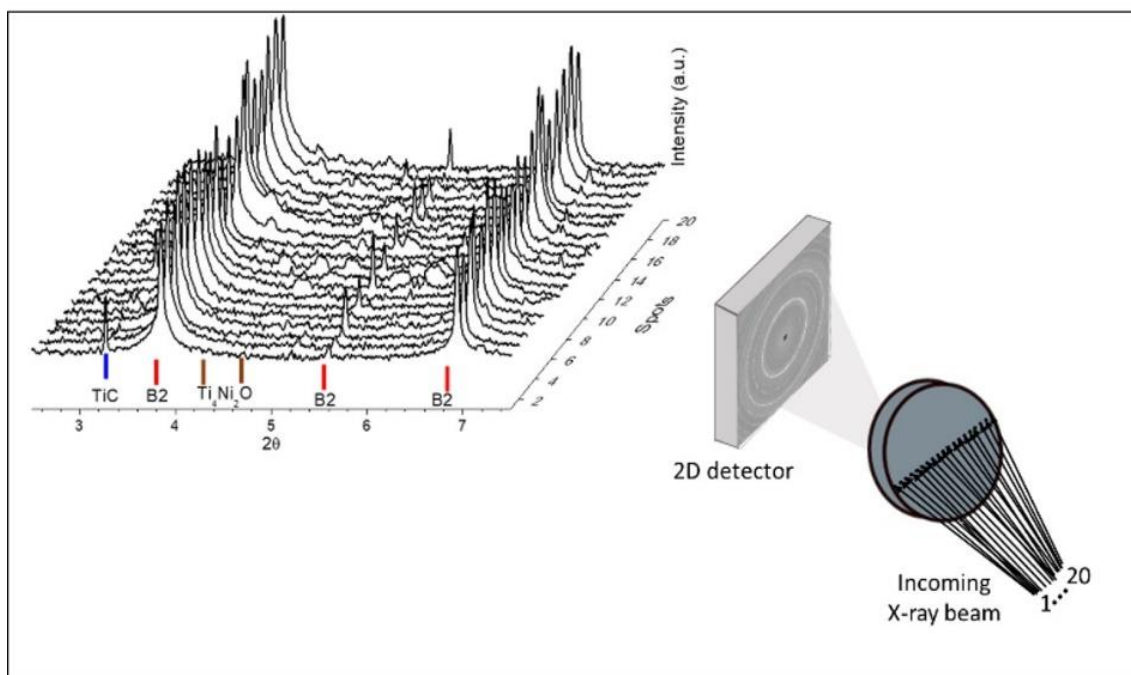


Figure 3.8 - Scheme of the SR-XRD measurement at room temperature along the sample diameter.

The second type of measurement was performed to observe the mechanical behavior (uniaxial tensile tests) of the functionally graded orthodontic archwire with *in-situ* XRD experiments. The tensile tests were performed in an INSTRON, using a 20 kN load cell. The test consisted of a complete cycle with discrete steps at 0.6%, 1.9%, 2.8%, 5.9% and 6.3%, run with a cross-head speed of 0.5 mm/min and maximum stroke of 8% of the gauge length. For these uniaxial loading in tension, the directions parallel to the loading axis ($\phi 0$) and perpendicular to the loading axis ($\phi 90$) were chosen to be observed.

For this measurement, a wavelength of 0.124 \AA (98 keV) and a beam spot $200 \times 200 \text{ \mu m}^2$ was used to scan the samples, at room temperature, along its gauge length (32 mm), where the gauge length is representative of the total length of the localized heat treatment, (as shown in Figure 3.9) and a two-dimensional (2D) detector PERKIN ELMER XRD 1621 was placed at 1.62 m from the sample. The raw 2D images were treated using Fit2D program (Hammersley, 1996) in order to calculate the

individual XRD patterns for 360 bins of the azimuthal angle from 0 to 360°. (Appendix A.1)

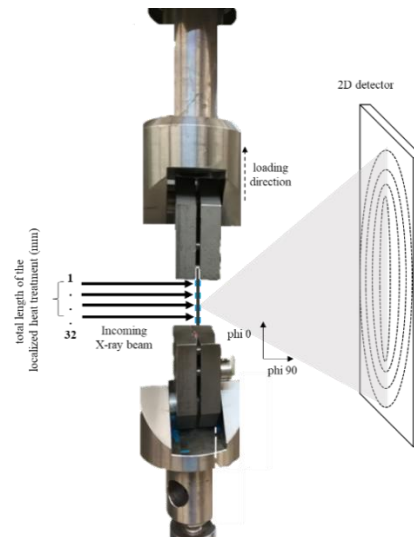


Figure 3.9 - Schematic representation of the SR-XRD measurement at room temperature along gauge length (32 mm), total length of the localized heat treatment. Phi 0 and phi 90 to the normal direction. (more details in the text)

The third type of measurement was performed to simulate some steps of the thermomechanical process with *in-situ* XRD experiments (thermomechanical cycles). These experiments were performed using wavelength from 0.124 Å (98 keV) with a distance sample-detector of 1.37 m. The modified Dilatometer Bähr DIL 805 A/D at the HEMS, equipped with a load cell of 20 kN, has been used to simulate different thermomechanical cycles. The induction coils were designed to permit the X-ray beam through without hitting any metallic component (Figure 3.10).

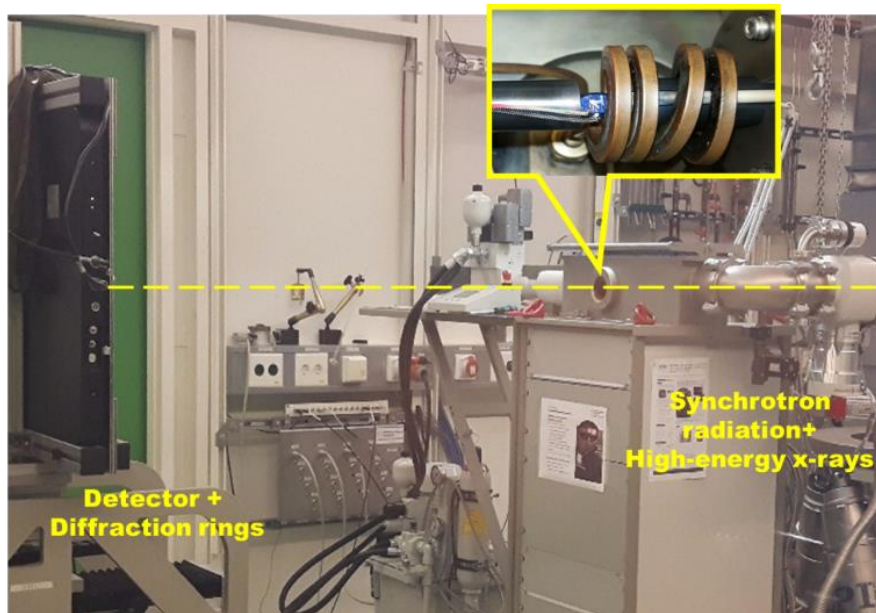


Figure 3.10 - Scheme of the direction of the beam, part of the interior of the equipment and the position of the detector in relation to the sample.

The sample was heated from 25 °C up to 850 °C (under vacuum), with a heating rate of 200 °C/min. After the first step of the heating to 850 °C, the sample was submitted to an isothermal holding step for 5 min, to ensure the thermal equilibrium conditions. Then, the sample was deformed (at 850 °C) with a strain rate of 10^{-3} s^{-1} .

After this, the sample was cooled during a short time. This step was applied to simulate the transport of the material from the furnace to the forging. This cycle was followed by the second, third and fourth heating steps with the same conditions of the first deformation step (heating - deformation - cooling).

After these four steps of hot deformation, the sample was heated up to 850 °C, cooled to room temperature, held for 5 minutes and deformed with a strain rate of 10^{-1} s^{-1} . Afterwards, the sample was heated up to 850 °C, cooled to room temperature, held for 5 minutes and deformed (10^{-1} s^{-1}). The total length change was $\varphi = 0.20$.

After the deformation steps, an aging at 500 °C during 30 minutes was performed, followed by cooling down to room temperature.

This experiment was performed in order to assess the proposed changes of the processing variables as an alternative to the preliminary ones. Figure 3.11 shows the scheme of the thermomechanical cycle.

The XRD analysis, was performed on transmission mode and the Debye-Scherrer rings were captured using a 2D detector from PerkinElmer. The raw 2D images were treated using Fit2D program (Hammersley, 1996) in order to calculate the individual XRD patterns by integration from 0° to 360° (azimuthal angles).

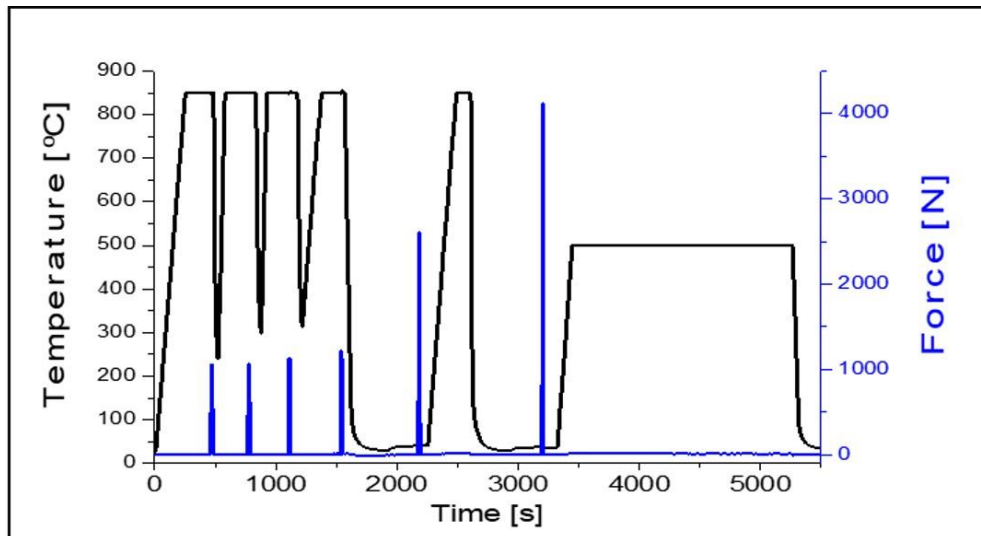


Figure 3.11 - Scheme of the thermomechanical process with *in-situ* deformation experiments (thermomechanical cycles performed in DESY)

3.3.5.4. LNLS - XRD 1 / CNPEM

In order to evaluate the hot-workability and processing parameters of a cast and hot deformation Ni-Ti alloy, the x-ray scattering and Thermo-Mechanical simulation (XTMS) experiments were carried out using the XRD1 beamline, LNLS - CNPEM, Campinas - Brazil. The uniaxial compression tests were carried out under an argon inert gas atmosphere (under a vacuum atmosphere 10^{-2} mbar) and deformation by an advanced thermo-mechanical simulator, the Gleeble® Synchrotron system with Kapton protection, as shown in Figure 3.12.

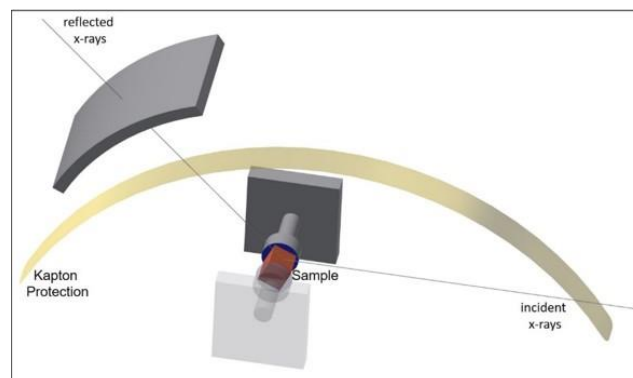


Figure 3.12 - Thermo-mechanical simulator, the Gleeble® Synchrotron system and scheme of the measurement.

Therein, the sample was heated to 850 °C with a heating rate of 200 °C/min and held for 3 min. After that, the sample was compressed with a strain rate of 10^{-1}s^{-1} to a total length change of $\phi = 0.12$ (equal to 12 % height reduction) and subsequent linear cooling to room temperature. This heating / deformation / cooling cycle was repeated 4 times, as shown in Figure 3.13. The diffraction patterns were recorded with a Mythen-1K detector, using a wavelength of 1.0332 Å (12 keV). The evaluation of raw data as well as the generation of θ angle \times intensity plots was conducted by means of the software Origin. High Score from PANalytical was used for peak identification. The focus of this measurement was to verify the thermomechanical behavior under high-speed deformation, to simulate the rate of the deformation during the forging process.

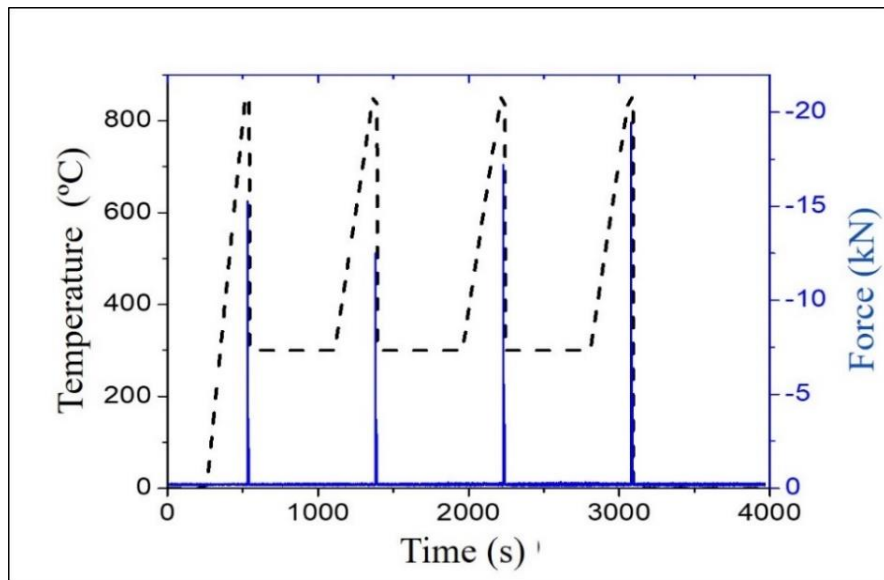


Figure 3.13 - Scheme of the thermomechanical process applied with strain rate of 10^{-3} s^{-1} (hot deformations performed in LMLS).

3.3.6. Differential Scanning Calorimetry (DSC)

Calorimetric measurements were performed by Differential scanning calorimetry (DSC - DSC 204 F1 Phoenix from Netzsch) and it was used to characterize the phase transformation temperatures of all samples. This analysis was used according to the following scheme:

(a) for the transformation temperatures characterization, the sample (10 to 12 mg) was heated to 150 °C at a heating rate of 10 °C/min and subsequently cooled to -150 °C at a

cooling rate of 10 °C/min again heated to 150 °C at a heating rate of 10 °C/min and followed by cooling to room temperature (Figure 3.14a).

(b) to study the ageing effect, the samples (10 to 12 mg) were heated to 500 °C at a continuous heating rate of 10 °C/min followed by cooling to room temperature at a cooling rate of 20 °C/min. Immediately after the first run, the same sample was heated to 150 °C and subsequently cooled to -150 °C again heated to 150 °C and followed by cooling to room temperature (Figure 3.14b). The heating up to 500 °C is used to identify the possibility of the occurrence of recovery, recrystallization and/or precipitation. In the second run (up to 150 °C / -150 °C / 150 °C / Room Temperature) the new phase transformation temperatures are determined.

In all cases, the phase transformation temperatures were determined by the tangent methods.

Before examination by DSC, the samples were cut with a precision cutting machine and then chemically etched (10 vol% HF + 45 vol% HNO₃ + 45 vol% H₂O) in order to remove the layer deformed by the cutting operation. The DSC curves are represented in charts, which show heat flow per unit mass (mW / mg) versus the temperature (°C).

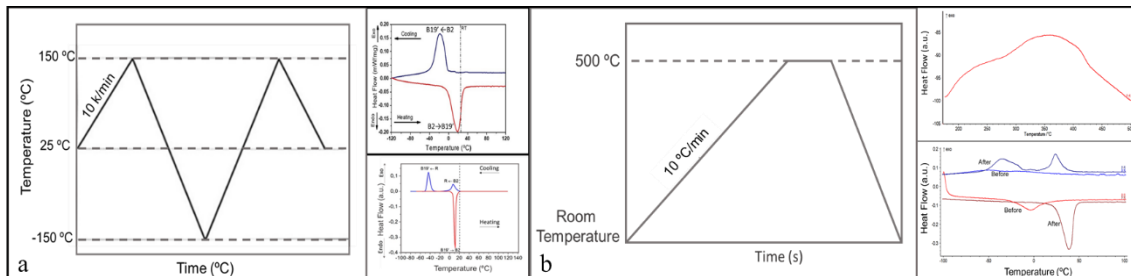


Figure 3.14 - Differential scanning calorimetry schemes.

3.3.7. Thermomechanical Analysis (TMA)

3.3.7.1. Dilatometric Analysis

The dilatometry technique is applied to investigate the dimensional changes of the materials when subjected to temperatures variation. It is a powerful technique in the analysis of the phase transformation of Ni-Ti alloys with shape memory alloys because it allows to determine small dimensional variations in the material. It is possible to

determine the expansion coefficient and to identify any structural change in the material. Any linear dimension variation of the solid, such as length, width or thickness, is called linear dilation. A change in temperature dT promotes a variation ΔL of the linear dimension. The variation ΔL is proportional to the ΔT and to the original dimension (Eq. 3.3). The linear expansion coefficient (α) has different values for different materials and crystalline structures.

$$\alpha = \frac{\Delta L/L}{\Delta T} \quad 3.3$$

When a phase transformation is observed, a slope change in the thermal expansion curve occurs until the end of the transformation is achieved.

3.3.7.2. Three-point Bending Tests

In the orthodontic archwires, other thermomechanical analysis have been performed using three-point bending mode. Orthodontic archwires were tested in a temperature range from -10 to +100 °C, using a heating rate of 2 °C/min and cooling rate of 1 °C/min. For this measurement a support span of 9 mm and an actuation force following a triangular waveform (frequency 0.01Hz) was used; the force was ranging from 100 mN to 1250 mN, in order to accommodate the different deformation characteristics of the austenite (higher temperature range) and R-phase and martensite phase (lower temperature range). The maximum deflection of the wires ranged from 100 μm to 750 μm .

The TMA analysis, (dilatometry analysis and three-point bending analysis) were performed using a PT 1600 from Linseis.

3.3.8. Mechanical testing

3.3.8.1. Three-point bending tests

To simulate the orthodontic treatment in an oral environment and the simulated force exerted on a lingually displaced maxillary lateral incisor (ISO 158411:2014), a three-point bending test was carried out for each orthodontic archwire.

The tests were performed at different temperatures: 5 °C (cold water), 20 °C (commonly room temperature in the orthodontic room), 25 °C (conventional room temperature) and

37 °C (human body temperature). The archwire was heated/cooled by immersion in a thermally stabilized water bath for approximately 5 min to reach the test temperature. The length size of each wire segment, 15 mm, was chosen in accordance with ISO 15841:2014. (ISO, 2014) All samples were loaded with the same protocol on a tensile machine (Shimadzu AG-50kNG equipped with a 500 N load cell). Each archwire was first loaded to a deflection of 2 mm and then unloaded at a rate of 0.5 mm/min. The mechanical properties were analyzed at 1.0, 0.75 and 0.5 mm during unloading at deflection curves (Figure 3.15). This describes the average slope of the unloading curve in relation to its force level.

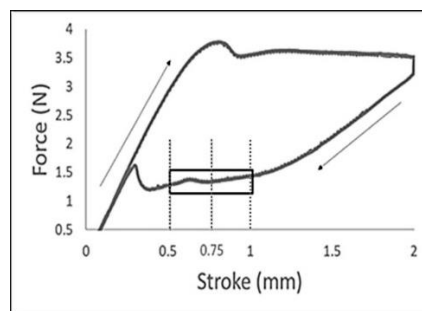


Figure 3.15 - Displacements (0.5, 0.75 and 1.0 mm) analyzed in deflection curve (slope of the deactivation curve - superelastic behavior).

4

Results and Discussion

In this section, all characterization results and thermal and thermomechanical treatment applied for all alloys studied, as well as the orthodontic archwires characterization are discussed. These results are divided in five sections:

- Section 4.1: Results of the characterization of the starting materials (alloys 1, 2 and 3, in the as-cast and remelted conditions) before rotary forging process. In addition, a brief observation on the forging process of the alloys 1, 2 and 3 are depicted. These observations were performed in the first hot deformation and second cold deformation steps for all the alloys.
- The results of this section are presented following the sequence along the initial thermomechanical processing steps. Thus, in the Section 4.2 the characterization of the samples obtained in the first hot forging step (NiTi_1_1F1h), third hot forging step (NiTi_1_3F3h), first cold forging step (NiTi_1_5F4h1c) and second cold forging step (NiTi_1_6F4h2c) was performed;
- Section 4.3 illustrates the characterization of the thermally treated samples to investigate the heat treatment effects on the solution heat treated ingot and between consecutive thermomechanical processing steps.
- Section 4.4 illustrates the tests carried out aiming to verify and discuss the conditions previously proposed in the Section 4.3.
- Finally, Section 4.5 shows the orthodontic archwires characterization results. In addition, a possible improvement for the final product regarding the thermomechanical processing is presented and discussed. This improvement is related to the obtainment of functionally graded wires.

4.1. Starting Materials (as-cast and remelting condition)

In this section the characterization results of the three alloys in the as-cast and remelted condition, to understand the forging route and to check their properties were reported. Before explaining the characteristics of the starting materials, it is easier to remember here that we will present results of the alloys with different Ni content (“alloy 2” and “alloy 3”) in order to compare with the results for the “alloy 1”.

The phase transformation temperatures of the NiTi₁ (as-cast and remelted), NiTi₂ (as-cast and remelted) and NiTi₃ (as-cast and remelted) samples were observed by DSC. Additionally, the phases presented at room temperature were identified by SR-XRD.

Figure 4.1a depicts the DSC curves of the as-cast and remelted samples (alloy 1). This alloy was designed to have higher Ni-content. The temperature range that was used to perform the DSC test was not enough to show the transformation temperatures in the as-cast sample. However, this was expected, since the samples melted did not present adequate homogeneity in composition to show the transformation temperature near room temperature. (Frenzel, 2010) (Saburi, 1998) It is possible to observe that the remelting step (VAR process) was enough to identify the transformation B2 ↔ B19' with a high degree of control over the microstructural homogeneity. The remelted sample showed an A_F temperature close to room temperature (30.1 °C, see Table 4.1), which is expected for this Ni content alloy (Ostuka, 2005).

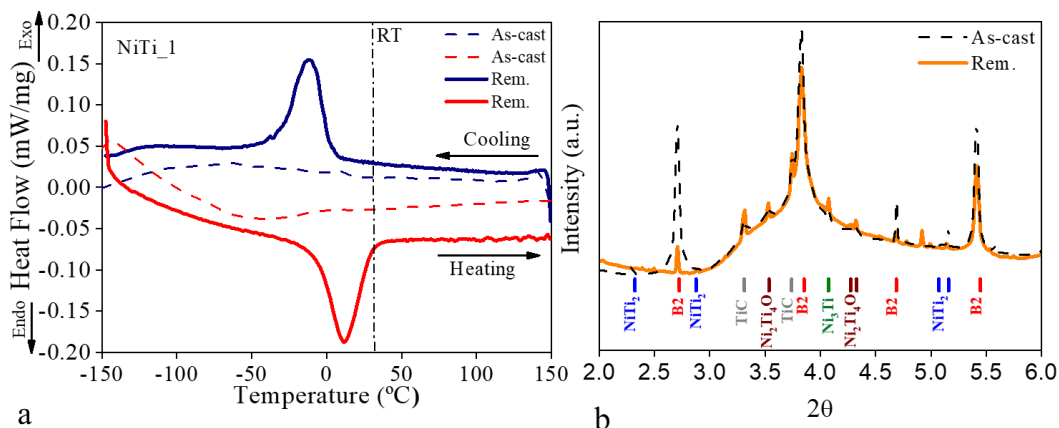


Figure 4.1 - (a) DSC curves NiTi₁_as-cast and remelted samples (b) SR - XRD - NiTi₁_as-cast and remelted samples

It is known that the VIM process allows the formation of compounds resulting from the reaction of Ni and/or Ti with impurities such as oxygen and carbon ($\text{Ni}_2\text{Ti}_4\text{O}$ and TiC). (Frenzel, 2004a) (Zhang, 2005) SR-XRD results demonstrate the presence of these compounds for both samples (Figure 4.1b). At this step it is also possible the formation of precipitates such as Ni_3Ti and Ti_2Ni (Coda, 2012). However, with the subsequent heat treatment these may be dissolved.

Figure 4.2a shows the DSC curves of the as-cast and remelted samples (alloy 2). This alloy was designed to have an equiatomic composition. For this sample the temperature range that was used to perform the DSC test was not enough to show the transformation temperature in the sample as-cast. This behavior is consistent with the sample NiTi_1 _as-cast results, since both samples are in the as-cast condition. The result of the alloy in the remelted condition does not present a defined phase transformation temperature. It is possible to observe just one broad peak corresponding to the martensite – austenite phase transformation during heating, and that the A_f is lower than room temperature (-12.2°C , see Table 4.1). This temperature indicates a Ni content higher than expected, increasing Ni content, gives decreasing transformation temperature. The results of SR-XRD also present compounds formed by the impurities (oxygen and carbon) coming from the process VIM and still rich precipitates in Ni and Ti (TiNi_3 and Ti_2Ni), (Figure 4.2b). (Otubo, 2008)

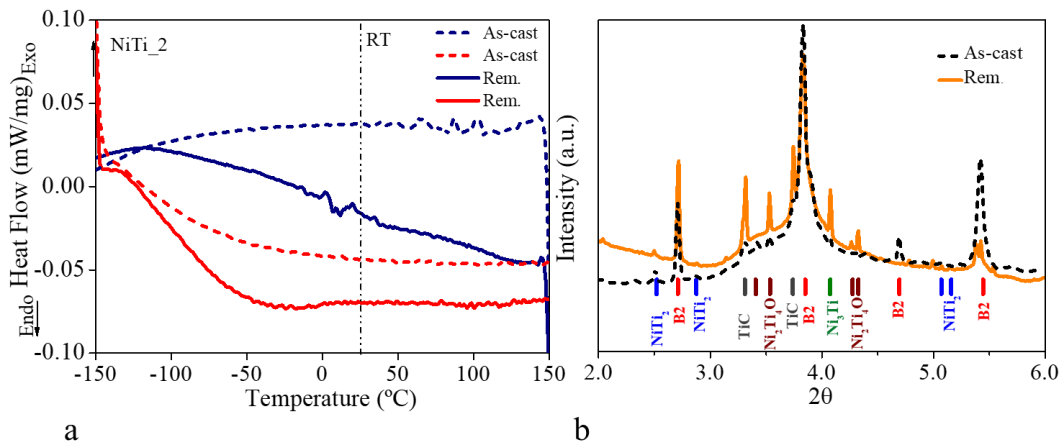


Figure 4.2 - (a) DSC curves NiTi_2 _as-cast and remelted samples (b) SR - XRD - NiTi_2 _as-cast and remelted samples

DSC curves of the as-cast and remelted samples (alloy 3) is shown in Figure 4.3a. This alloy was designed to have higher Ti-content. Again, the temperature range that was used to perform the DSC test was not enough to show the phase transformation

temperature in the sample as-cast. This was expected, as previously observed and discussed for the “alloy 1” and “alloy 2” (Frenzel, 2010)(Saburi, 1998). It is possible to observe that the second remelting step (VAR process) was enough to identify the transformation $B2 \leftrightarrow B19'$. Remelted sample showed A_f temperature above room temperature (65.6 °C, see Table 4.1), which is expected for the Ti-rich Ni-Ti alloy. Again, the compounds of Ti_4Ni_2O and TiC were present and shown by SR-XRD results (Figure 4.3b). In addition, SR-XRD results showed the $B19'$ phase at room temperature, which supports the Ti-rich Ni-Ti alloy characteristic. When comparing to DSC results at room temperature (highlighted by the vertical line in Figure 4.3 a), the presence of $B19'$ phase was expected. For the same reason depicted for the “alloy 1” and “alloy 2”, the presence of the precipitates such as Ni_3Ti and Ti_2Ni was observed. (Bhagyaraj, 2013) The literature reported that in either equiatomic or Ti-rich composition, the Ti_2Ni phase is formed during solidification from the melting process alloy. Besides, the volume fraction of Ti_2Ni increases with the increase of Ti content in the alloy.(Nishida, 1986)(Wu, 2010)

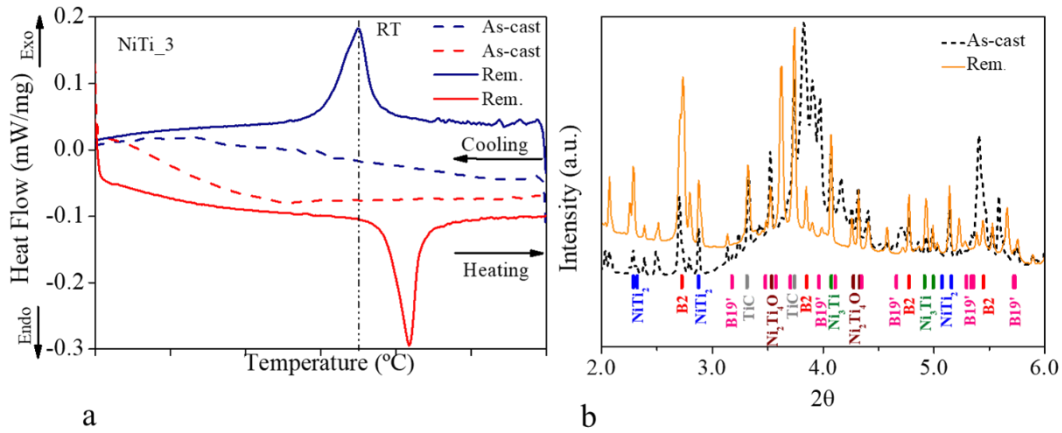


Figure 4.3 - (a) DSC curves NiTi_3_as-cast and remelted samples (b) SR - XRD - NiTi_3_as-cast and remelted samples

Table 4.1 - Transformation Temperatures in degree Celsius of as-cast and remelting 1, 2 and 3 samples.

Samples	B2→B19'			B19'→B2		
	Cooling			Heating		
	M_s	M_p	M_f	A_s	A_p	A_f
1_as-cast	-2.5	-18.3	-113	-130	18.9	29.8
2_as-cast	-	-	-	-	-	-
3_as-cast	-	-	-	-	-	1.8
1_remelted	0.7	-10.8	-28.0	-6.4	11.6	30.1
2_remelted	-	-	-	-132	-48.7	-12.2
3_remelted	35.5	24.9	2.4	43.3	59.1	65.6

(-) no detected

After these observations the “alloy 1”, “alloy 2” and “alloy 3” (remelted condition) were solubilized at 950 °C during 2 hours and then heated up to 500 °C. This heating allowed to identify some phenomena during heating that confirm the alloys characteristic.

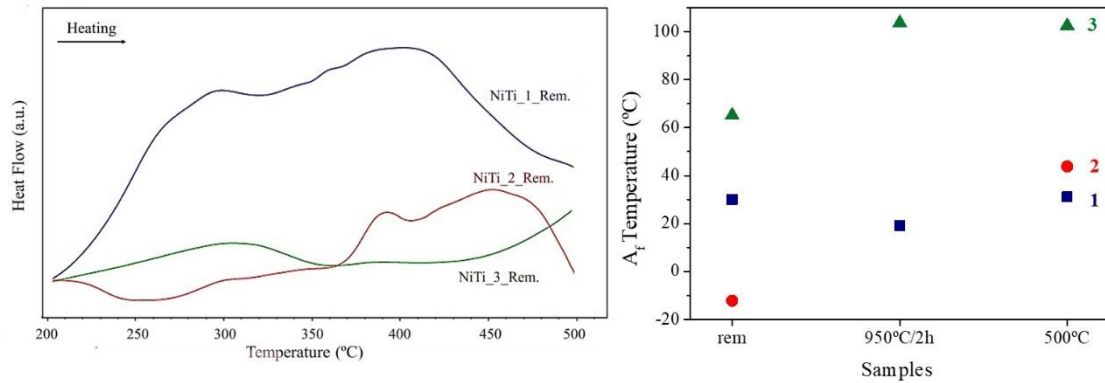


Figure 4.4 – DSC results: (a) heating up to 500 °C, (b) A_f temperature (remelted condition, after solution heat treatment at 950 °C during 2 h and after heating up to 500 °C).

The effect of the heating on the three alloys are shown in Figure 4.4a. The “alloy 1” and “alloy 2” present some phenomena (exo.) from 300 °C to 450 °C. This effect is not observed for the “alloy 3” alloy. This behavior can be confirmed by A_f temperature (Figure 4.4b):

- “alloy 1” sample, after heat treatment at 950 °C for 2h, showed a decrease of the A_f temperature, probably due to the dissolution of the precipitates (Ni_3Ti) that were identified in NiTi_1_rem sample. When the sample was heated up to 500 °C the A_f temperature increased, indicating that the metastable precipitates (Ni_4Ti_3) were formed. Ni_4Ti_3 is the first precipitate to occur, at lower temperatures and shorter holding times. Pelton *et al.* (2000) showed a TTT diagram for Ni-Ti system with focus on shorter holding times for the precipitation phenomenon onset. In this study, the authors used a Ni-rich Ni-Ti alloy such as the main alloy (NiTi_1). In this TTT diagram, it is possible to observe that the Ni_4Ti_3 formation can occur in the temperature range from 350 to 500 °C, during a short holding time, even for a few seconds. (Pelton, 2000)
- “alloy 2” sample, after heat treatment at 950 °C for 2 h, did not show a clear phase transformation in the temperature range that was used to perform the DSC test. When the sample was heated up to 500 °C, the A_f temperature increased, this probably

indicates the beginning of the precipitates formation. Such a behavior is expected for the equiatomic and Ni-rich Ni-Ti alloys. (Otsuka, 2005)

- “alloy 3” sample, after heat treatment at 950 °C for 2 h, showed an increase of the A_f temperature, probably because the Ti-rich precipitates (Ti_2Ni) that were identified in NiTi_3_rem sample were dissolved. When the sample was heated up to 500 °C the A_f temperature did not change. Owing to the characteristics of Ti-rich Ni-Ti alloys, the precipitates are formed at higher temperature than the one used in this measurement. Therefore, this behavior proves that this alloy is Ti-rich Ni-Ti alloy. (Bhagyaraj, 2013)

4.1.1. Microstructural Characterizations of the alloys 1, 2 and 3 (first hot deformation and second cold deformation samples)

The hot and cold working characterizations are necessary to understand the influence of both deformations on the materials properties with different Ni content.

The characterization of the first hot rotary forging step and second cold rotary forging step samples was performed by: DSC, SR-XRD.

DSC measurement was used to verify the transformation temperature (Figure 4.5a). NiTi_1 sample result shows the transformation temperature close to room temperature. NiTi_1_6F-4h2c, second cold rotary forging step sample depicts the A_f temperature below room temperature. This temperature it is expected to Ni-rich Ni-Ti alloys. These SMAs display a superelastic behavior at room temperature. (Saburi, 1998)

The sample NiTi_2_1F_1h presents the transformation temperature out of the range used in this technique (-150 to 150 °C). This behavior was discussed in remelted condition results. NiTi_2_6F_4h2c DSC results shows one transformation broad peak on heating and on cooling, suggesting that $B2 \leftrightarrow B19'$ takes place in one single step. However, the partial overlap of the temperature ranges of DSC peaks during cooling and heating, suggest a two-steps transformation as $B2 \leftrightarrow R \leftrightarrow B19'$. The very broad peak may also to the deformation of the material. The increment of the deformation probably promoted the grain refinement, but not enough to reveal the adequate functional properties. Just in this result of the 6F_4h2c step it is possible to observe a peak transformation. (Otsuka, 2005)

NiTi_3_1F_1h results, show the A_f temperature above room temperature. After this deformation route, the R-phase was evident on cooling curve, through two-steps transformation as $B2 \rightarrow R \rightarrow B19'$. On heating curve, one step transformation was observed as $B2 \rightarrow B19'$. The phase transformation temperatures above room temperature is expected on Ti-rich Ni-Ti alloys. (Otsuka, 2005)

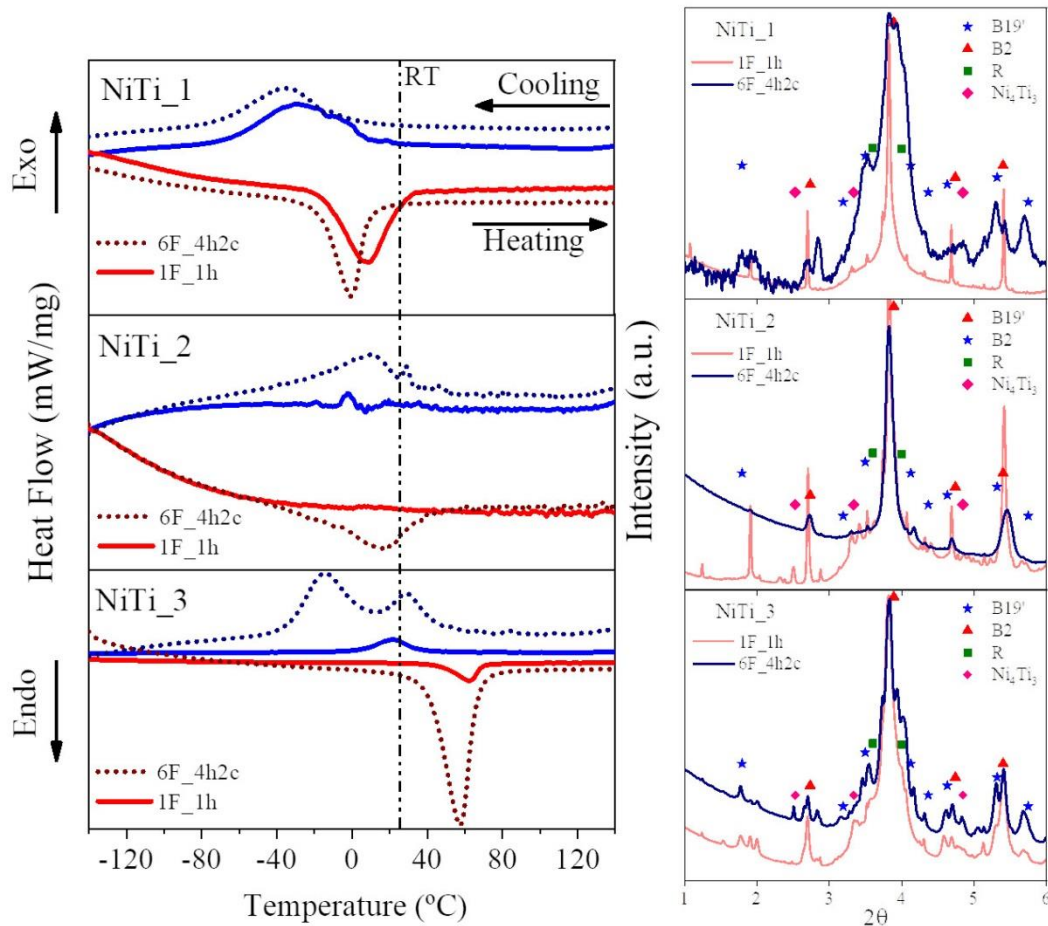


Figure 4.5 - (a) DSC curves (b) SR-XRD diffractograms of the 1, 2 and 3 alloys at first hot deformation step (1F_1h) and at first cold deformation step (6F_4h2c).

To have a complete microstructural characterization of all samples, synchrotron-based x-ray diffraction was performed. Figure 4.5b shows the superimposition of the diffractograms, at room temperature, of the 1F_1h and 6F_4h2c (1, 2 and 3 alloys) samples. A clear distinction between the three alloys is noticed: while the NiTi_1_1h sample is fully austenitic, the NiTi_2_1F_1h and NiTi_3_1F_1h present a mixture of austenite, R-phase and martensite. The NiTi_1_6F_4h2c and NiTi_3_6F_4h2c samples present a mixture of austenite, R-phase and martensite. The broadening of the $(110)_{B2}$ peak may be associated with the presence of precipitates. NiTi_2_6F_4h2c sample is

fully austenitic. This is corroborating the DSC results, because the deformation influence is observed just at last deformation step.

The results presented confirmed that the sample 1 is the most suitable sample for producing a material that can present at room temperature the superelastic behavior. Therefore, this alloy was the chosen material to continue in the next steps of this work.

4.1.2. NiTi_1_Rem Alloy 1 As Remelted

For an initial exploration of this “alloy 1”, we focused on the behavior of an alloy which offers conventional B2 \leftrightarrow B19' transformation behavior (Ni-rich Ni-Ti alloy). Thus, to confirm these characteristics other tests were carried out.

The chemical composition of the NiTi_1_rem sample was verified by WDS analysis which revealed that the material is Ni-rich Ni-Ti alloy, as shown in Table 4.2. (Ribeiro, 2015)

Table 4.2 - Remelted Samples Ni and Ti contents (%at) (WDS - analysis)

Contents	NiTi_1_as-cast	NiTi_1_rem
(%at.)	WDS	WDS
Ni	51.52	51.03
Ti	48.48	48.97

The values that are shown in Table 4.1 do not present a significant difference between the composition before (as-cast condition) and after remelting process (remelted condition). This result indicates that the argon atmosphere was effective and did not promoted a significant surface oxidation, as reported in literature. (Coda, 2012) (Morgan, 2008) (Kabiri, 2012)

Figure 4.6a and b show secondary electron (SE) and back-scattered electron (BSE) micrographs of the NiTi_1_rem sample. The microstructure of the NiTi_1_rem sample (Figure 4.6a) reveals grains of metallic matrix (dark areas) surrounded by particles (lighter areas).

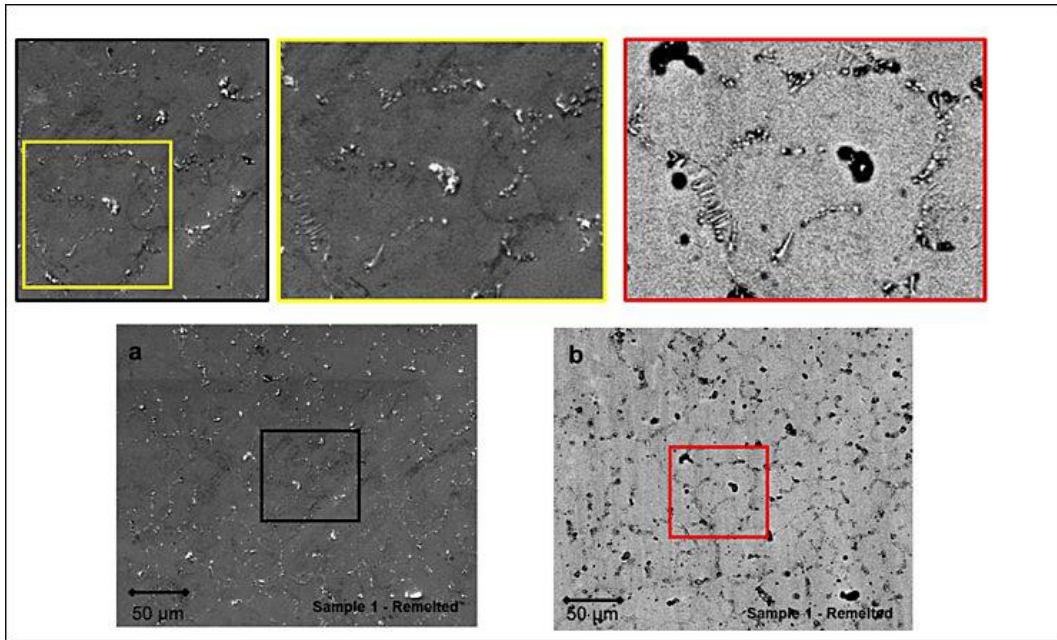


Figure 4.6 - SEM images of NiTi_1_rem: (a) Secondary electron image, (b) Backscattered image

Figure 4.6b was generated using backscattered electrons and enhanced the contrast between the Nitinol matrix material and the oxide and/or carbide inclusions. The characteristic observed using secondary electrons are associated with inclusions. EDS analysis (Figure 4.7a) indicates that these particles would be related to inclusions coming from the VIM process, because they are associated with Ti, C, O and Ni at lower levels. (Coda, 2012) (Qihui, 2018) Thus, these can be associated to TiC, Ti_2Ni_4O , as observed in SR-XRD results (Figure 4.1b). (Frenzel, 2004a) In addition, the EDS analysis allowed to verify the chemical composition at some points on the matrix, which to suggest that Ni-rich precipitates are presents, since the matrix are rich in Ti.

Figure 4.7b depicted the micrograph of the NiTi_1_Rem sample and revealed grains uniformly distributed. As can be seen, the remelted specimen mostly consists of highly segregated and coring products (microsegregation). The microstructure is a typical cast structure, in agreement with other studies. (Jiang, 2012) The presence of large TiC precipitates may be noted. The presence of the austenite and martensite phases in the NiTi_1_rem sample has been also confirmed by EBSD technique and the results are shown in Figure 4.7 c and d. A typical refined grain with serrated boundaries is observed. In the Figure 4.7c austenite phase is indexed and in Figure 4.7d the austenite phase is not indexed and reveals the presence of the second phase. The studied NiTi_1_rem sample did not show preferred orientation and the crystallographic

orientation of grain is uniformly distributed (Figure 4.7c). Other authors have also observed the same behavior after melting process. (Świec, 2016) (Qihui, 2018) Luo *et.al.*, studied an near equiatomic Ti-50.6 at.% Ni alloy produced by vacuum arc remelting and reported that the material shows the microstructure consists of austenite grains and few second phase particles appear at both the grain boundary regions and interiors. (Luo, 2017)

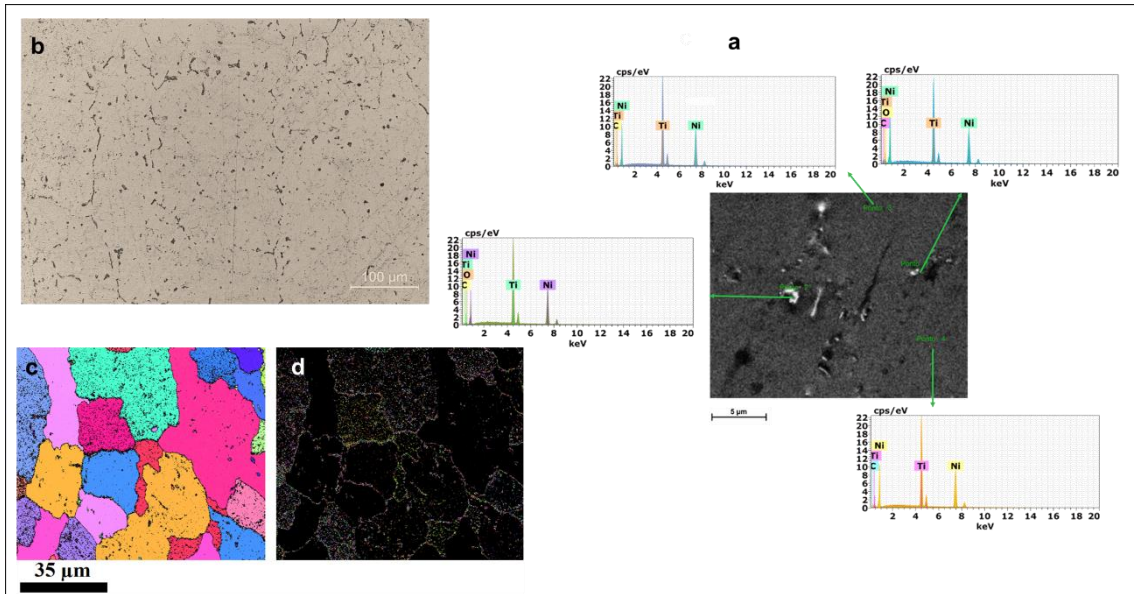


Figure 4.7 – (a) EDS results of the NiTi_1_Rem sample, (b) Micrograph of the NiTi_1_rem. (c and b) EBSD map of NiTi_1_rem sample at room temperature.

4.1.3. Starting Materials Summary

The casting process was not focus of this study. However, this stage of the Ni-Ti alloy manufacturing is fundamental to understand the alloy characteristics and to design the thermomechanical process. This stage has a great influence on the microstructure and homogeneity of the ingots produced.

Although this study does not have a control of this stage, some sample observations are important in order to understand the thermomechanical process. Firstly, the NiTi_1-Rem sample depicts a typical remelted structure characteristics; The presence of oxygen and carbon are common in this casting processes, Ni-rich precipitates are presents on the matrix, but these could be dissolved in the heat solution treatment.

According to the characteristics discussed in this section, the ingot NiTi_1_Rem shows conditions for be processed and still obtain a product with the desired functional properties.

4.2. Initial Thermomechanical Process (Rotary Forging Steps)

This study aimed to characterize the rotary forging steps and to understand the forging route. The separation of hot and cold working was necessary to understand the influence of both kinds of deformation processes on the materials properties.

Thus, this section discusses the characterization of rotary forging steps in order to identify possible parameters changes in the initial process.

4.2.1. Hot Rotary Forging Steps

Starting from the melting process, the ingot was heated up to 800 °C for 30 minutes before the start of the deformation. Firstly, hot working was applied to reduce the size of the start ingot, to set up the homogenization of the microstructure and to modify the solidification grain texture adjustment.

4.2.1.1. First Hot Rotary Forging Step¹

Figure 4.8 depicts the transformation temperatures and the phases that are present at room temperature for the first hot rotary forging step (NiTi_1_1F_1h). This sample is fully austenitic slightly above room temperature, $A_f = 27.5$ °C (Table 4.3). For all the DSC results, room temperature is highlighted with a vertical line. Furthermore SR-XRD patterns depict the presence of a mixture of the B2 and B19' phases.

The DSC curves show one transformation (broad) peak on heating and one on cooling, suggesting that B2 ↔ B19' took place in one single step, but the XRD high/low temperature results (Figure 4.9) showed the presence of the intermediate R-phase (Figure 4.8). Thus, from XRD high/low results, we may conclude that during

¹ The below results (section 4.2.1.1) were already published in a paper in the journal *Powder Diffraction*, entitled Microstructural Characterization of NiTi Shape Memory Alloy Produced by Rotary Hot Forging. (Rodrigues *et al.*, 2017a)

cooling/heating, there is a two-step phase transformation ($B2 \leftrightarrow R \leftrightarrow B19'$). This information is not evident in DSC results, but it is consistent with the partial overlap of the temperature ranges of DSC peaks during cooling and heating, due to the smaller thermal hysteresis of the $B2 \leftrightarrow R$. The introduction of dislocations network by deformation can change the transformation path from $B2 \leftrightarrow B19'$ into $B2 \leftrightarrow R \leftrightarrow B19'$, due to the previous deformation imposed. (Otsuka, 2005)

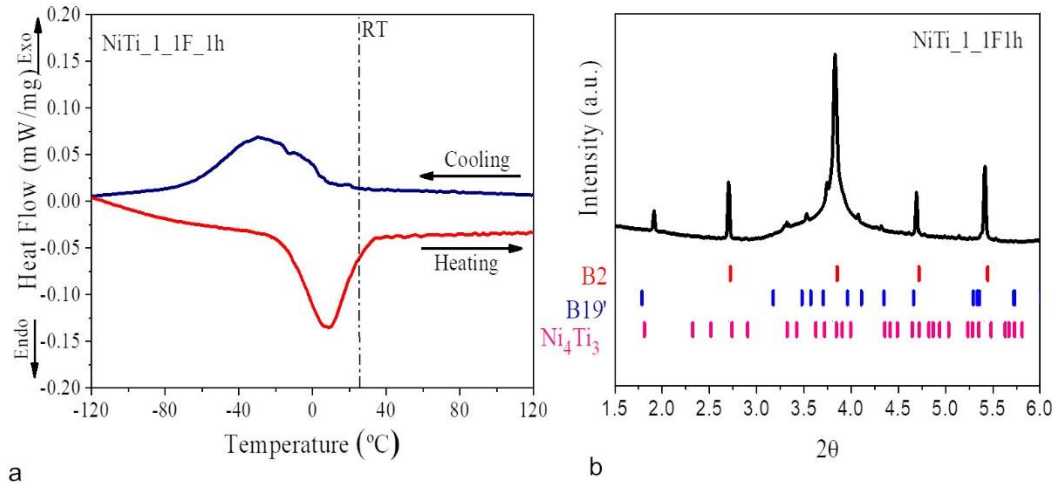


Figure 4.8 – (a) DSC curves NiTi_1_1F_1h sample (b) SR - XRD of NiTi_1_1F_1h sample.

X-Ray diffraction assay at high/low temperatures was performed at the temperatures previously determined by DSC on cooling and heating range. The aim of this analyze was to confirm the phases present. For the higher temperature (above 30 °C), the $(110)_{B2}$ is clearly visible (Figure 4.9 heating). During cooling, under 30 °C, there is an abrupt decrease of the intensity of the $(110)_{B2}$ peak and two peaks associated to R-phase, close to $(110)_{B2}$ peak, were noticed. During further cooling, other peaks associated to B19' appeared (Figure 4.9 cooling). The SR-XRD did not depict the R-phase, because this technique was performed at room temperature. In accordance with XRD at high/low temperature, the R-phase was not evident at this temperature.

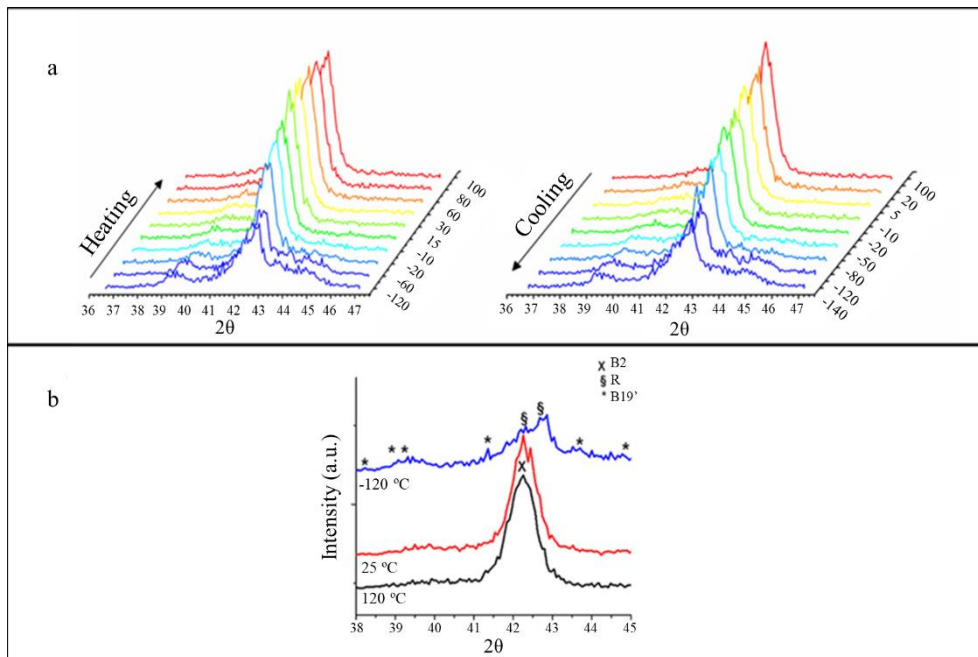


Figure 4.9 - XRD results at high/low temperature: (a) during heating and cooling, between -120 and 120 °C (b) separate diffractograms for three different temperatures (-120, 25 and 120 °C)

As mentioned previously this sample presented the inclusion of a dislocation network imposed by the deformation, therefore it is necessary to verify the behavior in relation to the phenomena of microstructural restoration. To understand the microstructural restoration phenomena after the first hot deformation, the discussion will be focused on an analysis of the influence of the heat treatment on the static phenomena that may occur. Such discussion is necessary because these phenomena are responsible for the success of the thermomechanical processes.

A set of thermal treatments (Figure 4.10a) has been carried on by heating the sample at a constant rate of 10 °C/min to sequentially higher temperatures ranging from 250 to 500 °C. The applied temperature range was chosen based on the common temperature where such phenomena occurred (i.e. static recovery and recrystallization phenomena).

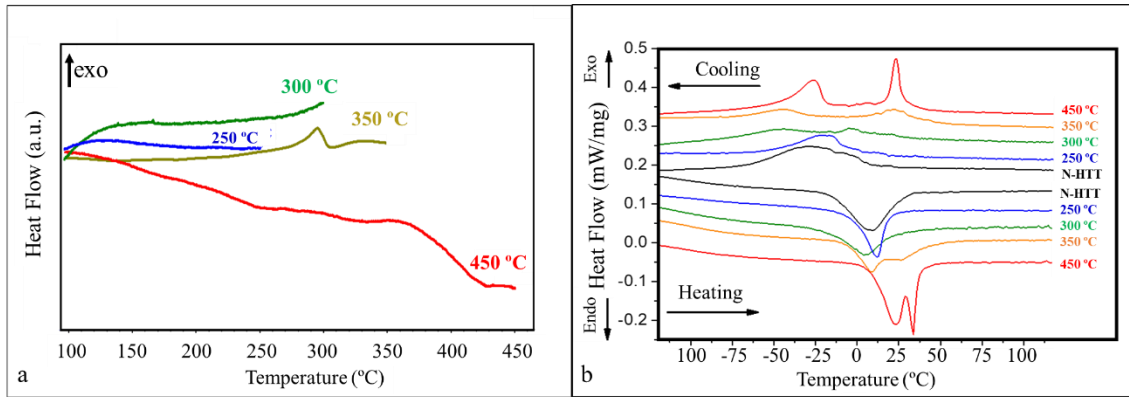


Figure 4.10 – (a) Heat release by continuous heating of the NiTi alloy to different maximum temperatures. (b) DSC curves: NiTi_1_1F1h (N-HTT = NiTi_1_1F1h without heat treatment) and NiTi_1_1F_1h heat treated from 250 to 450 °C.

Some exothermic reactions were observed for all curves; it can also be observed that the phenomena are better visualized in 450 °C curves (Figure 4.9a). The influence of the heat treatments can be observed in the phase transformation temperatures. Analyzing the DSC curves after heat treatment (Figure 4.11b), the following is observed: (i) at 250 and 300 °C curves the transformation peak is shifted to lower temperatures, indicating a stress relaxation / decreased density of structural defects; (ii) while at 350 and 450 °C curves the same peak shifted to higher temperatures, indicating a decrease of the Ni content as a consequence of the possible formation of precipitates. Thus, 350 and 450 °C can be highlighted as two ageing temperatures that most impact the phase transformation temperatures.

Fan *et al.* (2017), reported a similar behavior in $\text{Ni}_{51}\text{Ti}_{49}$ alloy heat treated at 500 °C during 1.5h. After aging, R-phase transformation occurred during the cooling process and then resulted in a two-stage $\text{B2} \leftrightarrow \text{R} \leftrightarrow \text{B19}'$ transformation. Fan *et al.* (2017) reported that the R phase transformation is mainly introduced by the coherent and semi-coherent Ni_4Ti_3 precipitates (Fan, 2017). Other authors have also observed the same behavior after heat treatment with the same temperatures and alloy composition. (Pelton, 2000) (Khalil-Allafi, 2002)

This previous analysis of heat treatment temperatures enables to verify that the range from room temperature to 500 °C would be appropriate to identify the occurrence of possible microstructural evolution. Therefore, the results corresponding to heating up to 500 °C are presented and discussed for all the processing steps below.

In a deformed material, due to the stored energy, reliable calorimetric measurements of restoration phenomena can be observed in a range temperature which no phase transformations are relevant (such as precipitation).

Figure 4.10a shows the heating curves from room temperature to 500 °C (NiTi_1_1F_1h sample). In this case two stages were detected, the broad peak ($\delta H=1.3$ J/g) at 60 – 250 °C, corresponding to the heat evolved during recovery, and the peak at 360 °C (260 – 450 °C / $\delta H=2.7$ J/g) corresponding to the heat evolved during recrystallization.

These results corroborate the XRD measurements carried out with heating. According to Humphreys *et al.* (2004b), the broadening, measured through the Full Width at Half Maximum (FWHM), and the shift of the x-ray diffraction peaks (110)_{B2} confirm the occurrence of the recovery followed by static recrystallization (Figure 4.11b and c). (Humphreys, 2004b)

However, due to the small size of the Ni₄Ti₃ precipitate, lab source XRD is not feasible to determine its presence. The FWHM decreased from 250 °C to 450 °C, which suggests a recovery (up to 300-350°C) / recrystallization (above 350°C) of the austenite structure (Humphreys, 2014). In addition, it was evident that the austenite peak shifted to smaller 2 θ angles, corresponding to larger d-spacing due to heating.

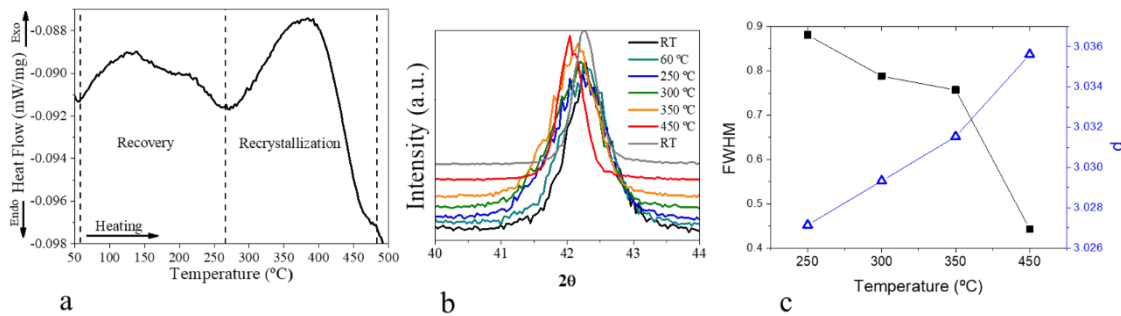


Figure 4.11 – Recovery recrystallization results: (a) DSC curves heat treated to 500 °C; (b) XRD at high temperature and (c) FWHM and *d*-spacing observed.

4.2.1.2. Third Hot Rotary Forging Step

The third deformation corresponds to the deformation of $\phi = 0.2$ (20% diameter reduction in relation to first hot rotary forging step). As this sample presents more

deformation, some different characteristics are observed when comparing to the first step.

DSC and SR-XRD results of the third hot rotary forging step (NiTi_1_3F_3h) are shown in Figure 4.12. The transformation temperatures obtained by DSC analysis (Figure 4.12a) showed that the sample is austenitic at room temperature. The austenite finish is close to room temperature ($A_f = 19.5\text{ }^\circ\text{C}$, see Table 4.3). Meanwhile, SR-XRD results illustrate the presence of only B2. (Figure 4.13b).

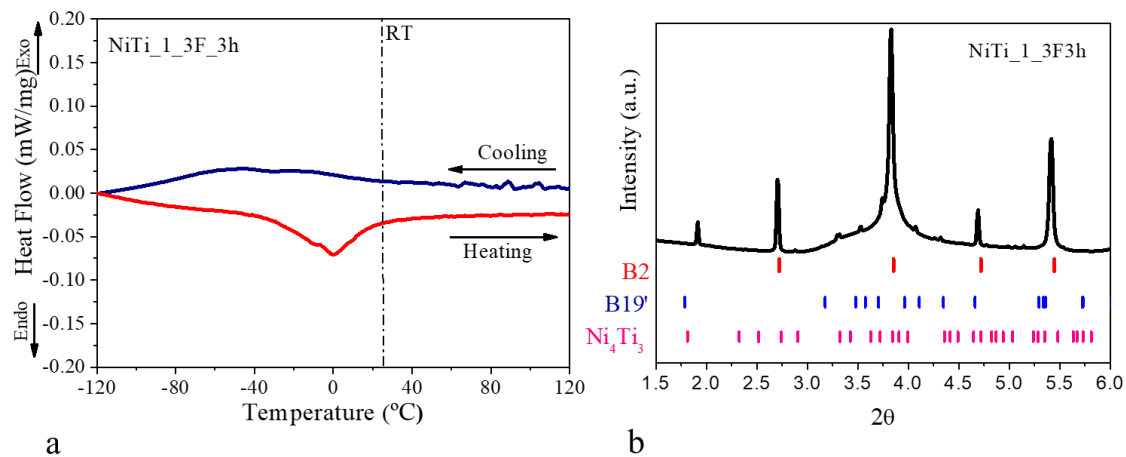


Figure 4.12 - (a) DSC curves NiTi_1_3F_3h sample (b) SR - XRD of NiTi_1_3F_3h sample.

The DSC curves showed one transformation peak (very broad) on heating and another one on cooling, suggesting that $B2 \leftrightarrow B19'$ took place in one single step. However, the partial overlap of the temperature ranges of DSC peaks during cooling and heating suggests a two-steps transformation as $B2 \leftrightarrow R \leftrightarrow B19'$. The very broad peak is consistent with the deformation suffered by the material. XRD at high/low temperature result (Figure 4.13) showed that the intermediate R-phase was formed. Similarly, to the NiTi_1_1F_1h sample results, a two-step phase transformation occurred ($B2 \leftrightarrow R \leftrightarrow B19'$). The occurrence of two-steps transformation ($B2 \leftrightarrow R \leftrightarrow B19'$) was associated to the occurrence of Ni_4Ti_3 precipitation. (Lekston, 2007)(Otsuka, 2005)

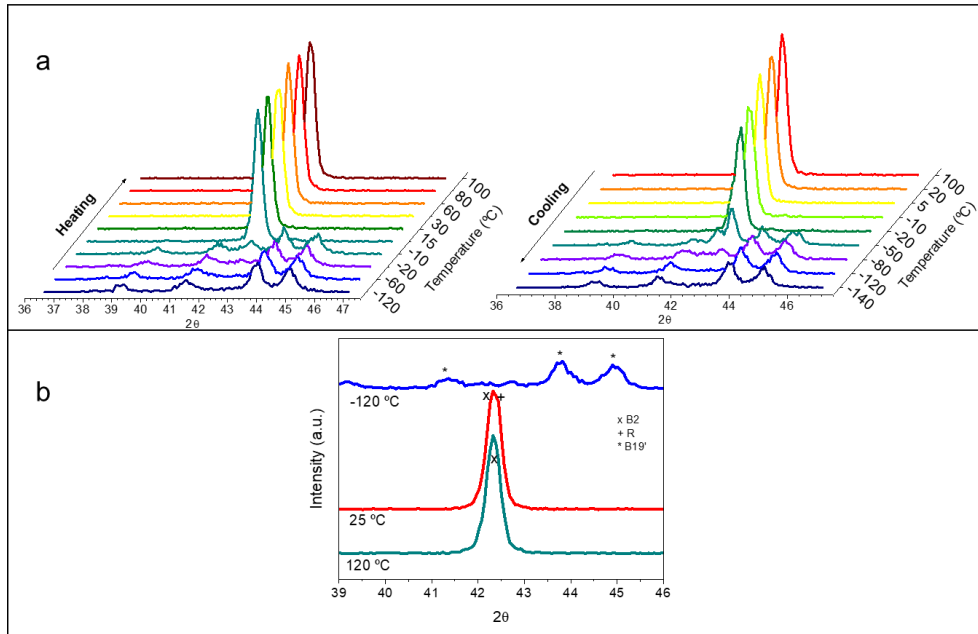


Figure 4.13 - NiTi_1_3F_3h XRD results at high/low temperature: (a) during heating and cooling, between -120 and 120 °C (b) separate diffractograms for three different temperatures (-120, 25 and 120 °C)

Figure 4.14a shows the heating curves from room temperature to 500 °C (NiTi_1_3F_3h sample). In this case, two exothermic events were detected, the broad peak ($\delta H = 0.9$ J/g) at 50 – 180 °C, corresponding to the heat evolved during recovery, and the peak at 380 °C (300 – 490 °C / $\delta H = 1.8$ J/g) corresponding to the heat evolved during the recrystallization. Different recrystallization temperatures are shown along the deformation process, and the higher recrystallization temperature was observed for 3F_3h sample in comparison with the 1F_1h. Although the same behavior was observed in both hot rotary forging steps samples, XRD studies in the 3F_3h sample were carried out during the cooling and heating in order to confirm the occurrence of the R-phase during the phase transition. The XRD patterns are shown in Figure 4.14b and c. (Świec, 2016)

From 250 °C to 300 °C the FWHM decreased and stabilized up to 350 °C, suggesting a recovery. Between 350-450 °C the FWHM decreased. In addition, it is evident that the austenite peak shifted to smaller 2θ angles, corresponding to a larger d-spacing due to heating. After heating up to 500 °C, the A_f temperature increased ($A_f = 39.9$ °C) and the R-phase was evident. Such behavior indicates that the precipitation phenomenon

occurred, and Ni_4Ti_3 precipitates were formed. (Pelton, 2000)(Fan, 2017) (Khalil-Allafi, 2002)

As mentioned previously, it is difficult to determine by XRD technique the presence of Ni_4Ti_3 precipitates.

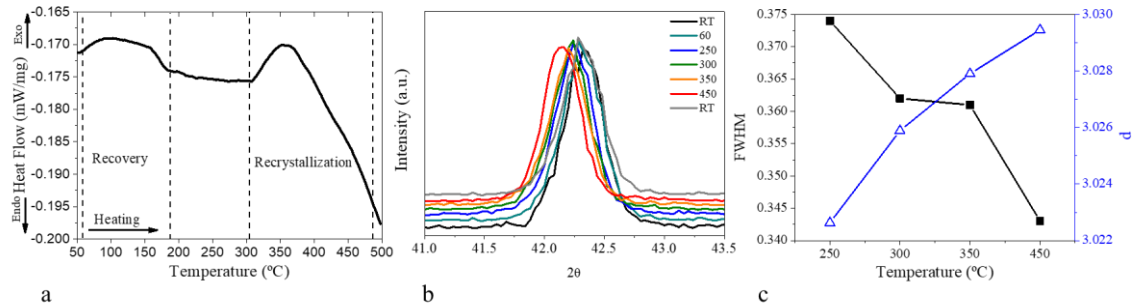


Figure 4.14 – NiTi_1_3F_3h - Recovery recrystallization results: (a) DSC curves heat treated to 500 °C; (b) XRD at high temperature and (c) FWHM and d -spacing observed.

4.2.2. Cold Rotary Forging Steps

After hot rotary forging steps, the cold rotary forging steps were applied. Intermediate heat treatments at 800 °C during 10 min were performed followed by quenching into water. This step is important to assure a particular microstructure and an improvement of the functional properties. (Suzuki, 1998)(Habu, 2009).

4.2.2.1. First Cold Rotary Forging Step

The first cold deformation corresponds to a total length change of $\phi = 0.5$ (equal to 50 % diameter reduction). As this sample was deformed at room temperature, some different behaviors are observed when comparing to the hot steps.

DSC curves for first cold rotary forging sample (NiTi_1_5F_4h1c) showed one exothermic peak during cooling and heating (Figure 4.15a). The A_f temperature was below room temperature ($A_f = 8.7$ °C, see Table 4.3). This material is superelastic at room temperature. Until this deformation step, the starting temperature of thermal peaks corresponding to phase transition decreased with increasing deformation degree. SR-XRD results illustrate the presence of a mixture of the B2, B19' phases (Figure 4.15b).

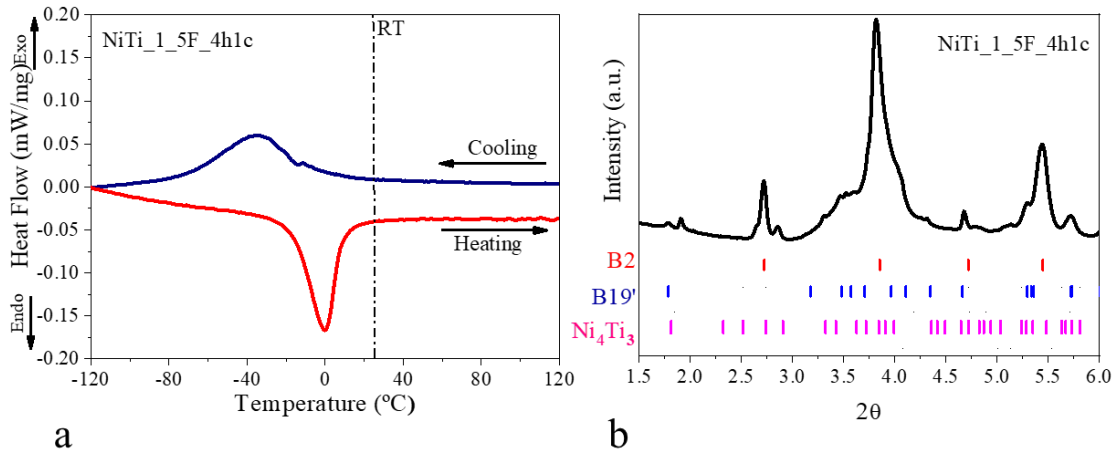


Figure 4.15 – (a) DSC curves NiTi_1_5F_4h1c sample (b) SR - XRD of NiTi_1_5F_4h1c sample.

A partial overlap of the temperature ranges of DSC peaks during cooling and heating occurred, suggesting a two-steps transformation as $B2 \leftrightarrow R \leftrightarrow B19'$ (Figure 4.15a). The hysteresis value indicates the presence of R-phase. Then, this characteristic was confirmed by the XRD high/low temperature (Figure 4.16). During cooling and heating the intermediate R-phase was formed. Thus, a transformation of two-stage was observed ($B2 \leftrightarrow R \leftrightarrow B19'$) for both cooling and heating curves. The alloy heterogeneity compositional, namely richer Ni content in few regions of the material matrix, explains the occurrence of the Ni₄Ti₃ precipitation. (Jiang, 2015)

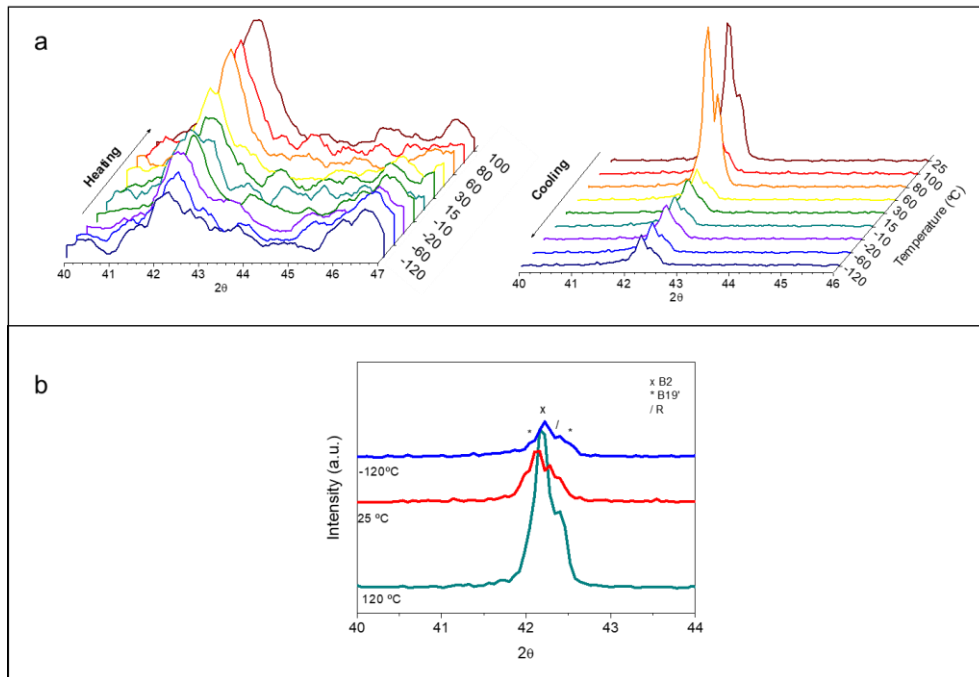


Figure 4.16 – NiTi_1_5F_4h1c XRD results at high/low temperature: (a)during heating and cooling, between -120 and 120 °C (b) separate diffractograms for three different temperatures (-120, 25 and 120 °C).

The recovery and recrystallization phenomena were investigated during a heating up to 500 °C on NiTi_{1_5F_4h1c} sample by DSC, complemented by information on transformation temperatures obtained by DSC tests (-150 °C to 150 °C), before and after ramp, as shown in Figure 4.17. The XRD at high temperature could not be performed due to the small size of the samples, which prevented satisfactory measurement.

Figure 4.17a shows the heating curves from room temperature to 500 °C (NiTi_{1_5F_4h1c} sample). In this sample two exothermic events were detected. The broad peak ($\delta H = 12.9$ J/g) in the temperature range from 50 to 350 °C, corresponding to the heat evolved during recovery and the peak at 405 °C (extending from 350 to 475 °C / $\delta H = 8.3$ J/g) corresponding to the heat evolved during recrystallization and precipitation. (Humphreys, 2004b)

DSC curves recorded during thermal cycle (from -150 to 150 °C) after heating up to 500 °C showed one endothermic peak corresponding to reverse phase transformation. In addition, the transformation temperature shifted to a higher temperature ($A_f = 40$ °C). The presence of R-phase evidenced by the partial overlap of the endo and exothermal peaks suggests the formation of the Ni₄Ti₃ precipitate. (Jiang, 2015)

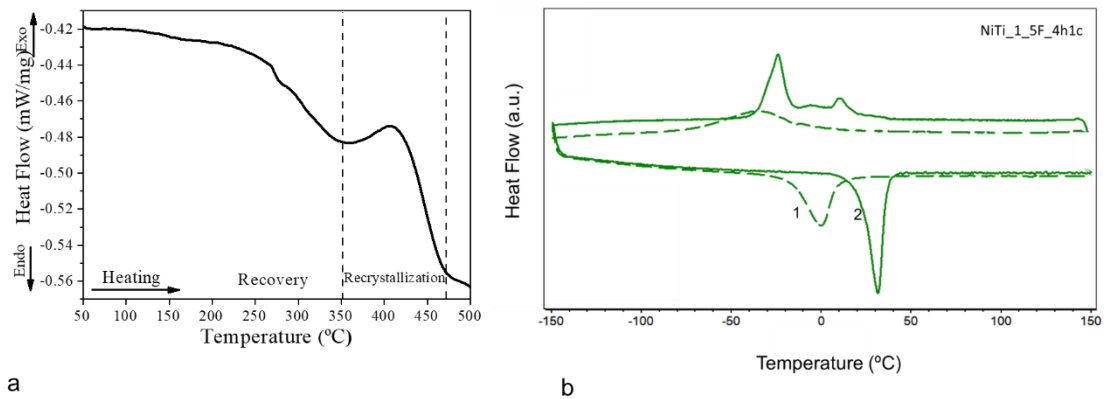


Figure 4.17 – NiTi_{1_5F_4h1c} - Recovery recrystallization results: (a) DSC curves heat treated to 500 °C; (b) DSC thermal characterization from -150 to 150 °C before and after heat treatment to 500 °C compared (1- before heat treatment -dash line and 2- after heat treatment – solid line).

4.2.2.2. Second Cold Rotary Forging Step

The second cold deformation corresponds to a deformation of $\phi = 0.7$ (equal to 70 % diameter reduction).

On the sample NiTi_1_6F_4h2c, the A_f temperature shifted to higher temperature ($A_f = 20.2$ °C, see Table 4.3) compared to NiTi_1_5F_4h1c A_f temperature ($A_f = 8.7$ °C). Even with increased cold deformation, the sample is still austenitic at room temperature (Figure 4.18b). At room temperature the SR-XRD showed the presence of a mixture of the B2, R-phase, B19', Ni_4Ti_3 (Figure 4.18b).

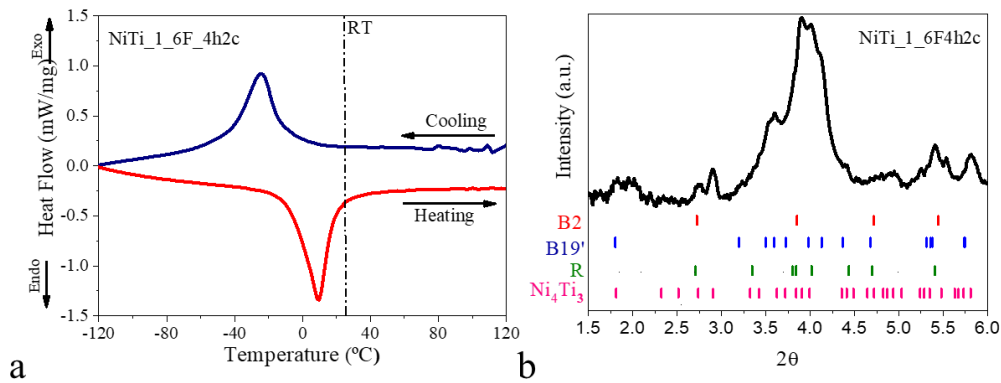


Figure 4.18 – (a) DSC curves NiTi_1_6F_4h2c sample (b) SR - XRD of NiTi_1_6F_4h2c sample.

The DSC chart depicts one transformation peak on heating and one on cooling, suggesting that $B2 \leftrightarrow B19'$ took place in a single step with a hysteresis value of 17.3 °C. Furthermore, X-Ray diffraction assay at high/low temperatures was performed to confirm the phases present. For higher temperature (at 100 °C), the $(110)_{B2}$ is clearly visible (Figure 4.19 heating). During cooling, below 25 °C, there is an abrupt decrease of the intensity of the $(110)_{B2}$ peak and two peaks were detected close to $(110)_{B2}$ peak being associated to the R-phase. (Lekston, 2007) In addition, it is possible to conclude that, during cooling/heating, there was a two-step phase transformation ($B2 \leftrightarrow R \leftrightarrow B19'$). Thus, from XRD results the R-phase was identified at room temperature, this corroborate the SR-XRD results.

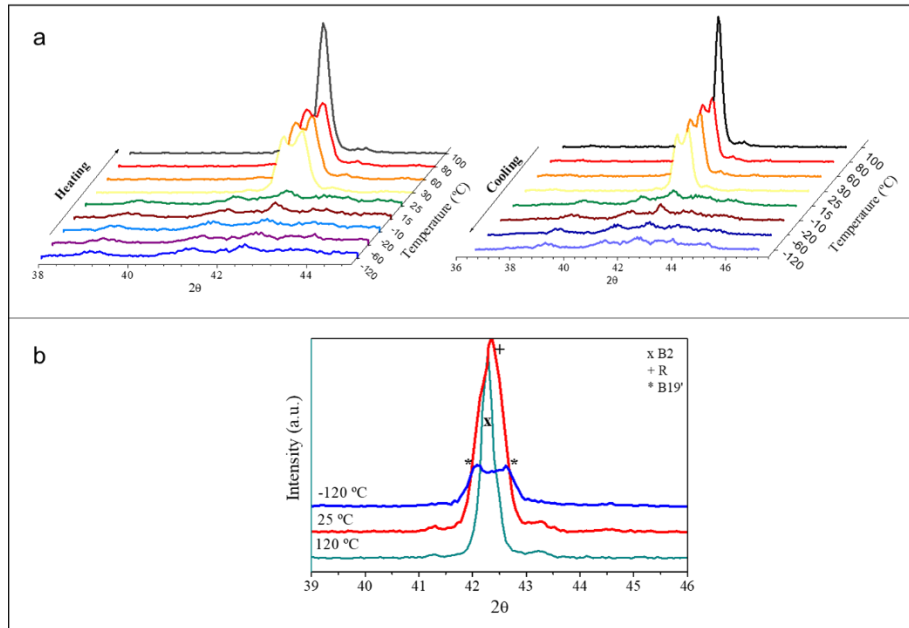


Figure 4.19 – NiTi_1_6F_4h2c XRD results at high/low temperature: (a) during heating and cooling, between -120 and 120 °C (b) separate diffractograms for three different temperatures (-120, 25 and 120 °C).

The recovery and recrystallization phenomena were observed by DSC test. Figure 4.20a shows the heating curves from room temperature to 500 °C (NiTi_1_6F_4h2c sample). It is seen that a continuous exothermic event started at ~230 °C until a larger exothermic peak occurred at 370 °C, finishing around 500 °C. This broad peak is attributed to structural relaxation and recovery and recrystallization phenomena. Even after the recovery occurred, the grains are still in a relatively high strain energy state. (Cun, 2016)

Saburi (1998) studied Ni-Ti alloys and reported recrystallization temperature when the samples were cold deformed (about 25%) and annealed between 500 °C and 600 °C. According to this author, cold deformed specimens (25%) annealed at 600 °C (temperature close to the recrystallization temperature) display a behavior similar to alloys annealed at 850 °C. (Saburi, 1998)

The recrystallization temperatures, of both cold deformed samples results, showed that increasing the percentage of cold work the rate of recrystallization is enhanced, once the recrystallization temperature is dropped.

Similar to the first cold forging step deformation, the DSC was performed during thermal cycle (from -150 to 150 °C) before and after heating up to 500 °C heating. The result showed two-stage phase transformation of B2→R→B19' on cooling and one

stage phase transformation of B19'→B2 on heating (Figure 4.20 b – line 2). In addition, the transformation temperature shifted to a higher temperature ($A_f = 49\text{ °C}$). Again, the presence of the R-phase suggests the formation of the Ni_4Ti_3 precipitate. (Jiang, 2015)

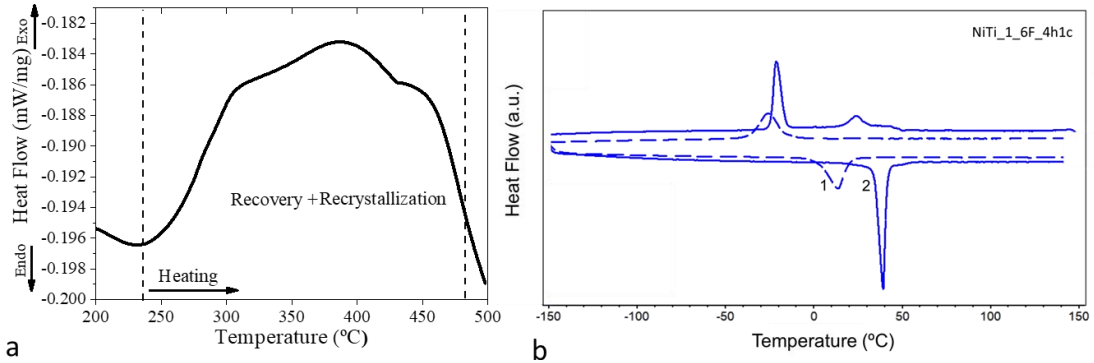


Figure 4.20 – NiTi_1_6F_4h2c - Recovery recrystallization results: (a) DSC curves heat treated to 500 °C; (b) DSC thermal characterization from -150 to 150 °C before and after heat treatment to 500 °C compared (1- before heat treatment -dash line and 2- after heat treatment – blue line).

During the investigation the assays results depicted that for all the samples, the temperature of 400 °C is enough to promote static restoration phenomena.

It is desirable that the intermediate heat treatment can promote the microstructural static restoration phenomena after the deformation steps. Then, it is supposed that the 800 °C applied between deformation steps was enough to promote these phenomena.

4.2.3. Rotary Forging Process Evolution

A wide range of mechanisms are responsible for the evolution of microstructures in the Ni-Ti alloys. The physical metallurgy of a thermomechanical treatment is dependent on the various metallurgical mechanisms that take place during processing. The interrelation of recrystallization, recovery, precipitation and phase transformations, leads to the development of the microstructure through thermomechanical process (Humphreys, 2004) (Treppmann, 1997).

To understand this behavior, the structural characterization results are shown in the following sections.

4.2.3.1. Microstructural and Compositional Evolution by Thermal and Chemical Analysis

Figure 4.21 shows the transformation temperatures of the samples along the rotary forging process and are compared to the values shown in Table 4.3. As shown before, all the samples showed one-step transformation on heating and one on cooling with a partially overlapped range of temperatures. However, all transformations occurred below 30 °C. Thus, the rotary forging process occurred at austenite field, once the hot steps were performed at ~800 °C, and the cold deformation steps presented the A_f temperature close to room temperature.

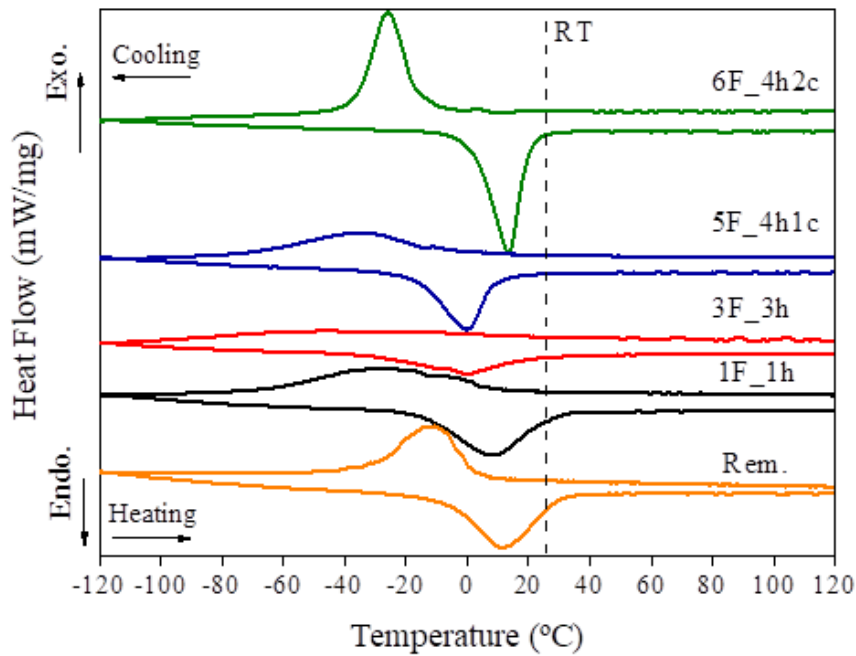


Figure 4.21 – DSC curves of the Rem., 1F1h,3F3h, 5F_4h1c and 6F_4h2c steps, cooling curves and heating curves.

Table 4.3 - Phase transformation temperatures in degree Celsius for NiTi_1 samples.

	Cooling (°C)			Heating (°C)		
	M_s	M_p	M_f	A_s	A_p	A_f
1F_1h	7.2	-29.4	-59.0	-15.1	9.2	27.5
3F_3h	13.5	*	-81.6	-25.5	-3.5	19.5
5F_4h_1c	-16.8	-35.1	-87.6	-16.5	-0.2	8.7
6F_4h2c	-15.6	-2.6	-36.2	1.7	13.4	20.2

The difference between NiTi₁_1F_1h DSC curves and NiTi₁_3F_3h curves is the partial transformation suppression observed in NiTi₁_3F_3h sample results. This behavior can be explained by the temperature reduction of the ingot/bar during the transporting from the furnace to the hammers which it becomes more expressive with the reduction of the cross section of the bar. It is supposed that the deformation temperature decreases gradually throughout the rotary forging steps. Thus, the deformation temperature of the sample 3F_3h was less than the deformation temperature of the sample 1F_1h. This promotes the partial suppression of phase transformations that occurs due to the possible present hardening in the B2 matrix (from 1F_1=198 HV to 3F_3h=300 HV (Ribeiro, 2015)), resulting from the third hot rotary forging step. (Otsuka, 2005)

The cold steps samples showed the stabilization of the austenite phase close to room temperature. The Ni content at these samples is higher enough to reduce the martensite transformation temperature (Figure 4.22). It is supposed that all cold processing occurred in the austenitic domain, and it is known that, when B2 is deformed above the level of superelastic recovery, an increase of martensitic transformation temperature will occur (Table 4.3 - 5F_4h1c and 6F_4h2c samples).(Elahinia, 2012)

Taking in consideration that the Ni content has an influence on the phase transformation temperature, a chemical analysis was performed. This analysis allows to observe the Ni, Ti, C and O contents evolution along the rotary forging processing. In order to verify the composition in the material, the analysis along the diameter of the NiTi₁_1F, NiTi₁_3F_3h and NiTi₁_5F_4h1c samples were done (Figure 4.22).

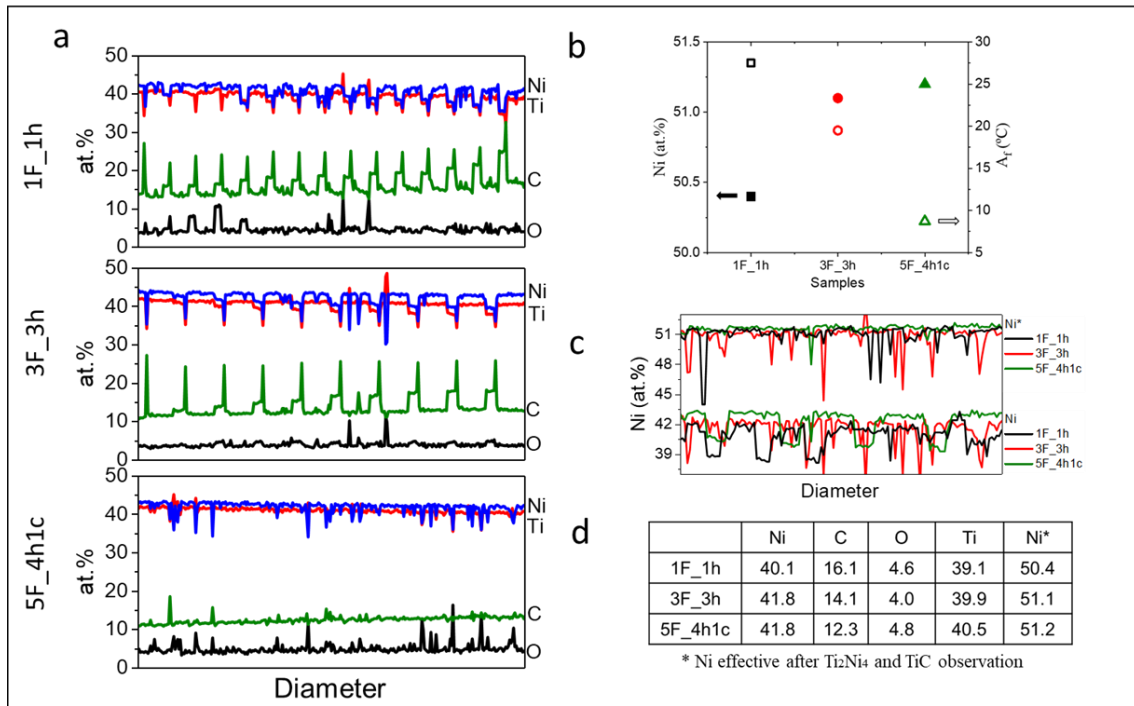


Figure 4.22 – Chemical analysis (EMPA) results (a) elements at.%; (b) Comparison between at.%Ni x A_f ; (c) elements at.% global composition values, in addition Ni effective after Ti₂Ni₄O and TiC observation.

It can be observed that the homogeneity produced by the forging process promotes an increase of the Ni content in the matrix by the dissolution of precipitates (Ni-Ti system) along the hot forging steps. In addition, inclusions such as carbides and oxides are fragmented, resulting in the reduction of their size and promotes a finer dispersion in the matrix (Figure 4.22a). The effective Ni on the matrix, when considered the impurities, is shown in Figure 4.22c and d. (Coda, 2012)

All the samples are Ni-rich alloys and showed an increase of Ni content of the matrix during the rotary forging process. This increase of the Ni content is inferred from the decrease on the austenite finish temperature as observed in the DSC results (Figure 4.22b).

To confirm the matrix homogenization along the rotary forging steps, a microstructural observation was performed by optical microscopy, as shown in Section 4.2.3.2.

4.2.3.2. Microstructural Evolution by Optical Microscopy

At the beginning of deformed process (NiTi_1_1F_1h sample) the grains are coarse, with average grain size 40 μm , as shown in Figure 4.23. This result demonstrated that the material has an austenite matrix at room temperature, in accordance with the DSC and SR-XRD results (Figure 4.7).

As result of the deformation, grains are elongated along the deformation direction. The deformation promoted the heterogeneous microstructure observed in Figure 4.23b.

The deformation evolution, represented by NiTi_1_3F_3h sample (Figure 4.23 c and d), showed characteristics of possible dynamic recrystallization occurrence during hot deformation. The elongated grains can also be readily seen in these figures. Ni-Ti SMA shows a significant grain elongation during dynamic recrystallization. (Humphreys, 2004)(Jiang, 2012) Therefore, in this condition the average grain size of the specimen is 36 μm , thinner than the average of the NiTi_1_1F_1h grain size (40 μm).

It can be seen from Figure 4.23 that recovery and recrystallization cause grain refining in the process of deformation. This is observed because the new generated grains replaced the original grains. Figure 4.23c shows the effect of recovery and recrystallization at increased high temperature deformation is more apparent than that in Figure 4.23a.

The original grains are elongated perpendicularly to the deformation direction (Figure 4.23 e and g) at cold steps. Increasing the deformation promotes the elongation of the grains and the decrease of the grain size. (Świec, 2016) The grains now are homogeneous in center and edge of the sample.

Moreover, during the remelting process there was a faster cooling in the area close to the ingot edge (part of the material in contact with the crucible) by water cooling. Thus, the difference between edge and center of the sample promoted the heterogeneous microstructure (Figure 4.23 b and d). Therefore, the grains close to the edge are finer, while the grains in the center are coarser. However, along the successive deformation steps, the difference is attenuated, as shown in Figure 4.23 f and h.

Furthermore, comparing with the original remelted microstructure, the microstructures of the samples after forging process still possess a lot of dendritic grains. The remelted sample contains B2 austenite and some second phases.

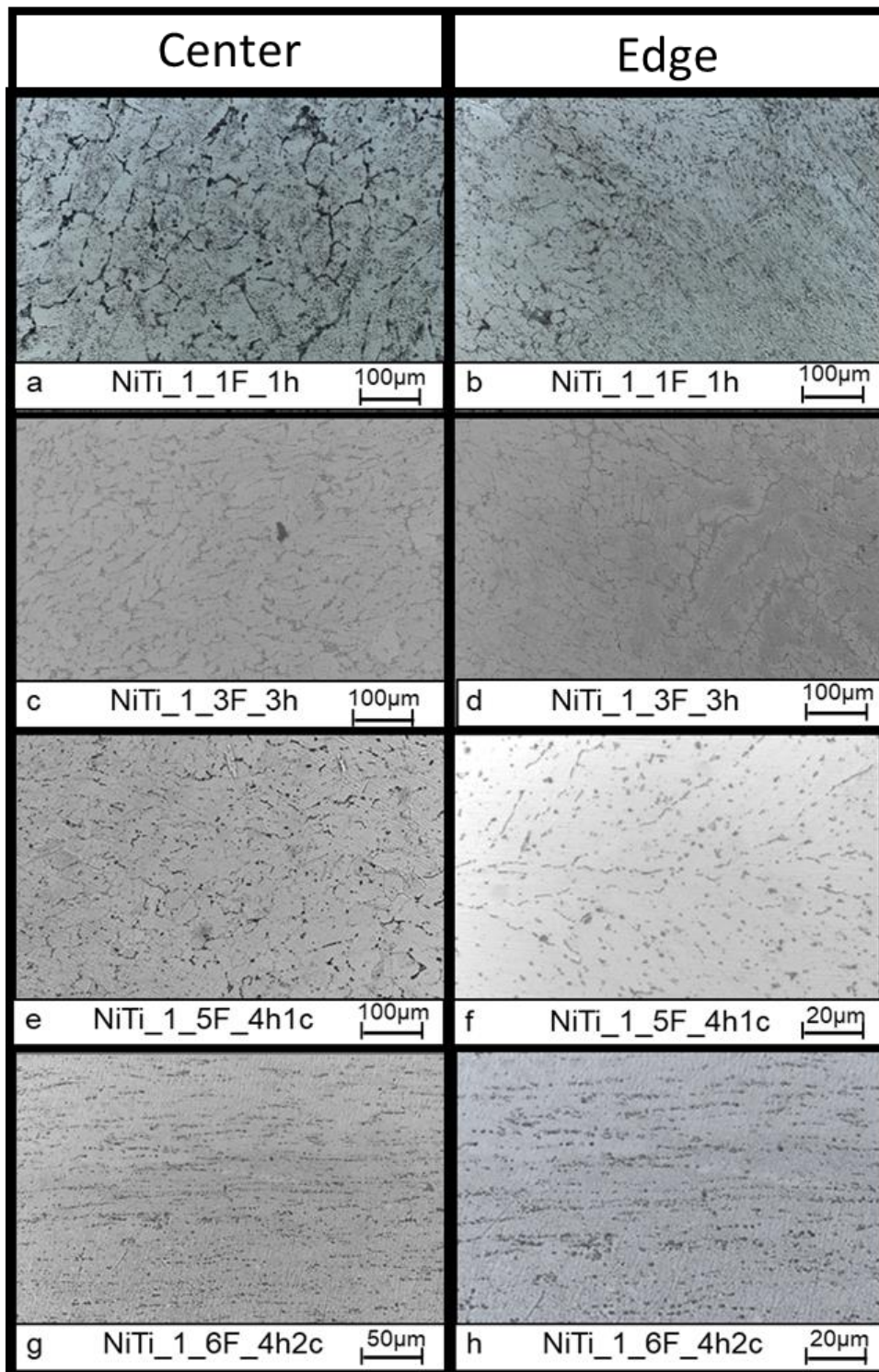


Figure 4.23 – Micrographs of the NiTi₁ alloy hot and cold deformations steps.

4.2.3.3. Microstructural Evolution by EBSD

Electron backscatter diffraction (EBSD) in the scanning electron microscope (SEM) is a powerful tool to measure the size, distribution and volume fraction of deformed and recrystallized grains because of its ability to obtain information about individual grains and to establish direct neighborhood relationships between these grains. It is often used to analyze the thermomechanical behavior of the SMAs.

The EBSD results of the evolution of the microstructures along the forging process is seen in the inverse pole figure maps estimated for both austenite and martensite phases. The inverse pole figure (IPF) colors refer to the directions perpendicular to the EBSD scan plane (cross-sectional plane of the cylindrical samples). To discuss the microstructure evolution, the Rem. sample results need to be compared with the results for deformed samples. The summarized view is:

1. Rem. sample: shows refined grains with serrated boundaries;
2. 1F_1h: shows large grains with serrations;
3. 3F_3h: shows large grains and recrystallized grains;
4. 5F_4h1c: presence of twin-like bands in the parent austenite grains;
5. 6F_4h2c: fine-grained distribution of austenite and martensite phases.

Figure 4.24 shows in the NiTi-B2-IPF maps the black regions which had data points of $CI \leq 0.1$. Typically, the B19' monoclinic martensite structure is often difficult to characterize by XRD and EBSD; it must be pointed out that the presence of martensite was also observed in these "black" regions, under the conditions of detection of minimum five diffraction bands and $CI > 0.1$. It must also be noted that each different microstructure had varying austenite grain sizes, as apparent in the IPF maps, hence it was impossible to maintain identical scan sizes for all specimens.

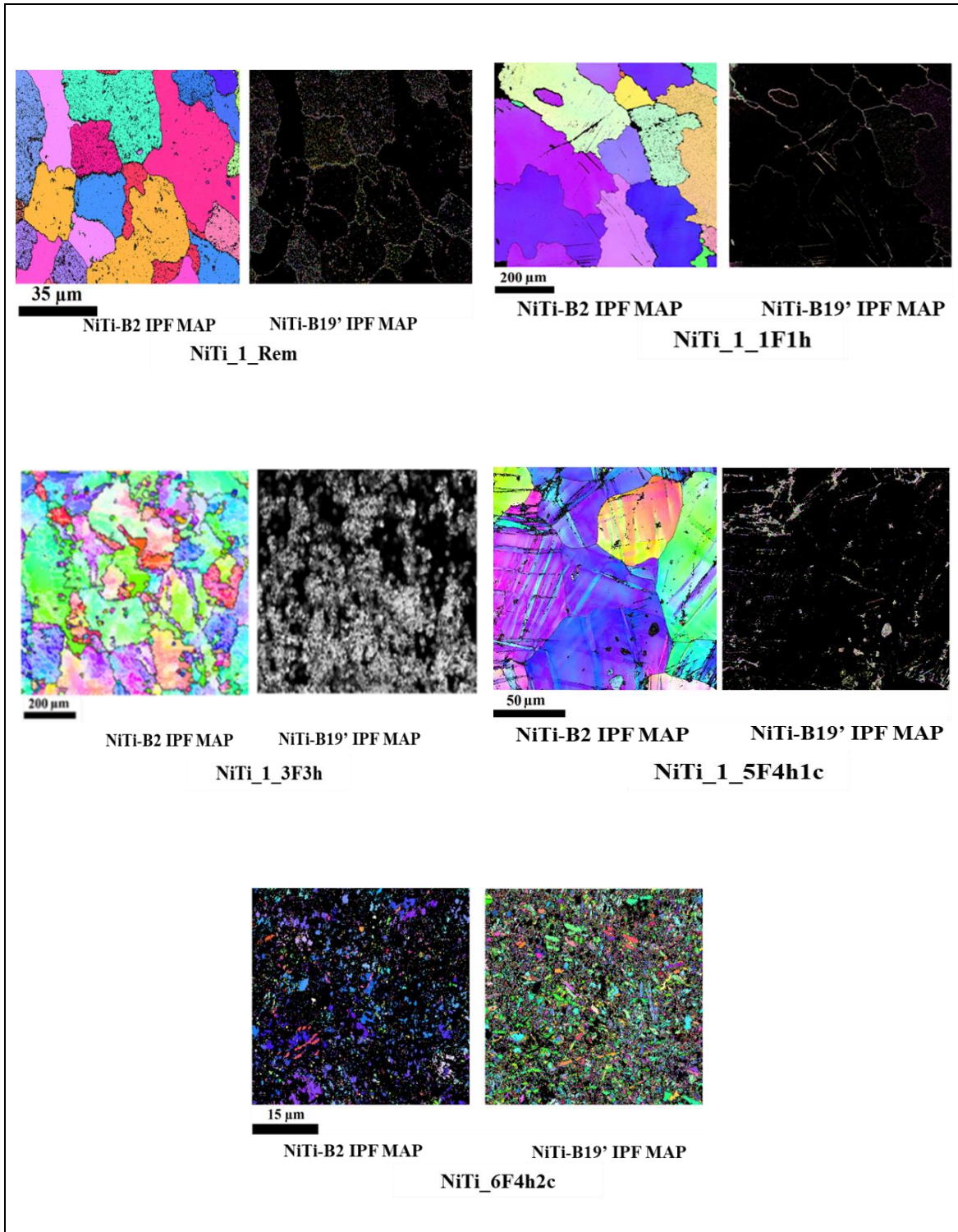


Figure 4.24 - Enlarged image quality maps of the NiTi_1 alloy hot and cold deformations steps.

NiTi_1_Rem sample showed a homogenized microstructure, where the serration in the boundaries can be associated to precipitation that promotes pinning during the boundary migration. SR-XRD measurements further clarified the possible presence of Ni_4Ti_3 , Ni_3Ti sometimes overlapping each other. The SR-XRD measurement for compositional analysis were performed on few randomly distributed precipitates of different size and shapes, indicated by suitable markers. The location of such precipitates was found both in the interior and at grain-boundaries. Ni_4Ti_3 or other complex precipitates could not be indexed by EBSD due to their smaller size, below the resolution of this technique.

This sample showed presence of martensite mainly visible in the grain boundaries. However, the presence of martensite is observed due to deformation applied or after thermomechanical process without intermediate heat treatment. For this case the presence of the martensite may have resulted from the cut and polishing treatment.

The mechanisms of dynamic recovery are dislocation climb, cross-slip and glide, which result in the formation of low angle boundaries that also occur during static recovery; these enable the subgrains to remain approximately equiaxed during the deformation. During the hot deformation some reorientation of subgrains may also occur. (Humphreys, 2004a)

Dynamic recrystallization generally starts at the old grain boundaries. New grains are subsequently nucleated at the boundaries of the growing grains and in this way a thickening band of recrystallized grains is formed. When there is a large difference between initial grain size and recrystallized grain size, a necklace structure of grain may be formed, and the material will become fully recrystallized. (Humphreys, 2004a)

NiTi_1_1F_1h sample showed large grains with serrated grain in boundaries. Along the rotary forging it is expected the pre-existence of the grain-boundaries elongated in deformation direction, causing grain boundary serration. In Figure 4.25 the black circles show out fine grains of austenite sparsely distributed along these serrated boundaries. These grains appear to be dynamically recrystallized. (Sakai, 2014) (Basu, 2015)

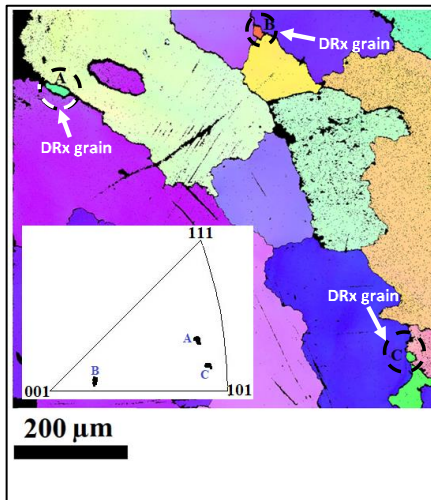


Figure 4.25 - Enlarged image quality maps of NiTi_1_1F_1h sample

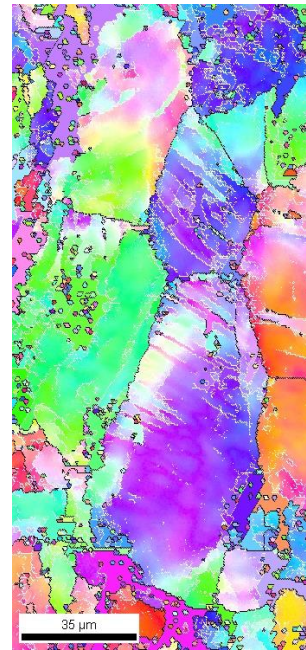


Figure 4.26 - Enlarged image quality maps of NiTi_1_3F_3h sample

NiTi_1_3F_3h sample showed a similar behavior to that of the NiTi_1_1F_1h sample. However, the increased deformation promotes a larger amount of the recrystallized grains.

It can be seen that the original grains are elongated perpendicularly to the deformation direction and the original grain boundaries show the fine DRX grains and typical “necklace structure” of DRX (Figure 4.26). As the deformation percentage increased, the number of DRX grains increased and the grain size decreased, as elucidated in Figure 4.26.

NiTi_1_5F_4h_1c sample showed that the combinations of hot and cold deformation with short annealing treatments induced significant differences in in-grain misorientation and grain boundary fractions for both phases. This microstructure was characterized by several twin-like features, typical of cold deformed microstructure. The twin-like bands were observed inside the parent austenite grains. Since the cold forging induced certain martensite variants which promoted specific preferential orientations;

however, above a certain stress value deformation by irreversible dislocation slip will occur. This behavior induced a formation of a new variant that could not have been formed during the process. The retained martensite appears as a result of the local strain inhomogeneity and the applied stresses. (Świec, 2016) (Laplanche, 2015)

The presence of phases mixture was shown in NiTi_1_6F_4h_2c sample. This mixture may be from B19', R-phase and precipitates such as Ni₄Ti₃. This result showed that cold deformation with short annealing treatments increase the differences in-grain misorientation and grain boundary fractions for all the phases.

4.2.3.4. Microstructural Evolution by SEM

As discussed, the material has structure characterized upon the conditions during solidification. Hence, the structure of Ni-Ti alloy depends not only upon the conditions under which the metal is cast and solidified, but also upon the composition of the alloy, as well as its thermal and process characteristics.

The surface morphologies of the samples are shown in Figure 4.27. All the samples displayed an oxide layer, resulting from the manufacturing process black phases in the micrographs. The presence of Ni-rich phases in the surface was observed in all the samples. After etching, most of the oxide layer was removed.

Along the thermomechanical process the elongation of the grains is evident. The B2 matrix is observed in all the samples. The Ni content increases, the size of the grains and the precipitates decrease, showing a higher distribution of large particles. Along the thermomechanical process the grains are equiaxial.

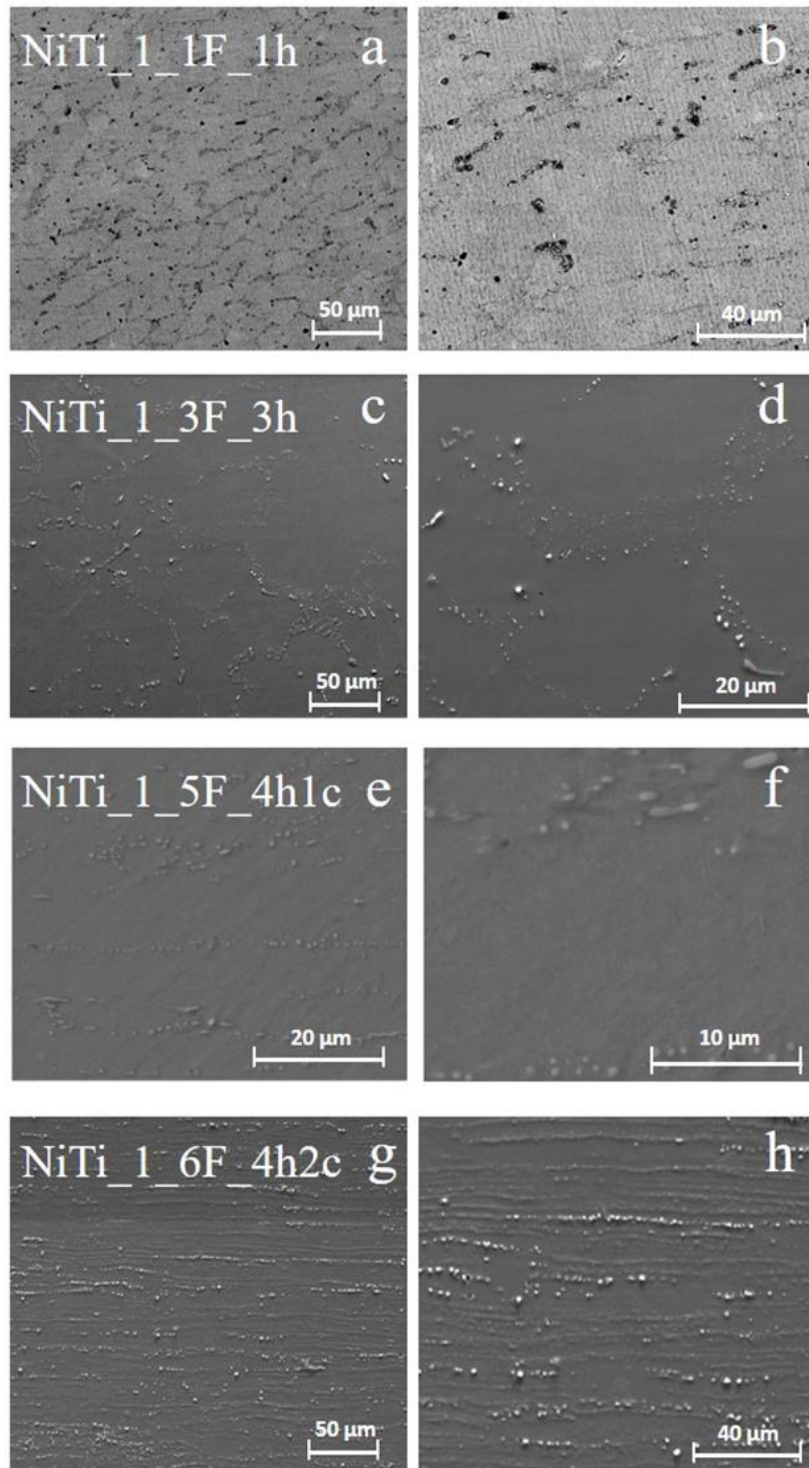


Figure 4.27 - SEM images of the NiTi_1 alloy hot and cold deformations steps (backscatter mode).

4.2.3.5. Textural Evolution

The texture is an important parameter describing the microstructure evolution along the deformation of the material. Usually, textures are determined by x-ray diffraction and represented by a pole figure. (Cullity, 1978) The purpose of the results presented in this section is to provide the information to the variation of the intensity of the $(110)_{B2}$, $(200)_{B2}$ and $(211)_{B2}$ peaks along the azimuthal angle ϕ (transmission mode), as shown in Figure 4.28 column a, and the pole figure (reflection mode) as shown in Figure 4.28 column b.

The variation of the intensity of the $(110)_{B2}$, $(200)_{B2}$ and $(211)_{B2}$ peaks along the azimuthal angle ϕ are represented by colors in Figure 4.28a: red line $(110)_{B2}$ intensity, black line $(200)_{B2}$ intensity and blue line $(211)_{B2}$ intensity. The position of the peak intensity along the azimuthal angle *versus* 2θ are shown in Figure 4.28 on the left top.

In this study the pole figures (covering an area of up to 69° from the center), were obtained by the reflection technique. The stereograms for $(110)_{B2}$, $(200)_{B2}$ and $(211)_{B2}$ are shown in Figure 4.28 on the right top.

The deformation in Ni-Ti alloys is complex and difficult to investigate in the initial stages of the deformation by hot forging processes. The texture in the cold deformed materials is better interpreted, because at this stage the percentage of the deformation is significant. The orientation changes that take place during deformation are not random.

Figure 4.28 shows the textural evolution along the deformation steps, where it is possible to observe a typical solidification texture for the NiTi_1_Rem sample. However, for the other samples (1F_1h, 3H_3h, 5F_4h1c and 6F_4h2c) it was only possible to observe a tendency of the texture. This is consistent with the deformation direction. The higher intensities were observed in the center of $\{110\}\langle 110 \rangle_{B2}$ and other intensities were identified $\{200\}\langle 110 \rangle_{B2}$.

The evolution of the intensity variation of the $(110)_{B2}$ and $(200)_{B2}$ peaks along the deformation steps is evident as shown in the NiTi_1_3F_3h. However, the sample NiTi_1_5F_4h1c and NiTi_1_6F_4h2c show a possible B19' (Figure 4.28a). The Appendix A02 shows separately each deformation result, to clarify the intensity observation.

The $\alpha\langle 110 \rangle$ fiber texture is desired after cold drawing in the product aimed to be produced from this thermomechanical process.

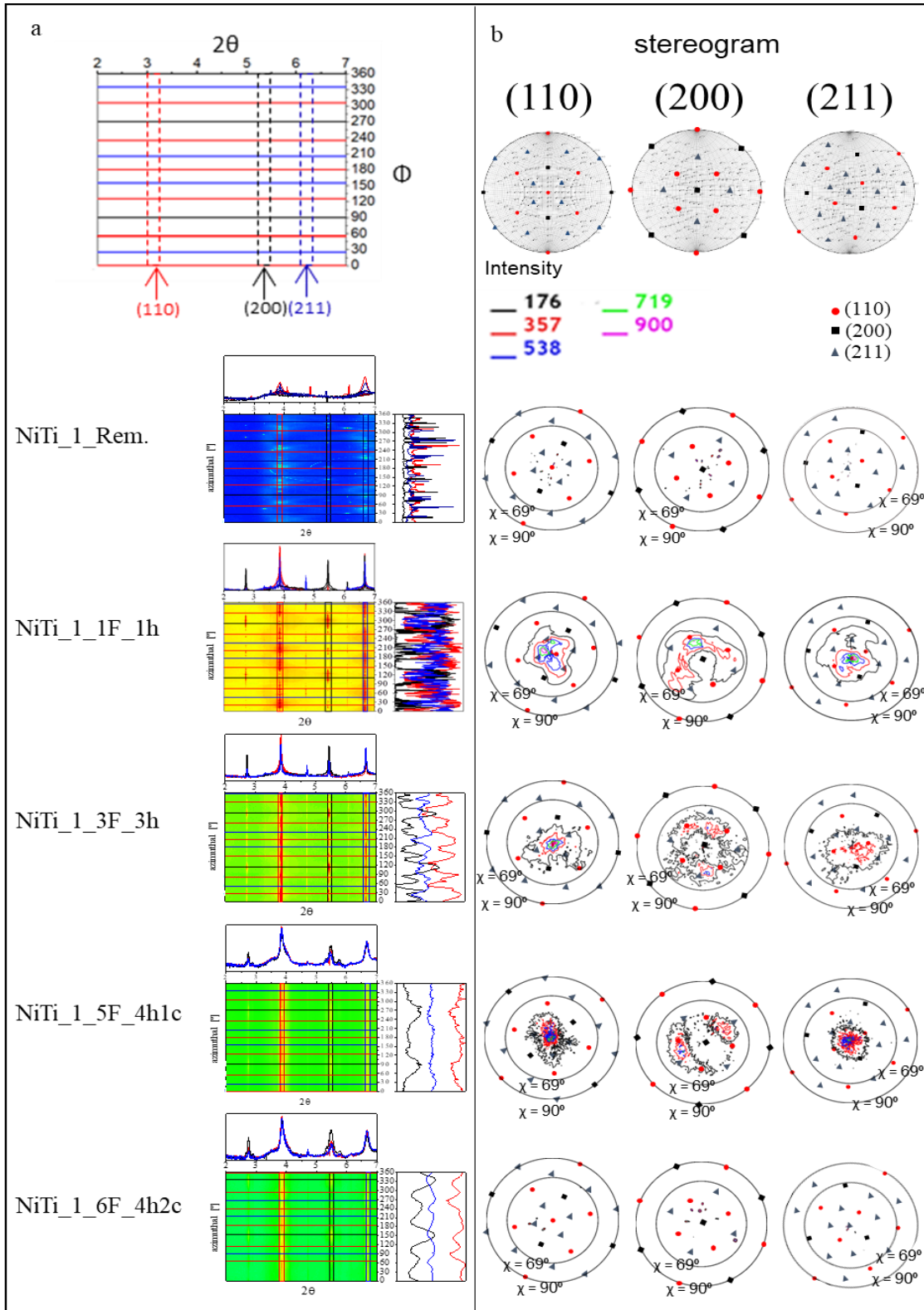


Figure 4.28 - Variation of the 2θ peak position and intensity of the (110)_{B2}, (200)_{B2}, (211)_{B2} peaks along the azimuthal angle (transmission mode) and Pole Figure (110)_{B2} (reflection mode) of the NiTi₁ alloy hot and cold deformations steps.

4.2.4. Rotary Forging Process Evolution Summary

In order to elucidate the effects of thermomechanical treatment on the alloy, the characterization results need to be observed together. During deformation the microstructure of alloy changed in several ways.

An important observation was that the grains changed their shape and there was a large increase of the total grain boundary area. The new grain boundary area had to be created during deformation and this was done by the incorporation of some dislocations that were continuously created during the deformation process. The orientations of single crystals and of the individual grains of a polycrystalline metal change relative to the direction(s) of the applied stress(es). These changes are not random and involve rotations which are directly related to the crystallography of the deformation. The results showed that this behavior occurred when the grains acquired a preferred orientation, which became stronger as deformation proceeded. The grain refinement was clearly evidenced in the microstructural observation, where in the last sample (6F_4h2c) equiaxial grains are evident. The presence of the R-phase in this sample was detected by SR-XRD and DSC.

The temperature (800 °C) applied in the intermediate heat treatments was suitable. However, for the third deformation, this temperature was not enough to promote the deformation in an adequate condition. This parameter needed to be changed, to improve the forging process. However, increasing this temperature above 900 °C is insecure. This temperature can promote second phase formation on the matrix (Otsuka, 2005). The temperature applied must allow the adequate high temperature deformation. The heat released during the transport of the material from the furnace to the forge must be considered. This issue is discussed on the next part of the study (section 4.3).

Dynamic phenomena which occurred during the deformation, were observed through the EBSD test and OM. As mentioned previously, increasing the deformation, a larger number of recrystallized grains were observed followed by other phase formation (R-phase and/or B19'), in the final deformation steps.

Other parameter that could be changed is the heat treatment time. But, if the time applied is longer, the probability of surface oxidation is real. The time in this situation needs to ensure a good homogenization of the temperature in all the material.

The time and temperature applied in this process did not increase the oxygen and carbon content on the material. In addition, along the deformation the inclusions present, have become small enough to promote their best dispersion in the matrix.

The 3F_3h step results show that the increased contact surface promotes a faster cooling of the material and, as a consequence, the deformation is more difficult to occur.

The second cold deformation step A_f is higher (20.2 °C) than first cold deformation step A_f (8.7 °C) which proves that the refinement of the material structure was reached. The A_f temperature close to room temperature and the structural refinement is desired for the application that this investigation aimed.

Analysis of the initial rotary forging process results allowed to identify the following points: (i) the heat treatment before the first hot deformation step (solution heat treatment applied to remelted ingot) needs to be changed, in order to dissolve the Ni-rich precipitates; (ii) the intermediate solution heat treatment requires different parameters (time and temperature), due to the cooling of the material (during ingot transportation from the furnace to the hammers) to allow the hot deformation to be performed; (iii) the initial rotary forging process presents the A_f temperature at 6F_4h2c step close to room temperature, this characteristic must be kept after the changes on the processing parameters.

4.3. Heat Treatments

Taking in consideration the discussion presented in Section 4.2, the heat treatment conditions in different rotary forging processing steps samples were investigated. Such investigation is important because for each rotary forging process step, a specific microstructure characteristic is required. Therefore, this section focused on the investigation of better parameters (time and temperature) to apply in the rotary forging process in the alloy 1. This step of the study was separated in

- (i) solubilization heat treatment adjustment to apply to the ingot (Rem. Sample – initial heat treatment),
- (ii) intermediate heat treatment between deformation steps and
- (iii) aging treatment,

aiming to select the parameters to improve the materials functional properties.

4.3.1. Initial Solution Heat Treatment

At the beginning of this study the sample NiTi_1_Rem sample was chosen to be investigated. This sample was chosen, because it was identified as presenting the best condition to obtain the superelastic alloy. For the alloys production success, it is important that the starting material shows the best homogenization condition as possible.

The DSC and SR-XRD methods were applied to determine the effects of the solution heat treatment on the transformation temperatures and the structural characteristic, which are very important properties for starting deformation steps.

The results are presented for the NiTi_1_Rem sample heat treated at 800 °C during 30 minutes (initial proposal for the solubilization path) and the alternative treatment that is proposed: 120 minutes soaking time at 950 °C (Figure 4.29).

Remelted sample showed A_f temperature above room temperature (30.1 °C, see Table 4.1), which is expected for this Ni content alloy (Coda, 2012). The section 4.1 discussed the presence of the precipitates from the remelted condition.

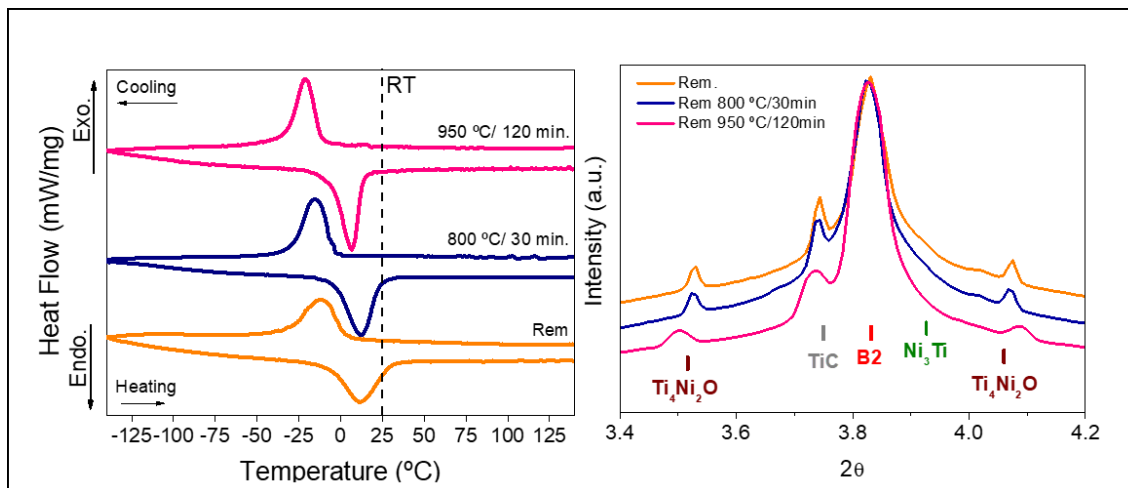


Figure 4.29 - a) comparison between DSC curves (a) and superposition of the SR-XRD patterns (b) of NiTi_1_Rem sample and NiTi_1_Rem heat-treated at 800 °C during 30 minutes and 950 °C during 120 minutes.

This heat treatment aims to obtain the microstructure without precipitates. The precipitates dissolutions promote an increase of the Ni content in the matrix,

consequently, a decrease of transformation temperature (Otsuka, 2005) (Frenzel, 2012). The decrease of the transformation temperature is desirable, since this sample needs to show a superelastic behavior at room temperature.

It is known that at the beginning of the Ni-Ti SMA manufacturing (as remelted condition) it is not possible to observe the functional properties. The thermomechanical process is required to promote these properties (Otsuka, 2005) (Saburi 1998) (Suzuki 1998).

It can be observed from the Figure 4.29 that after the solution treatment (950 °C/120 min) applied in NiTi_1_Rem sample, the matrix is still B2 austenite, but Ti₃Ni phase (identified in Section 4.1) disappears. Therefore, Ti₃Ni phase can be dissolved in the NiTi_1_Rem sample heat treated at 950 °C during 120 minutes; the broadening of the austenite peak, in NiTi_1_Rem and 800 °C/10 min sample patterns, may be associated with the presence of the R-phases at room temperature.

NiTi_1_Rem_950 °C/120 min. result depicts the transformation temperatures lower than for the NiTi_1_Rem_800 °C/30 min. result. The heat treatment (950 °C/120 min.) promotes the precipitates dissolution, thus, increasing the Ni content on the matrix. This means that heat treatment at 950 °C during 120 minutes, is the better solution heat treatment for this sample.

4.3.2. Solution Heat Treatment between deformations steps

The sample NiTi_1F_1h was chosen to investigate the solution heat treatment between deformations steps. This sample was chosen, because the first hot forging step it is important in the discussion about the microstructure modified by the deformation.

The results are presented for NiTi_1_1F_1h sample heat treated at 800 °C during 10 minutes (initial proposal for the thermomechanical path) and the alternative treatments that are proposed: 120 minutes soaking time at 800, 850, 900, 950 °C.

4.3.2.1. First Hot Forging Sample (NiTi_1_1F_1h)

Figure 4.30 shows the locations of all spots (10 spots along a radius) of the NiTi_1_1F_1h sample. The difference between the periphery (spot 1 – A) and the center (spot 10 - B) is clear. The patterns show the influence of the thermomechanical process

applied to the sample. Thus, only spots A and B were chosen to be discussed in more detail at this study.

The Debye–Scherrer rings that were recorded for each location (A and B), allow not only the visualization of the phases present, but also complementary information, as the more uniformly distributed intensity of the Debye–Scherrer rings, as a consequence of the first thermomechanical process step. At each spot (A and B) the B2 rings are identified (Figure 4.30).

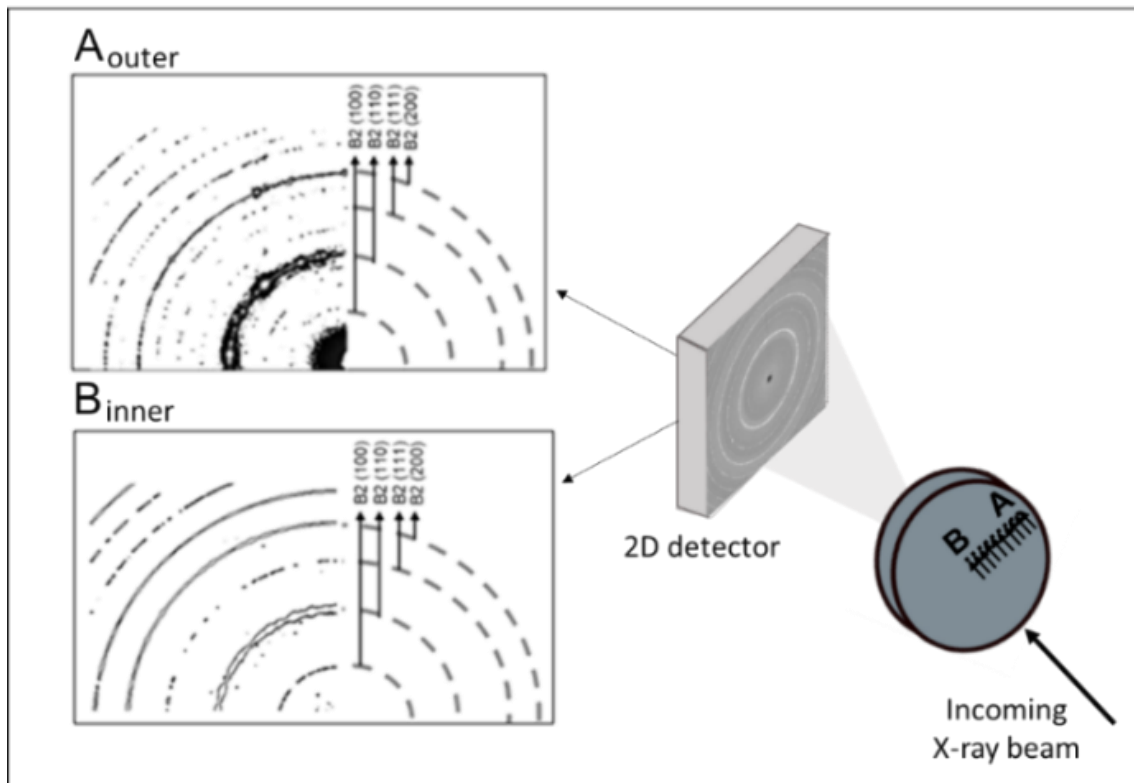


Figure 4.30 – Scheme of locations of the SR-XRD measurements on the samples and First structural characterization: A) Outer Spot - Debye–Scherrer rings, B) Inner Spot - Debye–Scherrer rings of first hot forging step (NiTi_1_1F_1h).

Figure 4.31 shows DSC curves of the first hot rotary forging step sample (1F) for spots A and B. For spot A, DSC measurement shows two-step transformation during cooling ($B2 \rightarrow R \rightarrow B19'$) and the reverse transition on heating. However, the spot B DSC measurement shows one single (very broad) peak during the cooling and the reverse transition on heating. However, a partial overlap, during cooling and heating, of the transformation temperatures ranges occurs, which can be explained by the existence of the R-phase transition. For the 1F sample, the transformation changes from B2–B19' to

B2–R–B19' may occur due to the introduction of dislocation networks by deformation. These dislocations networks can occur due to the previous deformation imposed, with more evidence at the edge of the sample (Otsuka, 2005).

Since the detailed study about these differences and the underlying reasons has been reported in the 4.2.1.1. section, only some key results are highlighted here for the convenience of the subsequent study about the influence of the solution heat treatment on the NiTi_1_1F_1h sample.

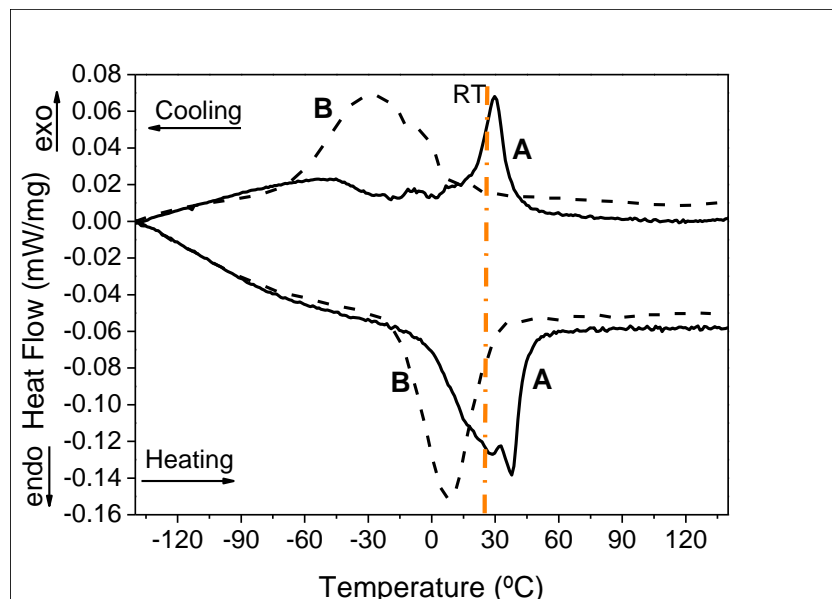


Figure 4.31 – DSC curves of the First Hot Forging Sample (NiTi_1_1F_1h)– Spot A (outer) and Spot B (inner)

4.3.2.2. First Hot Forging Sample (NiTi_1_1F_1h) and First Hot Forging Sample (NiTi_1_1F_1h) heat treated at 800 °C during 10 minutes.

To understand the influence of the heat treatment during 10 min on the 1F sample, a comparison between the Spot B of the first hot forging step sample (1F) and the Spot B of the 1F heat treated sample at 800 °C during 10 minutes is presented.

Figure 4.32a depicts SR-XRD patterns at room temperature. The 800 °C/10 minutes sample shows the presence of the B2 and Ni₄Ti₃. The Ni₄Ti₃ is suitable to appear during cooling to room temperature (Coan, 2017)

Figure 4.32b depicts the DSC measurements of the transformation behavior of the first step of hot rotary forging step sample (NiTi_1_1F_1h) and the NiTi_1_1F_1h sample after solution treatment at 800 °C during 10 minutes (800 °C/ 10 min). From the DSC measurements, it is visible that the characteristic temperatures (namely A_p and M_p) shifted to slightly higher temperatures with heat solution treatment. This shift of the transformation temperatures to higher temperatures, can be explained by the Ni-content change of the matrix: Ni decreases when Ni-rich precipitates are formed (such as Ni_4Ti_3 during cooling to room temperature) (Oliveira, 2018).

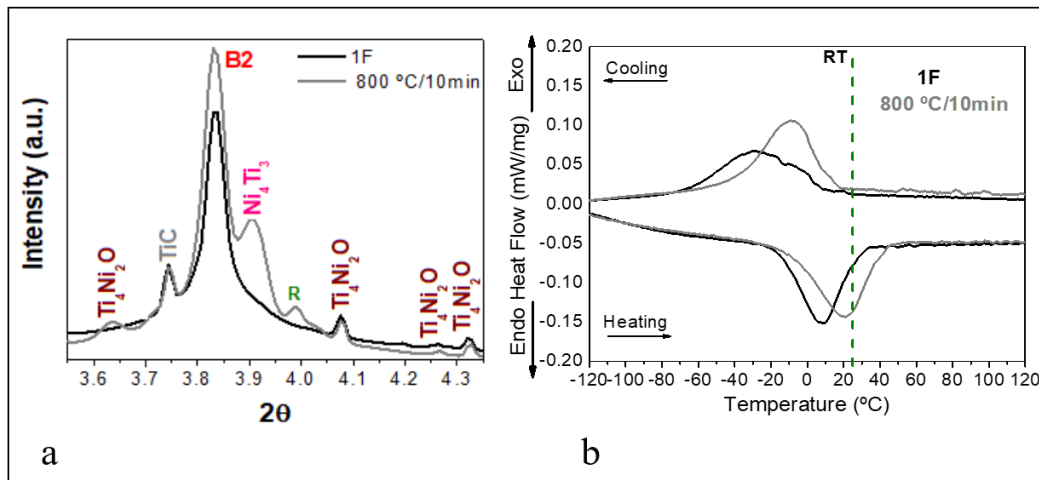


Figure 4.32 – a) comparison between SR-XRD pattern of First Hot Forging Sample (NiTi_1_1F_1h) and First Hot Forging Sample (NiTi_1_1F_1h) heat-treated at 800 °C during 10 minutes c) DSC curves.

4.3.2.3. Comparison of the First Hot Forging Sample heat treated at 800 °C during 10 minutes and First Hot Forging Sample heat treated at 800, 850, 900 and 950 °C during 120 minutes

The effect of different temperatures (800, 850, 900, 950 °C) during 120 minutes of the solution heat treatment on NiTi_1_1F_1h sample are now shown and discussed. For comparison, the NiTi_1_1F_1h sample heat-treated at 800 °C during 10 minutes was also included. From this point onwards, the samples are mentioned in accordance with the temperature and time of the heat treatment.

The time of 120 minutes of heat treatment was used based on different studies that used this heat treatment in order to obtain a homogenized matrix. A. Safdel *et al.* (2017) and S. Jiang *et al.*(2013b), subjected the Ni-Ti sample with a nominal composition of

Ni50.5 (at%) and Ni50.9Ti49.1 (mole fraction, %), respectively, to a solution treatment held for 2h at 850 °C and then water quenched the material. (Safdel, 2017) (Jiang, 2013b)

Figure 4.33a shows the DSC charts evolution with solution heat treatment temperature. There are two characteristic features that change with increasing temperature: (1) the type of transformation changes from overlapped curves at cooling and heating (800 °C/10 min and 800 °C/120 min samples) through one step (at 850 °C) and back to overlapped curves at cooling and heating (900 and 950 °C/120 min); (2) there are shifts in peak positions and in the temperatures where transformations start and finish. However, 850, 900 and 950 °C/120 min, show similar peak temperature. In addition, decreasing transformation start temperatures are observed as a result of the increase of the heat solution treatment temperature. Figure 4.33b shows all temperatures of distinct DSC peaks ('peak temperatures') observed in Figure 4.33a.

On cooling from the B2-regime, DSC curves of the heat-treated samples show the following features: (1) the temperature where the transformation starts is higher at 800 °C/120 min and decrease for 850, 900 and 950 °C/120 min solution heat treated samples. (2) The position of the DSC peak on cooling for the 800 °C/120 min sample is at the highest temperature. (3) The transformation peak temperatures for the 850, 900 and 950 °C/120 min samples have two common characteristics: for these solution heat treatment temperatures the peak temperatures on cooling and heating are very similar.

Apparently, for the solution heat treatment at 800 °C increasing the soaking time from 10 min to 120 min slightly increased the M_p .

Increasing the solution heat treatment from 800 to 850 °C (for 120 min soaking time) significantly decreases M_p ; further increase of the solution heat treatment does not change M_p significantly. On the other hand, A_p temperature is significantly reduced when the soaking time for 800 °C is increased from 10 to 120 min; but, for 120 min soaking time, increasing the annealing temperature from 850 to 950 °C does not change A_p temperature significantly.

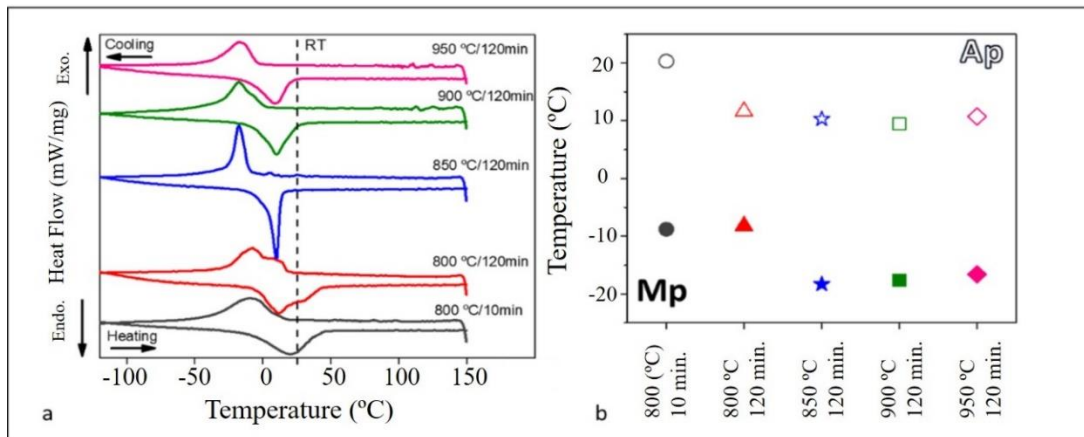


Figure 4.33 – a) DSC curves on cooling from the B2 regime and DSC curves on heating from the B19'. The five DSC curves show the influence of solution heat treatment. b) Peak temperatures - Mp cooling and Ap heating.

Figure 4.34 shows the Debye–Scherrer rings that were recorded for the periphery and the center region, which allows for visualization of the phases present.

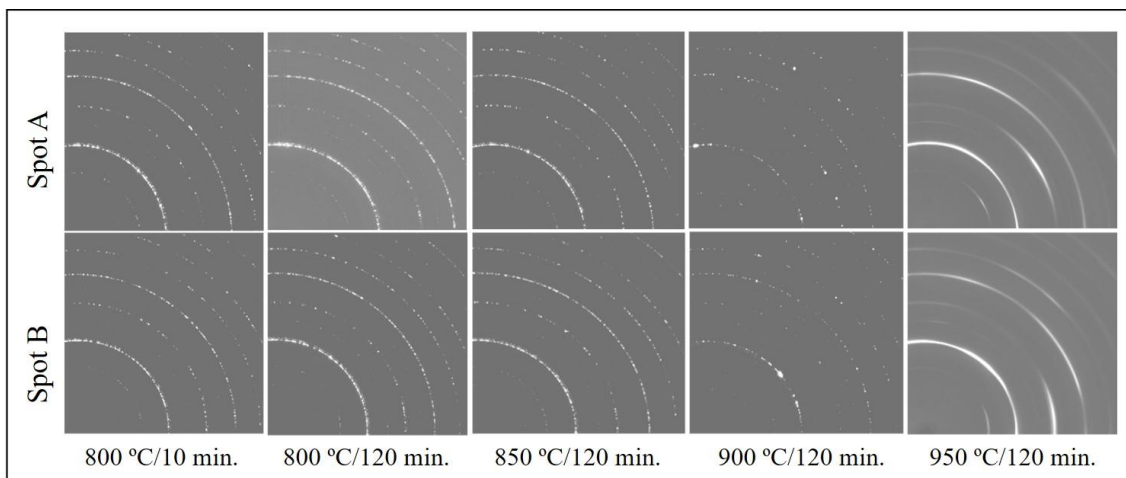


Figure 4.34 - Debye–Scherrer diffraction rings at the outer (A) and inner (B) of the mapped area presented in Figure 3 for each sample (800 °C/10 min, 800 °C/120 min, 850 °C/120 min, 900 °C/120 min and 950 °C/120 min).

Diffraction patterns of the 0 to 360° integration the Debye–Scherrer rings for A and B spots of all samples are presented in Figure 4.35. The cartesian and 3d plots of the Debye–Scherrer rings integrated along all azimuthal angle φ (from 0 to 360° in 1° bins) versus 2θ are shown in Figure 4.36.

Indexing of the diffraction patterns shows that in both spots (A and B) for all the samples the Ti_4Ni_2O are present as well as for NiTi_1_1F_1h sample (Figure 4.34).

This becomes evident analyzing the cartesian plotting of the intensity for different azimuthal angles versus 2θ (Figure 4.35). Examining the A and B spots do not show a significant difference between both regions.

At 800 °C/10 min, 800 °C/120 min and 850 °C/120 min, it is possible to observe the Ni_4Ti_3 precipitate. For the heat solution treatment temperature 900 °C, Ni_4Ti_3 precipitates are not evident.

In Figure 4.35, 800 °C/10 min, 800 °C/120 min and 850 °C/120 min samples show similar characteristics. Although the samples are mainly austenitic, small amounts of R-phase are detected in the diffraction pattern, for the measurement at room temperature.

For 800 °C/10 min, 800 °C/120 min and 850 °C/120 min samples, there is no difference in $(110)_{B2}$ peak along the azimuthal angles. The A and B spots for these samples do not show a significant difference between both regions.

The 900 °C/120 min sample is fully austenitic without evidence of the Ni_4Ti_3 precipitate (Figure 4.35). Again, this sample Figure 4.35 does not show a significant difference between both regions (A and B spots).

Sample 950 °C/120 min is more complex to analyze. This condition shows the fully austenitic matrix, without precipitates as well as for 900 °C/120 min sample (Figure 4.35). There is an increase in the intensity of the $(110)_{B2}$ peak and it is evident that the austenite peak shifts to smaller 2θ angles, corresponding to larger d-spacing. This can be explained by the higher temperature of treatment.

On the other hand, Figure 4.36 shows distinct B2 spots along the azimuthal angles. This indicates an evident growth of the grain.

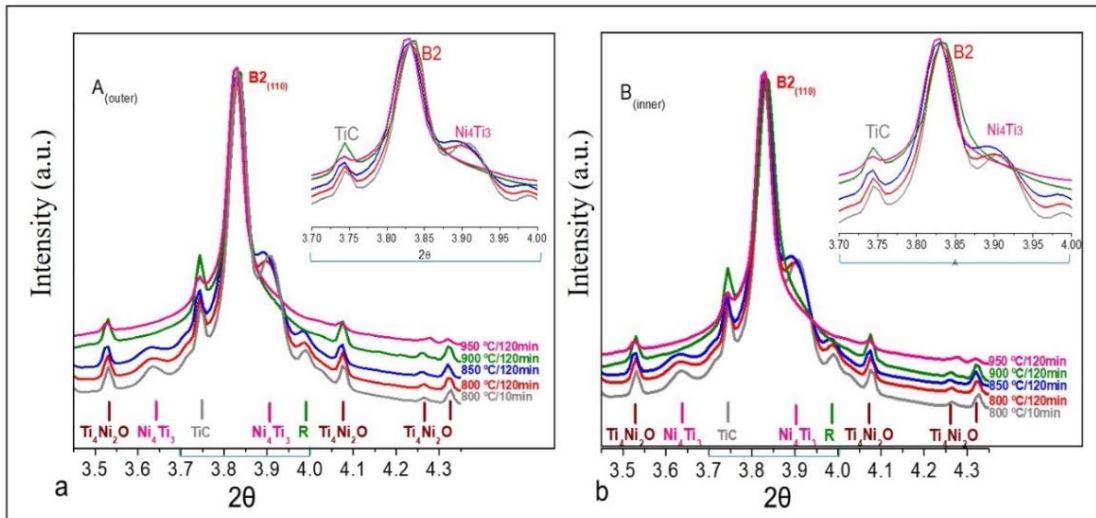


Figure 4.35 – a) outer (A) b) (B) inner – Sequence of XRD line diagrams at different solution heat treatment obtained by the integration of the diffraction patterns recorded at room temperature.

According to the presented results, it is possible to observe that the solution heat treatments 800 °C/10 min and 800 °C/120 min do not show significant differences between them. The solution heat treatment at 800 and 850 °C/120 min present the Ni₄Ti₃ precipitate after cooling to room temperature, while the solution heat treatment at 900 and 950 °C/120 min do not present. On the other hand, the solution heat treatment at 900 and 950 °C/120 min promote a grain growth. This can be observed in Debye–Scherrer rings (Figure 4.35): the rings show many discontinuities and isolated spots of very high intensities, as shown in Figure 4.36, where the intensity versus 2θ is plotted as a function of the azimuthal angle (φ).

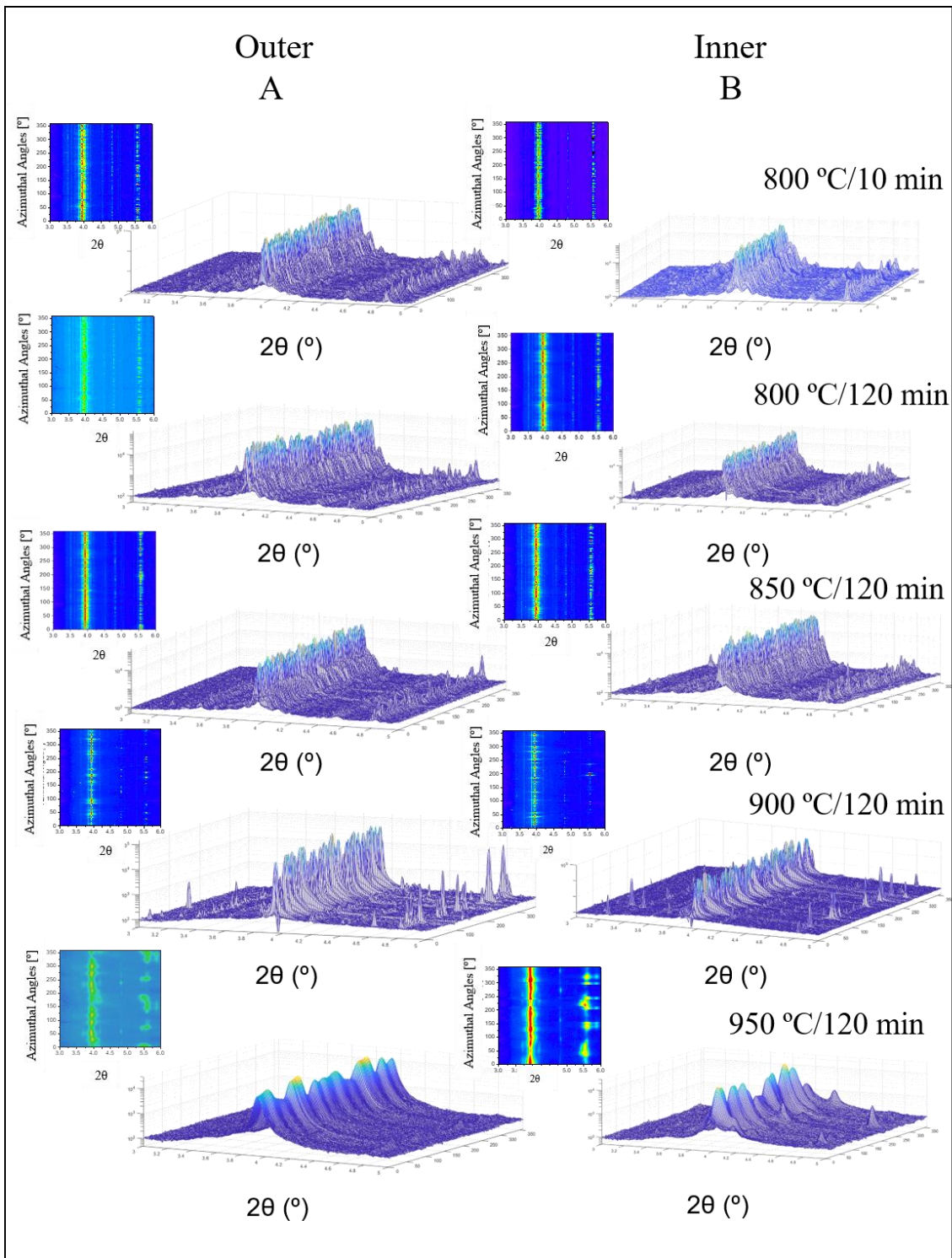


Figure 4.36 – Cartesian and 3d plots transform of Debye–Scherrer diffraction rings (azimuthal angles) vs. 2θ for A and B spots for each heat-treated sample.

The optical micrographs (Figure 4.37) show the difference on the grain size (Table 4.4): grain size increases when the temperature of the heat treatment increases. In the sample heat treated at 950 °C it is evident the grain growth, as shown by the XRD results.

Table 4.4 – Average of the Grain Size of the heat solution treated samples.
(ASTM E-112-96, 2000)

Sample	(μm)
800 °C/10 min	38.4
800 °C/120 min	41.4
850 °C/120 min	46.0
900 °C/120 min	61.3
950 °C/120 min	93.3

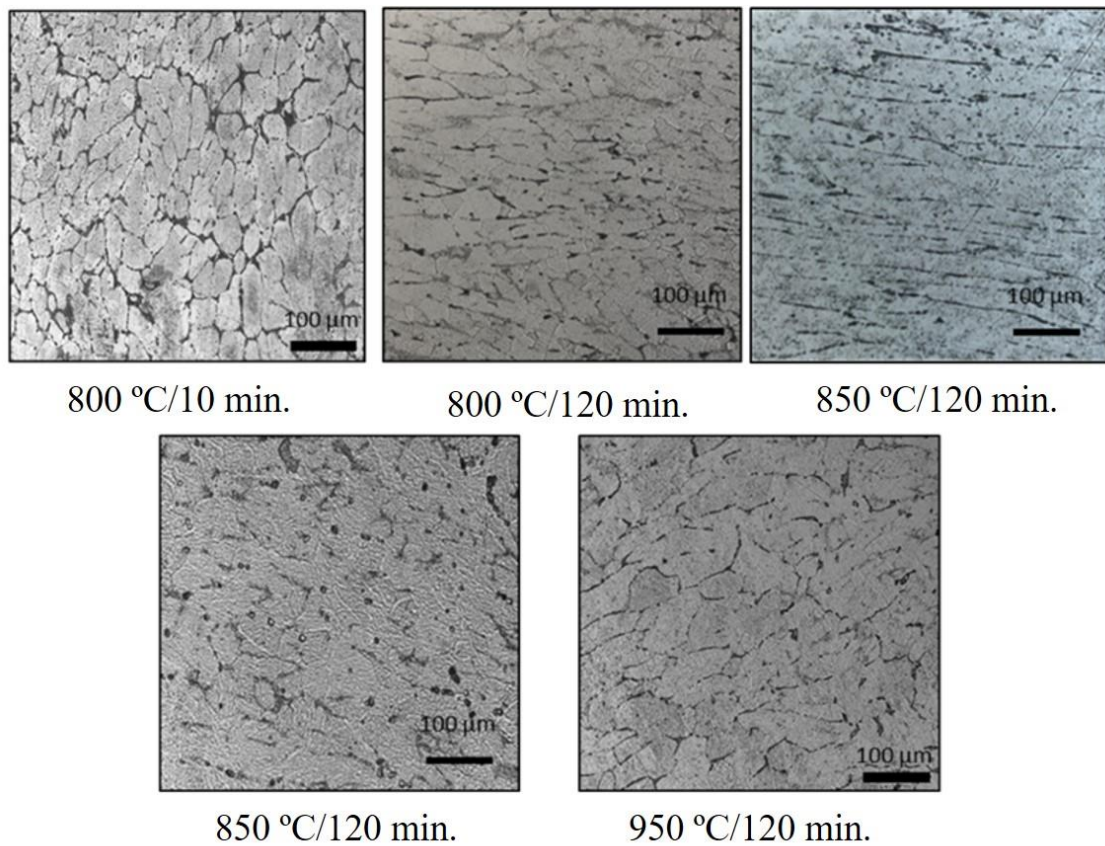


Figure 4.37 - Microstructure of the specimens submitted to solution heat treatment.

As 800 °C/10 min and 800 °C/120 min samples show the highest transformation temperatures at cooling and heating, little difference was observed between these samples. 850 °C/120 min sample shows the lower transformation temperatures. The 900 °C/120 min and 950 °C/120 min samples show the A_f close room temperature. All these conditions assure that the hot forging process will occur in the austenitic field.

Still, the 900 ° C/ 120 min and 950 ° C/120 min samples show significant grain growth which is not desired for the propose of this study.

Therefore, in the SR-XRD and DSC investigations, it is visible that for the solution heat treatment between forging steps, the temperature of the 850 °C is indicated.

Firstly, because the lower transformation temperature assures the stability of the austenite phase at room temperature. Secondly, at this condition, the grain growth is not observed. Finally, since the indicated hot processing temperature for these alloys is about 800 °C; the preliminary heat solution at 850 °C can assure that forging will be carried out at 800 °C, taking into account the transport of the material from the furnace to the forge. Based on these results 850 °C was applied in the test of heat treatment.

4.3.3. Intermediate Heat Treatment (850 °C during 15 minutes)

Heat treatment at 800 °C during 10 minutes and 800 °C during 120 minutes, showed a small difference between them. This study aimed to verify the influence of the heat treatment proposed (850 °C/15 min) on the phase transformation temperature.

The results are presented for the NiTi_1_1F_1h, NiTi_1_3F_3h and NiTi_1_5F_4h1c samples heat treated at 800 °C during 10 minutes followed by a comparison with the NiTi_1_1F_1h, NiTi_1_3F_3h and NiTi_1_5F_4h1c samples heat treated at 850 °C during 15 minutes. Both heat treatments were applied to investigate the microstructure after each deformation step before the next deformation step.

An important observation about this intermediate heat treatment is that for the heat treatment above 500 °C all the samples experimented the restoration/recrystallization phenomena. According to the partial phase diagram, based on Ni % at., for both temperatures (800 and 850 °C) that were applied, a fully homogenized matrix can be achieved (Figure 4.38).

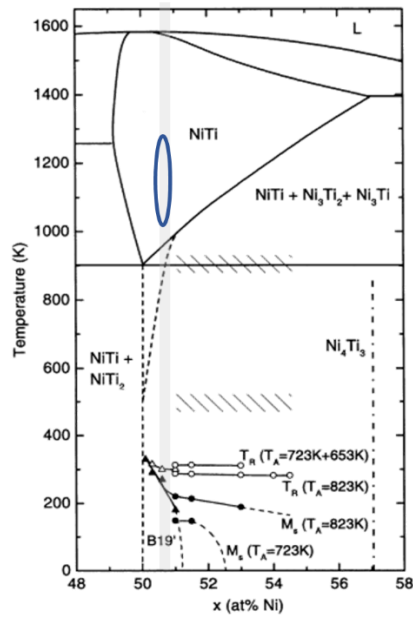


Figure 4.38 - Partial phase diagram of Ti-Ni system. (adapted from (Somsen, 1999))

Increasing from 10 minutes to 15 minutes was proposed because a long time in the furnace can promote a major surface oxide formation. The 10 minutes is not enough to assure the temperature homogenization on the material after hot forging steps (see, section 4.2.).

The transformation temperature does not change significantly for the different heat treatments. This indicates that the time of 15 minutes does not change the materials characteristics but ensures better homogenization, and a decrease of the transformation temperatures. Table 4.5. shows a comparison between transformation temperatures before and after heat treatment.

Table 4.5 - Phase transformation temperatures in degree Celsius for 1F_1h, 3F_3h and 5F_4h1c samples, before and after heat treatment (800 °C during 10 minutes and 850 °C during 15 minutes)

Sample	Cooling (°C)						Heating (°C)					
	M _s			M _f			A _s			A _f		
	Proc	800 °C 10 min	850 °C 15 min	Proc	800 °C 10 min	850 °C 15 min	Proc	800 °C 10 min	850 °C 15 min	Proc	800 °C 10 min	850 °C 15 min
1F_1h	7.2	8.9	6.2	-59.0	-35	-24	-15.1	-10.4	-0.4	27.5	28.5	25.5
3F_3h	13.5	1.0	-1.0	-81.6	-46	-35	-25.5	-23	-22	19.5	18	15.0
5F_4h1c	-16.8	-11.2	-13.0	-87.6	-34	-27	-16.5	-11.2	-0.4	8.7	10.4	7.5

4.3.4. Aging Treatment²

Ni-rich Ni-Ti alloys can exhibit shape memory and superelastic properties resulting from an austenite–martensite transformation under temperature change or applied stress. The properties of this transformation are strongly influenced by the presence of Ni₄Ti₃ precipitates in the B2 austenite matrix.

As the studied forging process aims the production of the alloy which is superelastic at room temperature, aging treatments in the final forging sample (6F_4h2c) were done, to verify their behavior after heat treatment.

For heat treatments at high temperatures, there is enough thermal energy to allow rapid diffusion of Ni and Ti atoms in the matrix. On the other hand, at a lower temperature nucleation rate is higher, but the diffusion coefficients are low. Both processes are equilibrated at intermediate temperatures (350 – 450 °C) to achieve maximum precipitation rates. As a consequence, the A_f increases due to the increased relative ratio of Ti/Ni in the matrix, as a consequence of the increasing Ni₄Ti₃ precipitation. The overall composition of the material does not change, but localized composition shifts induced by Ni-rich precipitates. (Pelton, 2000)

The size of the Ni₄Ti₃ precipitates increases with increasing aging temperature and aging time. The smaller Ni₄Ti₃ particles (e.g, less than about 100 nm) are coherent with the B2 austenite matrix. As mentioned previously, the presence of these precipitates can promote the R-phase formation. Therefore, the occurrence of two-stage phase transformation of B2↔R↔B19' is considered to be a consequence of the aging Ni-rich Ni-Ti SMA. (Jiang, 2015)

In order to assess which is the best temperature for the aging treatment, the thermophysical characteristics of the alloy were studied after cold deformation followed by a comparative aging treatment at 350 °C, 400 °C and 450 °C for 30 minutes.

² The below results (section 4.3.4) were already published in a paper in the *Ciência e Tecnologia dos Materiais*, entitled Influence of ageing treatment on the thermophysical characteristics and mechanical properties of forging wire Ni-rich NiTi alloy for superelastic applications (Rodrigues *et al.* 2017b).

Figure 4.39 shows the DSC curves for the samples: NiTi_1_6F_4h2c and NiTi_1_6F_4h2c aged at 350, 400 and 450 °C during 30 min. Table 4.6 shows the values of the A_f temperatures for the different conditions tested on this work.

Liu *et al.* (1997), reported that the transformation temperature could be increased by aging between 325 and 375 °C, because the internal elastic stress fields created during the precipitation process, inside the parent phase, affect the transformation temperature. (Liu, 1997) However, in this study the aging treatments of 400 and 450 °C are also favorable for such precipitate formation. Without the precipitation, the A_f temperature would be reduced. Therefore, it is possible to verify that the A_f for the sample aged at 350 °C during 30 minutes is below room temperature.

The DSC curves of the 400 and 450 °C aging treatment show one broad endothermic peak revealing multiple-stages transformation (Figure 4.38). DSC curves show a similar behavior for the endothermic peak corresponding to the reverse phase transformation. In addition, the transformation temperature shifted to a higher temperature ($A_{f\ 400\ ^\circ\text{C}} = 37.5\ ^\circ\text{C}$ and $A_{f\ 450\ ^\circ\text{C}} = 39.6\ ^\circ\text{C}$). The smaller hysteresis suggests the R-phase presence. (Otsuka, 2005) (Jiang, 2015)

According to McCormick, *et al.* (1994), this broad peak is related to a multiple-stage transition behavior in Ni-rich Ni-Ti alloy, which may appear on cooling and heating due to two separate martensitic transitions in separate regions of the grains (interior *versus* grain-boundary). Nevertheless, such local strain induced martensite would only affect microstructure adjacent to precipitates (McCormick, 1994) (Yeung, 2004). The aging results at 400 and 450 °C can be attributed to such multiple stage transition behavior.

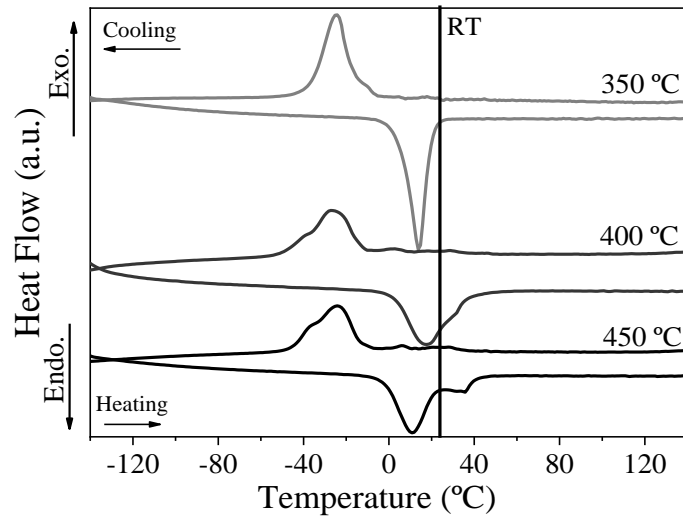


Figure 4.39 - DSC Curves of aging temperatures at 30 minutes soaking time: 350 °C, 400 °C and 450 °C.

The existence of R-phase in the sample heat treated at 400 °C during 30 minutes, as well as in the sample heat treated at 450 °C during 30 minutes, can again be justified by the presence of Ni_4Ti_3 precipitates. (Khalil-Allafi, 2002).

Additionally, the presence of these precipitates can be beneficial because precipitation-hardening increases the yield strength of austenite, which in turn contributes to better functional stability. The presence of Ni_4Ti_3 precipitates is more evident after heat treatment at 450 °C, as evidenced by broadening of the peak, on cooling and heating (Figure 4.39).

Table 4.6 – Values of austenitic transformation final temperature for the NiTi₆F₄h2c and NiTi_{1_6}F₄h2c aging treated samples, in Celsius degrees.

Samples	A_f (°C)
NiTi₆F₄h2c	20.2
350 °C/30 min	20.0
400 °C/30 min	37.5
450 °C/30 min	39.6

Thus, the increase of the aging temperature and time in the aging heat treatments performed, probably promoted increasing precipitation of Ni_4Ti_3 , thus decreasing Ni content and giving increased A_f temperature.

4.3.5. Thermomechanical Process Proposed (Rotary Forging Route)

The studied rotary forging process aimed to promote the material manufacturing with the most adequate functional properties, with an adequate chemical composition, followed by mechanical working, and heat treatment. The Ni-Ti alloys for orthodontic applications must have SME or SE at temperatures below the oral temperature.

After analyzing the results, some parameters were proposed to improve the rotary forging process. Figure 4.40 shows the rotary forging route proposed.

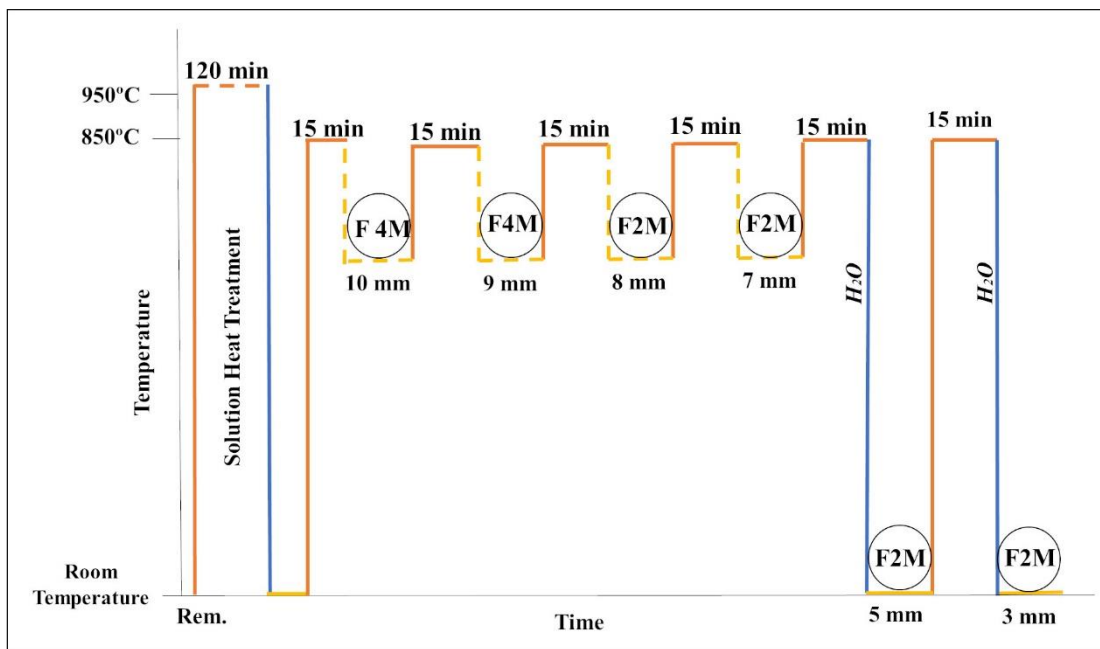


Figure 4.40 – Rotary forging route proposed with forging stages, temperature and time of the intercalated heat treatments and sample diameters.

The first topic observed was the heat treatment of the ingot before the first deformation. The solution heat treatment at 950 °C during 120 minutes, showed the better condition for this process step. The as remelted ingot, after this solution heat treatment, presents a fully austenitic matrix, i.e., without precipitates, and the phase transformation temperatures are below room temperature. Initiating the rotary forging process with a fully austenitic matrix will allow the control of the processing.

The reductions of the rod diameter will be obtained by the rotary forging process. This process requires to repeat the operation of heating in the furnace and transporting to the forge of the obtained rods several times. Thus, before each forging process the rods will

be heated to about 850 °C during 15 minutes. This parameter was chosen because it is necessary to ensure the homogenization of the material (hot and cold deformations). In addition, it ensures that the hot deformation is performed at a temperature close to 800 °C, considering the transport of the material from the furnace to the forge.

Ni-Ti SMAs products (e.g., bars, wires) are often finished by cold working to achieve dimensional control and enhanced surface quality. Heat treatment after cold working is necessary to minimize the effects of cold working and to restore the shape memory effect of SMAs. Therefore, in order to optimize the physical and mechanical properties of a Ni-Ti product and to achieve the desired properties, the material is cold worked and heat treated. In the presented results the aging treatment above 450 °C is suitable to promote the Ni₄Ti₃ precipitates formation.

4.4. Thermomechanical Process Simulation

This section shows the measurements that were performed to simulate the steps of the initial thermomechanical process (described in section 3.1.2 and illustrated in Figure 3.2) with *in-situ* deformation experiments (thermomechanical cycles – hot and cold steps). Based on the previous results, the measurements were performed using the NiTi_1_Rem sample solution heat treated (950 °C during 120 minutes), to understand the mechanical and structural behavior. To check the final properties a DSC test was performed.

4.4.1. Optimization of Hot and Cold Working Parameters Using Synchrotron Radiation

A deformation route was applied in order to observe the deformation parameters (time, temperature, stress and strain rate) during hot/cold working and aging treatment step. The thermomechanical cycles (under vacuum) performed are shown in Figure 4.41.

In the Figure 4.41, the hot deformations are represented by numbers 1, 2, 3 and 4 (green box) and the cold deformations are represented by numbers 5 and 6 (green box). The letter **a** (red box) represents the initial heating up to 850 °C before the first hot deformation. The letter **b** (blue box) represents the cooling before first cooling

deformation and after hot deformations. Letter **c** (red box) indicates the heating up to 500 °C after cold deformations. Letter **d** (yellow box) represents the aging treatment. Finally, the letter **e** (blue box) indicates the end of the thermomechanical measurement.

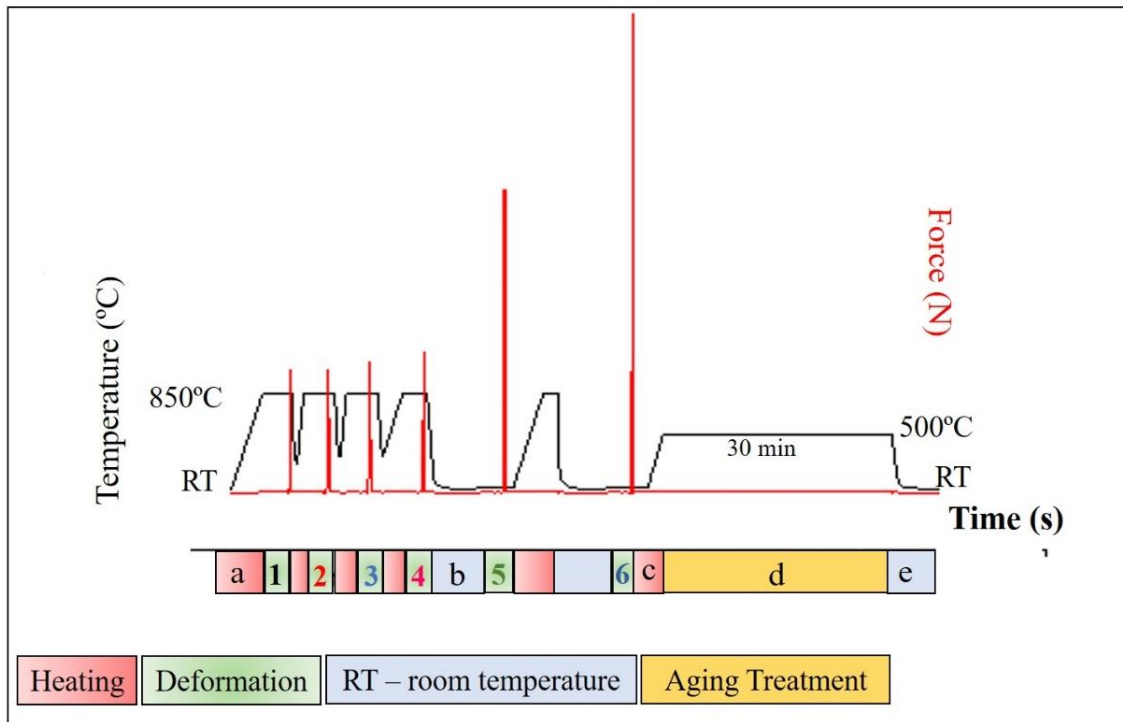


Figure 4.41 - Thermomechanical treatment simulation scheme applied with highlighted of the heating, deformations and aging treatment steps.

The initial sample (NiTi_1_Rem) was solution heat treated at 950 °C during 120 minutes, to obtain a homogeneous matrix, based on section 4.3.1 discussion.

Figure 4.42 depicts a sequence of the diffractograms of the heating up to 850 °C and *d*-spacing evolution (Figure 4.41a). In all the diffractograms sequence the material is fully austenitic. Due to heating it was evident that the austenite peak (110)_{B2} shifted to smaller 2θ angles, corresponding to larger *d*-spacing.

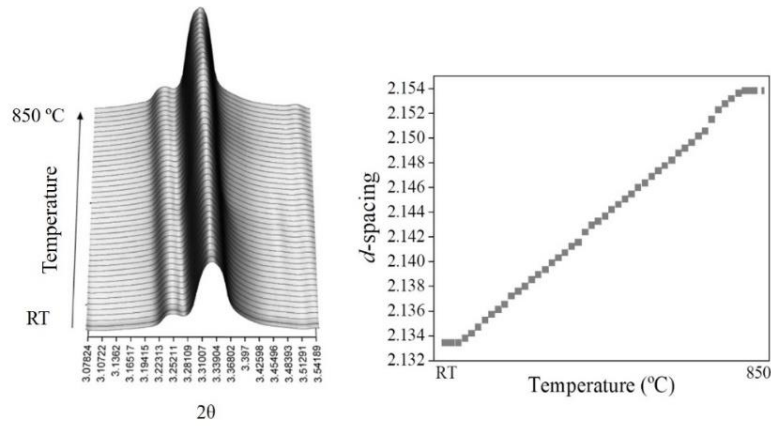


Figure 4.42 - SR - XRD patterns obtained during heating up to 850 °C and *d*-spacing evolution.

After heating up to 850 °C, the sample was deformed at high temperature (1, 2, 3 and 4 deformations) and at room temperature (5 and 6 deformations) with a strain rate of 10^{-3} s^{-1} . The total length change was 20%.

Flow curves obtained at different deformation conditions and work hardening rate analysis are shown in Figure 4.43. The following results were calculated in accordance with the methodology reported in the literature. (Mirzadeh, 2014) (Mirzadeh, 2009)(Mirzadeh, 2012) (Jiang, 2013) (Morakabati, 2011)

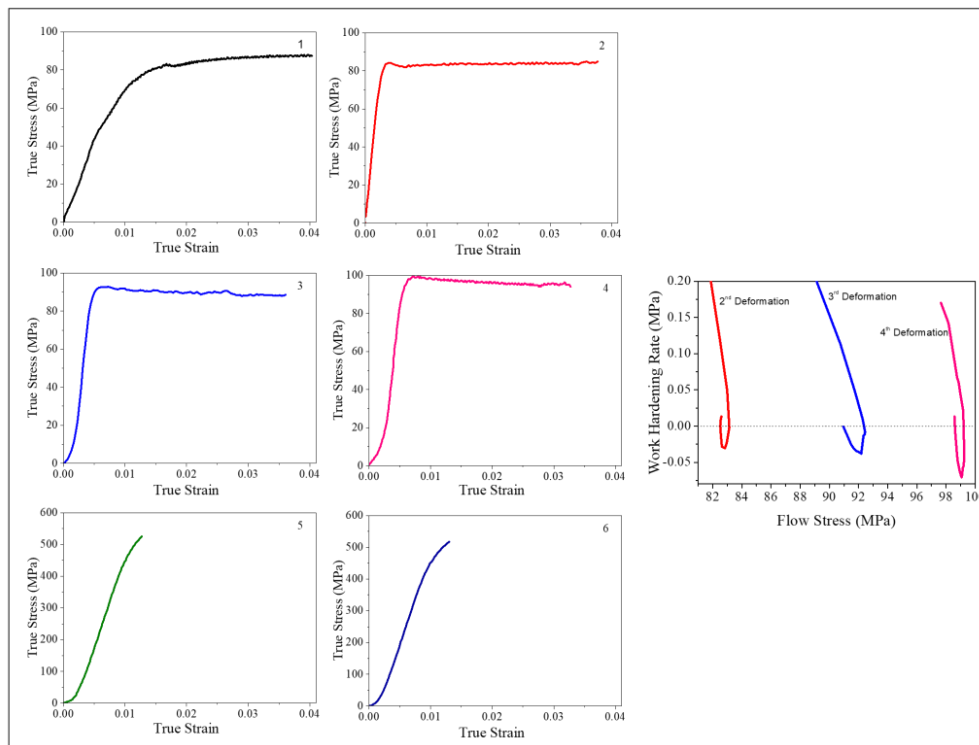


Figure 4.43 – Hot (1, 2, 3 and 4) and cold (5 and 6) true stress-true strain curves and work hardening rate analysis (2nd, 3rd and 4th deformations).

The hot deformations curves (1, 2, 3 and 4) exhibit typical single peak DRX (dynamic recrystallization) behavior with a broad peak followed by a gradual fall toward a steady state stress.

In the single peak behavior, it is known that the new cycles of DRX initiate before completion of the first cycle. After the first DRX cycle conclusion, the following DRX cycles are incomplete. The flow curve will represent the averaged flow stress of grains at different stages of recrystallization in the form of a broad peak along the deformation (Mirzadeh, 2014). This behavior is more evident in curves 2, 3 and 4. The curve 1 has an initial component of the deformation stabilization due to the gradual pushrods contact; for this reason, the discussion about its behavior will be not focused.

Figure 4.43 (2, 3 and 4) also show the flow stresses increase with increasing deformation at the same deformation temperature, which reveals that Ni-Ti alloy is sensitive to the increasing deformation at elevated temperatures (850 °C). This can be attributed to the increased rate of restoration processes and decreasing work hardening rate. At critical deformation degree, work-hardening leads to the rapid increase of stress, after this moment, the dynamic recrystallization leads to prevailing softening over hardening, so the flow stress of Ni-Ti SMA decreases. (Mirzadeh, 2014)

It has been shown that the onset of DRX can also be detected from inflections in plots of the strain hardening rate *versus* stress. Therefore, the onset of DRX was detected from the inflections in plots of the work hardening rate *versus* true stress (before the peak point of flow curves). These observations are considered as signs for the occurrence of DRX. In each curve of Figure 4.43, the work hardening rate decreases with the flow stress.

The curves gradually change to another linear line and then drop toward work hardening rate = 0 at peak stress. Afterwards, the work hardening rate becomes negative and then again tends to work hardening rate = 0 at steady-state stress. These results are consistent with the general DRX behavior. (Mirzadeh, 2009)(Mirzadeh, 2012)(Mirzadeh, 2014)

For these deformation parameters (850 °C and 10^{-3} s^{-1}), the critical stress increases from 82.87 MPa (2nd deformation), to 92.58 MPa (3rd deformation) and finally to 98.85 MPa (4th deformation). These values are in agreement with other studies with similar deformation conditions. (Jiang, 2013) (Morakabati, 2011)

The cold deformations curves (5 and 6) exhibit typical hardening behavior. Decreasing the deformation temperature, the true stress values increase. As it is seen the stress plateau region corresponding to SIM formation cannot be distinguished. The material at these stages showed a smaller deformation due to the measurement limitation. In these curves an elastic deformation of austenite as a parent phase only was observed. Safdel *et al.* (2017) reported a similar behavior in an alloy with 50.5 at %Ni during cold compression tests that were executed at 25 °C under the strain rate of 0.001 s⁻¹. However, this study showed a higher deformation with four stages: elastic deformation of austenite; initiation of SIM formation and plastic deformation of retained austenite; continuous SIM formation and elastic deformation of previous martensite; and the plastic deformation of martensite. (Safdel, 2017)

Hence, the dynamic recovery or dynamic recrystallization of Ni-Ti alloy is unable to be evaluated only by the true stress-true strain curves and structural analysis is a necessary approach. The evolution of FWHM, *d*-spacing and the superimposition of the diffractograms obtained during the deformations are shown in Figure 4.44.

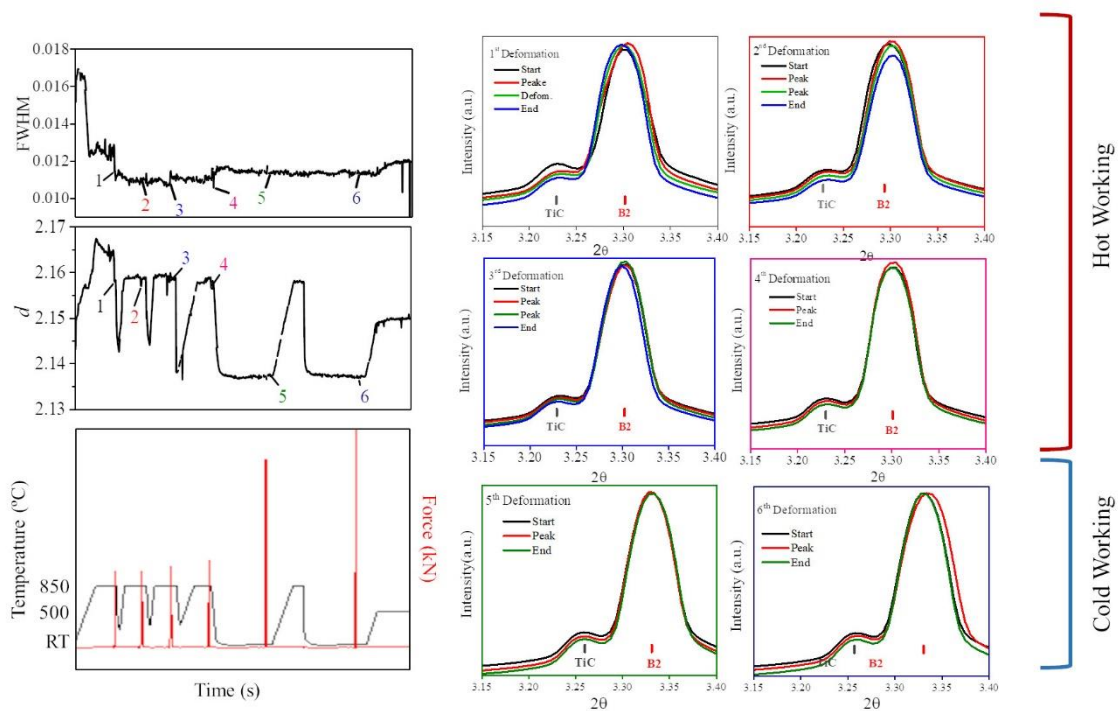


Figure 4.44 - FWHM, *d*-spacing and SR-XRD patterns of the hot and cold deformations during thermomechanical measurement with a strain rate of 10⁻³ s⁻¹.

In the superimposition of the diffractograms obtained during the deformations a clear distinction between the moment before, during and after deformation is noticed: while before and after deformations in 2θ is in the same position, the peak during the deformation is shifted to higher 2θ values, corresponding to smaller d -spacing due to the deformation performed. The shift of the austenite peak, which may be associated with the deformation performed, is marked by the red diffractogram. Each deformation is highlighted in Figure 4.44 by the corresponding numbers.

Analysis of $(110)_{B2}$ peak profiles indicated that FWHM is sensitive to the variation in microstructure and stress–strain accumulation in the material. During the deformations, the peak positions and FWHM vary significantly. The FWHM value is sensitive to the variation in microstructure and stress-strain accumulation in the material. Normally, an increase of stacking faults and the presence of deformation stress causes an increase of the FWHM. During the stress peak of deformation, the FWHM decreases. After deformation, the FWHM remained close to the last straining step, whereas the FWHM increases in the austenite indicating accommodation of strain. In summary, the presence of stress in the material causes an increase of the FWHM, while relaxation of stress decreases FWHM. (Vashista, 2012)

The superposition diffractograms of both cold deformations (5 and 6) depict the $(110)_{B2}$ peak in higher 2θ position, indicating the influence of the compressive deformation performed at room temperature. After last deformation, the material is fully austenitic.

The observation of Debye–Scherrer rings by the intensity *versus* 2θ is plotted as a function of the azimuthal angle (ϕ) (Figure 4.45). The evolution of the $(110)_{B2}$ peak along the deformations may be observed. The first deformation depicts discontinuities and isolated spots of very high intensities. From 2nd deformation to 6th deformation it is observed the homogenization of the peak intensities. This information is clear in Figure 4.46, where the cartesian plots (intensity *versus* 2θ are plotted as a function of the azimuthal angle (ϕ)) after each deformation. A texture evolution along the deformation may be also observed.

These deformations lead to texturing (crystallographic alignment) of the material. The texture has an influence on its mechanical properties as confirmed by the mechanical behavior (Figure 4.43) (Suresh, 2012). However, is not possible to define an exact texture by this measurement, because the deformation is not enough to allow this

appreciation. But for a qualitative observation it is possible to discuss some details. Increasing the deformation shows a trend to stabilize a deformation texture (Figure 4.46 - black line). The 1st deformation display a very weak texture and the texture is more strongly defined after 4th deformation and it remains until 6th deformation.

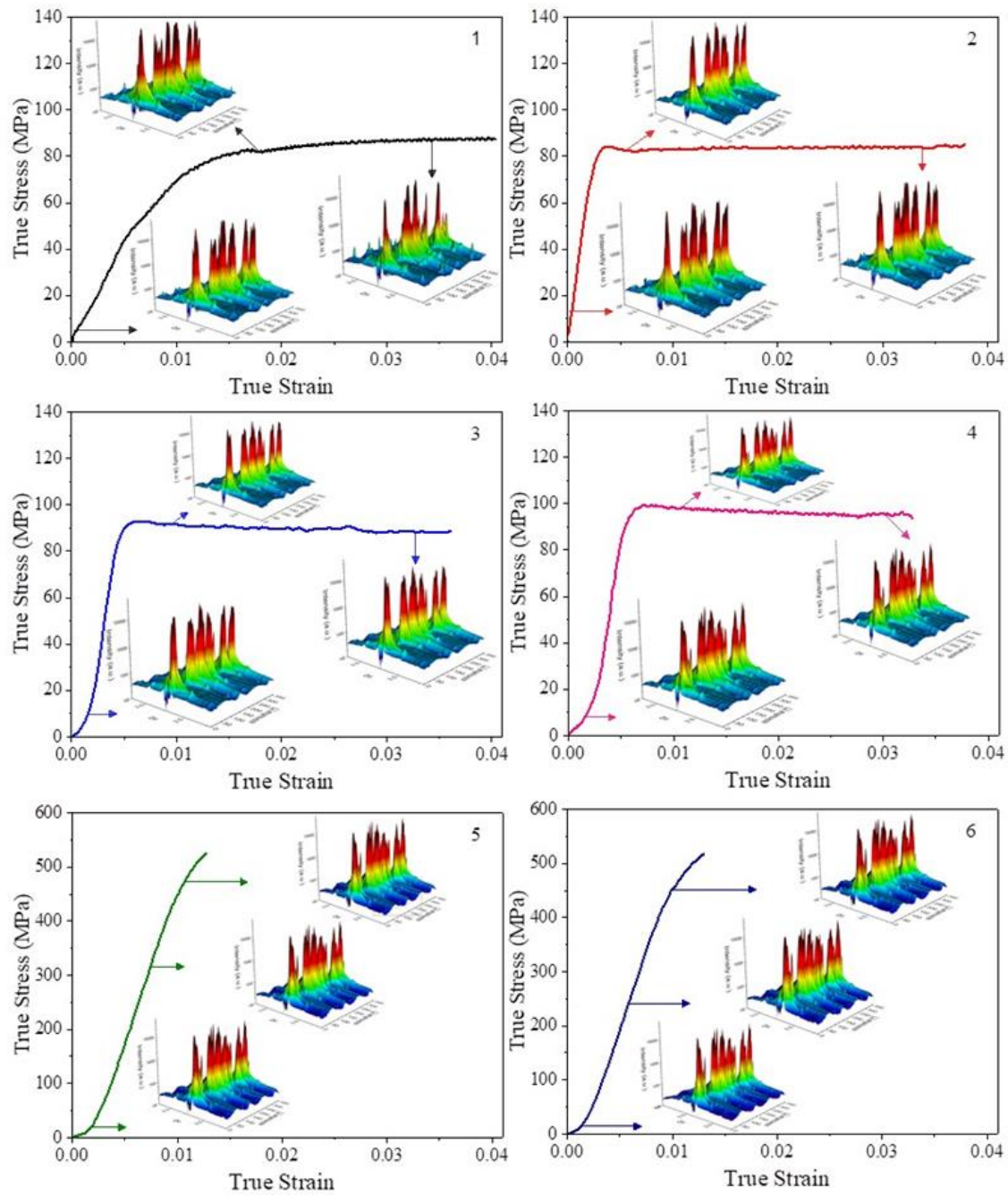


Figure 4.45 - 3D plots transform of Debye–Scherrer diffraction rings (azimuthal angles) vs. 2θ – before, peak and after each deformation (hot and cold).

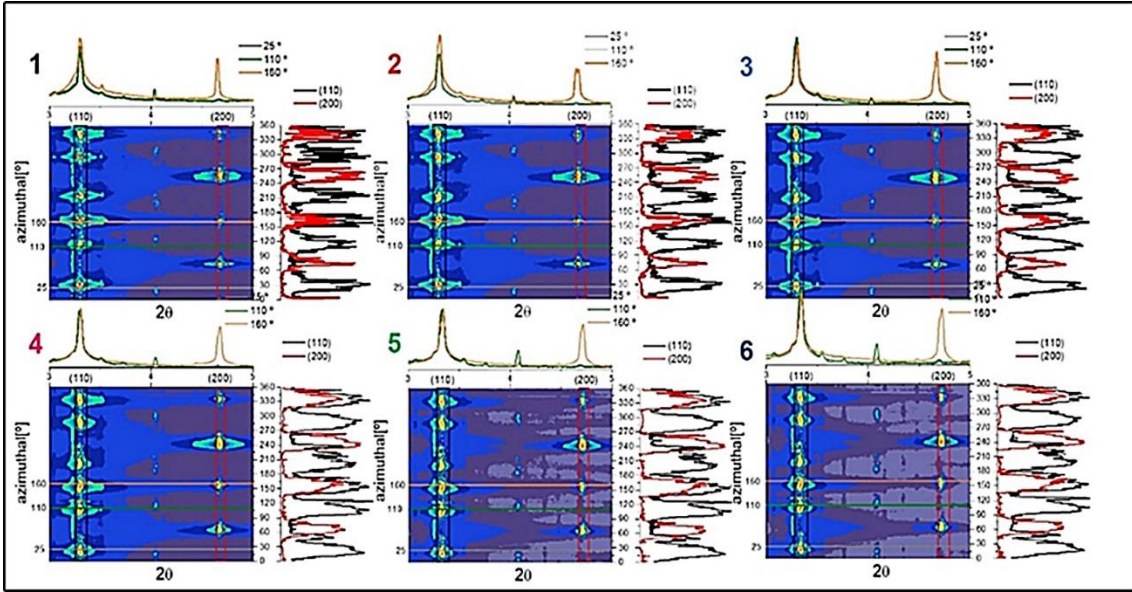


Figure 4.46 - Hot and cold deformations behavior and crystallographic orientation.

This study aims to process a material which displays a superelastic behavior at room temperature. In order to verify this behavior, the superposition of the diffractograms after hot deformations (Figure 4.41-b) and after cold deformations (Figure 4.41-c) are shown in Figure 4.47. These results illustrate that the material is fully austenitic for both situations at room temperature.

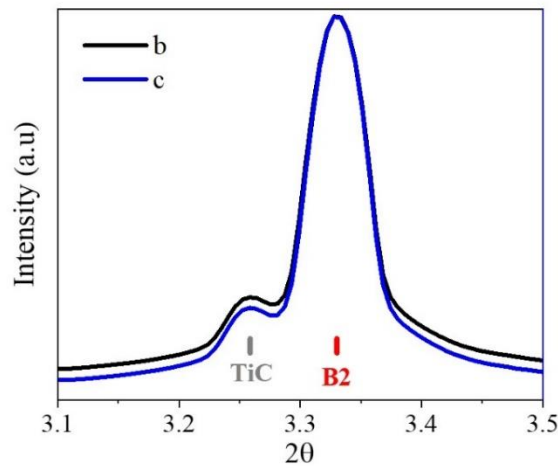


Figure 4.47 - SR-XRD patterns after hot deformations (b) and after cold deformations (c).

The cold deformation after hot deformation confirms that this step is important to assure a particular microstructure and an improvement of the functional properties. (Suzuki, 1998)(Habu,2009). However, it is known that the aging treatment may promote the metastable precipitates formation, such as Ni_4Ti_3 . It is also known that Ni_4Ti_3 is the first precipitate to occur, at lower temperatures and shorter permanence times.

According to previous results discussed in section 4.3.4, the temperature of 500 °C was chosen to test the aging treatment during this measurement test. Figure 4.48 shows the aging treatment evolution from 1 minute to 30 minutes.

In order to clarify the influence of the aging treatment on the of the Ni_4Ti_3 precipitates formation, the superposition of the diffractograms for each minute is shown in Figure 4.48. The aging time global view is shown in Figure 4.48 and a broadening of the $(110)_{\text{B}2}$ peak along the time can be noticed on the right-hand side of this peak. The peak observed on the right-hand side, corresponding to Ni_4Ti_3 and was indexed using the 00-39-1113 ICDD card.

The volume fraction of the Ni_4Ti_3 precipitates increased up to 20 minutes. However, after this time (from 21 to 30 minutes) the volume fraction did not show a significant change. This means that it is not necessary to perform the aging treatment for a long time to obtain the metastable precipitates formation. Thus, a short time of the aging treatment is enough to adjust the transformation temperature. Due to the occurrence of Ni-rich precipitates (Ni_4Ti_3), there is a Ni depletion in the surrounding matrix and a subsequent increase of the transformation temperature (Otsuka, 2005).

Therefore, the occurrence of two-stage phase transformation of $\text{B}2 \leftrightarrow \text{R} \leftrightarrow \text{B}19'$ is considered to be a consequence of the aging Ni-rich Ni-Ti SMA. (Jiang, 2015)

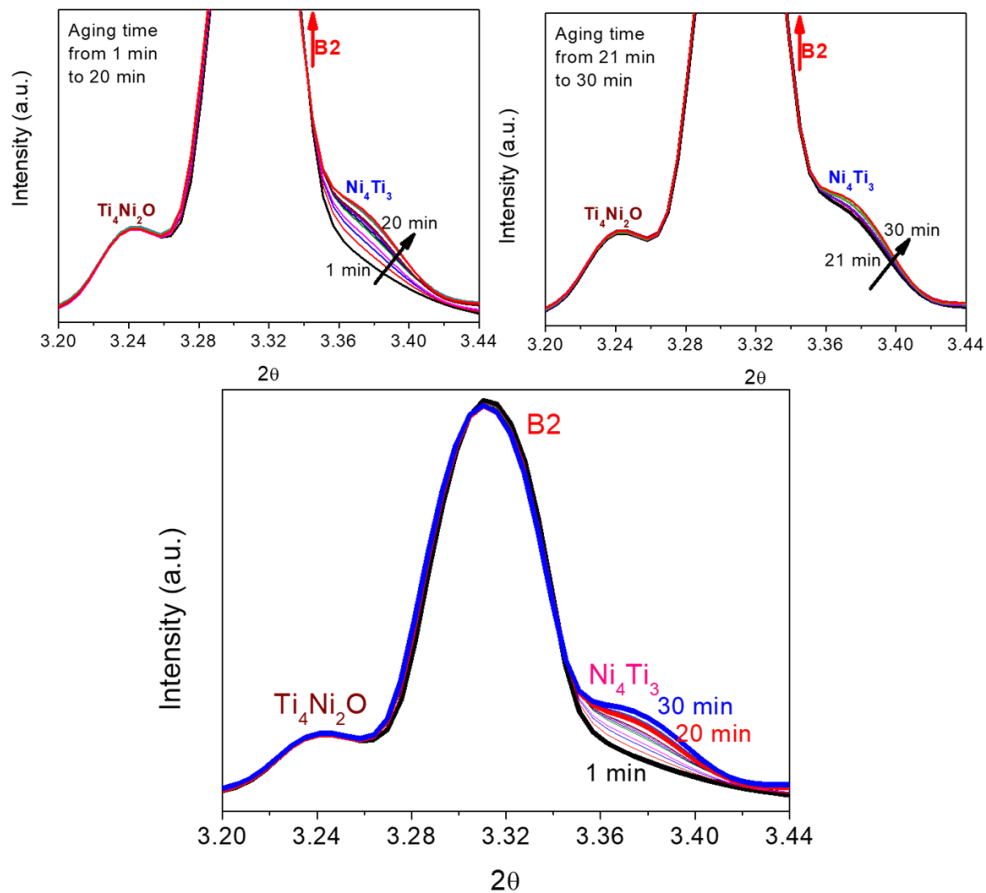


Figure 4.48 – Superposition of SR-XRD patterns of each minute during aging treatment at 500 °C during 30 minutes.

DSC measurement was used to investigate the phase transformation behavior of the NiTi₁ sample after thermomechanical measurement. As shown in Figure 4.49, one step phase transformation (B2 ↔ B19') was detected in solution heat treated condition sample (at 950 °C during 2h) on the cooling and heating. The transformation temperatures were below room temperature, because of the higher Ni content, as discussed previously (section 4.3.1). This confirms that the solution heat treatment is efficient to promote complete matrix homogenization. After thermomechanical test, R-phase was observed on the cooling curves, resulting in a two steps transformation (B2 ↔ R ↔ B19'). The R-phase transformation is mainly introduced by the Ni₄Ti₃ precipitates, as shown in Figure 4.50. On heating, the sample after thermomechanical simulation shows only one transformation peak, suggesting that B19' ↔ B2 took place in one single step. The transformation temperatures of the NiTi₁_Rem sample

(solution heat treated at 950 °C during 120 minutes) increased after the thermomechanical process applied ($A_f = 30$ °C).

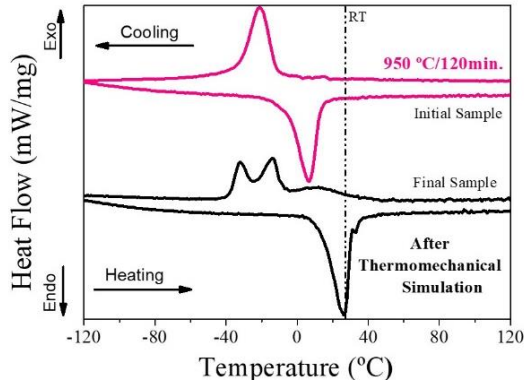


Figure 4.49 - DSC curves of the initial (NiTi₁_rem. Heat treated at 950 °C/120 min.) and final (after thermomechanical simulation) samples.

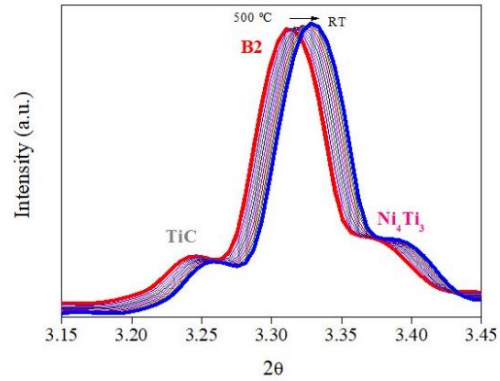


Figure 4.50 – Superposition of the SR-XRD patterns obtained during cooling after aging treatment at 500 °C during 30 min.

The proposed thermomechanical treatment combined with aging treatment provided enough conditions for the precipitation process, which decreased the Ni content on the matrix, increasing the transformation temperatures. In addition, the R phase observed at room temperature in the sample after thermomechanical simulation (DSC results - Figure 4.49 – black curves) was corroborated with the presence of Ni₄Ti₃ precipitates, as shown in Figure 4.50 through diffractograms superposition of the cooling to room temperature after aging treatment. The existing phases after the thermomechanical treatment are austenite and Ni₄Ti₃ (Figure 4.50).

4.4.2. Optimization of Hot Deformations with Different Strain Rate

Taking into consideration that the real deformation during forging process has a strain rate higher than 10^{-3}s^{-1} , other hot deformation conditions were tested. The strain rate of 10^{-1}s^{-1} at 850 °C (12% total length change) was applied in order to verify the occurrence of the recovery and recrystallization phenomena during deformations.

Flow curves obtained at different deformations and work hardening rate analysis are shown in Figure 4.51. The higher strain rate applied in this measurement resulted in less

defined curves. Due to small deformation, the strain rate applied during this measurement was too fast to obtain more data that could be used to discuss the results.

Anyway, the hot deformation curves (1, 2, 3 and 4) exhibit typical single peak DRX (dynamic recrystallization) behavior with a broad peak followed by a gradual fall of stress.

Higher strain rate also shows that the flow stresses increase with increasing deformation at the same deformation temperature. However, the 2nd deformation shows the opposite behavior. This can be explained by the deformation accommodated, due to the tantalum plate protection used during the deformation. This behavior was discussed previously during the results of the deformation with strain rate of 10^{-3}s^{-1} .

Again, DRX behavior was observed in all deformations. However, the work hardening rate behavior is more evident. This can be explained through the combination of the higher strain rate deformation and temperature. The curves behavior show that the strain rate was high enough to promote the single peak followed by the stress stabilization.

For these deformation parameters ($850\text{ }^{\circ}\text{C}$ and 10^{-1} s^{-1}) the critical stress increases from 170 MPa (1st deformation), to 150 MPa (2nd deformation), then to 189 MPa (3rd deformation) and finally to 220 MPa (4th deformation). These values are in agreement with other studies with similar deformation conditions. (Jiang, 2012)(Morakabati, 2011)

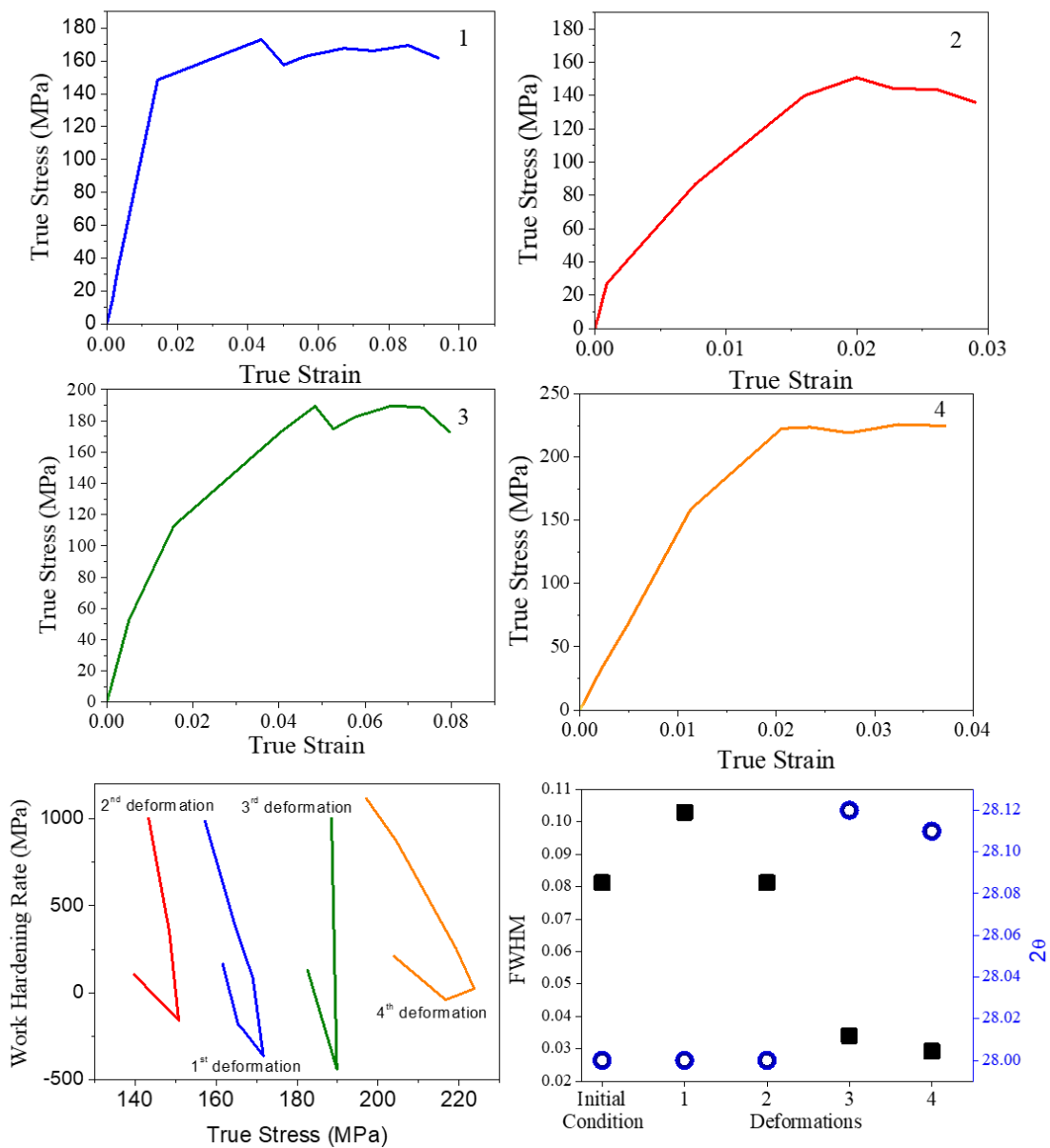


Figure 4.51 – NiTi₁_Rem. true stress-true strain curves of the hot deformations (at 850 °C) evolutions with strain rate of $10^{-1}s^{-1}$ and comparison between the FWHM and 2θ evolution.

Due to measurement limitation a simple analysis of the FWHM against 2θ was performed. After the 1st deformation, the FWHM increased. On the other hand, further deformation promoted a decrease of the FWHM due to recrystallization. It is known that the 2θ did not show a change after the deformations, but only during the deformation. The increasing deformation shifted the 2θ to higher angles, indicating a smaller d-spacing. This occurs due to the compressive deformation.

The cold deformations were not applied in this measurement.

The behavior after hot deformations was compared to the first measurement. At the first measurement (strain rate of 10^{-3} s^{-1}) after the hot deformations, the SR-XRD patterns show that the sample was fully austenitic at room temperature.

For this measurement (strain rate of 10^{-1} s^{-1}), the DSC test was performed to investigate the phase transformation.

As shown in Figure 4.52, one step phase transformation ($B2 \leftrightarrow B19'$) was detected in solution heat treated sample (at $950 \text{ }^\circ\text{C}$ during 2 h) on the cooling and heating, as well as in the solubilized sample after deformation (at strain rate of 10^{-3} s^{-1}). The transformation temperatures were below room temperature, because of the higher Ni content, as discussed previously (section 4.3.1). After thermomechanical test, the phase transformation shifted to lower temperatures. This indicates that the hot deformation promoted the dynamic recrystallization phenomenon occurrence and the homogenization of the matrix.

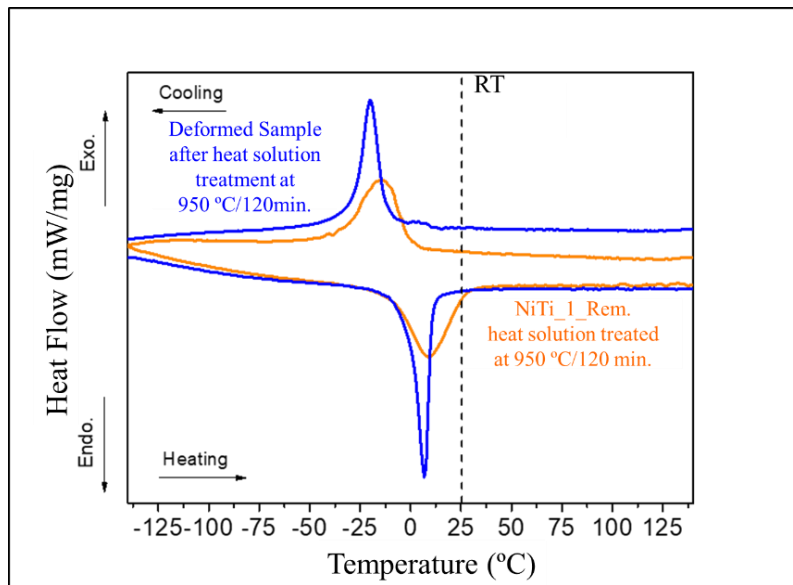


Figure 4.52 - DSC curves of the NiTi_1_Rem heat treated at $950 \text{ }^\circ\text{C}$ during 120 min and after hot deformations with strain rate of 10^{-1} s^{-1} .

Both strain rates applied in this study show that the dynamic recrystallization occurred. It is possible to highlight that the temperature of the $850 \text{ }^\circ\text{C}$ is suitable for hot deformations with these strain rates.

4.4.3. Aging Treatment Optimization

It has been recognized that the martensitic transformation behavior in the Ni-Ti SMAs is associated with the distribution of Ni_4Ti_3 particles, while the distribution behavior of Ni_4Ti_3 precipitates can be affected by several factors, including the heat treatment condition, initial Ni/Ti atomic ratio and the applied external stress.

The literature reported that the compression aging of single crystalline materials under a stress about 50 MPa promotes the Ni_4Ti_3 particles formation.

Ke *et al.* (2012), reported a study about the microstructure evolution of Ni_4Ti_3 precipitates during stress-free and stress-assisted aging of bi-crystalline Ni-Ti shape memory alloys with 51.5% at.Ni. The results showed that during stress-free aging, the Ni_4Ti_3 precipitates exhibited a heterogeneous distribution while stress-assisted aging could give rise to homogeneous distribution of the precipitates on the matrix (Ke, 2012).

Cong *et al.* (2014), reported a study of the thermomechanical properties and phase transformation behaviors of slightly Ni-rich Ni-Ti biomedical shape memory wires containing homogeneously distributed nanoscale precipitates induced by stress-assisted aging. The results showed that the size and volume fraction of precipitates increased with prolonged aging time (at 500 °C under 70 MPa) (Cong, 2014).

In order to understand the influence of the applied stress applied during aging treatment, the synchrotron radiation test was applied. The evolution of Ni_4Ti_3 precipitates during stress-assisted aging at 500 °C during 30 minutes under 70 MPa for NiTi_Rem sample was observed. These results were compared with the stress-free aging performed during the thermomechanical simulation (section 4.4.1.).

Figure 4.53 shows the broadening of the $(110)_{\text{B}_2}$ peak is still visible and other extra peaks, corresponding to Ni_4Ti_3 , were observed. All these peaks were indexed using the same 00-39-1113 ICDD card corresponding to Ni_4Ti_3 . The Ni_4Ti_3 intensity in the diffractograms is very low when compared to the observed austenite. Moreover, the most intense peak for this precipitate occurs very close to the $(110)_{\text{B}_2}$ peak and therefore is partially overlapped, as highlighted in the Figure 4.54.

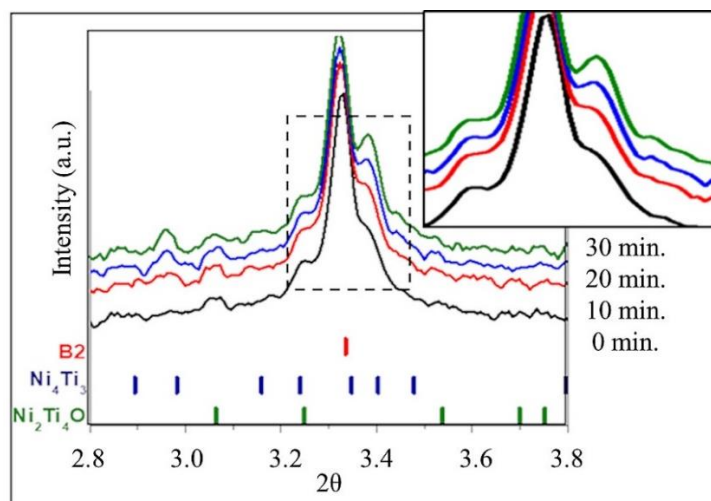


Figure 4.53 – Superposition of the SR-XRD patterns (0, 10, 20 and 30 minutes) during stress-assisted aging treatment at 500 °C during 30 min under 70 MPa.

The stress-free aging results show that the volume fraction of the Ni_4Ti_3 precipitates increases up to 15 minutes, while the stress-assisted aging results show that the volume fraction of the Ni_4Ti_3 precipitates increases up to 20 minutes.

However, the intensity of the Ni_4Ti_3 (close to $(110)_{\text{B2}}$ peak) is higher in the stress-assisted aging measurement compared to the stress-free aging measurement as shown at Figure 4.54.

The compression load that was applied during aging treatment improved the precipitation of Ni_4Ti_3 . This promotes an increase on the Ti/Ni ratio in Ni-Ti matrix. The Ni-content ratio in Ni-Ti matrix permits the control of the phase transformation temperature, which is desirable for developing shape memory alloys for medical application. Transformation temperatures were increased after aging, giving an excellent combination of shape memory effect and superelastic behavior at room/oral temperatures, as required by the orthodontic applications aimed for this material.

As mentioned previously, the size and volume fraction of the precipitates increase along the aging time. The external stress has an evident effect in the precipitation kinetics in Ni-Ti alloy.

However, stress-free aging shows that the volume fraction does not strongly change during aging. Equilibrium volume fractions are reached after short ageing times (15 min).

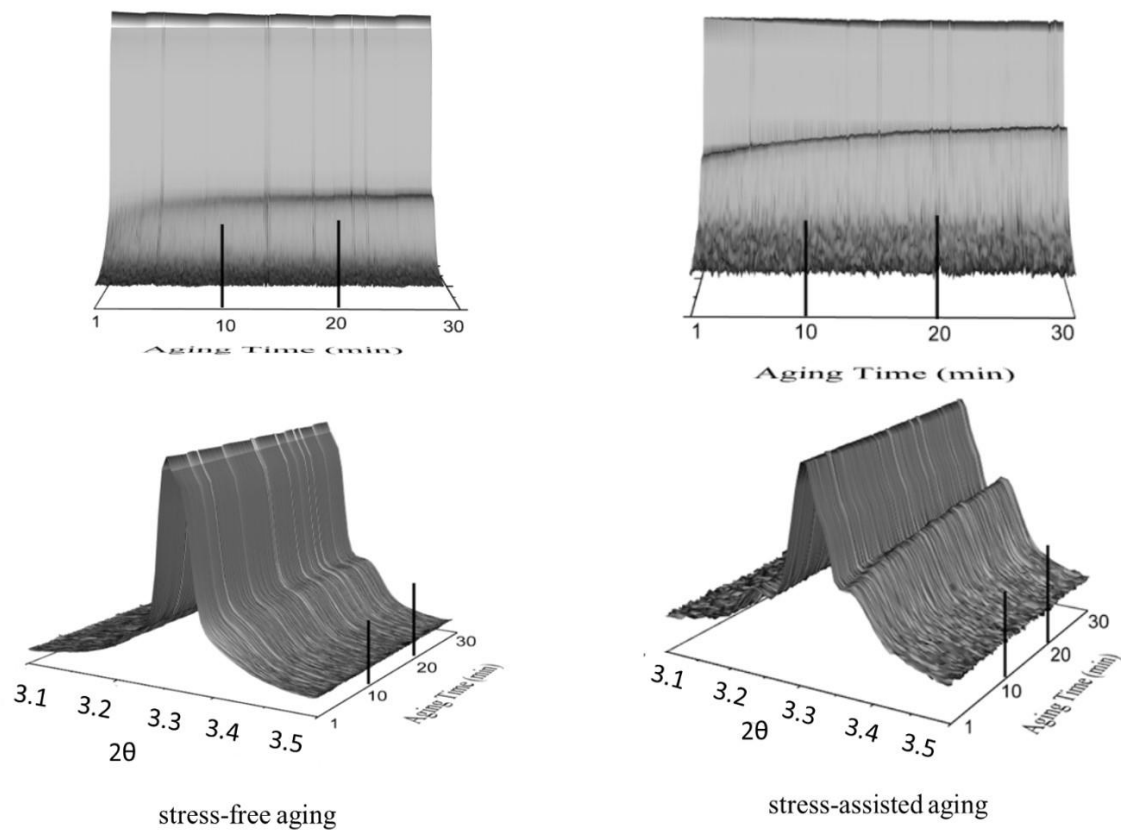


Figure 4.54 - Superposition diffractograms of the stress-free and stress-assisted aging treatment at 500 °C during 30 minutes.

After both aging treatments, R-phase was observed on the cooling curves. The stress-free aging may have promoted the heterogeneous distribution of the precipitation on the matrix, because it was observed in the DSC cooling curve a multi-stage phase transformation, while the stress-assisted aging may have induced the homogeneous distribution of the precipitation on the matrix resulting in a two steps transformation ($B2 \leftrightarrow R \leftrightarrow B19'$).

On heating, both samples showed only one transformation peak, suggesting that $B19' \leftrightarrow B2$ transformation took place in one single step. Moreover, the stress-assisted aging promoted a shift of the transformations temperature to slightly higher temperature (e.g., A_f temperature from 30 °C to 34 °C) most probably related to the higher fraction of Ni_4Ti_3 precipitation.

Figure 4.55 also shows that a rather substantial portion of the observed functional changes are in fact due to the diffusion-controlled mechanism of Ni_4Ti_3 precipitation even at stress-free aging. The generation of dislocations, the precipitation of Ni_4Ti_3 , and the interaction between these microstructural features, have a combined effect on the functional properties of Ni-Ti along the time.

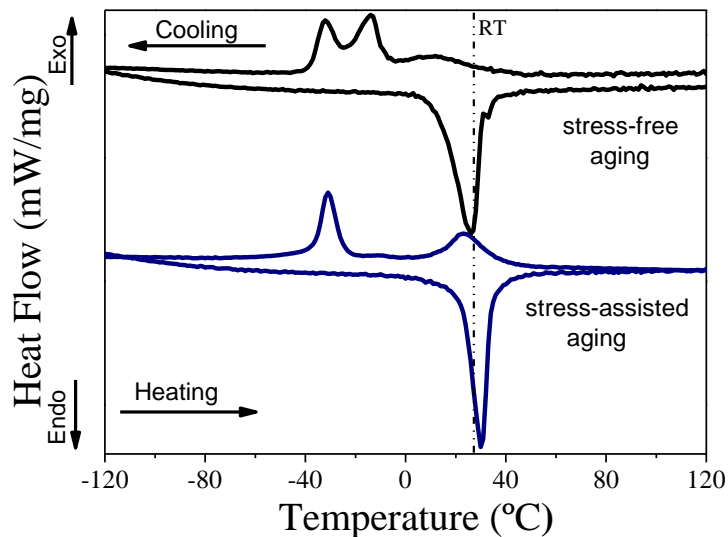


Figure 4.55 – DSC curves of the NiTi_1_Rem sample after stress-free and stress-assisted aging.

4.4.4. Thermomechanical Process Simulation Summary

In summary, a material with R-phase at room temperature and austenite phase close to oral temperature was achieved using the thermomechanical simulation proposed. The following are the major conclusions that can be drawn:

- The thermomechanical simulation indicated that the dynamic recrystallization occurred for both measurements, with strain rates of 10^{-3} and 10^{-1} s^{-1} at $850 \text{ }^\circ\text{C}$;
- The hot deformations at $850 \text{ }^\circ\text{C}$ combined with strain rates of 10^{-3} and 10^{-1} s^{-1} , show that these parameters were enough to identify the dynamic recrystallization phenomenon.
- The *in-situ* experiments of high temperature deformations using SR-XRD reflection mode (Grazing Incidence X-ray Diffraction) need to be improved. The amount of the data obtained during the test was not enough to investigate the details of dynamic recrystallization occurrence;

- From the deformation processing proposed according to NiTi_1_Rem experiment, the optimum intermediate heating temperature was confirmed as 850 °C, allowing a good hot-deformation condition even considering the temperature drop during transfer of the material from the furnace to the forging;
- After cold deformation, the material was still fully austenitic at room temperature;
- After aging at 500 °C, the material showed A_f temperature below oral temperature ($A_f = 30$ °C). This characteristic is desirable for the product that is required to be superelastic at the body temperature;
- The stress-assisted aging promoted the Ni_4Ti_3 formation. This aging treatment allows to obtain a more homogeneous precipitation. The control of this precipitation allows to adequate the design for the material in accordance with different applications;
- The thermomechanical route proposed may allow to produce a material with a superelastic behavior close to the body temperature, such as orthodontic archwires. The presence of the R-phase at room temperature is an interesting feature achieved, because this phase enables easier materials deformation followed by thermally induced shape memory effect at oral temperature.

4.5. Orthodontic Archwires

In this section the orthodontic archwires characterization results are discussed, in order to identify the most relevant properties of the product. Firstly, the difference between superelastic archwire and thermo-active archwire characteristics were investigated.

The superelastic archwires, are austenitic close to room temperature and undergo martensitic transformation by mechanical deformation, while the thermo-active archwires are partially martensitic and display a thermally induced shape memory effect and the transition temperatures $B19' \rightarrow B2$ occur close to oral temperature.

Thinking of the biological condition, the GAC developed a functionally graded Ni-Ti archwire and offers the BioForce archwires. These archwires apply low and gentle forces in the incisive teeth, increasing the forces across the premolars up to the molars teeth. This force begins at 0.8 N and increases up to 3 N, to provide the appropriate

force to each tooth, promoting the comfort of the patient. Thus, the BioForce archwire characterization was performed in order to understand their behavior. (Mullins, 1996)

Following this trend, the introduction of graded functionality in commercial superelastic orthodontic archwires was analyzed. There are few studies concerning the manufacturing of the functionally graded Ni-Ti orthodontic archwires reported in the literature. (Sevilla, 2008) (Sudershan, 2015)

In order to understand the behavior of the functional gradient along the archwire length, at room temperature, the discussion is carried on analyzing separately the archwires with different characteristics. Such separation is needed as the introduction of graded functionality was performed in commercial homogeneous superelastic archwire.

4.5.1. Superelastic orthodontic archwire

The A_f temperature is the most important temperature to determine from the clinical and manufacturers point of view, because at this temperature the alloy is stable and exhibits the final adequate shape for the application that is aimed.

The superelastic orthodontic archwire (Morelli SE) transformation temperatures were obtained by DSC analysis and are shown Figure 4.56. This sample is austenitic at room temperature ($A_f = 20$ °C). This result was similar to results reported by Spini *et al.* (2017) ($A_f = 19.82 \pm 1.57$ °C). This result indicates the capability of actuation via the superelastic effect during the orthodontic treatment. The A_f temperature being below oral temperature, there is no phase transformation. The transformation takes place before the archwire is positioned on the teeth (Ohara, 2016).

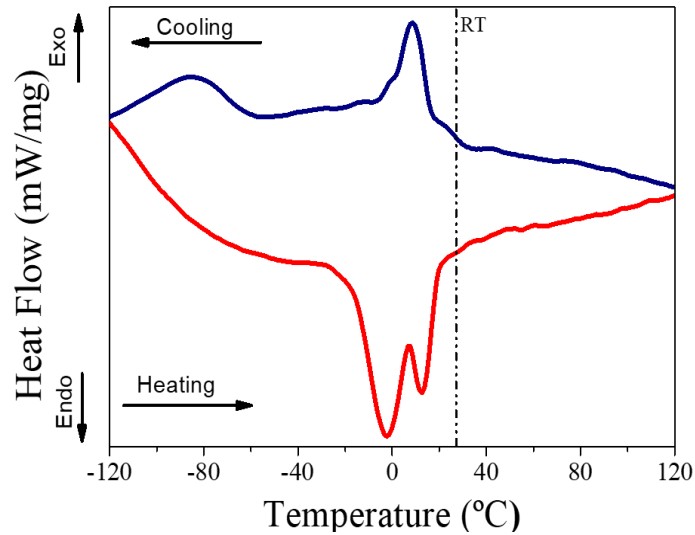


Figure 4.56 -DSC curves of the superelastic orthodontic archwire

The DSC result shows two transformation peaks on heating and on cooling, indicating the R phase presence ($B2 \leftrightarrow R \leftrightarrow B19'$). The SR-XRD results (Figure 4.57) show the intermediate Ni_4Ti_3 presence at room temperature, along the archwire length analyzed. This precipitate is common due to the orthodontic archwires manufacturing.

As discussed previously, the cold working is used to produce the final product shape. The final process of Ni-Ti SMA fabrication is shape memory treatment. To memorize the shape of the wire an intermediate heat treatment (between 400 and 500 °C) during 10 to 100 minutes (depending on the material) was performed. It is necessary a fastening of the wire in order not to change of the shape during the heat treatment. (Suzuki, 1998)

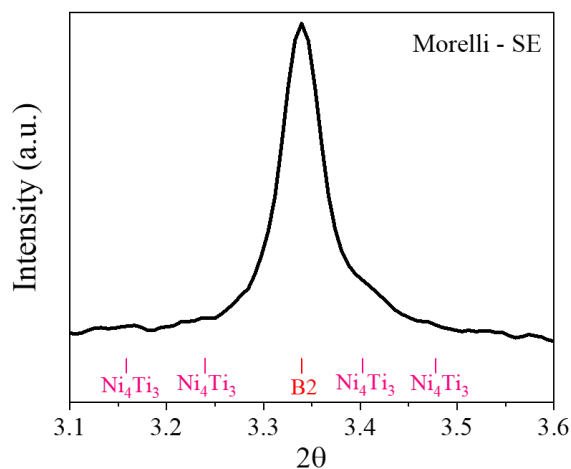


Figure 4.57 - SR-XRD pattern at room temperature of the superelastic archwire.

The load developed by these wires depends on the geometrical properties, the temperature and level of strain. Normally, this archwire generates constant forces in a wide range of displacement during the orthodontic treatment. It is worth remembering that this behavior occurred due to material chemical composition, and the thermomechanical process applied.

4.5.2. Thermo-active orthodontic archwire

Figure 4.58a depicts the DSC curve of the thermo-active archwire. Upon cooling a two-step transformation was observed. Upon heating, one step transformation is clearly observed. It can also be observed that the high temperature peaks in both cooling and heating ramps are symmetric. As the heat treatment fixed transformation temperatures, symmetrical and well-defined peaks would be expected.

The R-phase presence in thermo-active archwire at room temperature ($A_f = 18\text{ }^\circ\text{C}$) favors the thermally induced shape memory effect. In addition, the transition temperatures $B19' \rightarrow B2$ occur close to oral temperature ($\sim 34\text{ }^\circ\text{C}$).

Similar information can be obtained from thermomechanical analysis (TMA) using three-point bending mode (Figure 4.58b). The archwire clearly manifest the $B19' \rightarrow B2$ via both the DSC and TMA method. Also, A_s and A_f temperature values evaluated through TMA resulted higher than those measured via DSC (TMA – $A_s = 6.0\text{ }^\circ\text{C}$ and $A_f = 20.5\text{ }^\circ\text{C}$ and DSC - $A_s = 7.3\text{ }^\circ\text{C}$ and $A_f = 17.7\text{ }^\circ\text{C}$). The difference between these results can be explained by technique limitation. However, the difference between these values in practice has no significant difference. It can be observed that the variation of the length is consistent with the transition temperature range. This means that transformations from martensite to austenite are occurring at oral temperature and the superelastic behavior is reached. Such verifications are in line with what was observed from the DSC measurements.

Spini *et al.* (2014), reported the A_f ($20.39\text{ }^\circ\text{C}$) of the same thermo-active archwire was close to room temperature and lower than the oral temperature, being completely in an austenitic phase (greater rigidity) for clinical applications.

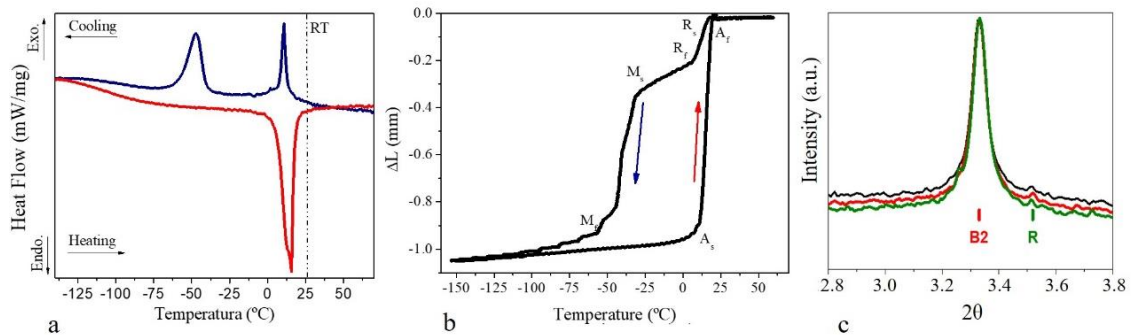


Figure 4.58 - DSC curves, dilatometry measurement curve and SR-XRD patterns at room temperature of the thermo - active archwire.

From the DSC and TMA measurements presented previously it can be inferred that the R-phase is present at room temperature. Both these techniques are not able to confirm the exact phase that is present at room temperature. As such, to obtain this information the three diffractograms of different regions along the archwire length are presented in Figure 4.58c. All the regions show the presence of B2 and R-phase. The SR-XRD results confirm the DSC and TMA results.

Namely, this archwire, with R-phase presence at room temperature, show an easier way to position it on the tooth. In contrast to this, the mouth environment causes the phase to change to austenite, increasing the force applied to the tooth during the orthodontic treatment (with the increasing temperature).

4.5.3. Ni-Ti orthodontic archwires with graded actuating forces

Three sections (Incisive - S01, Premolar - S02 and Molar - S03) of the Ni-Ti orthodontic archwires with graded actuating forces (Ni-Ti orthodontic Archwire – BioForce Dentsply GAC International, Inc., Central Islip, NY, USA) were investigated, to provide a better understanding of their functional behavior, as shown in Figure 4.59.

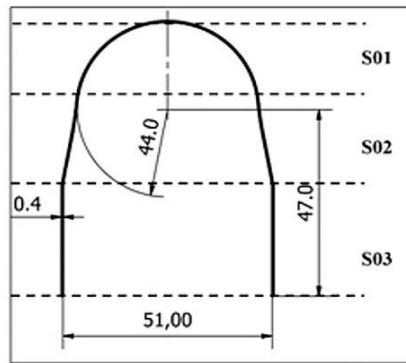


Figure 4.59 - Scheme of the sections S01, S02, S03 of the studied orthodontic archwire. Dimensions in mm.

Figure 4.60 depicts the DSC curves of the three sections. The phase transformation temperatures are shown in Table 4.7.

The S03 shows an A_f near room temperature while S01 and S02 segments have slightly transformation temperatures above that, but closer to oral temperature (~ 34 °C); so, all the curves on heating presented A_f temperatures lower than 37 °C (human body temperature), indicating the capability of actuation via the superelastic effect during orthodontic treatment.

The DSC results show a two-step transformation during the cooling, suggesting that $B2 \leftrightarrow R$ and $R \leftrightarrow B19'$ transformation occurred. For all archwire segments, the presence of intermediate R-phase is in agreement with other studies. (Bradley, 1996) (Sudershan, 2015)

On heating, S01 and S02 segments show only one transformation peak, suggesting that $B19' \leftrightarrow B2$ transformation took place in one single step. S03 heating curve shows a peak on the onset side which would indicate the presence of the R-phase.

Typically, this orthodontic archwire presents A_f temperatures close to oral temperature, thus allowing the austenitic transformation to occur as the temperature is increased from room temperature to oral temperature.

Due to these characteristics, a DSC analysis was performed in the range of 5 to 40 °C (Figure 4.61) to observe the $B2 \leftrightarrow R$ -phase transformation.

Other studies (Nespoli, 2015) (Brantley, 2003) used DSC measurements to show the R-phase transition. They observed the broadening of the heating peak and expected a

mixture of the phases (B2 - R - B19') for archwire segments. At human body temperature (37 °C), however, all the wire segments are fully austenitic. For all archwire segments, cooling curves show the presence of intermediate R-phase. (Brantley, 2001) (Bradley, 1996)

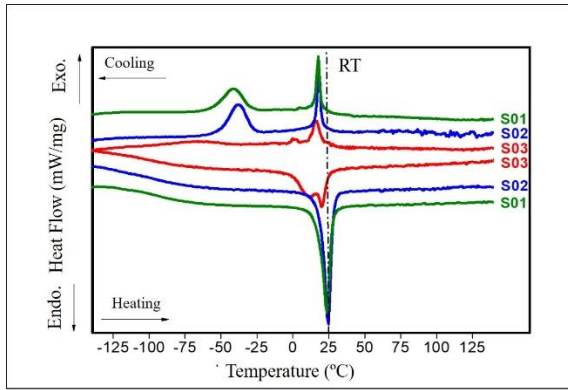


Figure 4.60 - DSC curves of three sections (S01, S02 and S03) of the Ni-Ti orthodontic archwires with graded actuating forces.

Table 4.7 – Phase transformation temperatures of the S01, S02 and S03 of the Ni-Ti orthodontic archwires with graded actuating forces, in Celsius degrees.

	Cooling				Heating	
	R_c	R_f	M_c	M_f	A_c	A_f
S01	19.8	15.5	-29.2	-56.5	17.9	28.3
S02	20.0	16.2	-27.6	-50.7	19.5	27.6
S03	20.8	10.9	-42.6	-104	-2.6	24.9

The results are confirmed by the literature that show the A_f temperature of orthodontic archwires with graded actuating forces for the molar segment, pre-molar segment and incisive segment are 25.9 ± 0.7 °C, 27.5 ± 1.2 °C and 30.2 ± 0.5 °C, respectively (Sudershan, 2015).

Considering the R-phase presence, three-point bending results performed by TMA are plotted together with DSC and are shown in Figure 4.61. The three-point bending test for all three sections showed that the deflection of the wire stays constant at the highest temperature range (above 30 °C) where the austenite is thermally stable (full recovery of the deformation by superelastic effect). With decreasing temperature, this deflection amplitude rate starts increasing up to a maximum that occurs at a temperature above 25 °C. These results are confirmed by the mechanical tests that show that S01 and S02 segment have somewhat lower actuating forces than the S03 segment (Figure 4.63).

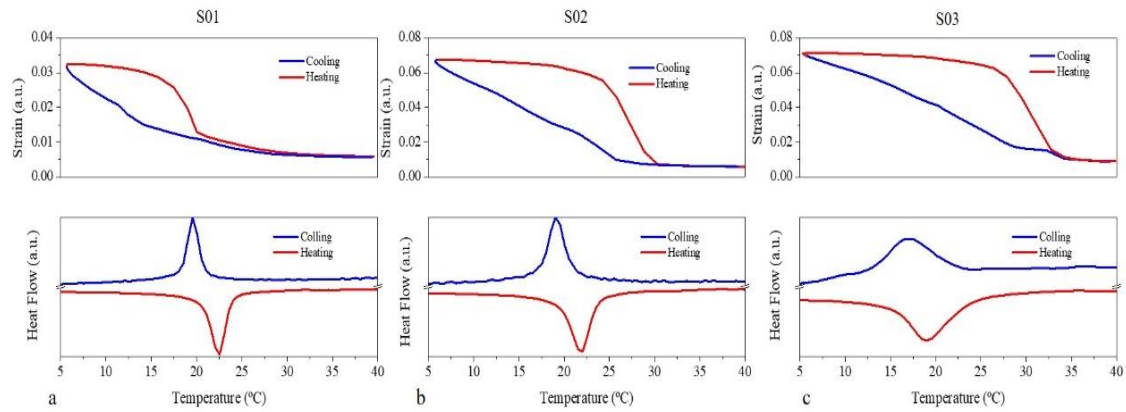


Figure 4.61 - DSC and three-point bending (TMA) results for the three sections of the Ni-Ti orthodontic archwires with graded actuating forces.

Figure 4.62a shows the schematic of the measurement along the length of the archwire (50 mm with the spacing distance of the 1 mm) at room temperature.

Figure 4.62b shows the present phases in each segment through a scheme with three diffraction patterns, one pattern of each segment (In Figure 4.61a the S03 diffraction patterns is highlighted by red line, S02 diffraction patterns is highlighted by blue line and S01 diffraction patterns is highlighted by green line).

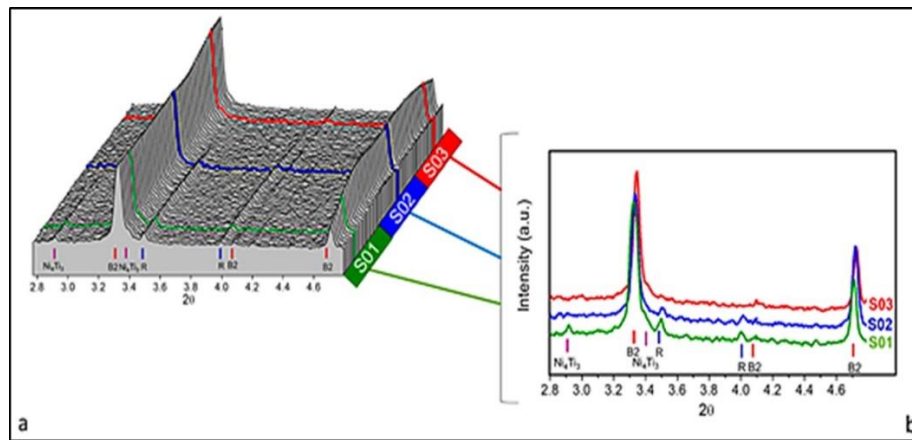


Figure 4.62 - SR-XRD patterns at room temperature for the three sections along the Ni-Ti orthodontic archwires with graded actuating forces length. a) superimposition of the XRD patterns of all scans along the wire to observe the graded functionally wire. b) diffraction patterns for the three sections to compare the phases present at room temperature.

Diffraction patterns obtained at S03 are well indexed by B2 austenitic phase. The B2 peak was observed with different intensities along the functionally graded wire and the R-phase is identified at sections S01 and S02. The Ni_4Ti_3 precipitate was observed at S01.

The existence of R-phase in S01, as well as in the premolar section (S02), can be justified by the heat treatment applied on the archwire (Ni_4Ti_3 formation). (Khalil-Allafi, 2002). The presence of Ni_4Ti_3 precipitates is more evident in S01, as evidenced by broadening of the peak, which is marked by purple line in Figure 4.62b.

It is supposed that in the heat-treated sections, precipitation phenomena, namely of Ni_4Ti_3 , originates a Ni depletion of the surrounding matrix. As such, this composition variation is responsible for a change in the transformation temperatures, allowing for R-phase to be present at room temperature (see Table 4.7). These observations support the existence of a functional gradient.

Figure 4.62 shows the load-deflection curves for the test of three sections at room temperature. At room temperature, the three sections present some unrecovered deformation, which is more significant in segments S01 and S02. This deformation could be recovered by shape memory effect with the increase of the temperature.

There is a clear difference between the mechanical behavior of the different sections. According to the DSC test (Table 4.7), the S03 specimen shows lower A_f temperature, i.e. the higher Ni content on the matrix, which is confirmed by mechanical testing. It can be seen that the upper plateau increases, which indicates a higher critical stress for the stress-induced martensite to be formed. Again, these observations support the existence of a functional gradient along the wire. (Sakima, 2006) (Nespoli, 2015)

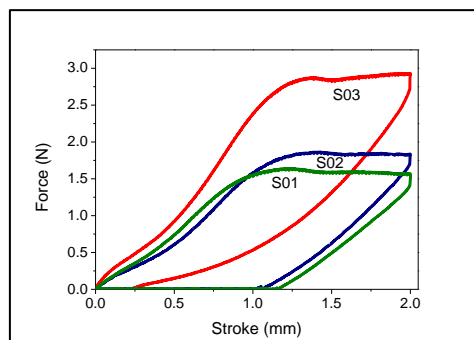


Figure 4.63 - Plot of representative load-deflection data for the three sections of the Ni-Ti orthodontic archwires with graded actuating forces testing at room temperature.

The analyzed points of the displacement (0.5, 0.75 and 1.0 mm) are the points related to the clinically advisable rate of biological tooth movement, which is about 0.5 to 1.0 mm in 4 to 5 weeks. (Pilon, 1996) (Eagly, 1991) (Proffit, 2018) For this reason, all the values reported here represent data from the force-displacement curves during unloading portion in the range 0.5 to 1.0 mm. These curves are depicted in Figure 4.64a, b and c.

Figure 4.64d, e and f depict the slopes of the superelastic lower plateau of each segment at the studied temperatures.

During the orthodontic treatment, 37 °C is the most important actuation temperature. Thus, the observation about 37 °C will be discussed first. The results at this temperature show that the range of actuating forces is significant for all the sections. None of the sections showed unrecovered deformation after the three-point bending test. A much wider range of force of the unloading superelastic plateau was recorded for the S03 segment compared to the S01 and S02 segments. For S03 the forces varied from 2.09 to 1.92 N, S02 from 1.43 to 1.28 N and S01 from 0.88 to 0.56 N (Figure 4.64d). As expected, molar segment yielded higher actuating force values.

The results at 25 °C temperature are similar to 37 °C results, once the A_f is close to this temperature. For 25 °C, lower actuating forces are observed when compared to the corresponding actuating forces at 37 °C. At 25 °C there is also full recover of the deformation (superelastic behavior). The wider range of force of the unloading superelastic plateau was recorded for the S03 as expected. The average of the slope of actuating forces (superelastic behavior) are: S01 from 0.48 to 0.14 N, S02 from 1.24 to 0.90 N and S03 from 1.11 to 0.79 N (Figure 4.63e).

The results for 20 °C will be discussed taking into consideration the fact that this is a common room temperature in the orthodontic clinical room. As mentioned before, this measurement was performed by immersion in a water bath with a controlled temperature. The S01 section does not present a significant actuation force. A light actuation force was just observed for the S03 and S02. This indicates that the deformation is easier at this temperature and can be bent into desirable shapes without breaking or deforming permanently. The average of the slope of actuating forces (superelastic behavior) are: S01 is null, S02 from 0.05 to 0.46 N and S03 from 0.5 to 0.95 N (Figure 4.63f).

The graph comparing the different segments tested at 5 °C did not show unloading plateaus. This suggests that all the segments were not in austenitic field, depicting that 5 °C is below the A_f temperature for this orthodontic archwire.

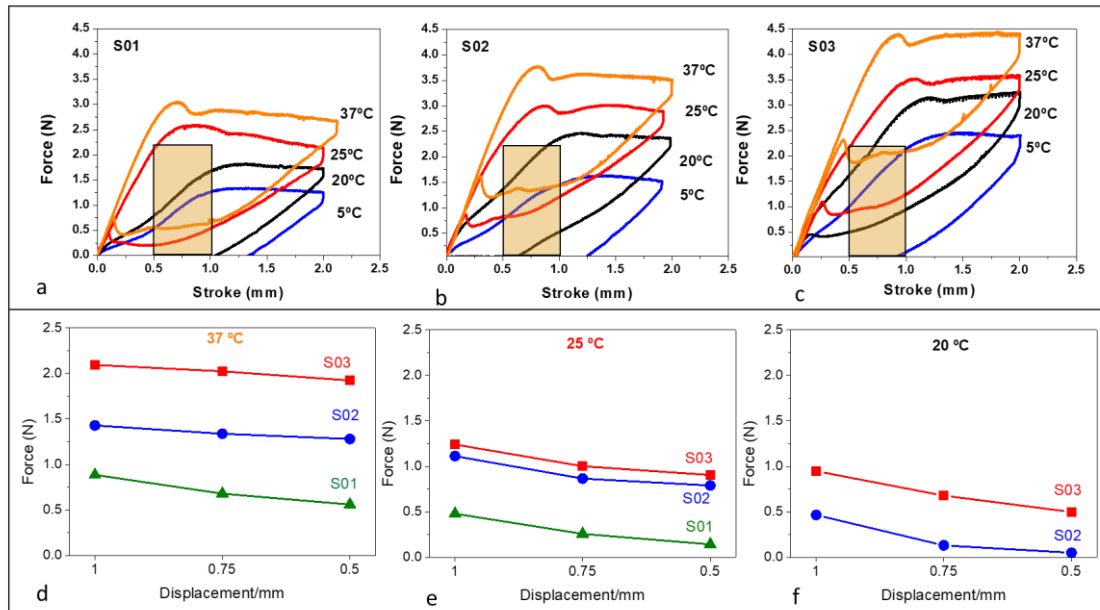


Figure 4.64 - Force x Stroke curves for the three sections of the Ni-Ti orthodontic archwires with graded actuating forces (a) S01, (b) S02, (c) S03 at four temperatures (5, 20, 25 and 37 °C). (d) Slope 37 °C, (e) slope 25 °C and (f) slope 20 °C.

Extrapolating these results to a clinical situation, it can be suggested that when the patient ingests warm drinks the force delivered by these archwires increases and stimulates tooth movement. Conversely, cold drinks might reduce the force delivered by these archwires.

In general, the manufacturing of the Ni-Ti orthodontic archwire has a complex metallurgical process. The chemical composition, the heat treatment, and thermomechanical process influence the properties of the wires.

The different sections of the Ni-Ti orthodontic archwire used in this study showed: i) different structural characteristic; ii) distinct phase transformation temperatures; iii) different load-deflection curves for all the tested condition.

Finally, at the body temperature (37° C) all the samples showed a superelastic effect when they were analyzed. At this temperature, the forces were light and continuous in 2 mm of deflection. All the sections showed the typical plateau for superelasticity. The section S03 as the molar segment, S02 as the premolar segment, and S01 as incisive segment, showed decreasing actuation force (average of the slope of actuating forces - superelastic behavior) from 2 N, 1.3 N and 0.7 N, respectively, similar behavior is reported in the literature (Sudershan, 2015). The lower load levels correlated with the A_f

temperatures suggests that the actuating force levels at which the superelastic effect occurs are lower for the segments of the wire which have higher A_f temperatures.

The different behavior between the sections evaluated in this study probably may be attributed to a thermal process applied.

4.5.4. Commercial Ni-Ti Orthodontic Archwires Summary

It is expected that the Ni-Ti orthodontic archwires show the adequate functional properties and generates continuous and light forces during the orthodontic treatment. The Ni-Ti orthodontic archwires with graded actuation forces needs to develop these forces in different ways for each tooth. The following conclusions can be drawn from this work:

- Commercial Ni-Ti orthodontic archwires investigated in this study present the A_f temperature close to room temperature and at oral temperature all the archwires are fully austenitic;
- The superelastic orthodontic archwire do not show different mechanical behavior in the environment oral;
- The orthodontic archwire with graded actuation forces tested has different mechanical properties along the length of the wire;
- For the orthodontic archwire with graded actuation forces, the functional gradient is put into evidence on SR- XRD analysis;
- For the orthodontic archwire with graded actuating forces there are significant differences in the forces and moments of the unloading superelastic plateaus, comparing the different sections of the archwire at different temperatures;
- Clinically, the A_f temperatures below oral temperature are interesting because at these temperatures they show an easier formability.

4.5.5. Functionally Graded Orthodontic Archwires

The functional gradient was introduced in the superelastic Ni-Ti orthodontic archwire (Morelli - SE) that was discussed previously in section 4.5.1.

Figure 4.65 shows the DSC curves of the three zones of the Ni-Ti orthodontic archwire heat treated (300 °C during 10 minutes) where internal is the heat-treated zone, transition is intermediate zone (between heated and no heated sections) and external is no heat-treated zone. The phase transformation temperatures are shown in Table 4.8.

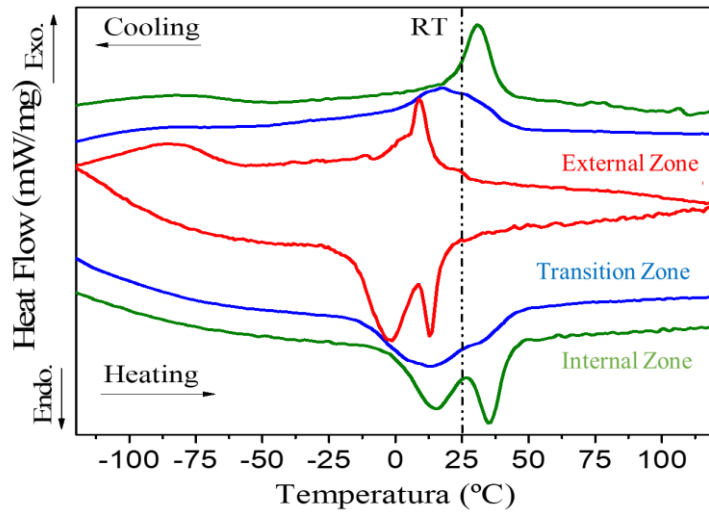


Figure 4.65 - DSC curves of the three zones of the Ni-Ti orthodontic archwire heat treated (300 °C during 10 minutes).

Table 4.8 - Transformation temperature of the three zones of the Ni-Ti orthodontic archwire heat treated (300 °C during 10 minutes), in Celsius degree.

Sample (zone)	Cooling				Heating			
	R_s	R_f	M_s	M_f	R_s	R_f	A_s	A_f
Internal	35	8	-59	x	-2	x	x	45
Transition	37	13	-47	x	-11	x	x	43
External	31	-20	-61	x	-34	x	x	17.7

x- not detected

The internal and external zones DSC results show two transformation peaks on heating and on cooling, indicating the R phase presence ($B2 \leftrightarrow R \leftrightarrow B19'$). On the other hand, the transition zone DSC curves show one transformation (broad) peak on heating and one on cooling, suggesting that $B2 \leftrightarrow B19'$ took place in one single step, but due to narrow thermal hysteresis the presence of the R-phase may be considered.

Similarly, to commercial orthodontic archwires with graded actuation forces, the three zones presented different A_f temperatures. This is due to the presence of a gradient of transformation temperatures, which arise from the gradient of chemical compositions, within the heat-treated zone. (Shariat, 2017)

From the DSC measurement it can be inferred that a microstructural gradient is present in this treated archwire. This technique is not capable of providing a localized analysis along the heat-treated archwire. To identify the microstructural behavior of the whole length of the heat-treated archwire (300 °C during 10 minutes), the SR-XRD analysis

was performed, as shown in Figure 4.66. This measurement allows to identify the heat-treated zone and the symmetry of the heat treatment behavior.

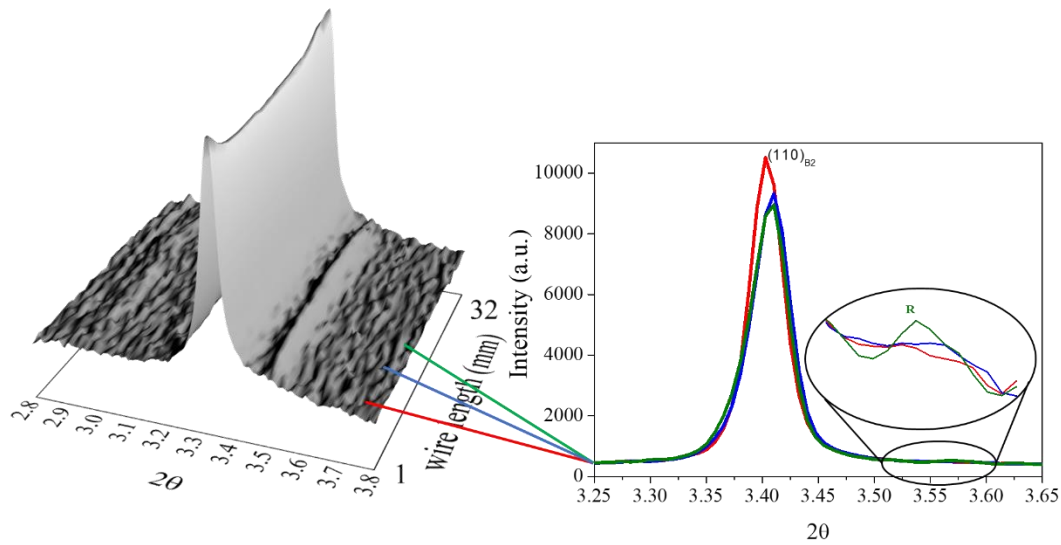


Figure 4.66 - SR-XRD partners along the Ni-Ti orthodontic archwire heat treated (300 °C during 10 minutes) length.

Figure 4.66 depicts the diffractograms (integrated for Phi from 0 to 360°) and three diffractograms of different regions of the functionally graded orthodontic archwires (zoom): internal zone (green line), transition zone (blue line) and external zone (red line).

The superposition of the three diffractograms allowed us to identify a clear difference between the zones. The intensity of the $(110)_{B2}$ peak decreasing from the external zone to the internal zone is noticed. The external zone is fully austenitic, while the internal zone shows the presence of the R-phase.

The existence of R-phase can be justified by the presence of Ni_4Ti_3 precipitates. The Ni_4Ti_3 presence is due to the higher temperature reached during the heat treatment at the internal zone. It is known that this precipitate may occur, at lower temperatures and shorter permanence time (Otsuka, 2005).

Pelton *et al.* (2000) used an alloy with similar characteristics as the one used as base material (superelastic orthodontic archwire) for this study. They reported that it is possible to observe the Ni_4Ti_3 precipitation in a temperature range from 300 to 500 °C, in a short-elapsd time, of a couple of seconds.

A simple observation of the superelastic archwire texture was necessary to understand the behavior during the mechanical test of the functionally graded archwire; where the tensile and compressive sides are ϕ_0 and ϕ_{90} respectively. Figures 4.67 show the pole figures, for superelastic archwire. This sample has two overlapped textures: $\{110\}\langle 110\rangle$ and $\{200\}\langle 110\rangle$.

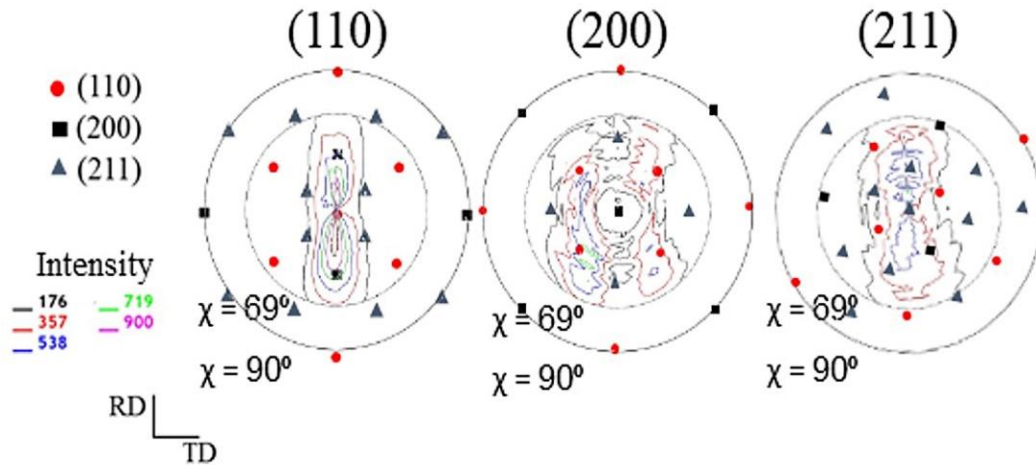


Figure 4.67 - Pole Figures of superelastic archwire.

Other authors have reported the same texture components on Ni-Ti drawn wires. (Hasan, 2008) (Sun, 2018)

The single scan (sscan measurement) was performed along the 32 mm total length of the heat-treated arch-wire. Due to symmetry, we are presenting the results only from the center point (at 16 mm from one edge) to the end (32 mm) (Figure 4.68). The intensity of $(200)_{B2}$ along the orthodontic archwire is higher for ϕ_0 than for ϕ_{90} . The $(110)_{B2}$ intensity increases from the center (16 mm) to the edge (32 mm), while R-phase (indicated by an arrow in Figure 4.68) is decreasing. This behavior is more evident in ϕ_0 than in ϕ_{90} .

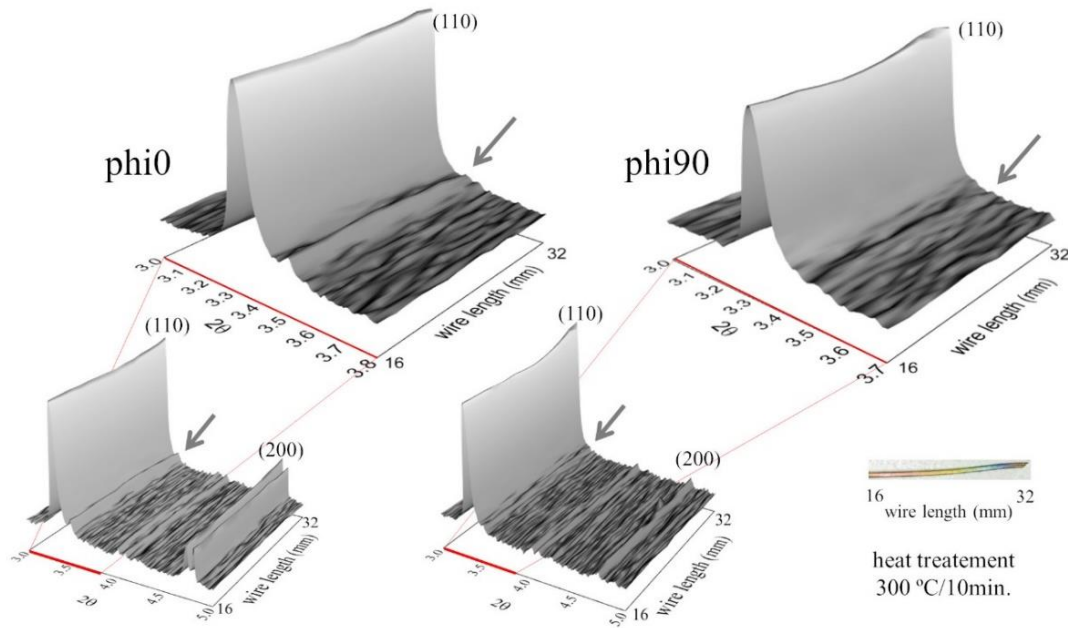


Figure 4.68 – SR-XRD diffractograms - intensity versus 2θ of the phi0 and phi90 of the Ni-Ti orthodontic archwire heat treated (300 °C during 10 minutes) between 16 and 32 mm of length.

Orthodontic applications of Ni-Ti alloys require a suitable mechanical behavior during the treatment, in order to take advantage of superelasticity. In this study an observation of the structural behavior during the tensile test was performed. Therefore, a deeper approach to mechanical behavior will not be carried out in this discussion.

During the tensile test (Figure 4.69a and b) a typical yielding behavior associated with a stress plateau due to reversible stress-induced martensite (SIM) transformation occurring between austenite and martensite is observed. Specific steps of the stress-strain curve were previously selected in accordance with displacement during the orthodontic treatment (Figure 4.69). During this test, the SR-XRD images were *in-situ* collected along the gauge length (32 mm) of the heat treated (300 °C during 10 minutes) Ni-Ti orthodontic archwire.

For these uniaxial loading in tension, the directions parallel to the loading axis (phi0) and perpendicular to the loading axis (phi90) were chosen. The SR-XRD results (the intensity versus 2θ) are plotted as 3D representations of the 2θ scans, as a function of the position along the heat-treated segment of the orthodontic archwire for the two azimuthal angles. (Figure 4.69a and b).

The Figures 4.69 and 4.70 show the results of the deformation evolution during the tensile test. In Figure 4.69 all the length of the archwire was observed for each step of the deformation, for phi0 and phi90, while Figure 4.70 shows a single diffractogram of

each zone (internal zone - transition zone - external zone) at different tensile steps (cyclestep measurement) for ϕ_0 and ϕ_{90} .

During loading, the intensity of the B2 peaks is decreasing and a combination of the appearance of new peaks and peak overlap can be observed, which is an indication of the evolution of a new phase at high stress. These phases were indexed as monoclinic B19' and R-phase which were formed by deformation.

The stress-induced R-phase peaks are seen in Points 1 – 0.6% and 2 – 1.9% (red and green boxes), not overlapped by the much more intense austenite $(110)_{B2}$ peak. The presence of the R-phase indicates that a certain level of stress has been reached which is below the martensitic phase transformation stress plateau. The presence of the R-phase can be observed in tensile curves for both ϕ (ϕ_0 and ϕ_{90}), where a change in slope can be noticed in the elastic deformation portion of the austenite in the tensile curve. The R-phase can be clearly identified in Figure 4.70, by green line, in the ϕ_0 and ϕ_{90} diffractograms of each zone.

The B19' was observed at 2.8% of the deformation, which corresponds to the zone around the middle of the plateau on the tensile curve (Point 3 – orange box). It is observed that the R-phase coexists with B19' and B2 phases up to 5.9% (Point 4 – black box). At 6.3%, the material is fully B19' (Point 5 – blue box). During loading, the B19' peaks are increased while B2 peaks decreased until they disappear. (Young, 2010)(Héraud, 2015) On the other hand, the reverse behavior can be observed during unloading: 2.8% and 0.6% (Points 6 and 7 – purple and pink boxes). The SXRD patterns obtained at unloading, at 0.6%, show the peaks of B2 phase. It is then observed that the stress-induced R-phase is reversible, as well as for B19' phase. These results are in accordance with literature. (Benafan, 2017)

On loading, the SIM is starting from the middle region of the archwire and, with further strain, it progresses till it reaches both ends of the wire. This behavior is coherent with observations reported in the literature. (Sevilla, 2008) (Meng, 2016) (Shariat, 2017)

The behavior observed during the tensile loading was attributed to SIM. The strain was reversible, and the plastic deformation did not occur within the austenite phase under the stress tested, as reported by other authors. (Benafan, 2017)

Examining the tensile and compressive sides (ϕ_0 and ϕ_{90} , respectively) shows a striking difference in the martensite variants of the stress-induced martensitic formed.

The martensite must find a different way to accommodate the stress state, because it is not possible to expand in the $\phi 0$ direction on the compressive side as it is for the tensile side to expand in the $\phi 90$ direction.

Figure 4.71a shows the comparison between maximum of the $(110)_{B2}$ intensity along the deformation of each zone for $\phi 0$ and $\phi 90$. In the internal zone the higher intensity was observed in $\phi 0$ for the first three steps. The intensities are similarly to the steps where the material is fully martensitic. At unloading step (06%) the $(110)_{B2}$ peak increased with the same behavior. At internal zone the transformation was reversible. A similar behavior was observed in transition zone results. However, in external zone the material is fully martensite after deformation. This behavior confirms the previous observation, that the martensitic transformation beginning at the middle of the wire, where the higher temperature was reached during the heat treatment. (Benafan, 2017)

The prominent $(110)_{B2}$ peak in $\phi 0$ splits into two martensite peaks, $(020)_{B19}$ and $(021)_{B19}$ show intense stress-induced texturing, while the $(110)_{B2}$ peak in $\phi 90$ splits into three martensite peaks, $(110)_{B19}$, $(002)_{B19}$ and $(111)_{B19}$ show intense stress-induced texturing as shown in Figure 4.70. These results are similar to those reported in the literature. (Hasan, 2008)

Figure 4.71b shows the comparison between 2θ $(110)_{B2}$ along the deformation of each zone for $\phi 0$ and $\phi 90$. The 2θ for $\phi 0$ and $\phi 90$ are similar in all the zones. As mentioned previously, the tensile and compressive directions display a preferential behavior. At $\phi 0$ the 2θ $(110)_{B2}$ during the tensile test shifted to higher 2θ values, due to the decreased of the d -spacing, while at $\phi 90$ the 2θ $(110)_{B2}$ shifted to lower 2θ values because the d -spacing increases due the tensile *versus* compressive components.

In this measurement the superelastic plateau occurred at roughly 25 N. The results showed that this treated archwire displays different behavior along its length. A complete loading–unloading cycle was observed; the deformation behavior is largely superelastic.

The heat treatment at 300 °C during 10 minutes (by Joule effect) has significant influence on the structural behavior along the archwire length. The precipitation phenomena, namely Ni_4Ti_3 , originates a Ni depletion of the surrounding matrix; these

precipitates can induce the R-phase presence. The heat treatment at 300 °C during 10 minutes increased the austenite finish temperature.

The behavior of the heat-treated archwire heat-treated does not compare to the commercial orthodontic archwires with graded actuating forces, because the heat treatment applied needs further improvement. The first results presented here about the materials behavior after heat treatment demonstrate that this mechanism is more complex than previously reported.

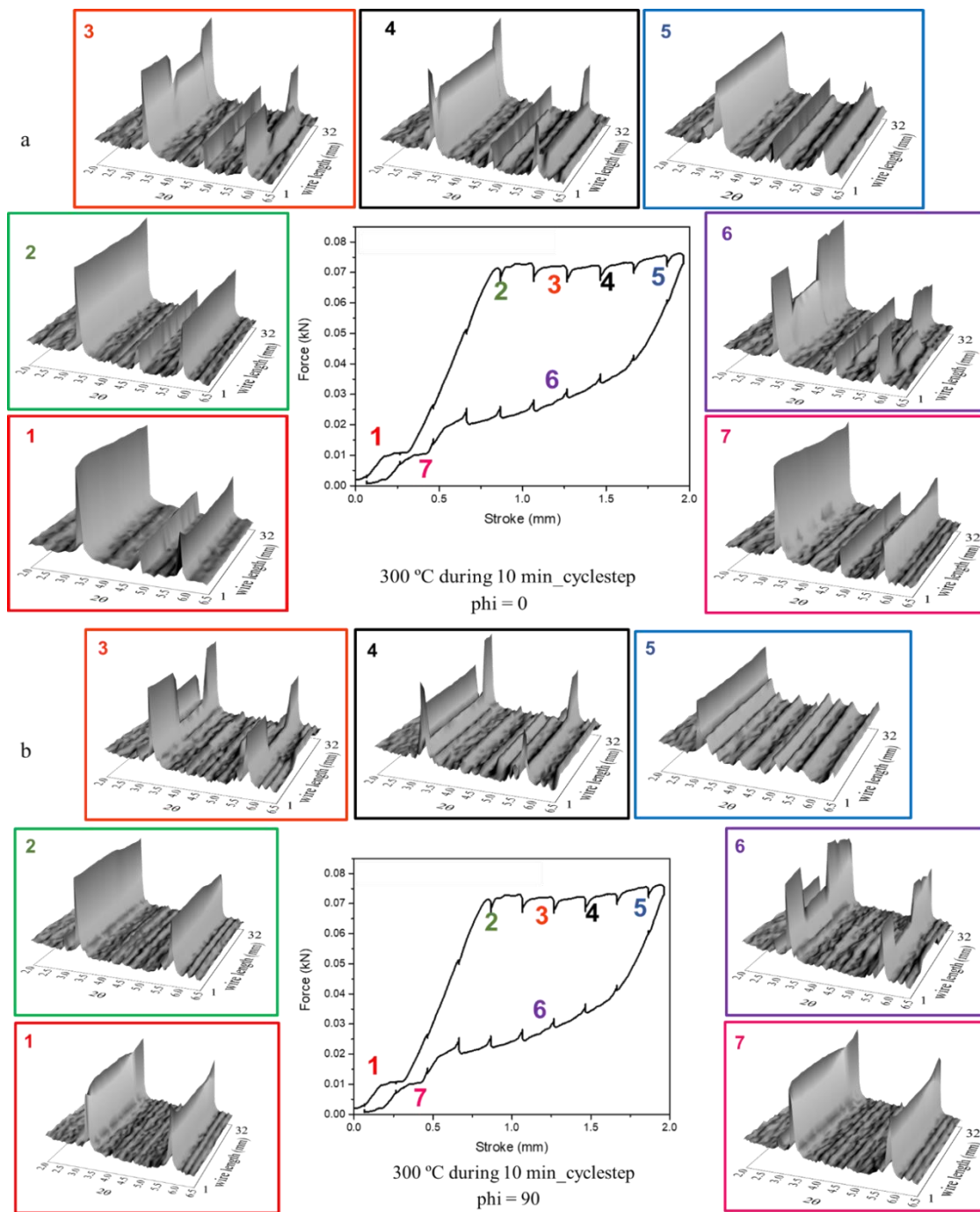


Figure 4.69 - In situ SXR D analysis during tensile test (a - $\phi=0$ and b - $\phi=90$) of the Ni-Ti orthodontic archwire heat treated (300 °C during 10 minutes).

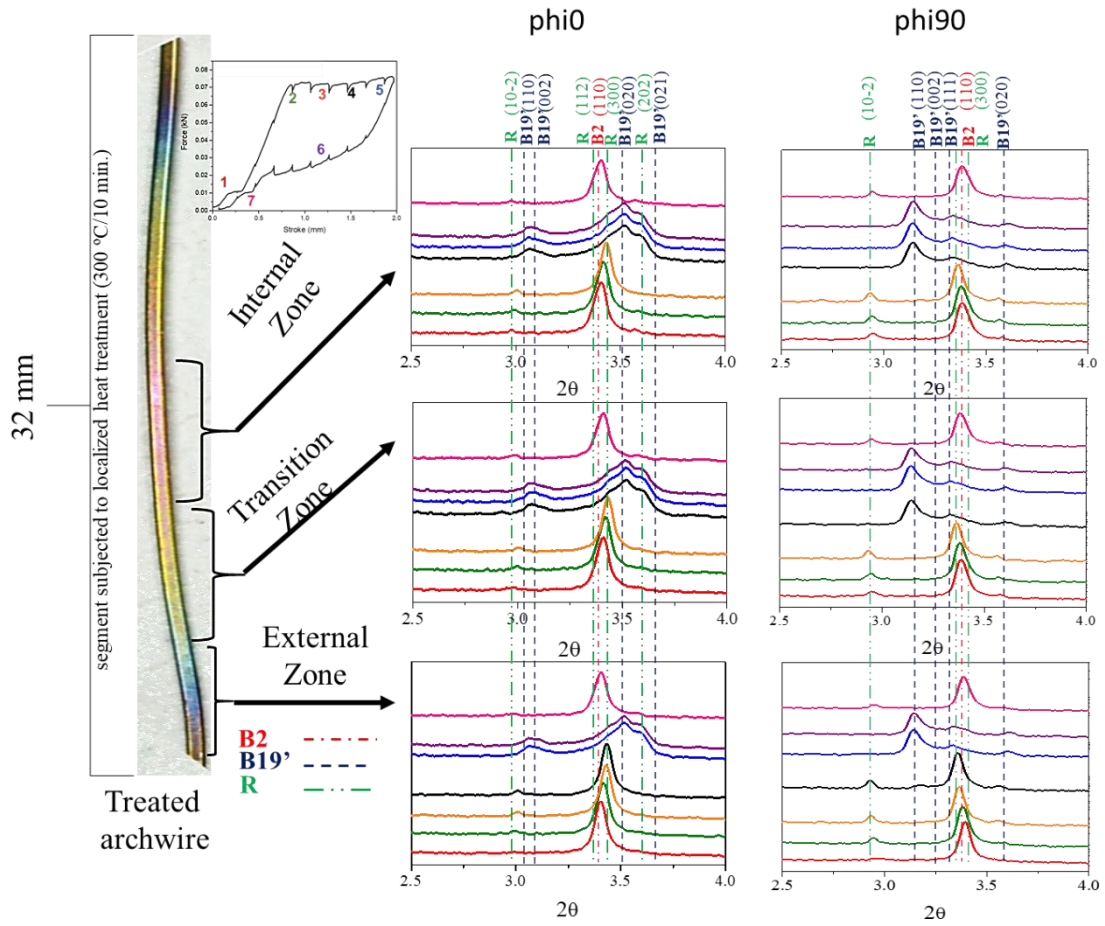


Figure 4.70 - Single diffractogram of each zone (zone 1 – treated zone, zone 2 – intermediate zone and zone 3 – no treated zone) during the tensile test - $\phi 0$ and $\phi 90$.

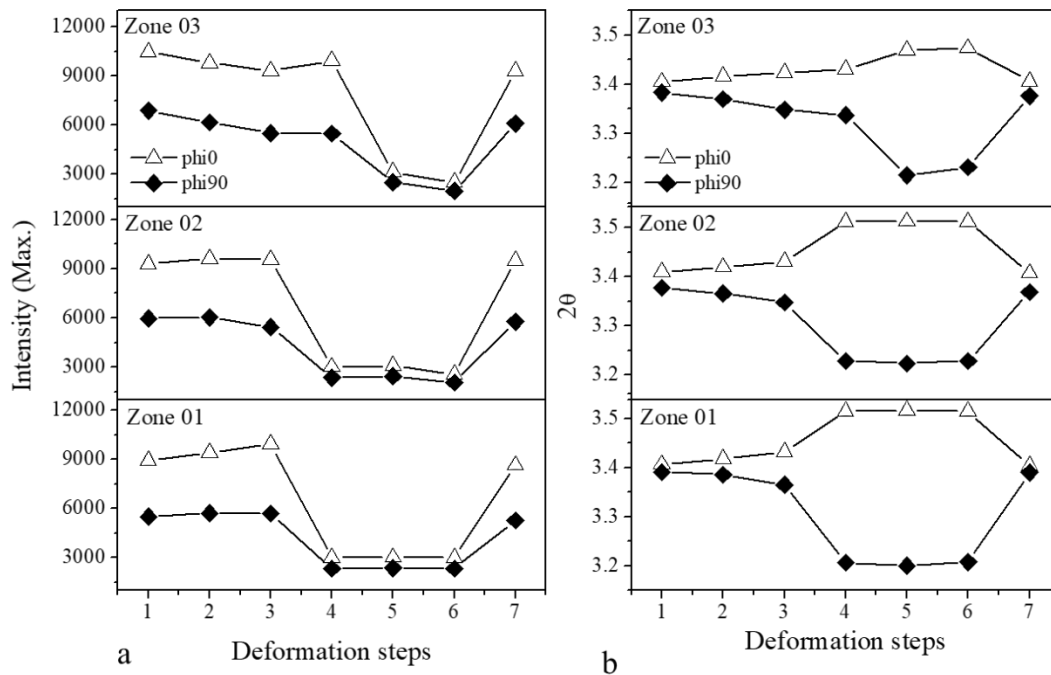


Figure 4.71 – Comparison between: (a) maximum of the $(110)_{B2}$ intensity and (b) 2θ along the deformation of each zone - $\phi 0$ and $\phi 90$.

Conclusions and Future Work

We studied three different Ni-content alloys to be processed: Ni-rich “alloy 1” with 50.8% at. Ni, close to equiatomic “alloy 2” with 49.9% at. Ni and Ti-rich “alloy 3” with 49.3% at. Ni (global composition). We have also analyzed commercial orthodontic archwires.

The main conclusions of these studies will be presented in separate sections according to the different processing steps and, finally, for the analyses of commercial orthodontic archwires.

5.1. As-cast and remelt

The functional characteristics, namely A_f temperature, of the three alloys were identified. Alloy “1” has been chosen as the main alloy to be investigated due to its most interesting functional characteristics.

For all these alloys the solubilization treatment has given a fully austenitic matrix at room temperature.

The optimization condition of the solubilization treatment has led us to consider 950 °C during 120 minutes as the most favorable processing parameters.

5.2. Hot Forging Steps

The characterization of the forging steps allowed us to verify that the deformation temperature that was applied promoted the dynamic recrystallization.

The microstructural analysis of these forging steps, as well as the in-situ study for simulation of hot working, led us to propose 850 °C during 15 minutes as the most favorable condition for the intermediate annealing.

This parameter choice was supported by the need to guarantee that hot deformation would take a place in the most favorable condition for dynamic recovery and recrystallization to occur, even considering the possible cooling of the material during the transportation from furnace to forging equipment.

5.3. Cold Forging Steps

The analysis of the forging steps confirmed that the microstructural refinement was ensured, always guaranteeing at the same time a fully austenitic matrix close to room temperature; at the last cold forging step some residual R-phase and/or B19' were identified at room temperature.

The microstructural analyses of the final forging steps, as well as in-situ studies on simulated thermomechanical cycles, allowed us to propose a most convenient intermediate annealing treatment: 850 °C during 15 minutes, just like the previous processing step (hot forging).

5.4. Aging Heat Treatment

Preliminary studies at 350, 400, 450 and 500 °C allowed us to identify 500 °C as the most suitable aging heat treatment temperature.

The analysis of structural evolution during aging (stress-free and stress-assisted aging) allowed us to confirm a significant acceleration of the Ni₄Ti₃ precipitate kinetics when a compressive loading is applied. The kinetics of the stress-assisted aging was stabilized at the end of 15 minutes compared to 20 minutes for the stress-free aging.

5.5. Orthodontic Archwires Characteristics

Two commercial orthodontic archwires were analyzed in order to better understand the expected characteristics for the material to be used in their fabrication.

Morelli archwires (superelastic and thermo-activated) were studied to identify two classes of situations: A_f below room temperature (superelastic) and A_f slightly above room temperature (thermo-activated). The superelastic archwires, are austenitic close to room temperature and undergo martensitic transformation by mechanical deformation, while the thermo-activated archwires are partially martensitic at room temperature and display thermally induced shape memory effect when heated to oral temperature.

Also, BioForce archwires were studied in order to investigate a very recent innovation: the introduction of a functional gradient. We have also analyzed the possibility of introducing this functional gradient on conventional commercial archwires (sold as uniform archwires). The results of our study prove the feasibility of the use of a portable equipment to introduce localized heat treatments that may be custom-designed.

5.6. Future Work

The melting/casting of these alloys require further improvement in order to reduce the inclusions contents (TiC and Ti_2Ni_4O).

The presence of the inclusions in the current study did not represent a significant limitation as they did not result in fracture during the steps under analysis. Nor should they represent a limitation to the analysis of microstructural evolution during the successive thermomechanical steps, in agreement with other authors findings. (Coda, 2012) (Reinholz, 2012)

A further analysis with lab scale reproduction of the thermomechanical processing incorporating the proposed changes is suggested as a continuation of these studies.

A more detailed microstructural analysis (TEM and EBSD) of the aging (stress-free and stress-assisted) is suggested as a continuation.

Using our experience on the aging of commercial alloys, a prototype for localized heat treatments of conventional archwires may be designed.

References

- ASTM - American Society for Testing and Materials, Metals Test Methods and Analytical Procedures: ASTM E-112-96. Annual. B. ASTM Stand, vol. 03.01 (2000).
- Basu R., Jainb L., Majic B. and Krishnanc M. Dynamic recrystallization in a Ni-Ti-Fe shape memory alloy: Effects on austenite-martensite phase transformation. *Journal of Alloys and Compounds*, vol. 639 (2015) 94-101.
- Benafan O., Garg A., Noebe R.D., Skorpenske H.D., An K. and Schell N. Deformation characteristics of the intermetallic alloy 60NiTi. *Intermetallics*, vol. 82 (2017) 40-52.
- Bhagyaraj J., Ramaiah K.V., Bhaumik S.K. and Gouthama. Behavior and effect of Ti₂Ni phase during processing of NiTi shape memory alloy wire from cast ingot. *Journal of Alloys and Compounds*, vol. 581 (2013) 344–351.
- Bradley T., Brantley W. and Culbertson B.M. Differential scanning calorimetry (DSC) analyses of superelastic and nonsuperelastic nickel-titanium orthodontic wires. *American Journal of Orthodontics and Dentofacial Orthopedics*, vol. 109 (1996) 589–597.
- Brantley W. A., Iijima M. and Grentzer T. H. Temperature-modulated DSC provides new insight about nickel-titanium wire transformations. *American Journal of Orthodontics and Dentofacial Orthopedics*, vol. 124 (2003) 387–394.
- Brantley W. and Eliades T. Orthodontic materials: scientific and clinical aspects, 1st ed. New York: Thieme, Stuttgart (2001) 1 – 310.
- Buehler W.J. and R.C. Wiley. The properties of TiNi and Associated Phases, NOLTR 61-75, AD 266607 (national Technical Information Service Document (NTISD) Number), U.S. Naval Ordnance Laboratory (1961) 1-102.
- Cardoso C., Quintão A., Helena I. and Portella V. Orthodontic Wires: Knowledge Ensures Clinical Optimization. *Dental Press Journal of Orthodontics*, vol. 14 (2009) 144–157.
- Cash A., Curtis R., Garrigia-Majo D. and McDonald F. A comparative study of the static and kinetic frictional resistance of titanium molybdenum alloy archwires in stainless steel brackets. *European Journal of Orthodontics*, vol. 26 (2004) 105–111.
- Chowdhury P. and Sehitoglu H. A revisit to atomistic rationale for slip in shape memory alloys. *Progress in Materials Science*, vol. 85 (2017) 1-42.
- Coan S., Shamimi A. and Duerig T.W. Effect of Cooling Rates on the Transformation Behavior and Mechanical Properties of a Ni-Rich NiTi Alloy. *Shape Memory Superelasticity*, vol. 3 (2017) 315-321.
- Coda A., Zilio S., Norwich D. and Sczerzenie F. Characterization of Inclusions in VIM/VAR NiTi Alloys. *Journal of Materials Engineering and Performance*, vol. 21 (2012) 2572–2577.
- Cong D.Y., Saha G. and Barnett M.R. Thermomechanical properties of Ni–Ti shape memory wires containing nanoscale precipitates induced by stress-assisted ageing. *Acta Biomaterialia*, vol. 10 (2014) 5178–5192.

- Cullity B. D., Elements of x-ray diffraction, 2nd ed. Addison-Wesley Publishing Company, (1978).
- Cun Y., Bachir A., Cui C., Yinong L., Hong Y., Xiaohua J., Song C., Daqiang J., Zunping L., Dennis B. and Yang R. Synchrotron high energy X-ray diffraction study of microstructure evolution of severely cold drawn NiTi wire during annealing. *Acta Materialia*, vol. 115 (2016) 35–44.
- Dehghani K. and Khamei A. A. Hot deformation behavior of 60Nitinol (Ni60wt%–Ti40wt%) alloy: Experimental and computational studies. *Materials Science and Engineering: A*, vol. 527 (2010) 684–690.
- Dolce M. and Cardone D. Mechanical behaviour of shape memory alloys for seismic applications 2. Austenite NiTi wires subjected to tension. *International Journal of Mechanical Sciences*, vol. 43 (2001) 2657–2677.
- Drennen D. C., Jackson C. M. and Wagner H. J. The Development of Melting and Casting Procedures for NiTiNOL Nickel-Base Alloys, United States (1968).
- Eagly A.H., Makhijani M., Ashmore R. and Longo L. What Is Beautiful Is Good, But...: A Meta-analytic review of research on the physical attractiveness stereotype. *Psychological Bulletin*, vol. 110 (1991) 109-128.
- Elahinia M. H., Hashemi M., Tabesh M. and Bhaduri S. B. Manufacturing and processing of NiTi implants: A review. *Progress in Materials Science*, vol. 57 (2012) 911–946.
- Fan G., Chen W., Yang S., Zhu J., Ren X. and Otsuka K. Origin of abnormal multi-stage martensitic transformation behavior in aged Ni-rich Ti–Ni shape memory alloys. *Acta Materialia*, vol. 52 (2004) 4351–4362.
- Fan Q.C., Zhang Y.H., Wang Y.Y., Sun M.Y., Meng Y.T., Huang S.K. and Wen Y.H. Influences of Transformation Behavior and Precipitates on the Deformation Behavior of Ni-Rich NiTi Alloys. *Materials Science and Engineering: A*, vol. 700 (2017) 269-280.
- Frenzel J., George E. P., Dlouhy A., Somsen C., Wagner M. F. X. and Eggeler G. Influence of Ni on martensitic phase transformations in NiTi shape memory alloys. *Acta Materialia*, vol. 58 (2010) 3444–3458.
- Frenzel J., Neuking K. and Eggeler G. Induction Melting of NiTi Shape Memory Alloys– The Influence of the Commercial Crucible Graphite on Alloy Quality. *Materialwissenschaft und Werkstofftechnik*, vol. 35 (2004a) 352–358.
- Frenzel J., Zhang Z., Neuking K. and Eggeler G. High quality vacuum induction melting of small quantities of NiTi shape memory alloys in graphite crucibles. *Journal of Alloys and Compounds*, vol. 385 (2004b) 214–223.
- Frenzel J., Zhang Z., Somsen C., Neuking K. and Eggeler G. Influence of carbon on martensitic phase transformations in NiTi shape memory alloys. *Acta Materialia*, vol. 55 (2007) 1331–1341.
- Funakubo H., Shape Memory Alloys. Gordon and Breach Science Publishers, vol. 1 (1987) 1-276
- Gioka C. and Eliades T. Superelasticity of nickel-titanium orthodontic archwires: metallurgical structure and clinical importance. *Hellenic Orthodontic Review*, vol. 5, (2002) 111–127.

Habu T. Fabrication of shape memory alloy parts, In: Shape Memory Alloys for Biomedical Applications 1st ed, Editors: Yoneyama T., Miyazaki S., Woodhead Publishing (2009) 86-100

Hammersley A.P., Svensson S. O., Hanfland M., Fitch A. N. and Hausermann D. Two-dimensional detector software: From real detector to idealised image or two-theta scan. *High Pressure Research*, vol. 14 (1996) 235–248.

Harrison J. D. Measurable Changes Concomitant with the Shape Memory Effect Transformation In: Engineering Aspects of Shape Memory Alloys. Editors: Wayman C. M., Duerig T. W., Stöckel D., Melton D, Ed. London: Butterworth-Heinemann, (1990) 106–111.

Hasan M., Schmahl W.W., Hack K., Heinen R., Frenzel J., Gollerthan S., Eggeler G., Wagner M., Khalil-Allafi J. and Baruj A. Hard X-ray studies of stress-induced phase transformations of superelastic NiTi shape memory alloys under uniaxial load. *Materials Science and Engineering: A*, vol. 481 (2008) 414–419.

Héraud L., Castanny P., Laillé D. and Gloriant T. In situ synchrotron X-ray diffraction of the martensitic transformation in superelastic Ti-27Nb and NiTi alloys: a comparative study. *Materialstoday Proceedings*, vol. 2 (2015) S917-S920.

Hoseini M., Mostafavi S. M. S., Rezaei N. and Boluri E. J. Orthodontic Wire Ingestion during Treatment: Reporting a Case and Review the Management of Foreign Body Ingestion or Aspiration (Emergencies). *Case Reports in Dentistry*, vol. 2013 (2013) 1-3.

Humphreys F. J. and Hatherly M. Hot Deformation and Dynamic Restoration Chapter 13 in Recrystallization and Related Annealing Phenomena. Editors: F.J. Humphreys and M. Hatherly 2nd Edition (2004a) 415-451.

Humphreys F.J. and Hatherly M. Recovery After Deformation, Chapter 6 in Recrystallization and Related Annealing Phenomena Authors: F.J. Humphreys and M. Hatherly 2nd Edition (2004b) 169-213.

Hurst C. L., Duncanson M. G., Nanda R. S. and Angolkar P. V. An Evaluation of the Shape-Memory Phenomenon of Nickel-Titanium Orthodontic Wires. *American Journal of Orthodontics and Dentofacial Orthopedics*, vol. 98 (1990) 72–76.

Iijima M., Ohno H., Kawashima I., Endo K. and Mizoguchi I. Mechanical Behavior at Different Temperatures and Stresses for Superelastic Nickel-Titanium Orthodontic Wires Having Different Transformation Temperatures. *Dental Materials*, vol. 18 (2002) 88–93.

International Organization for Standardization. ISO 15841: Dentistry – wires for use in orthodontics. Geneva: ISO 15841:2014 - Dentistry - Wires for use in orthodontics (2014).

Jiang S. and Zhang Y. Microstructure Evolution and Deformation Behavior of As-Cast NiTi Shape Memory Alloy Under Compression. *Transactions of Nonferrous Metals Society of China*, vol. 22 (2012) 90–96.

Jiang S.Y, Zhang Y.Q., Zhao Y.N., Liu S.W., Li H. and Zhao C.Z. Influence of Ni₄Ti₃ precipitates on phase transformation of NiTi shape memory alloy. *Transactions of Nonferrous Metals Society of China*, vol. 25 (2015) 4063–4071.

- Jiang S.Y., Ahng Y.Q and Zhao Y.N. Dynamic recovery and dynamic recrystallization of NiTi shape memory alloy under hot compression deformation, *Transactions of Nonferrous Metals Society of China*, vol. 23 (2013a) 140-147.
- Jiang S.Y., Zhao Y.N., Zhang Y.Q., Hu L. and Liang Y.L. Effect of solution treatment and aging on microstructural evolution and mechanical behavior of NiTi shape memory alloy. *Transactions of Nonferrous Metals Society of China*, vol. 23 (2013b) 3658–3667.
- Johnson, E. Relative stiffness of beta titanium archwires. *The Angle Orthodontist*, vol. 73 (2003) 259–269.
- Kabiri, Y., Kermanpur, A. and Foroozmehr A. Comparative study on microstructure and homogeneity of NiTi shape memory alloy produced by copper boat induction melting and conventional vacuum arc melting. *Vacuum*, vol. 86 (2012) 1073-1077
- Ke C., Cao S.S., Ma X. and Zhang X. P. Modeling of Ni₄Ti₃ precipitation during stress-free and stress-assisted aging of bi-crystalline NiTi shape memory alloys. *Transactions of Nonferrous Metals Society of China*, vol. 22 (2012) 2578-2585.
- Khalil-Allafi J., Eggeler G., Dlouhy A., Schmahl W. W. and Somsen C. On the influence of heterogeneous precipitation on martensitic transformations in a Ni-rich NiTi shape memory alloy. *Materials Science and Engineering: A*, vol. 378 (2004) 148–151.
- Khalil-Allafi J., Ren X. and Eggler G. The Mechanism of Multistage Martensitic Transformations in Aged Ni-rich NiTi Shape Memory Alloys. *Acta Materialia*, vol. 50 (2002) 793-803.
- Khamatkar A. Ideal Properties of Orthodontic Wires and Their Clinical Implications – A Review. *IOSR-JDMS*, vol. 14 (2015) 47-50
- Khamei A. and Dehghani K. Microstructural evolution during the hot deformation of Ti-55Ni (at. pct) intermetallic alloy. *Metallurgical Transactions A, Physical Metallurgy and Materials Science*, vol. 41 (2010) 2595–2605.
- Kotha, S. R, Alla R., Shammam M. and Ravi R. An Overview of Orthodontic Wires. *Trends in Biomaterials & Artificial Organs*, vol. 28 (2014) 32–36.
- Kusy R.P. and Whitley J. Q. Thermal and mechanical characteristics of stainless steel, titanium-molybdenum, and nickel-titanium archwires. *American Journal of Orthodontics and Dentofacial Orthopedics*, vol 131 (2007) 229-237.
- Kusy R.P. Orthodontic Biomaterials: From the Past to the Present. *Angle Orthodontist*, vol. 72 (2002) 501-512.
- Laplanche G., Birk T., Schneider S., Frenzel J. and Eggeler G. Effect of temperature and texture on the reorientation of martensite variants in NiTi shape memory alloys. *Acta Materialia*, vol. 127 (2017) 143-152.
- Laplanche G., Kazuch A. and Eggeler G. Processing of NiTi shape memory sheets – Microstructural heterogeneity and evolution of texture. *Journal of Alloys and Compounds*, vol. 651 (2015) 333–339.
- Lekston Z. Zuko M., Lelatko J., Stroz D. Gorycka T., Wierzchon T., Sieniawski J. and Dybich J. The Structure and Properties Formation of the NiTi Shape Memory Rods after Hot Rotary Forging. *Key Engineering Materials*, vol. 687 (2016) 11–18.

- Lekston Z. and Gliewka E. X-ray diffraction studies of NiTi shape memory alloys. *Archives of Materials Science and Engineering*, vol. 28 (2007) 665-672.
- Liu Y., Chen X. and McCormick P.G. Effect of low temperature ageing on the transformation behavior of near-equiatomic NiTi. *Journal of Materials Science*, vol. 32 (1997) 5979 — 5984.
- Liu Y., Mahmud A., Kursawe F. and Nam T. Effect of pseudoelastic cycling on the Clausius-Clapeyron relation for stress-induced martensitic transformation in NiTi. *Journal of Alloys and Compounds*, vol. 449 (2008) 82–87.
- Luo J., Bobanga J.O. and Lewandowski J.J. Microstructural heterogeneity and texture of as-received, vacuum arc-cast, extruded, and re-extruded NiTi shape memory alloy. *Journal of Alloys and Compounds*, vol. 712 (2017) 494-509
- Malik N., Dubey R., Kallury A., Chauksye A., Shrivastav T., and Kapse B. R. A Review of Orthodontic Archwires. *International Journal of Orofacial Research*, vol. 5 (2015) 6–11.
- McCormick P.G., Liu Y., Chena Y. and Favier D. Multistage transformation behaviour in NiTi. Proceedings of the Symposium K: Environment Conscious Materials of the 3rd IUMRS *International Conference on Advanced Materials, Sunshine City, Ikebukuro, Tokyo, Japan, August 31–September 4, 1993*, (1994) 1105-1108.
- Melsen B., Cattaneo P. M., Dalstra M. and Kraft D. C. The Importance of Force Levels in Relation to Tooth Movement. *Seminars in Orthodontics*, vol. 13 (2007) 220–233.
- Meng Q., Wu Z., Bakhtiari R., Zhang J., Yang H. and Liu Y. Stress serration and archshaped Lüders stress plateau behaviour of Ti–50.8 at% Ni wire prepared by selective electrical resistance over-aging. *Smart Materials and Structures*, vol. 25 (2016) 115035.
- Mirzadeh H. and Parsa M. H. Hot deformation and dynamic recrystallization of NiTi intermetallic compound. *Journal of Alloys and Compounds*, vol. 614 (2014) 56–59.
- Mirzadeh H., Cabrer A., Najafizadeh A. and Calvillo P.R. EBSD study of a hot deformed austenitic stainless steel. *Materials Science and Engineering A*, vol. 538 (2012) 236-245.
- Mirzadeh H., Najafizadeh A. and Moazeny M. Flow Curve Analysis of 17-4 PH Stainless Steel under Hot Compression Test. *Metallurgical and Materials Transactions A*, vol. 40A (2009) 2950-2958.
- Mirzadeh H., Najafizadeh A. Prediction of the critical conditions for initiation of dynamic recrystallization. *Materials and Design*, vol. 31 (2010) 1174–1179.
- Miyazaki S. Martensitic transformation in TiNi alloys In: Thin Film Shape Memory Alloys. Editors: Miyazaki S., Fu Y. Q. and Huang W. M., Eds. Cambridge: Cambridge University Press, (2009) 73–87.
- Miyazaki S., Otsuka K. and Wayman C. M., The shape memory mechanism associated with the martensitic transformation in Ti-Ni alloys-II. Variant coalescence and shape recovery. *Acta Metallurgica*, vol. 37 (1989) 1885–1890.
- Mohd J., Leary M., Subic A. and Gibson M. A review of shape memory alloy research, applications and opportunities. *Materials & Design*, vol. 56 (2014) 1078–1113.

- Morakabati M., Kheirandish S., Aboutalebi M., Taheri A. K. and Abbasi S. M. A study on the hot workability of wrought NiTi shape memory alloy. *Materials Science and Engineering: A*, vol. 528 (2011) 5656–5663.
- Morgan N., Wick A., DiCello J. and Graham R. Carbon and Oxygen Levels in Nitinol Alloys and the Implications for Medical Device Manufacture and Durability. In: *Proceedings of International Conference on Shape Memory and Superelastic Technologies*, California, 2008 ASM International (2008) 821-828.
- Muguruma T., Iijima M. and Mizoguchi I. Corrosion of laser-welded stainless-steel orthodontic wires. *Orthodontic Waves*, vol. 77 (2018) 18–23
- Mullins W. S., Bagby M. D. and Norman T. L. Mechanical behavior of thermo-responsive orthodontic archwires. *Dental Materials*, vol. 12 (1996) 308–314.
- Nakahata T. Industrial processing of titanium-nickel (Ti-Ni) shape memory alloys (SMAs) to achieve key properties, In: *Shape Memory and Superelastic Alloys: Technologies and Applications*, 1st ed. Editors: Yamauchi K., Ohkata I., Tsuchiya K., and Miyazaki S., Ed. Philadelphia: Woodhead Publishing Limited, (2011) 53–62.
- Nespoli A., Villa E., Bergo L., Rizzacasa A. and Passaretti F., DSC and Three-Point Bending Test for the Study of the Thermo-Mechanical History of NiTi and NiTi-based Orthodontic Archwires: The Material Point of View. *Journal of Thermal Analysis and Calorimetry*, vol. 120 (2015) 1129–1138.
- Nishida M., Wayman C. M. and Honma T. Precipitation processes in near-equiatomic TiNi shape memory alloys. *Metallurgical and Materials Transactions A*, vol. 17 (1986) 1505–1515.
- Ohara A. Clinical Importance of austenitic final point on the selection of nickel-titanium alloys for application in orthodontic-use arches. *Revista Odontológica Mexicana*, vol. 20 (2016) 162–169.
- Olbricht J., Yawny A., Pelegrina J.L., Dlouhy A. and Eggeler G. On the Stress-Induced Formation of R-Phase in Ultra-Fine-Grained Ni-Rich NiTi Shape Memory Alloys *Metallurgical and Materials Transactions A*, vol. 42A (2011) 2256-2574.
- Olbricht J., Yawny A., Pelegrina J.L., Eggeler G. and Yardley V.A. Characteristics of the stress-induced formation of R-phase in ultrafine-grained NiTi shape memory wire. *Journal of Alloys and Compounds*, vol. 579 (2013) 249-252.
- Oliveira J. P., Cavaleiro A.J, Schell N., Stark A., Miranda R., Ocana J.L. and Braz Fernandes F.M. Effects of laser processing on the transformation characteristics of NiTi: A contribute to additive manufacturing. *Scripta Materialia*, vol. 152 (2018) 122-126.
- Otsuka K. and Ren X. Physical metallurgy of Ti–Ni-based shape memory alloys. *Progress in Materials Science*, vol. 50 (2005) 511–678.
- Otsuka K. Science and Technology of Shape-Memory Alloys: New Developments. *MRS Bull.* (2002) 91–100.
- Otubo J., Rigo O. D., Coelho A. A., Neto C. M. and Mei P. R. The influence of carbon and oxygen content on the martensitic transformation temperatures and enthalpies of NiTi shape memory alloy. *Materials Science and Engineering: A*, vol. 481–482 (2008) 639–642.

- Panton B., Michael A., Zhou Y. N. and Khan M. I. Effects of post-processing on the thermomechanical fatigue properties of laser modified NiTi. *International Journal of Fatigue*, vol. 84 (2017) Article: *In Press*.
- ParyabM., Nasr A., Bayat O. and Vahid Abouei A. E. Effect of heat treatment on the microstructural and superelastic behavior of NiTi alloy with 58.5wt% Ni. *MJoM*, vol. 16 (2010) 123–131.
- Paula S., Heitor J., Godinho P., Braz Fernandes F.M. and Sérgio C. Textural Evolution in Ti-rich and Ni-rich Ni-Ti Shape Memory Alloys Submitted to Thermomechanical Treatment. In: *Proceedings of 62th ABM Annual Congress*, (2007) 3426–3434.
- Pelton A. R., Dicello J. and Miyazaki S. Optimization of processing and properties of medical grade Nitinol wire. *Minimally Invasive Therapy & Allied Technologies*, vol. 9 (2000) 107–118.
- Pilon J. J., Kuipers-Jagtman A.M. and Maltha J. C. Magnitude of orthodontic forces and rate of bodily tooth movement. An experimental study. *American journal of orthodontics and dentofacial orthopedics*, vol. 110 (1996) 16–23.
- Povoden-Karadeniz E., Cirstea D.C, Lang P., Wojcik T. and Kozeschnik E. Thermodynamics of Ti–Ni shape memory alloys. *CALPHAD: Computer Coupling of Phase Diagrams and Thermochemistry*, vol. 41 (2013) 128–139.
- Proffit W., Fields H., and Sarver D., Contemporary Orthodontics. Elsevier Inc., 5th ed., (2013) 1-678.
- Proffit W., Fields H., and Sarver D., Contemporary Orthodontics. Elsevier Inc., 6th ed., (2018) 1-784.
- Qiuhui Q., Peng H., Fan Q., Zhang L. and Wen Y. Effect of second phase precipitation on martensitic transformation and hardness in highly Ni-rich NiTi alloys. *Journal of Alloys and Compounds*, vol. 739 (2018) 873–881.
- Ramaiah K.V., Saikrishna C.N., Bhaumik S.K., Bhattacharya A., Nandy T.K. and Sagar P.K. Melting and processing of Ni-Ti shape memory alloys, *Metals Mater. Process*, vol. 18 (2006) 411-420.
- Reinholz B. and Brinckmann S. Phase transformations in the proximity of TiC precipitates in a NiTi matrix during fatigue. *International Journal of Fatigue*, vol. 41 (2012) 72–82.
- Ribeiro S. B., Andrade T. G., Paula A. S., Lins J. F. C., Mahesh K. K. and Braz Fernandes F. M. Textural Evolution Evaluated by EBSD and XRD after Thermal Treatment in Ni-Ti Shape Memory Alloy. *Materials Science Forum*, vol. 702–703 (2011) 884–887.
- Ribeiro S., Recuperação e Recristalização de Liga NiTi Deformada por Compressão e Tratada Termicamente no Intervalo entre 150 E 500 °C, Universidade Federal Fluminense, PhD Thesis, Brazil (2015).
- Riley M. and Bearn D. R. A systematic review of clinical trials of aligning archwires. *Journal of Orthodontics*, vol. 36 (2009) 42–51.
- Rodrigues P., Braz Fernandes F.M., Paula A.S., Oliveira J.P., Ribeiro S., Teixeira E. and Schell N. Microstructural characterization of NiTi shape memory alloy produced by rotary hot forging. *Powder Diffraction*, vol. 32 (2017a) S201–S206.

- Rodrigues P.F., Braz Fernandes F.M., Teixeira E., Baptista S., Paula A.S. and Oliveira J.P. Influence of ageing treatment on the thermophysical characteristics and mechanical properties of forging wire Ni-rich NiTi alloy for superelastic applications. *Ciência & Tecnologia dos Materiais*, (2017b) e23-e26.
- Rodrigues P.F., Inácio P., Camacho E., Santos T. and Braz Fernandes F.M. Structural Characterization of Functionally Graded Shape Memory Alloys. *TMQ – Techniques, methodologies and quality*, (2018) Article: *In Press*.
- Saburi T. Ti-Ni Shape Memory Alloys. in: *Shape Memory Materials, in Shape Memory Materials*. 1st ed. Editors: Wayman C.M., Otsuka K. Ed. New York: Cambridge University Press (1998) 49–96.
- Safdel A., Zarei-Hanzaki A., Shamsolhodaie A., Krooß P. and Niendorf T. Room temperature superelastic responses of NiTi alloy treated by two distinct thermomechanical processing schemes. *Materials Science and Engineering A*, vol. 684 (2017) 303-311.
- Sakai T., Belyakov A., Kaibyshev R., Miura H. and Jonas J. Dynamic and post-dynamic recrystallization under hot, cold and severe plastic deformation conditions. *Progress in Materials Science*, vol. 60 (2014) 130–207.
- Sakima M.T., Dalstra M. and Melsen B. How does temperature influence the properties of rectangular nickel-titanium wires? *European Journal of Orthodontics*, vol. 28 (2006) 282–291.
- Sevilla P., Martorell F., Libenson C., Planell J.A. and Gil F.J. Laser welding of NiTi orthodontic archwires for selective force application, *Journal of Materials Science: Materials in Medicine*. vol. 19 (2008) 525–529.
- Shariat B.S., Meng. Q., Mahmud A.S., Wu Z., Bakhtiari R., Zhang J., Motazedian F., Yang H., Rio G., Nam T. and Liu Y. Functionally graded shape memory alloys: Design, fabrication and experimental evaluation. *Materials & Design*, vol. 124 (2017) 225–237.
- Simões J., Pereira F. F. R., Otubo J. and Araújo C. J. Influence of Heat Treatments on a NiTi Shape Memory Alloy Obtained Using Vacuum Induction Melting and Reprocessed by Plasma Skull Push-Pull. *Materials Research*, vol. 1765 (2015) 121–126.
- Sittner P., Landa M., Luka P. and Novak V. R-phase transformation phenomena in thermomechanically loaded NiTi polycrystals. *Mechanics of Materials*, vol. 38 (2006) 475–492.
- Somsen C., Zähres H., Wassermann E.F., Kakeshita T. and Saburi T. Influence of thermal annealing on the martensitic transitions in Ni–Ti shape memory alloys. *Materials Science and Engineering: A*, vol. 273 (1999) 310-314.
- Spini T. Avaliação da qualidade de fios ortodônticos de níquel-titânio termoativados através das propriedades termomecânicas obtidas de análise térmica (DSC, DMA) e ensaio mecânico (flexão de três pontos). Universidade Federal do Mato Grosso do Sul, PhD Thesis, Brazil (2017).
- Spini T., Valarelli F., Cançado R., Freitas K. and Villarinho D. Transition temperature range of thermally activated nickel-titanium archwires. *Journal of Applied Oral Science*, vol. 22 (2014) 109-117.

- Srinivasan N. and Prasad Y. V. R. K. Characterisation of dynamic recrystallisation in nickel using processing map for hot deformation. *Materials Science and Technology*, vol. 8 (1992) 206-212.
- Sudershan A. Thermomechanical Characterization of Variable Force NiTi Orthodontic Archwires. Marquette University, USA, Masters Thesis (2015)
- Sun B., Lin J. and Fu M.W. Dependence of processing window and microstructural evolution on initial material state in direct electric resistance heat treatment of NiTi alloy. *Materials & Design*, vol. 139 (2018) 549-564.
- Suresh K. S., Kim D. I., Bhaumik S. K. and Suwas S. Interrelation of grain boundary microstructure and texture in a hot rolled Ni-rich NiTi alloy. *Scripta Materialia*, vol. 66 (2012) 602–605.
- Suzuki Y. Fabrication of shape memory alloys, In: Shape Memory Materials, 1st ed., Editors: Otsuka K. and Wayman C. M., Ed. New York: Cambridge University Press, (1998) 33–148.
- Świec P., Zubko M., Lekston Z. and Stróż D. Structure and Properties of NiTi Shape Memory Alloy after Cold Rolling in Martensitic State. *Acta Physica Polonica A*, vol. 130 (2016) 1081-1084.
- Tang W. Thermodynamic study of the low-temperature phase B19' and the martensitic transformation in near-equiatomic Ti-Ni shape memory alloys. *Metallurgical and Materials Transactions A*, vol. 28 (1997) 537–544.
- Tang W., Sundman B. Sandström R. and Qiu C. New modelling of the B2 phase and its associated martensitic transformation in the Ti–Ni system. *Acta Materialia*, vol. 47 (1999) 3457-3468.
- Treppmann D. and Hornbogen E. On the Influence of Thermomechanical Treatments on Shape Memory Alloys. *Journal de Physique IV*, vol. 07 (1997) C5 211-220.
- Vashista M. and Paul S. Correlation between full width at half maximum (FWHM) of XRD peak with residual stress on ground surfaces. *Philosophical Magazine*, vol. 92 (2012) 4194-4204.
- Willemsse P., Koopman B. and Beyer J. The Texture Development of Ti-Ni-Cu Wire During Thermomechanical Cycling. *Journal de Physique IV*, vol. 1 (1991) C5 329 - 333.
- Wang X., Li K., Schryvers D., Verlinden B. and Humbeeck J.V. R-phase transition and related mechanical properties controlled by low-temperature aging treatment in a Ti–50.8 at.% Ni thin wire. *Scripta Materialia*, vol. 72–73 (2014) 21–24.
- Wu L.M. and Wu S.K., The Evolution of Ti₂Ni Precipitates in Annealed Ti₅₁Ni₄₉ Shape Memory Melt-Spun Ribbons. *Philosophical Magazine Letters*, vol. 90 (2010) 261–268.
- Wu M. H. Fabrication of Nitinol Materials and Components. *Materials Science Forum*, vol. 394–395 (2002) 285–292.
- Yeung K. W. K., Cheung K.M.C., Lu W.W. and Chung C.Y. Optimization of thermal treatment parameters to alter austenitic phase transition temperature of NiTi alloy for medical implant. *Materials Science and Engineering A*, vol. 383 (2004) 213-218.

Young M.L., Wagner M.F., Frenzel J., Schmahl W.W. and Eggeler G. Phase volume fractions and strain measurements in an ultrafine-grained NiTi shape-memory alloy during tensile loading. *Acta Materialia*, vol. 58 (2010) 2344–2354.

Zhang J., Fan G., Zhou Y., Ding X., Otsuka K., Nakamura K., Sun J. and Ren X. Does order–disorder transition exist in near-stoichiometric Ti–Ni shape memory alloys? *Acta Materialia*, vol. 55 (2007) 2897–2905.

Zhang Z., Frenzel J., Neuking K. and Eggeler G. On the reaction between NiTi melts and crucible graphite during vacuum induction melting of NiTi shape memory alloys. *Acta Materialia*, vol. 53 (2005) 3971–3985.

Zhou Y., Zhang J., Fan G., Ding X., Sun J., Ren X. and Otsuka K. Origin of 2-stage R-phase transformation in low-temperature aged Ni-rich Ti–Ni alloys. *Acta Materialia*, vol. 53 (2005) 5365–5377.

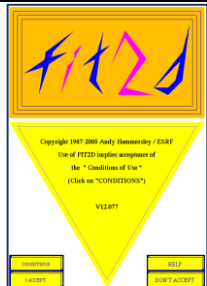

Appendix

A.1 – FIT2D³

FIT2D is both a general purpose and specialist analysis program supporting one and two dimensional data processing. For the XRD experiments, raw data are collected as 2D images (TIF format) of Debye-Scherrer rings. FIT2D allows the 2D images to be integrated to 1D profile with user specified 2θ . It provides a variety of different output possibilities, such as different 2θ scans, for different azimuth ranges; a 1D profile of intensity of a ring as a function of azimuth; or a polar transform of the data.

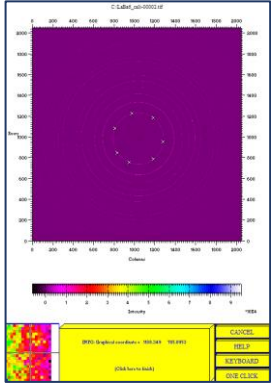
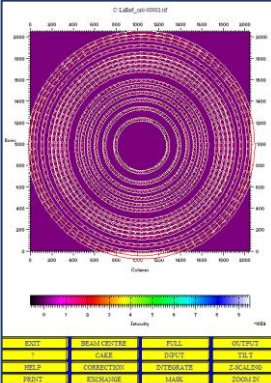
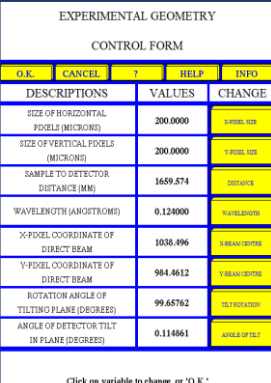
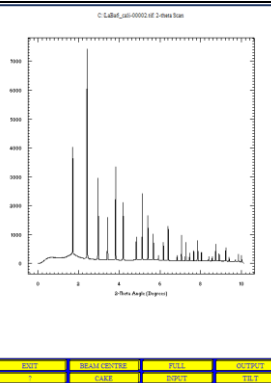
The diffraction patterns must be calibrated for accurate analysis. In our case, LaB₆ powder standard was used. This powder is generally put on sample holder and exposed to x-ray with similar experimental parameters as for the sample (same detector distance, etc). Additional patterns may be taken at different detector positions in order to gain precision. Those well-known samples allow corrections for detector tilt, sample-detector distance and beam center position. Such operations were done using the Fit2D software package available from ESRF³ (Hammersley, 1996).

In the next table we present the typical interfaces of the FIT2D program for the most common procedures used in this work.

Instructions	Interfaces of the FIT2D program	Comments
<p>1- Open FIT2D program and I ACCEPT.</p> <p>2- Check the Values and select OK</p>	 <p style="text-align: center;">1</p>	 <p style="text-align: center;">2</p>

³ Website: <http://www.esrf.eu/computing/scientific/FIT2D/>

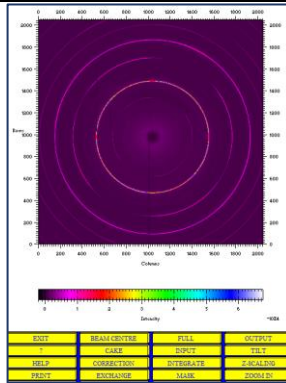
<p>3- Select POWDER DIFFRACTION – 2D sub-menu.</p>	<p style="text-align: center;">3</p>	
<p>4- Select INPUT sub-menu</p>	<p style="text-align: center;">4</p>	
<p>5- In this step a <i>tif</i> file will be chosen.</p>	<p style="text-align: center;">5</p>	
<p>Calibration</p>		
<p>6- The calibrant sub-menu is selected and the LaB₆ chosen. 7- In FIT2D There are some calibrant options</p>	<p style="text-align: center;">6</p>	<p style="text-align: center;">7</p>

<p>8- Some points are user-selected for a specific ring through the graphical interface</p>	 <p style="text-align: center;">6</p>	<p>It is generally found that the best fit is obtained when taking into account only well separated rings.</p>
<p>9- After finishing the selection of the points, other rings are then selected for inclusion in the refinement procedure</p>	 <p style="text-align: center;">7</p>	
<p>10- A number of parameters can be entered by user, including pixel size. 11- Choose to refine sample detector distance. 12- Select OK</p>	 <p style="text-align: center;">11</p>	<p>Other parameters can be chosen to be refined.</p> <p>It is advised not to refine wavelength and distance together.</p>
<p>13- Select OUTPUT</p>	 <p style="text-align: center;">13</p>	<p>The output formats are also variable such as CHIPLLOT, SPREAD SHEET formats, as well as ASCII format, which can be used for multiple purposes for further analysis.</p>

Data Analysis

Integration 0 - 360°

6- Select INTEGRATE sub-menu



6

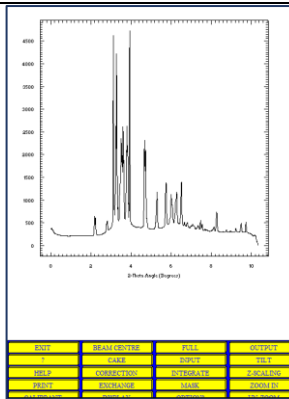
7- Input the correct parameters
8- OK

EXPERIMENTAL GEOMETRY CONTROL FORM				
O.K.	CANCEL	?	HELP	INFO
DESCRIPTIONS	VALUES			
SIZE OF HORIZONTAL PIXELS (MICRONS)	200.0000	HORIZONTAL		
SIZE OF VERTICAL PIXELS (MICRONS)	200.0000	VERTICAL		
SAMPLE TO DETECTOR DISTANCE (MM)	1652.000	DISTANCE		
WAVELENGTH (ANGSTROMS)	0.124000	WAVELENGTH		
X-PIXEL COORDINATE OF DIRECT BEAM	960.2349	X-COORDINATE		
Y-PIXEL COORDINATE OF DIRECT BEAM	1004.761	Y-COORDINATE		
ROTATION ANGLE OF TILTING PLANE (DEGREES)	0.0	TILTING PLANE		
ANGLE OF DETECTOR TILT IN PLANE (DEGREES)	0.0	ANGLE OF TILT		

Click on variable to change, or 'O.K.'

7

9- Select OUTPUT



9

The output formats are also variable such as CHIPLLOT (2 columns 2 θ / Intensity), SPREAD SHEET (2D matrix of intensities; rows: azimuthal angle; columns: 2θ), in ASCII format, which can be used for multiple purposes for further analysis.

3 - Input the macro and select the first and last tif. file

```
%!* \ BEGINNING OF GUI MACRO FILE
```

```
%!* \
```

```
%!* \ This is a comment line
```

```
%!* \
```

```
EXIT
```

```
POWDER DIFFRACTION (2-D)
```

```
INPUT
```

```
#IN
```

```
O.K.
```

```
O.K.
```

```
CAKE
```

```
KEYBOARD
```

```
1744.500
```

```
1746.000
```

```
1
```

```
5.0000000E+01
```

```
2.5000000E+01
```

```
1
```

```
5.0000000E+01
```

```
5.0000000E+01
```

```
1
```

```
2.0000000E+01
```

```
1.2500000E+01
```

```
1
```

```
2.5000000E+01
```

```
1.2500000E+0
```

```
INTEGRATE
```

```
X-PIXEL SIZE
```

```
200.0000
```

```
Y-PIXEL SIZE
```

```
200.0000
```

```
DISTANCE
```

```
1771.147
```

```
WAVELENGTH
```

```
0.124
```

```
X-BEAM CENTRE
```

```
1013.434
```

```
Y-BEAM CENTRE
```

```
1030.978
```

```
TILT ROTATION
```

```
0.0
```

```
ANGLE OF TILT
```

```
0.0
```

```
O.K.
```

```
START AZIMUTH
```

```
0.0000
```

```
END AZIMUTH
```

```
360.0000
```

```
INNER RADIUS
```

```
100.000
```

```
OUTER RADIUS
```

```
1000.000
```

```
SCAN TYPE
```

```
2-THETA
```

```
AZIMUTH BINS
```

```
360
```

```
RADIAL BINS
```

```
900
```

```
O.K.
```

```
EXIT
```

```
OUTPUT
```

```
SPREAD SHEET
```

```
YES
```

```
#OUT
```

```
EXIT
```

```
MACROS / LOG FILE
```

```
%!* \ END OF IO MACRO FILE
```

A.2 – Analysis of 2θ position and austenite peaks intensity along the azimuthal angle.

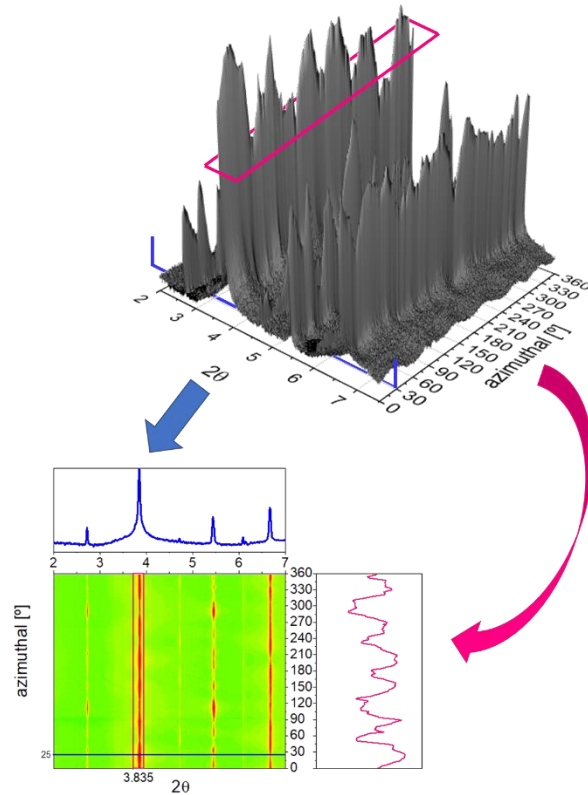


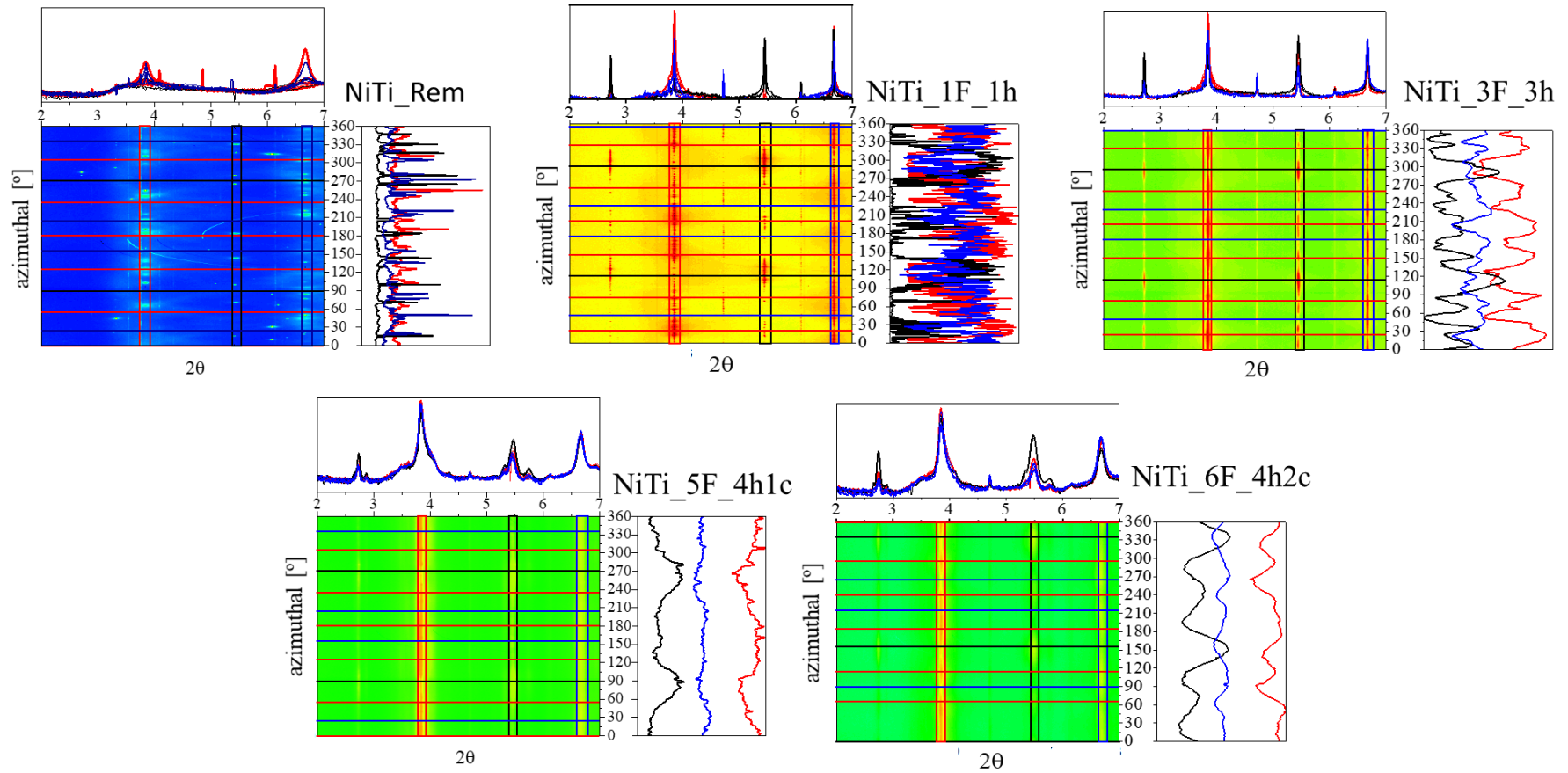
Figure A.2 -1 The 2-D and 3-D in situ x-ray diffraction example to variation of the 2θ peak position and intensity of the $(110)_{B2}$, $(200)_{B2}$ and $(211)_{B2}$ peaks along the azimuthal angle.

An analysis example of the variation of the 2θ peak position and intensity of the $(110)_{B2}$, $(200)_{B2}$ and $(211)_{B2}$ peaks along the azimuthal angle - ϕ [360°] is shown in Figure A.2-1, by the level chart:

-Blue Arrow: corresponds the observation of a single Phi. The 2θ position of each austenite peak can be observed by the upper box to the level chart. In this example the phi 30 is represented, highlighted by the blue line in the 3d chart.

-Pink arrow: corresponds to the observation of the variation of the austenite peaks intensities. The variation of the intensity of the peak positioned at 2θ equals to 3.835 along the azimuthal angle that can be observed by the right box of the level chart. In this example the $(110)_{B2}$ peak depicted is highlighted by the pink rectangle in the 3d chart.

A.3 – Supplementary Figures - Figure 4.28



A.3-1 Variation of the 2θ peak position and intensity of the (110)_{B2}, (200)_{B2} and (211)_{B2} peaks along the azimuthal angle for each rotary forging steps.

